N° d'ordre : 4659

THÈSE

PRÉSENTÉE A

L'UNIVERSITÉ BORDEAUX 1

ÉCOLE DOCTORALE DES SCIENCES CHIMIQUES

Par R. Anand Theerthan

POUR OBTENIR LE GRADE DE

DOCTEUR

SPÉCIALITÉ : Science des matériaux

Effect of electric and magnetic stresses on ferroelectric single crystals and ceramics

Directeur de recherche : M. M. Maglione

Soutenue le : 5 décembre 2012

Après avis de :

M. **Antoine Maignan**	Directeur de recherche – CRISMAT (CNRS)	Rapporteur
M. **Marin Alexe**	Directeur de recherche – MPI Halle	Rapporteur

Devant la commission d'examen formée de :

M. **Claude Delmas**	Directeur de recherche – ICMCB (CNRS)	Président du Jury
M. **Jean Etourneau**	Professeur – ICMCB (CNRS)	Membre invité
M. **Antoine Maignan**	Directeur de recherche – CRISMAT (CNRS)	Rapporteur
M. **Marin Alexe**	Directeur de recherche – MPI Halle	Rapporteur
M. **Mario Maglione**	Directeur de recherche – ICMCB (CNRS)	Examinateur
M. **Josep Fontcuberta**	Professeur – ICMAB (Barcelona)	Examinateur
M. **Vincent Rodriguez**	Professeur – ISM (Bordeaux)	Examinateur

N° d'ordre : 4659

THÈSE

PRÉSENTÉE A

L'UNIVERSITÉ BORDEAUX 1

ÉCOLE DOCTORALE DES SCIENCES CHIMIQUES

Par R. Anand Theerthan

POUR OBTENIR LE GRADE DE

DOCTEUR

SPÉCIALITÉ : Science des matériaux

Effect of electric and magnetic stresses on ferroelectric single crystals and ceramics

Directeur de recherche : M. M. Maglione

Soutenue le : 5 décembre 2012

Après avis de :

M. **Antoine Maignan**	Directeur de recherche – CRISMAT (CNRS)	Rapporteur
M. **Marin Alexe**	Directeur de recherche – MPI Halle	Rapporteur

Devant la commission d'examen formée de :

M. **Claude Delmas**	Directeur de recherche – ICMCB (CNRS)	Président du Jury
M. **Jean Etourneau**	Professeur – ICMCB (CNRS)	Membre invité
M. **Antoine Maignan**	Directeur de recherche – CRISMAT (CNRS)	Rapporteur
M. **Marin Alexe**	Directeur de recherche – MPI Halle	Rapporteur
M. **Mario Maglione**	Directeur de recherche – ICMCB (CNRS)	Examinateur
M. **Josep Fontcuberta**	Professeur – ICMAB (Barcelona)	Examinateur
M. **Vincent Rodriguez**	Professeur – ISM (Bordeaux)	Examinateur

Laboratoire : Institut de Chimie de la Matière Condensée de Bordeaux

Code unité : UPR 9048

Adresse : 87, Avenue du Docteur Albert Schweitzer, 33608 Pessac Cedex

Site internet : http://www.icmcb-bordeaux.cnrs.fr

..... This thesis is dedicated to my loving aunt Saroja and my parents who have been the pillars of my life

Abstract:

The mobility of free charges and its localization mechanism has considerable effect on the dielectric properties of the materials. Therefore single crystal of Fe doped $BaTiO_3$ and $KTiOPO_4$ (KTP) which have predominantly electronic and ionic conductivity respectively were studied under external stresses like electric and magnetic field. The application of external magnetic field affects the hopping of electrons which lead to tuning of polaron losses in $BaTiO_3$ whereas in case of KTP localization of K^+ ions give rise to splitting of piezoelectric resonance and it can be tuned by external electric field. In the second part new phosphates of formula $BaFeTi(PO_4)_3$ and $BiFe_2(PO_4)_3$ were synthesized to look for polarization property. However Bi^{3+} ions are not localized on their inversion symmetry site which is promising. Finally spinel Co_3O_4 was investigated under dielectric and Electron Paramagnetic Resonance spectroscopy which reveal an induction of polar state under external magnetic field.

Résumé:

La présence de charges libres a des conséquences considérables sur les propriétés diélectriques des matériaux. Pour mettre en évidence ces contributions, nous avons étudié l'influence de contraintes électriques et magnétiques sur des monocristaux de $BaTiO_3$ dopé Fer et de $KTiOPO_4$ (KTP). Dans $BaTiO_3$, l'application d'un champ magnétique perturbe le mécanisme de pertes diélectriques résultant de mécanismes polaroniques. Dans le KTP c'est la localisation des ions K^+ qui est perturbée par un champ électrique comme nous l'avons démontré en étudiant la séparation des raies de résonances piézoélectriques. Dans une deuxième partie, nous avons synthétisé et étudié la polarisation de phosphates de composition $BaFeTi(PO_4)_3$ and $BiFe_2(PO_4)_3$. Cependant, l'ion Bi^{3+} n'est jamais positionné sur son site d'inversion, ce qui est prometteur. Enfin, nous avons étudié la spinelle Co_3O_4 par spectroscopie diélectrique et RPE et nous avons montré l'induction d'un état polaire sous l'effet d'un champ magnétique.

General Introduction:

In recent years coupling between electrical and magnetic properties in a material is sought after very rigorously. Related to this, terms such as multiferroic, magnetocapacitance and magneto dielectrics came into existence where there is a coupling between dielectric (ferroelectric) and magnetic (ferromagnetic) property. Contributions for such a coupling could be both intrinsic and extrinsic. From the view point of ferroelectrics the intrinsic contribution is due to the lattice related electronic and ionic local displacement whereas the extrinsic contributions arises due to long range motion of free charges, for example creation of space charge. Similarly, extrinsic contribution to the coupling between electrical and magnetic property can also be due to the motion of free charge, a case in point is the magnetocapacitance due to the presence of magnetoresistive artifact as explained by Catalan [1]. Other extrinsic factors are strain, composite etc.

This thesis is thus focused on distinguishing the intrinsic and extrinsic coupling in dielectric and ferroelectric materials. In particular we will focus on the motion of free charges and its response to the external stresses like electric and magnetic field and how it can alter the dielectric properties of the material. Other extrinsic factors leading to coupling between electric and magnetic property will not be discussed since it is out of scope of the present thesis. We performed experiments on 4 cases, first two cases belong to well-known ferroelectric materials and the last two cases have not been investigated for their polarization properties until now. In the first two cases, everyday ferroelectrics like $BaTiO_3$ and $KTiOPO_4$ (KTP) were considered. To avoid unwanted interface contribution to the dielectric properties these materials were taken in the form of single crystals with well controlled stoichiometry and extended defect density. In $BaTiO_3$ unavoidable point defects such as oxygen vacancies or intentionally substituted defects like iron usually increase conductivity. Recently Maglione has shown that this electronic conductivity due to free charges at high temperatures can localize at interfaces such as domain walls which eventually lead to artificial magnetocapacitance (AMC) under magnetic field at the domain wall relaxation temperature [2]. Here we probe for AMC at low temperatures ($\approx$ 30 K) where the polaron relaxation occurs. We will show here that the polaron relaxation leading to dielectric losses can be tuned by dc magnetic field without change in the capacitance proving that no interface is involved. It will be shown further that dc magnetic field affects the way the electrons are hopping between different centers with the help of ESR spectroscopy and this is observed close to the relaxation maximum where the temperature and frequency are favorable. This tuning is not observed in the nominally pure ferroelectric single crystals like $BaTiO_3$, $SrTiO_3$ and $KTaO_3$. The charge carrier concentration in nominally pure crystals is less in

comparison to intentionally substituted single crystal like Fe doped $BaTiO_3$ which forbade them from being coupled to dc magnetic field.

Next we focused on the ionic conductivity in KTP due to the long range motion of potassium ions through the channels. The ionic conductivity in KTP slows down below 200 K and becomes insulator. This transition from superionic to insulator influences the piezoelectric property of KTP which splits the piezo resonance. It will be shown that accumulation of mobile ions leading to space charge is the major factor influencing the piezo resonance. This space charge can then be tuned by external stresses like electric field which in turn tune the piezoelectric resonance. μ-Second Harmonic Generation (SHG) microscope was used to visualize and map the space charge distribution. This powerful technique has shown that the mobile charges accumulate not only at the surface of the sample but also at other interfaces like domain walls. Therefore this coupling of ionic conductivity to piezoelectric resonance is intrinsic to KTP and can be anticipated to exist in other ferroelectrics showing polarization as well as ionic conductivity. To our knowledge this is the first time a link between polarization and ionic conductivity is found.

The next family of compounds synthesized and studied was phosphates of Nasicon (Sodium superionic conductor) structure. Some of the known phosphates like KTP and potassium dihydrogen phosphate (KDP) are good ferroelectrics however they are not magnetic. The Nasicon type phosphates allow for the incorporation of various transition metal and alkali cations which might lead to interesting electrical and magnetic property. At the same time Nasicon phosphates are known for their high ionic conductivity which might screen the polarization, in addition no known ferroelectrics exist in the phosphates of this structure. Therefore phosphates with barium and bismuth at A site were synthesized and they are $BaFeTi(PO_4)_3$ and $BiFe_2(PO_4)_3$. The choice of barium and bismuth is due to their ionic radius which is quite large that might limit their mobility and therefore their ionic conductivity. The compound $BaFeTi(PO_4)_3$ was already synthesized by Masse in 70's [3]. In this compound titanium sits in the octahedra environment (TiO_6) similar to $BaTiO_3$ which might induce polarization. However the space group of this compound is centrosymmetric and thus cannot lead to ferroelectric behavior. Nonetheless as expected barium compound behaves as a good dielectric with a low loss. At low temperatures a canted antiferromagnetic order sets in leading to interesting magnetic behavior. Unfortunately no coupling between dielectric and magnetic order is observed. The bismuth compound $BiFe_2(PO_4)_3$ is synthesized for the first time. Bismuth in A site is very interesting because of the polarizability of its lone pair. While macroscopic magnetic and dielectric properties show more or less the same trends as the Ba compound, the local symmetry at Bi site is promising. Indeed, we could successfully grow single crystals of $BiFe_2(PO_4)_3$ allowing for complete structural determination. It appears that Bi is not sitting at the inversion symmetry site

being off centered along the (001) direction due to the active lone pair. This uniaxial displacement is randomly distributed and this lack of correlation does not allow for long range ferroelectric order.

The last compound which was studied during this PhD is Co_3O_4, a spinel which is well known in the fields of magnetism and ionic conductors. This simple compound belongs to the broad family in which electronic ferroelectricity is actively investigated nowadays like $CoCr_2O_4$, $FeCr_2O_4$, $MnCr_2O_4$ etc [4] [5] [6]. We show that, at the magnetic transition of about 30K, a distinct dielectric and polarization anomaly can be induced by a magnetic field. We again made our best to remove all spurious conductivity contributions to this result, which would be an evidence for a new type 2 multiferroics. A strong support for this comes from EPR investigation which showed a canting of antiferromagnetic moments on cooling the ceramics under a magnetic field which eventually lead to polarization according to spin current model proposed by Katsura et al.

1. Chapter 1 will be dedicated to bibliography work done during this thesis
2. Chapter 2 will give the experimental details of this thesis
3. Chapter 3 will discuss the tuning of polaron losses under dc magnetic field in Fe doped $BaTiO_3$ single crystals
4. Chapter 4 will investigate coupling between ionic conductivity and piezoelectric resonance in KTP
5. Chapter 5 will give the synthesis and characterization of Nasicon type phosphates
6. Chapter 6 will study the intrinsic magnetoelectric coupling in Co_3O_4.

References:

[1] G. Catalan. *Appl. Phys. Lett*, 88:102902, 2006.

[2] M. Maglione. *J. Phys: Conden. Matt*, 20:322202, 2008.

[3] R. Masse. *Bull. Soc. Fr. Minéral. Cristallogr*, 95:405, 1972.

[4] Y. Yamasaki, S. Miyasaka, Y. Kaneko, J.P. He, T. Arima and Y. Tokura. Phys. Rev. Lett, 96:207204, 2006.

[5] N.Mufti, A.A.Nugroho, G.R. Blake and T.T.M. Palstra. *J. Phys: Condens. Matt*, 22:075902, 2010.

[6] A. Maignan, C. Martin, K. singh, Ch. Simon, O.I. Lebedev and S. Turner. *J. Sol. Stat. Chem*, doi: 10.1016/j.jssc.2012.01.063, 2012.

Contents:

Chapter 1

I. Dielectrics, ferroelectrics and multiferroics:

I.1. Dielectrics:

Dielectrics are insulators through which no steady conduction current can flow and when it is subjected to external electric field electric charges in the material shift from its equilibrium position causing polarization [1].

I.1.1. Dipole Moment and Polarization:

A pair of equal and opposite charges situated close enough compared with the distance to an observer is called an electric dipole (Figure I-1). Its dipole moment is given by

$$\vec{\mu} = q * d \qquad \textbf{Eq 1}$$

Here μ is the electric dipole moment in C m, q is electric charge in coulomb and d is the distance between the two equally opposite charges.

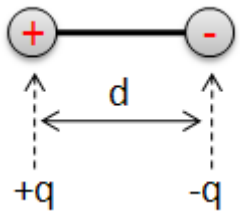

Figure I-1: Two equal and opposite charges separated by a distance d creates a dipole

Now, the polarization P is given by

$$\vec{P} = \sum \frac{\mu}{V} = <\mu>.N_V \qquad \textbf{Eq 2}$$

Where < μ > is the average vector dipole moment; N_V is the density of dipoles (per m^3) and polarization has the unit of $C.m^{-2}$ (Coulomb per Square meter) *i.e* Polarization has the dimension of an area charge which is evident from the following

Let us consider a simple parallel plate capacitor with homogenously polarized material inside the plates (Figure I-2). Assuming all dipoles have the same direction then the charge density inside a small probing volume is zero because there are as many positive charge as negative charges. But at the surface there are still uncompensated charges which are separated by the thickness of the dielectric slab. Hence we have surface polarization charge which is given by

$$\vec{P} = \frac{\sum_V \vec{\mu}}{V} = \frac{\sum_S \vec{\mu}}{V_S} = \frac{d.\sum_S q}{d.A} = \frac{\sum_S q}{A} \qquad \textbf{Eq 3}$$

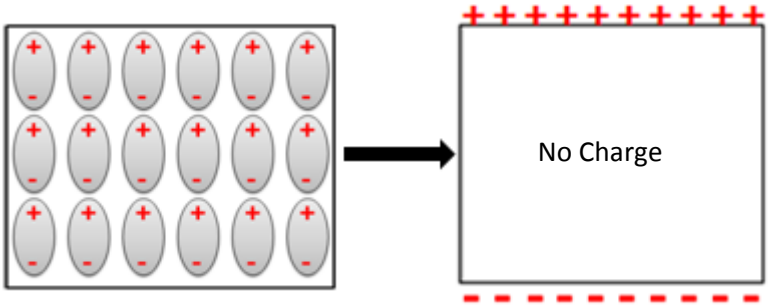

Figure I-2: Creation of surface charge due to polarization of the material. Note in the bulk there is no net charge since there is equal number of positive and negative charge.

I.1.2. Dielectric Displacement and Polarization:

The charge per unit area that would be generated at the surface of a layer of dielectric when placed in an electric field E is called dielectric displacement. It is given by

$$\vec{D} = \varepsilon_r . \varepsilon_0 . \vec{E} \qquad \textbf{Eq 4}$$

Where ε_r is the relative dielectric permittvity and ε_0 the one of vacuum. This can also be represented as

$$\vec{D} = \vec{D}_0 + \vec{P} = \varepsilon_0 . \vec{E} + \vec{P} \qquad \textbf{Eq 5}$$

Where D_0 is dielectric displacement in vacuum, P is the polarization of the material. But from empirical law we have

$$\vec{P} = \varepsilon_0 . \chi . \vec{E} \qquad \textbf{Eq 6}$$

Here χ is the dielectric susceptibility and by substituting Eq 6 in Eq 5 and comparing with Eq 4 we get

$$\varepsilon_r = 1 + \chi \qquad \textbf{Eq 7}$$

The above relation is valid only when $\vec{P}$ is parallel to $\vec{E}$ which is only possible in isotropic material. For anisotropic material $\vec{P}$ is not parallel to $\vec{E}$ then the quantities ε_r and χ are tensors.

I.1.3. Mechanism of Polarization:

The presence of permanent dipoles or creation of induced dipoles due to the displacement of positive and negative charge by the application of external electric field give rise to polarization. In general polarizability of the material arises due to number of mechanisms. If α represents the total polarizability of the material then it can be expressed as the sum of four terms.

$$\alpha = \alpha_e + \alpha_I + \alpha_O + \alpha_S \qquad \text{Eq 8}$$

where α_e, α_I, α_O and α_S are electronic, ionic, orientational and space charge polarization respectively. We will see each of them in the following.

- *Electronic Polarization:* This kind of polarization exists in all dielectrics. It arises due to the electronic polarization associated with the displacement of the electron cloud versus the nucleus. It is shown clearly in Figure I-3. Then the polarizability is approximately proportional to the volume of the electron shell. Therefore it is temperature independent and large atoms have a large electronic polarizability.

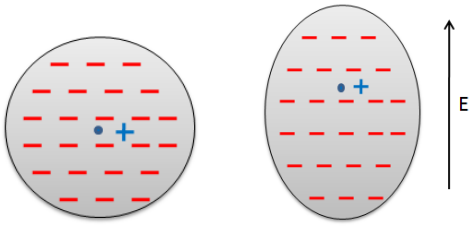

Figure I-3: Electron cloud surrounding the nucleus. When there is no external field the center of positive charge coincides with the center of negative charge. After the application of external field the positive and negative charge are no more at the center and a dipole is created due to electronic polarization.

- *Ionic Polarization:* This kind of polarization mainly occurs in ionic crystals and it is due to the displacement of positive and negative sublattices under an applied electric field. For example consider a simple ionic crystal NaCl. Each of Na^+ - Cl^- is a natural dipole but the net polarization is zero because for every dipole there is an equal dipole in opposite direction. Now if an external field is applied then the ions feel the force in opposite direction and a dipole is induced. This is shown schematically in Figure I-4

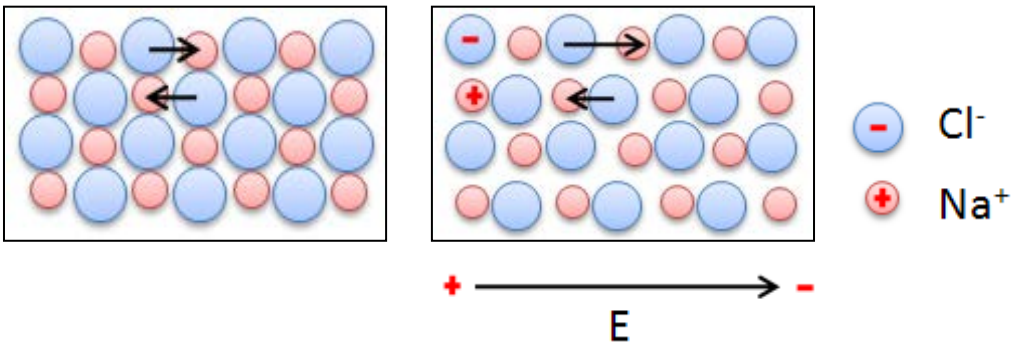

Figure I-4: (Left figure) Lattice of NaCl, there is charge neutrality in the material due to the existence of equal and opposite dipole, indicated by black arrows. (Right figure) With the application of external electric field, charge neutrality is broken and polarization is induced. Notice the dipole length indicated by black arrows.

- *Orientation Polarization:* In some materials there are built –in dipoles, for example water molecule. This is because positively charged H atoms have charge center different from negatively charged oxygen atom. But these dipoles are statistically distributed since they can rotate freely and the net dipole moment is zero as shown in the figure I-5 a. In the presence of applied field these permanent dipoles experience torque and consequently they orient along the direction of the field. This is shown schematically in figure I-5 b.

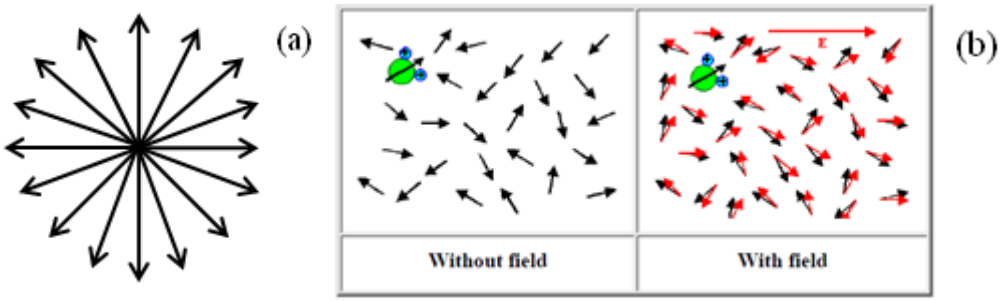

Figure I-5: (a) Statistical distribution of permanent dipoles leading to no polarization, (b) Orientation of dipoles along the direction of applied field which induces polarization.

- *Space Charge Polarization:* This kind of polarization arises due to the presence of charges which are not locally bound to the lattice. These charges then migrate and cause spatial inhomogeneity of charge carrier density. They may accumulate on grain boundaries, electrode and dielectric interfaces giving rise to interfacial polarizability [2] [3]. In a low frequency of a.c. field they behave as a macroscopic dipole.

As we can see from figure I-6 different kind of polarization takes place at different frequency range. At very low frequency all the above polarization may take place and the value of polarizability is same as that in static field. As the frequency is increased only certain polarization mechanisms are favored. It is important to note that both orientation and space charge polarization lead to relaxation phenomenon which manifest at low frequencies whereas electronic and ionic polarization lead to resonance phenomenon which exhibits at high frequencies. Major difference between the resonance and the relaxation is the nature of forces acting on the dipoles. In case of resonance, force is elastic (restoring) whereas for relaxation it is of inelastic (friction). Hence relaxation involves loss of energy by dissipation which we will see at section I.1.5 in detail.

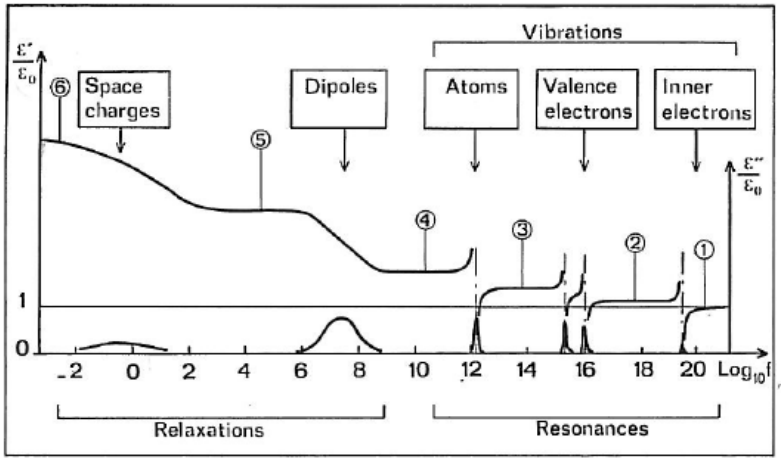

Figure I-6: Different types of polarization and their contribution to the complex dielectric permittivity (see next part) due to the application of a.c field. Adapted from ref [1]

I.1.4. Complex Permittivity:

When a dielectric material is introduced in an alternating electric field there will be a phase lag between the applied field and the response of the system. This is mainly because real dielectrics are always slightly conducting or polar and therefore their capacitance is no longer perfect *i.e.* current is not exactly 90° out of phase with the applied voltage. Conductivity arises from the motion of charges and if these charges are free then the conductivity is independent of the frequency of the applied voltage and the complex permittivity for this case is given by

$$\varepsilon^* = \varepsilon - i\frac{\sigma}{\omega} \qquad \textbf{Eq 9}$$

Where ε is the permittivity of the dielectric material, σ is the frequency independent conductivity and ω is the frequency of the applied field.

If the conductivity is due to bound charges as in oscillating dipoles then the conductivity itself is frequency dependent and it is a complex quantity and the real part of the permittivity ε^* is not exactly ε. Hence the complex permittivity is given by

$$\varepsilon^* = \varepsilon' - i\varepsilon'' \qquad \textbf{Eq 10}$$

Where ε' and ε'' are real and imaginary part of the permittivity and they are frequency dependent. Then the loss factor is given by

$$tan\,\delta = \frac{\varepsilon''}{\varepsilon'} \qquad \textbf{Eq 11}$$

I.1.5. Dielectric Relaxation:

Relaxation may be defined as the time lag in the response of a system to a change in the physical force to which it is subjected [4]. It depends on chemical surrounding of the dipole and the temperature. Let us consider number of identical dipoles at temperature T in a constant, uniform applied field. Now if the field is abruptly cut off, torque experienced by the dipole due to the presence of external field diminishes instantly and the dipoles will slowly reorient themselves by means of multiple collisions leading to disappearance of statistical orientation. This reorientation of dipole is not instantaneous and it takes characteristic time. This time is called relaxation time τ. Hence there will be a smooth change over from polarization with field to zero within the relaxation time τ as shown below.

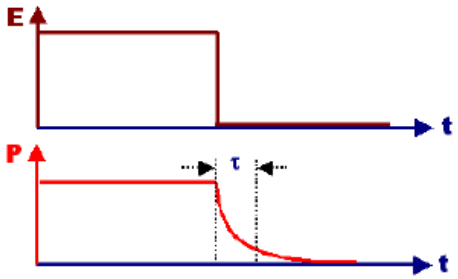

Figure I-7: Characteristic decay of polarization with a time constant τ after switching of the electric field.

Now the dielectric displacement due to dipole orientation in an alternating field is given by

$$D(\omega) = \varepsilon^*(\omega).E(\omega) \qquad \textbf{Eq 12}$$

and the frequency dependent permittivity is given by

$$\varepsilon^* = \varepsilon_\infty + \frac{\varepsilon_S - \varepsilon_\infty}{1 + i\omega\tau} \qquad \textbf{Eq 13}$$

Where ε_S- static low frequency permittivity, ε_∞ - high frequency permittivity, ω – angular frequency and τ-relaxation time. This is called Debye relaxation [5]. A schematic representation of such relaxation is shown below.

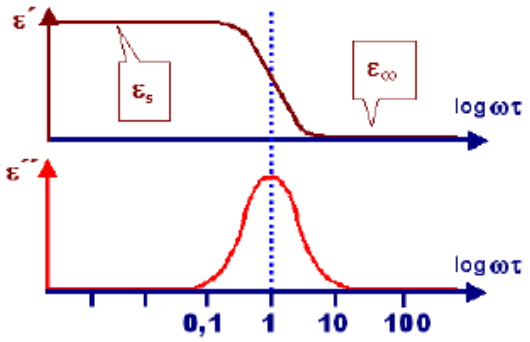

Figure I-8: Debye relaxation

Note that there is a peak in the imaginary part of the permittivity when there is a transition from low frequency permittivity to high frequency permittivity. This peak is called loss peak since its represents loss (conducting) mechanism in the material.

Then the real and imaginary parts of ε^* is given by

$$\varepsilon'(\omega) = \varepsilon_\infty + \frac{\varepsilon_S - \varepsilon_\infty}{1 + \omega^2\tau^2} \qquad \textbf{Eq 14}$$

$$\varepsilon'' = (\varepsilon_S - \varepsilon_\infty)\frac{\omega\tau}{1 + \omega^2\tau^2} \qquad \textbf{Eq 15}$$

According to the equation above, the complex plane plot of ϵ'' versus ϵ' then gives semicircle as shown below in figure I-9. This is called the Cole-Cole plot. In the case of single relaxation process with a single relaxation time like Debye relaxation we will have a semicircle with its center on the real axis.

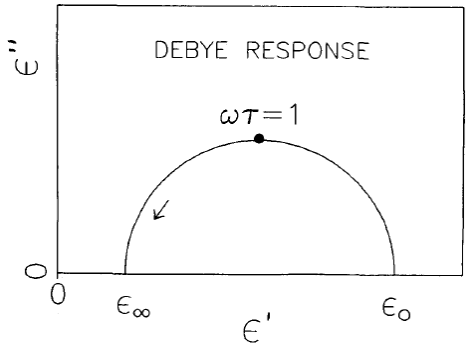

Figure I-9: Complex plane plot of ϵ'' versus ϵ'. Adapted from ref [6]

ε^* is now represented by the semi-circle of radius (ε_s - ε_∞)/2 and the top of the semicircle corresponds to ωτ=1

I.1.5.1. Distribution of relaxation time:

In the previous section we have seen the Debye relaxation and how we obtain semicircle when it was represented by complex plane plot. Debye relaxation is mostly valid for non-interacting dipoles or for a set of dipoles which have the loss of energy proportional to frequency leading to spontaneous relaxation. This is seen only in some ferroelectrics [7]. More often in real materials this is not the case since several parallel relaxation process occur leading to distribution of relaxation time. Figure I-10 gives the real and imaginary part of dielectric constant plotted against frequency for the case of the ideal Debye relaxation and distributed relaxation seen in real materials. Debye relaxation follows from Eq. (13) whereas the experimental data follows distribution of relaxation time in real materials.

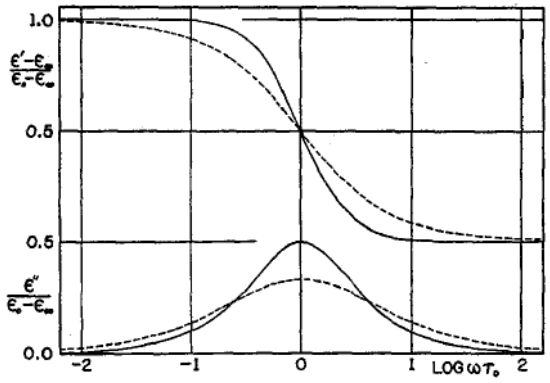

Figure I-10: Real and Imaginary part of dielectric constant plotted against frequency. Solid lines represent Debye relaxation, the dashed lines shows experimentally found behavior.

We can see from the plot that experimental behavior in real materials is different from the ideal Debye relaxation. For the experimental curve, frequency range of dispersion is broader and the maximum of absorption is smaller compared to the ideal Debye relaxation. Significance of this departure from true Debye behavior is well appreciated in the form of Argand diagram or complex plane plot. Cole-Cole in their historical paper in 1941 considered large set of data in polar liquids and solids and found that for all these materials the complex plane plot of the dielectric constant has its center below the real axis i.e. the semicircle is inclined compared to the true Debye response which has the center on the real axis. Hence the depressed semicircle can be expressed in the form of angle suspended between the arc and the real axis which is $\alpha\pi/2$ since this angle is independent of the frequency. They arrived at the expression which very well represents the dispersion of the relaxation from the true Debye response [8]. This is given by:

$$\varepsilon = \varepsilon_\infty + \frac{\varepsilon_S - \varepsilon_\infty}{1 + (i\omega\tau)^{1-\alpha}} \qquad \textbf{Eq 16}$$

The above equation represents the effect of distribution of relaxation times and the parameter α gives a measure of the breath of the distribution. For α=0 the equation reduces to simple Debye expression. For materials which deviate from the Debye behavior α can a take value between 0 and 1. This is clearly seen in the figure I-11 given below which is a complex plane plot of dielectric constant for polar liquids and solids.

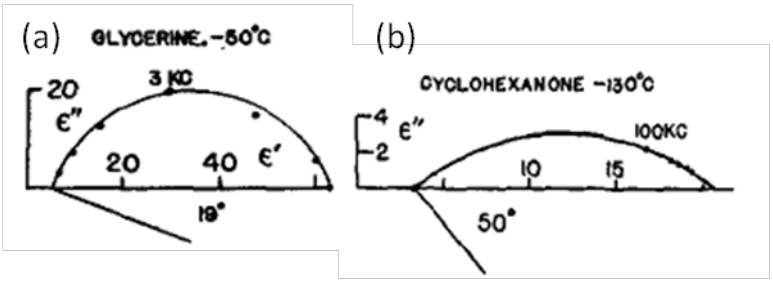

Figure I-11: Complex dielectric constant of (a) liquid, (b) solid. Note the depression of the semicircle indicated by the angle from the true Debye response. Adapted from ref [8]

It is evident from the above figure that the constant α clearly represents the departure from true Debye behavior by means of providing us with the angle suspended between the arc and the real axis, more the value of α more is the deviation from Debye response. The fact that many dissimilar dielectrics display similar dispersion characteristic suggests that a more general fundamental mechanism is at play. But Cole-Cole did not describe the physical nature of this general mechanism.

Though distribution of relaxation time gives us a quantitative value about the deviation from the normal Debye behavior, it does not give any physical proof why the distribution takes place. More over low temperature behavior of dielectrics are incompatible with thermally activated response and distribution of relaxation time follows thermal activation. Hence many approaches were developed to explain the deviation from the ideal Debye Model. The principal approaches were: (a) distribution of hopping probabilities, (b) correlation function approaches, (c) local field theories, (d) diffusive boundary condition (Warburg impedance), (e) interfacial phenomena effects (Maxwell-Wagner) and (f) transport limitation at boundaries. A comparison of all these approaches and their short comings are given by Jonscher [9]. Based on the broad similarity of the dielectric response of the many materials Jonscher arrived at the “Universal law” of the dielectric with the help of many body interactions [7]. A complete description of the “Universal law” is out of scope of the present thesis. Instead we will see in the following section how the conductivity and the charge carrier localization affect the dielectric relaxation and also the real and imaginary part of the permittivity. This is of at most importance in any dielectrics where the conductivity in them cannot be neglected for practical application.

I.2. Contribution of free charges to dielectric permittivity:

I.2.1. Influence of dc conductivity on relaxation:

Contribution of the conductivity σ due to free charges to the permittivity ε^* is given by (-i σ/ω) as we have seen in section I.1.4. A conducting dielectric can be described as a non-conducting dielectric with resistance in parallel, and then the equation of complex permittivity is given by

$$\varepsilon^*(\omega) = \varepsilon_\infty + \frac{\varepsilon_S - \varepsilon_\infty}{1 + i\omega\tau} - i\frac{\sigma}{\omega} \qquad \textbf{Eq 17}$$

The influence of the last term from the above equation can be seen in Figure I-12. Larger the conductivity further the diagram departs from the semicircle.

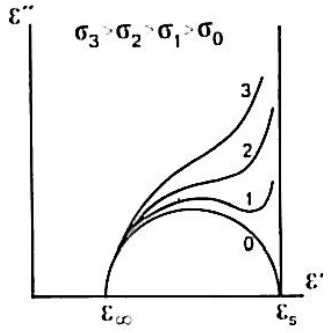

Figure I-12: Influence of the d.c. conductivity on the Argand diagram. Adapted from ref [1]

There are different types of conductivity, they are ionic, electronic and polaronic conductivity. Influence of each of these conductivities on the dielectric permittivity will be discussed in detail by the following section.

I.2.2. Conductivity contribution to the permittivity:

Having seen that the relaxations of most materials are far from the ideal Debye behavior, the focus of the current chapter is to deduce the effect of the free and mobile charges on these relaxations. That is, how the conductivity in the material whether it is electronic or ionic contributes to a change in the real or imaginary part of the permittivity. It is important to make a clear distinction between dipolar response and charge carrier response in a dielectric material. The dipolar response which is due to the dipoles in the material gives rise to a single loss peak. The charge carrier response gives rise to pure dc conductivity. Effect of d.c conductivity on the imaginary part of the permittivity is to incorporate a divergence at zero frequency. This is mostly true in case of free electrons like in metals or in crystalline semiconductors. In solids of dielectrics interest the conductivity is mostly due to hopping motion of charges. These charges hop between localized sites which can be determined by the defects in the solids or may be due to the very presence of the charge itself as in the case of

polarons. If the charges are confined to two centers then the situation is very much similar to a dipole. As the charges hop between the centers there will be a reorientation of these dipoles which will lead to a loss peak. Then the ac conductivity can be expressed as the sum of d.c and a.c component of the conductivity [10]

$$\sigma(\omega) = \sigma_0 + \omega\varepsilon^{"}(\omega) \qquad \textbf{Eq 18}$$

It is obvious from the above equation that the true a.c component of the conductivity is directly related to dielectric loss. This is very useful in distinguishing between d.c and a.c conductivity at low frequencies. Below is the plot of log conductivity versus log frequency for range of materials whose mechanism of conduction is electronic, ionic and also dipolar [11].

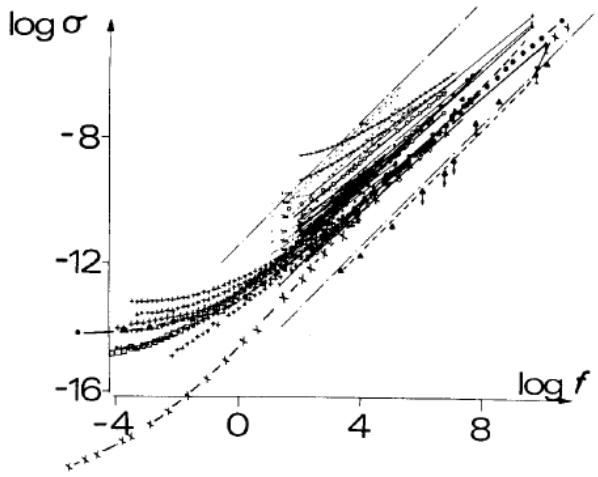

Figure I-13: Log conductivity versus log frequency for a range of materials which have electronic and ionic as well as conductivity contributions from dipolar mechanisms. Note the agreement between the high frequency slopes indicating the a.c conductivity Adapted from ref [11]**.**

Above figure clearly shows that there is a good agreement between all mechanisms of conduction in different materials at high frequency i.e. a.c conductivity for all the above material falls within a narrow range irrespective of their mechanism of conduction and it follows the same power law frequency dependence of

$$\varepsilon^{"} \propto \omega^{n-1} \qquad \textit{where } 0.6 < n < 1 \qquad \textbf{Eq 19}$$

While at low frequency there is a frequency independent conductivity which represents d.c. conductivity. But it can be noticed that saturation at low frequency is not fully complete, a certain slope can still be witnessed. In many instances it is considered to be a.c conductivity. Thus one way of distinguishing the d.c and a.c conductivity at such frequencies is that former almost never affect the real part of the permittivity whereas the latter affects the real part by means of strong dispersion. Figure I-14 gives the dielectric loss as a function of frequency for hollandite type ionic conductor [12].

For the present discussion, only the data at high temperatures will be considered whereas the data at low temperatures will be discussed later. It is apparent from the figure that at high temperatures there is a strong dispersion of dielectric loss compared to low temperature. If this dispersion of dielectric loss is accompanied by corresponding dispersion of real part of permittivity then the observed effect is due to a.c conductivity. The trend was also observed for many materials given in figure I-13 which has a weak frequency dependent conductivity at low frequencies. This behavior is perceived in most dielectrics at sufficiently high temperature and low frequency provided the density of charge carriers is high [13].

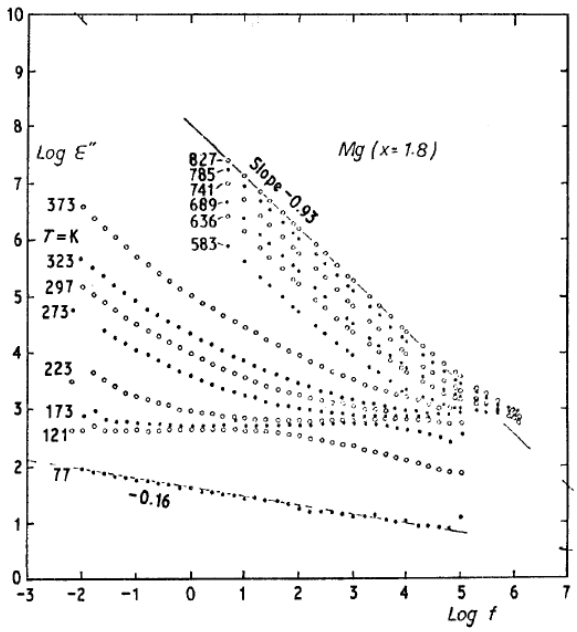

Figure I-14: Frequency dependence of the dielectric loss of an ionic conductor of Hollandite structure type $K_{1.8}Mg_{0.9}Ti_{7.1}O_{16}$. Note the strong dispersion at high temperature with small value of exponent 'n'. Adapted from ref [12]

We have seen that the conductivity can contribute to the real and imaginary part of the permittivity depending on whether its d.c or a.c conduction. But from here on we will only deal with a.c conductivity and its effect on the permittivity will be described based on examples of colossal dielectric constant, polarons and ionic conducting materials.

I.2.2.1. Case of Colossal Dielectric Constant Materials:

Colossal dielectric constant (CDC) materials show abnormally large values of dielectric constant over a broad temperature range. In ferroelectrics high value of dielectric constant is expected close to the vicinity of transition temperature T_C. Away from T_C the value of dielectric constant diminishes Figure I-15 gives the frequency dependent dielectric response of the equivalent circuit given as an inset to (a). The circuit consists of a leaky capacitor connected in series to bulk capacitor and it represents all doped and dirty semiconductors. The sum of d.c and a.c conductivity gives the intrinsic

bulk response where universal dielectric response (UDR) is used for representing a.c conductivity due to hopping charges. Then the complex conductivity is given by

$$\sigma^*_{instrinic} = \sigma'_i + i\sigma^{"}_i \qquad \textbf{Eq 20}$$

Where the real part of the conductivity is given by equation 18 which is the sum of d.c and a.c contribution and the imaginary conductivity stems from the intrinsic capacitance $\varepsilon_\infty C_0$, C_0 being the equivalent vacuum capacitance

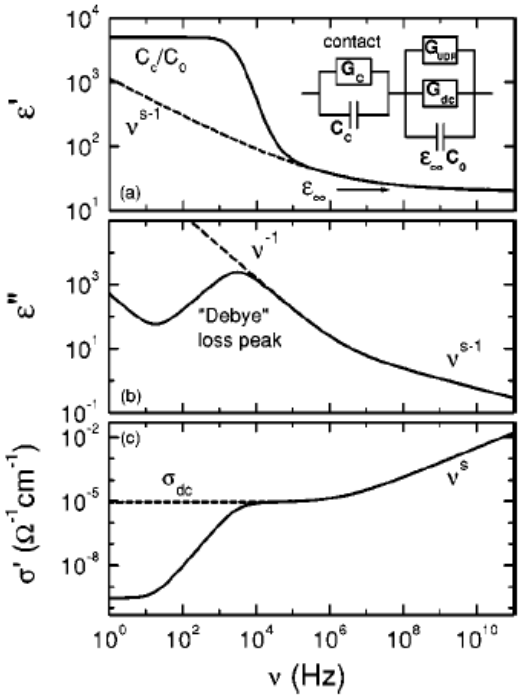

Figure I-15: Frequency dependent dielectric response of the circuit shown in inset of (a). Dashed lines correspond to intrinsic bulk response whereas solid lines correspond to total response. Adapted from ref [14]

The leaky capacitor in series (C_c-G_c) arises due to the formation of Schottky barrier at the electrode-sample interface owing to work function difference between the metal and the semiconducting sample. The solid lines describe the total response of the sample and the dashed lines give the intrinsic response of the bulk. It is apparent from the figure that conductivity falls drastically at low frequencies due to the dominating effect of contact resistance. The high frequency response gives the intrinsic response and it follows UDR. The step in the conductivity translates in to a peak in imaginary part of permittivity by the relation $\varepsilon''=\sigma'/\omega$ similar to dipolar relaxation yet it's a purely conduction mechanism. This is accompanied by a large step-like increase of the ε' at low frequencies due to contact capacitance which is to be added to the intrinsic capacitance. Hence the colossal value of capacitance in such system is primarily due to Maxwell-Wagner effect i.e. due to depletion layer capacitance arising at the electrode-sample interface by means of Schottky barrier.

To further differentiate such extrinsic effect from the true bulk behavior is to perform experiments under bias to change the depletion layer or to have an intermediate layer at the interface to avoid formation of Schottky barrier so that the intrinsic bulk contribution can be observed at ease. A.S.Shcheulin et al have measured single crystals of CdF_2 doped with indium in the radio frequency range [15].

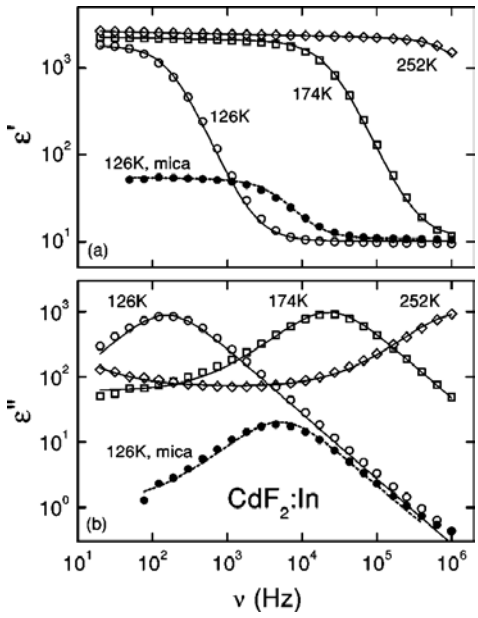

Figure I-16: Real and imaginary part of the permittivity as a function of frequency for single crystal CdF_2 doped with indium. Note the value of permittivity for sample with a thin layer of mica between electrode and the sample. The solid lines are fit to the equivalent circuit given in figure I-15.

Figure I-16 gives the frequency response of the real and imaginary part of dielectric constant. At low frequency, there is a large increase of ϵ' up to 2000 which are accompanied by well pronounced peak in ε". This can be interpreted with help of equivalent circuit described in figure I-15.

At low frequency due to the difference in the conductivity of the sample and the electrode, Schottky barrier forms at the interface. This leads to colossal value of dielectric constant owing to the thin layer capacitor in series to the bulk. Only at high frequency the intrinsic dielectric constant is revealed (ε_∞= 10) which is far from being colossal. They have also ruled out the possibility of dipole relaxation by illuminating the sample. In case of dipole relaxation, the relaxation time is independent of the intensity of light. Here the relaxation time was proportional to the intensity and hence provides key evidence for the presence of high charge carrier density. Ritus et al measured the same except here the electrode and the sample are separated by a thin layer of mica. This ensures that the Schottky barrier is not formed. It is obvious from figure I-16 that sample with mica layer has the same step like increase of the dielectric constant but the absolute value remains below 100. This

demonstrates that the measured high value of the permittivity without intermediate mica layer in the previous case is mainly due to the contact effect.

Many cases of CDC behavior reported in literature on wide variety of materials are mostly due to such extrinsic effects described above. Even $LaMnO_3$ the parent compound of CDC material show CDC which was attributed to contact dominated effect [16]. The colossal dielectric constant behavior of $CaCu_3Ti_4O_{12}$ (CCTO) was first reported by Subramanian et al [17]. Since then there are many articles dealing with the apparent origin of CDC behavior have appeared. Most of the authors attribute the effect to some kind of extrinsic contribution [18] [19] [20] [21]. In the case of single crystals, interface at the sample and the electrode is the major extrinsic contributor whereas in the case of ceramics grain boundary effects along with the surface effect had to be included. For the latter case it can be modeled with the help of equivalent circuit shown below.

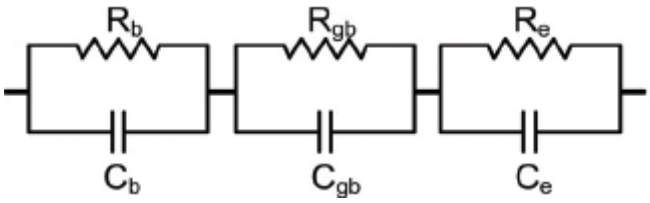

Figure I-17: Equivalent circuit of CCTO ceramic sample showing grain, grain boundary and electrode contribution.

Where R_b, R_{gb}, R_e are bulk, grain boundary and electrode resistance and C_b, C_{gb}, C_e are bulk, grain boundary and electrode capacitance. Then the complex impedance is given by

$$Z^* = \frac{1}{R_b^{-1} + i\omega C_b} + \frac{1}{R_{gb}^{-1} + i\omega C_{gb}} + \frac{1}{R_e^{-1} + i\omega C_e} = Z' - iZ'' \qquad \textbf{Eq 21}$$

Where

$$Z' = \frac{R_b}{1 + (\omega R_b C_b)^2} + \frac{R_{gb}}{1 + (\omega R_{gb} C_{gb})^2} + \frac{R_e}{1 + (\omega R_e C_e)^2} \qquad \textbf{Eq 22}$$

and

$$Z'' = R_b \left[\frac{\omega R_b C_b}{1 + (\omega R_b C_b)^2}\right] + R_{gb} \left[\frac{\omega R_{gb} C_{gb}}{1 + (\omega R_{gb} C_{gb})^2}\right] + R_e \left[\frac{\omega R_e C_e}{1 + (\omega R_e C_e)^2}\right] \qquad \textbf{Eq 23}$$

and the corresponding permittivity is given by

$$\varepsilon^* = \varepsilon' - i\varepsilon'' = \frac{1}{i\omega C_0 Z^*} \qquad \textbf{Eq 24}$$

It is apparent from the above equation that the resistance (or conductivity) of the grains, grain boundary and electrode influence the permittivity of the sample to a great extent. Depending on the absolute value of the respective resistance the permittivity or capacitance can be changed. Li et al have done simulation by varying the resistance. They have considered 3 different scenarios Type 1 $R_{gb} >> R_e$ and R_b, Type 2 where $R_{gb} = R_e >> R_b$ and Type 3 where $R_e >> R_{gb} = R_b$. The frequency response of capacitance for these 3 cases is given in Figure I-18 (a).

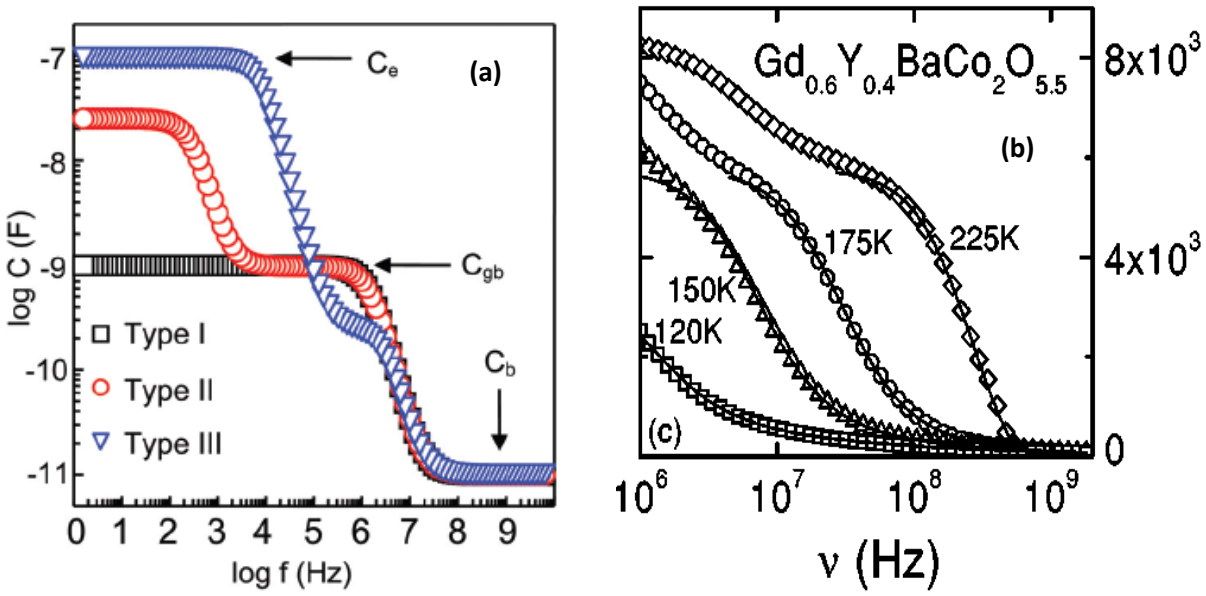

Figure I-18: (a) Simulation of frequency response of capacitance for 3 different cases with different grain boundary resistance. **(b)** Frequency response of real part of permittivity for $Gd_{0.6}Y_{0.4}BaCo_2O_{5.5}$. Note the two plateaus at low and high frequencies.

The above plot is similar to figure I-16 without the grain boundary contribution. For single crystals we have only the electrode capacitance contribution whereas for ceramics there is an internal barrier layer capacitance (IBLC) which also contributes to the total capacitance of the sample. IBLC is due to the difference in the Fermi level of the conducting grain and insulating grain boundary and its contribution is clearly visible as a plateau at higher frequency than the plateau due to contact electrode. This behavior was clearly demonstrated by Bobnar et al on perovskite derived cobaltite [22]. Figure I-18 (b) gives the real part of permittivity as a function of frequency for polycrystalline $Gd_{0.6}Y_{0.4}BaCo_2O_{5.5}$. Two plateaus are seen one at low frequency with ϵ' of 8000 ascribed to the electrode sample surface capacitance and the other at high frequency with ϵ' of 6000 ascribed to the grain - grain boundary IBLC. The intrinsic capacitance from the grain can be noticed only at very high frequency.

I.2.2.2. Case of Polaron and Space Charge Relaxation:

We have discussed in the beginning of this part that free electrons contribute to d.c conductivity whereas hopping of electrons between localized site contribute also to the a.c conductivity. Latter is the case for polarons which are hopping of electrons between the localized sites and deforming the lattice around the localizing sites. It can be visualized as shown in the figure I-19 (a) below. A slow moving electron in the lattice repels electron and attracts positive ions there by deforming the lattice.

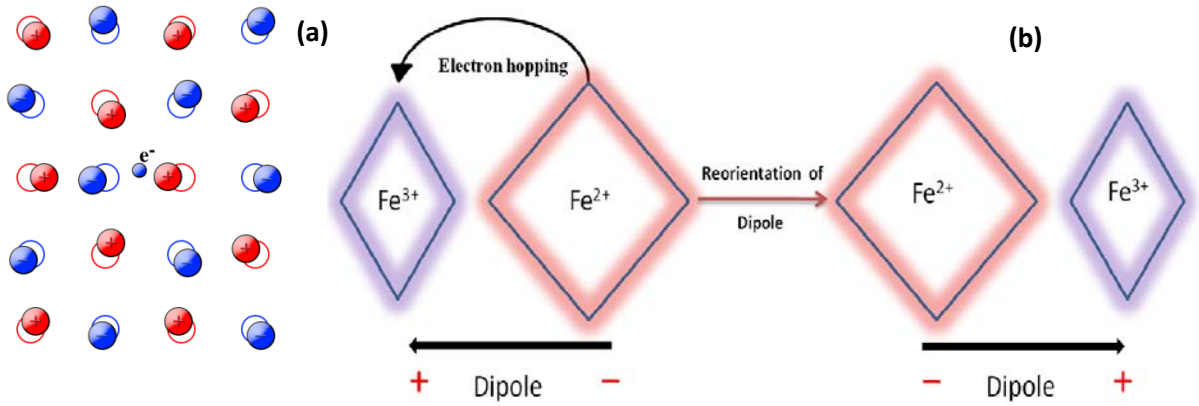

Figure I-19: (a) Schematic of polaron. An electron moving in the lattice is repelled by another electron and attracted by positive ions and there by deforming the lattice. (b) Reorientation of dipoles due to hopping of electrons between two oxidation states of iron in an octahedra environment.

When the hopping of electron is between two given sites then the situation is very much similar to dipole reorientation and leads to a loss peak. This is shown schematically in figure I-19 (b) for the case of different oxidation states of iron in an octahedral environment of the lattice. This behavior is observed in many ferroelectrics both pure and doped. Iguchi et al measured dielectric behavior of n-type barium titanate doped with La_2O_3 and Gd_2O_3 at low temperatures [23]. They found a loss maximum below 100K which moves to high frequency with increase in temperature indicating relaxation behavior. They have ascribed this relaxation to polaron relaxation and found that the activation energy of this relaxation is 0.068eV. This is similar to the 0.070eV obtained by plotting $\sigma T^{3/2}$ versus 1/T indicating the relaxation at low temperatures is due to hopping of polarons. O.Bidault et al in their pioneering paper has shown that polarons are the important contributors to the dielectric relaxation observed in many ferroelectrics ceramics or single crystals [24]. Figure I – 20 (a) gives the imaginary part of permittivity as a function of temperature for different $KTa_{1-x}Nb_xO_3$ at 4 kHz. Two things should be noticed importantly. The maximum of ϵ_2 occurs at the same temperature for all doping concentration and the height of the maximum increases with increase in doping concentration. It was shown in an earlier paper that the relaxation strength could be altered

by reoxidizing the $KTaO_3$: Fe sample, demonstrating that oxygen vacancies play a major role in such a relaxation [25].

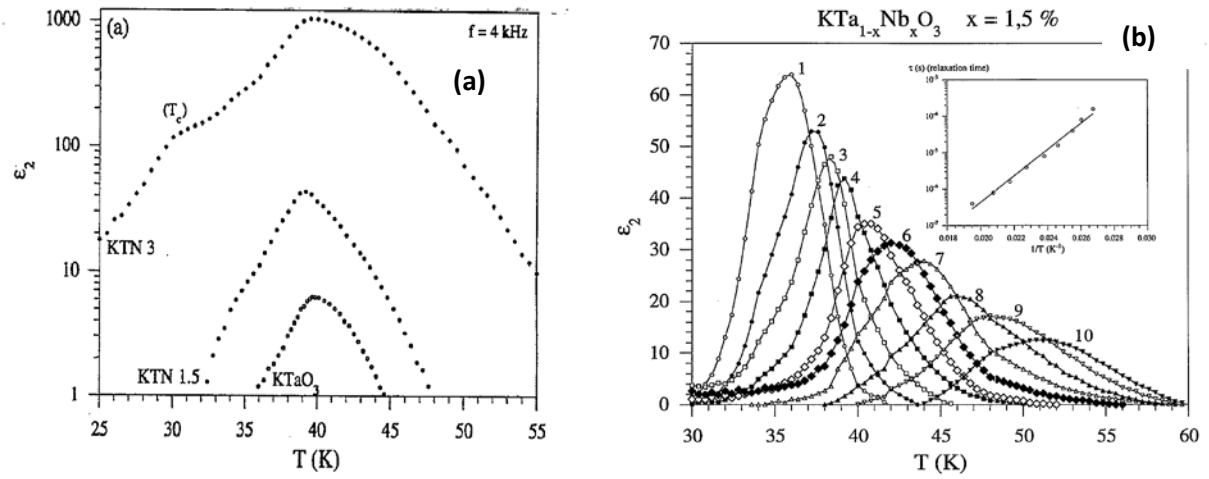

Figure I-20: (a) the imaginary part of permittivity as a function of temperature for different $KTa_{1-X}Nb_XO_3$ at 4 KHz. **(b)** Temperature dependence of imaginary part of permittivity for $KTa_{0.985}Nb_{0.015}O_3$ at several frequencies. Taken from ref [24]

Figure I-20 (b) shows the temperature dependence of imaginary part of permittivity for $KTa_{0.985}Nb_{0.015}O_3$ at several frequencies. It is evident from the figure that the relaxation maximum moves with frequency and temperature a typical sign for relaxation. Similar behavior was observed in many other oxides like rutile TiO_2, Sm_2O_3, WO_3 and P_2O_5 glass where dielectric relaxation due to hopping motions of polarons was confirmed. So it can be said without any ambiguity that very low activation energy (in the range of meV) and dependency of the relaxation maximum with charge carrier density is the signature of polaron relaxation in the material. The fact that it is found in many materials in different systems signifies that it is owing to a common origin which is unarguably oxygen vacancies which cannot be avoided and also due to the presence of ubiquitous heterovalent impurities like iron.

Polaron relaxations which are due to the hopping of electrons usually are microscopic where the dipoles are in the order of one lattice unit cell. It is usually observed at low temperatures and therefore requires low activation energy. However at high temperatures when the electron gets sufficient energy then they can travel to great lengths in the material and eventually localize at interface between the electrode and the sample. Such huge motion of electrons will contribute to the d.c conduction of the material. Symmetry of the charge carriers at the surface can be broken by applying an external electric field which leads to creation of a macroscopic dipole that undergoes Debye relaxation. Many such relaxations were evidenced in perovskite both in single crystals as well as in ceramics at high temperatures and it was ascribed to relaxation of space charge by Maglione et

al [26] [27]. Figure I-21 (a) gives the real part of permittivity as a function of frequency for several temperatures above T_C for $BaTiO_3$ single crystals. Two things can be noticed here, a step like dispersion at intermediate frequency and a monotonous increase at low frequency. With increase in temperature the step like dispersion moves to higher frequency exhibiting relaxation. According to space charge model given by Coelho the relaxation time is proportional to conductivity relaxation time [1].

$$\tau^* = \sigma/\varepsilon \qquad \textbf{Eq 25}$$

Where σ is the conductivity and ϵ is the dielectric constant. Then the relaxation time for the macroscopic dipole due to space charge is give by

$$\tau = d\sqrt{\tau^*/D} \qquad \textbf{Eq 26}$$

Where d is the sample thickness perpendicular to electrodes and D the free charges diffusion coefficient. It is evident from the above equation that the space charge relaxation has a definite relation with the conductivity of the sample. It is clearly demonstrated in the figure I-21 (b) which gives the Arrhenius plot of the high temperature relaxation rate and the conductivity. The similarity with the two curves is striking and the relaxation time and conductivity are thermally activated.

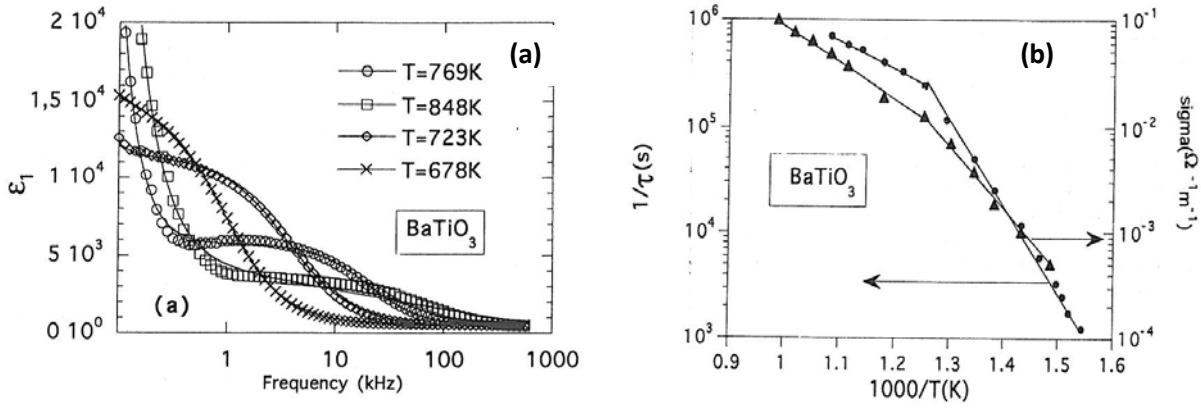

Figure I-21: (a) gives the real part of permittivity as a function of frequency at several temperatures for $BaTiO_3$ single crystals. **(b)** Arrhenius plot of high temperature relaxation rate and conductivity. Note the similarity between the two curves. Taken from ref [28]

The fact that the space charge relaxation of above kind is observed in many other perovskite irrespective of their texture (ceramics and crystals) and lattice properties, calls for a common origin. Bidault et al have shown that oxygen vacancies play a major role in the relaxation and are the necessary ingredients for space charge observed in many materials [27]. They have demonstrated that the relaxation strength of $BaTiO_3$ (BTO) single crystal can be changed by annealing the sample in different oxygen atmosphere. Reduced BTO crystal exhibited stronger amplitude of relaxation which

clearly displays the role of oxygen vacancy in relaxation. To conclude at high temperatures due to high conductivity macroscopic dipoles are formed which leads to space charge relaxation whereas at low temperatures energy is not sufficient enough to promote long range motion of charge carriers and hence short range hopping motion of electrons in the form of polaron takes place which lead to polaron relaxation.

I.2.2.3. Case of Ionic Conducting Materials:

Materials which conduct predominantly due to the motion of ions are called ionic conductors. Conduction in an ionic conductor is due to anions like oxygen ions in zirconia stabilized yttria or by cations like potassium ions in $KTiOPO_4$. Fast ionic conductors on the other hand have sufficient amount of vacancy preexisting in the structure hence can conduct at much lower activation energy than ionic conductors. Ionic conductors depend on temperature for their conduction and so they are most often thermally activated. At sufficiently high temperatures conduction is fairly easy and they lead to d.c conductivity while at low temperatures relaxation of conductivity takes place which can be evidenced with dielectric spectroscopy. Complex impedance plot is the most common way for distinguishing the contribution from grains, grain boundary and electrodes in ionic conductors. Figure I- 22(a) gives the complex impedance plot for ZrO_2-Y_2O_3 in both ceramics and crystal [29]. Three semicircles are seen they are attributed to grain, grain boundary and contact relaxation for the ceramic sample whereas only one semicircle corresponding to bulk is seen for the crystal. The frequency dependent conductivity and dielectric permittivity for the ceramic sample are given in figure I-22 (b). At lowest temperature permittivity is independent on frequency. As the temperature increases a dispersion is seen in ϵ' and a corresponding relaxation in conductivity can be noticed which is marked by arrows. This dispersion shifts to higher frequency with increase in temperature and it can be attributed to grain boundary relaxation. At the highest temperature an additional increase of ϵ' is seen and can be assigned to space charges which localize at the electrode due to the long range motion of oxygen ions.

For samples which are more insulating like in CeO_2 doped Scandia, frequency explicit plot has its own advantage over complex impedance plots in deducing the property of the material as demonstrated by Gerhardt [30]. Due to the conducting nature of ceria doped Scandia, semicircle is not seen in complex impedance plot at room temperature. But a dielectric loss peak is obtained when tan δ is plotted as a function of frequency and corresponding relaxation is seen in the real part of the dielectric constant (Figure I-22 (c) and (d)). This is mainly because for the same physical process peak in ϵ'' will show up at lower frequency whereas peak in electric modulus ($M^*=1/\varepsilon^*$) will show up at highest frequency and it is due to the difference in the relaxation time for each function. How much farther apart the peaks will be is defined by their relaxation ratio ($r=\varepsilon_s/\varepsilon_\infty$). If the relaxation ratio is

too high then the peaks will be much farther apart and if it is small then they will be close. It is clear from the above discussion whether it is long range conduction or localized conduction it eventually leads to some kind of dielectric relaxation and whether it can be observed within our frequency window depends on the relaxation strength.

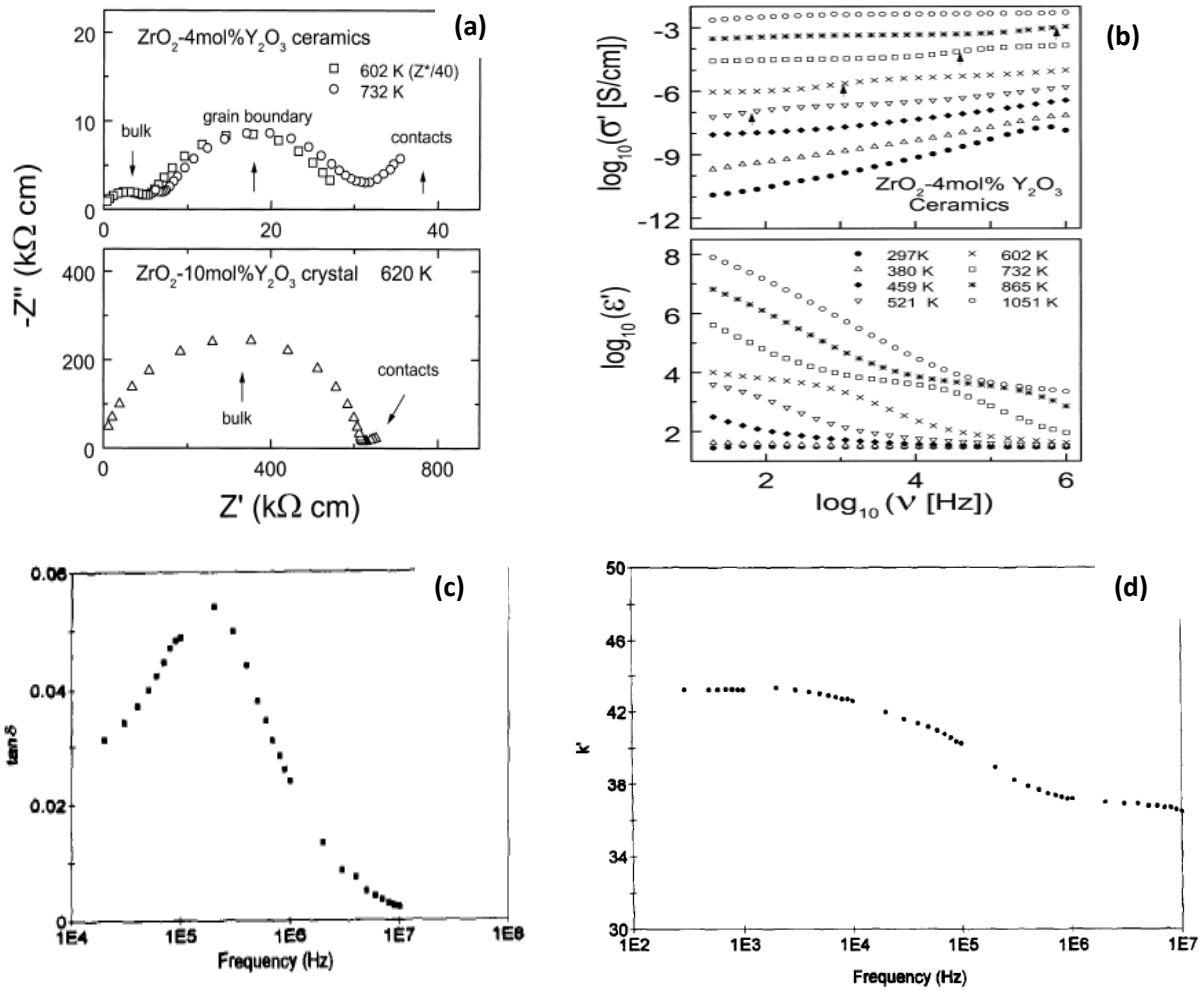

Figure I-22: (a) Complex impedance plot of ZrO_2 doped Y_2O_3 ceramic and single crystal. **(b)** Frequency dependent conductivity and dielectric permittivity for several temperatures of ZrO_2 doped Y_2O_3 ceramic. From ref [29]. Small step seen due to conductivity relaxation transforms into a step like dispersion in permittivity which moves with frequency. **(c)** Loss factor as a function of frequency for ceria doped scandia and **(d)** real part of permittivity as a function of frequency. Note the small relaxation step in K' due to defect relaxation and the corresponding peak in losses. Adapted from ref [30].

To summarize whatever the nature of conduction process in material whether it is electronic or ionic in nature if the temperature and activation energy are favorable then long range conduction takes place which eventually leads to grain boundary relaxation or space charge relaxation. At low

temperatures where the energy is not high enough to promote long range conduction then the hopping of charge carriers between the localized sites dominates subsequently to polaron relaxation.

I.3. Ferroelectrics:

I.3.1. Definition and Historical Background:

The application of electric field to the dielectric materials causes polarization but they are so small to cause any noticeable change in the structure and the elastic properties. On the other hand there are materials which exhibit polarization of greater magnitude even in the absence of electric field. When such spontaneous polarization can be reversed by electric field then the materials are called ferroelectrics [31]. The term ferroelectricity is used in analogy with ferromagnetism. Just as ferromagnetic materials exhibits spontaneous magnetic moment and hysteresis effect in relation with magnetization and magnetic field, ferroelectric materials display spontaneous polarization and hysteresis effect in relation with dielectric displacement and electric field [32]. Hence the prefix "*ferro*" was used to describe this property despite the fact that many ferroelectrics do not contain iron in their unit cell. Ferroelectricity depends on the symmetry of the crystal structure, of the 32 crystallographic point groups only 11 are centrosymmetric and 21 are non centrosymmetric without an inversion center. Out of the 21 non centrosymmetric point groups all but one are piezoelectric. There are 10 polar groups among the 20 non centrosymmetric point groups without an inversion center. Among the 10 groups, some materials can display ferroelectricity when the polarization can be reversed on the application of an electric field.

Compound	Chemical formula	Year discovered	Curie temperature, T_C (K)	Remanent polarization, P_s (μK·cm^{-2})	Crystal structure (at room temperature)
Rochelle salt	$KNaC_4H_4O_6{\cdot}4H_2O$	1921	255 and 297	0.25	Monoclinic between the Curie points Orthorhombic at other temperatures
Potassium dihydrogen phosphate	KH_2PO_4	1935	123	6.1	Orthorhombic
Barium titanate	$BaTiO_3$	1945	398	25	Tetragonal
Lithium niobate	$LiNbO_3$	1949	1,415	10–30	Trigonal
Potassium niobate	$KNbO_3$	1949	400	20–40	Orthorhombic
Lead zirconate titanate	$PbZr_{1-x}Ti_xO_3$	1949	Depends on composition	20–97	Tetragonal for Ti-rich Rhombohedral for Zr-rich
Lead titanate	$PbTiO_3$	1950	763	20–96.5	Tetragonal
Lead zirconate	$PbZrO_3$	1951	503	20–50	Orthorhombic
Guanidine aluminum sulphite hexahydrate	$C(NH_2)_3Al(SO_4)_2{\cdot}6H_2O$	1955	473	0.5	Trigonal
Lead bismute niobate	$PbBi_2Nb_2O_9$	1959	833	~3	Pseudotetragonal
Strontium bismute tantalate	$SrBi_2Ta_2O_9$	1960	600	30–70	Orthorhombic
Barium strontium titanate	$Ba_{0.73}Sr_{0.27}TiO_3$	1960	298	10–30	Tetragonal
Bismute titanate	$Bi_4Ti_3O_{12}$	1961	953	10–30	Orthorhombic

Table 1: A chronological list of ferroelectric materials and properties [33]

Ferroelectricity was first discovered by Valasek in Rochelle salt [34], but it was not considered for application until the discovery of $BaTiO_3$ by Von Hippel [35]. A list of chronological development in ferroelectric materials is given in table I along with their structure and remnant polarization [33]. Since then the field of ferroelectrics has received lot of interest and found much technological application.

Ferroelectric materials undergo structural phase transition from a paraelectric state to a ferroelectric state upon cooling through the Curie temperature T_C. The structural symmetry of the material changes from centrosymmetric to non centrosymmetric when it is cooled below T_C. Although in some materials there is more than one structural transition in that case Curie temperature is the first temperature in which a material becomes ferroelectric.

I.3.2. Ferroelectrics of Perovskite Structure:

Most of the technologically important ferroelectrics have perovskite structure. The structure is named after the mineral $CaTiO_3$ which has a general formula of type ABO_3. It has a simple cubic structure which consists of corner sharing BO_6 octahedra where B could be a cation of charge 4 or 5 (Ti^{4+}, Zr^{4+}, Sn^{4+}, Nb^{5+}, Ta^{5+} etc.) which sits in the center of the octahedra and A, a cation of charge 1 or 2 (Na^{+}, K^{+}, Ca^{2+}, Ba^{2+}, Pb^{2+}, etc.) is located in between the octahedra Figure I-23 (a). The structure is very tolerant to substitution both in A and B sites hence more complex ferroelectric materials are possible as in $Pb[Zr_X\ Ti_{1-X}]O_3$ with interesting properties. There are several perovskite ferroelectrics like $BaTiO_3$, $KNbO_3$ and $BiFeO_3$ to name but a few. Here we will consider $BaTiO_3$ in detail.

$BaTiO_3$ (BTO) at temperature above 393 K has a simple cubic structure with a space group Pm3m and it is in a paraelectric state. When it is cooled below this temperature it undergoes structural phase transition into tetragonal structure of space group P4mm which is in a ferroelectric state. When the structure changes from cubic to tetragonal, titanium displaces from its central position and moves close to one of the oxygen in octahedra thereby disturbing the uniform charge distribution (see Figure I-23). This leads to creation of dipole. Long range order of these dipoles leads to macroscopic ferroelectricity. Hence the ferroelectricity in BTO is of displacive type [36]. In ferroelectrics of KH_2PO_4 family the transition is predominantly of order disorder type [37] where the dipoles which are oriented in random direction at high temperatures align in one direction within a domain going through the transition.

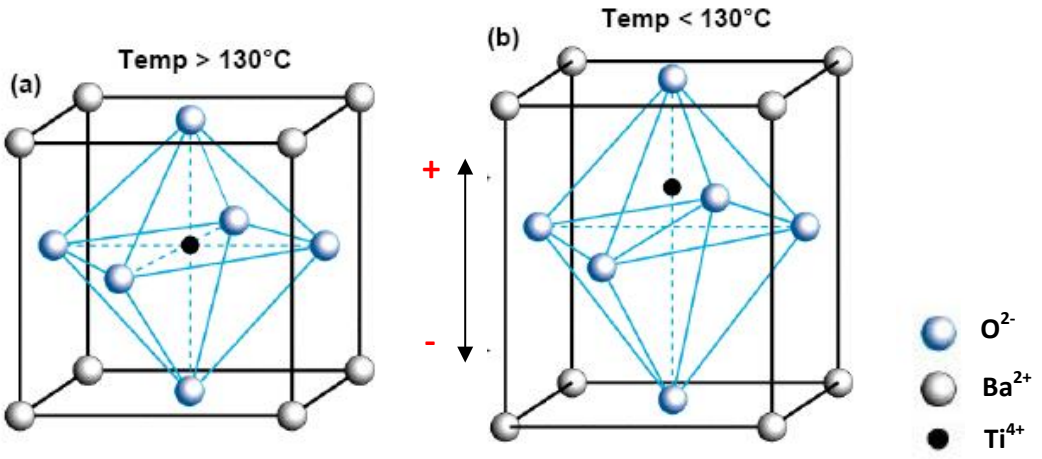

Figure I-23: $BaTiO_3$ cell is shown here with the barium atoms on the corners, the oxygen atoms on the face center and the titanium atoms in the center of the unit cell. (a) Paraelectric state, (b) Ferroelectric state. Note the change in lattice parameter in the ferroelectric state.

There are many other ferroelectrics whose structure is not perovskite and they are mostly based on oxides, phosphates, sulphates and borates. A comprehensive list of ferroelectrics and antiferroelectrics is given by Lines and Glass [31].

I.3.3. Phase Transition and Curie Weiss Behavior in Ferroelectrics:

The temperature at which a material becomes ferroelectric is called Curie temperature T_C. At $T > T_C$, there is no polarization and the material does not exhibit ferroelectricity while for $T<T_C$, spontaneous polarization appears in the material it becomes ferroelectric [31] [32]. Generally there may exist more than one Curie temperature in a material although there is only one Curie point. For example $BaTiO_3$ undergoes three phase transition as shown in figure I -24 from cubic to tetragonal, orthorhombic and rhombohedral at 393 K, 278 K and 183 K respectively but the Curie point here is the first transition at which it becomes ferroelectric i.e. 393 K. Some ferroelectric materials do not exhibit a Curie point because the material decomposes before the Curie temperature is reached as in the case of gunanidine aluminium sulphate hexahydrate $C(NH_2)_3Al(SO_4)_2.6H_2O$.

As $BaTiO_3$ undergoes phase transition from paraelectric to ferroelectric state there is a discontinuity in lattice constant, polarization and dielectric constant as shown in Figure I – 25 [38]. The discontinuity observed is due to the nature of transition in $BaTiO_3$ which is of first order and it is made apparent by a small hysteresis of transition. The temperature dependence of dielectric constant above Curie point ($T > T_c$) in most ferroelectric crystals is governed by Curie-Weiss law [38].

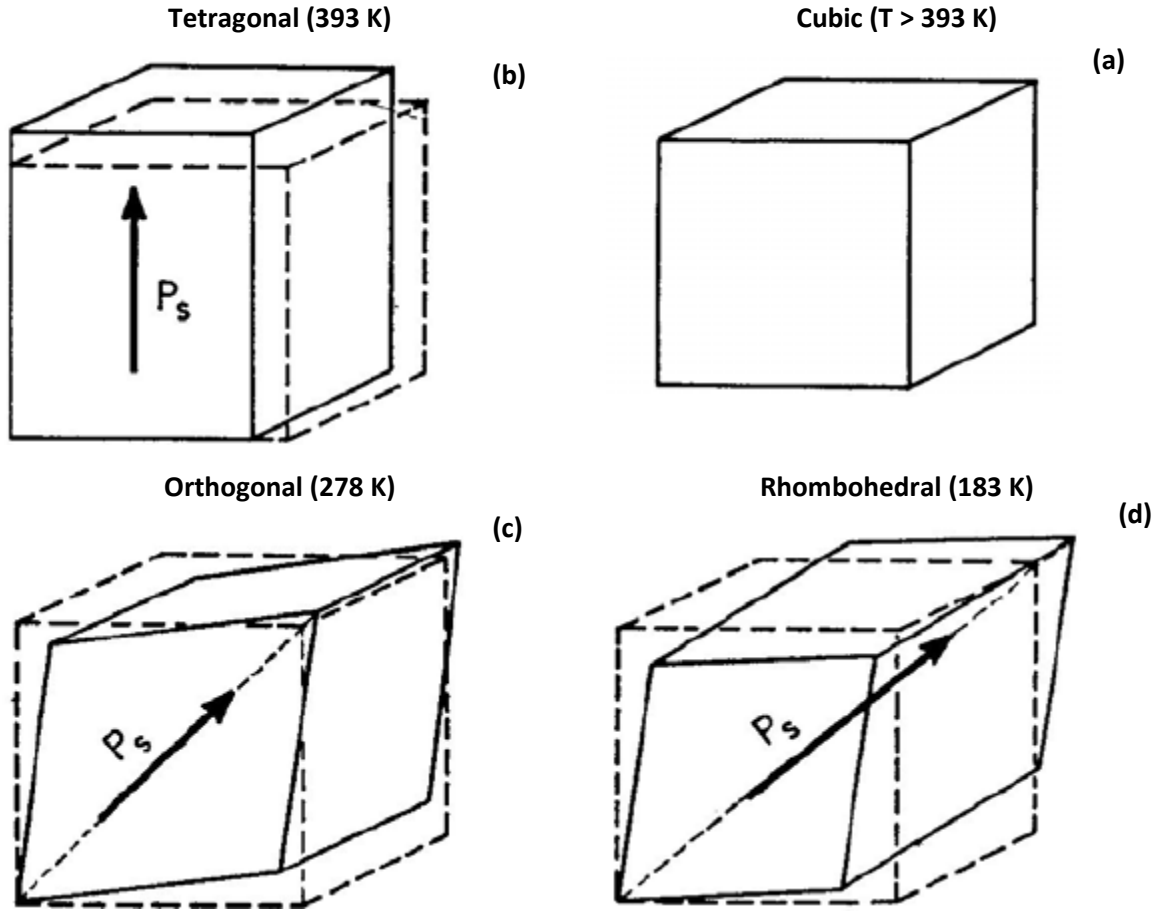

Figure I-24: Unit cells of the four phases of BaTiO3: a) Cubic, stable above 393 K (TC), b) Tetragonal, stable between 393 K and 278 K, c) Orthorhombic, stable between 278 K and 183 K, (monoclinic as drawn) d) Rhombohedral, stable below 183 K. The dotted lines in (b), (c), and (d) delineate the original cubic cell. Arrows indicate the direction of the spontaneous polarization, *P*s, in each phase [32].

$$\chi = \frac{C}{T - T_0} \qquad \text{Eq 27}$$

Where χ is the permittivity of the material, , C is the Curie constant and T_0 is the Curie-Weiss temperature. In general the Curie-Weiss temperature T_0 is different from Curie point T_C.

For first order transition T_0 is less than T_C ($T_0 < T_C$) whereas for the second order transition T_0 is same as T_C ($T_0 = T_C$) [39]. The order of phase transition is defined by the discontinuity in the partial derivatives of the Gibbs free energy of the ferroelectric at the phase transition temperature. Thus the spontaneous polarization and strain change continuously at the phase transition for a ferroelectric of second order phase transition and are discontinuous at the phase transition temperature for first order ferroelectrics [40].

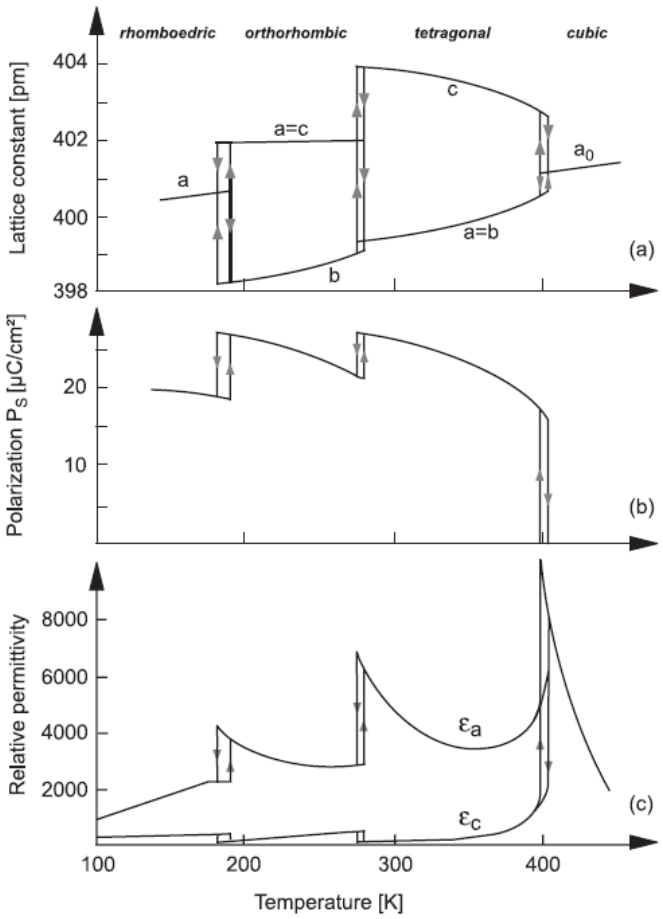

Figure I-25: Various properties of barium titanate as a function of temperature. Anisotropic properties are shown with respect to the lattice direction. (a) Lattice constants, (b) spontaneous polarization *Ps* and (c) relative permittivity ε_r [41].

Figure I-26 gives the temperature dependence of first order and second order phase transition along with relaxor ferroelectric which have diffuse phase transition with broad maximum in dielectric permittivity and strong frequency dispersion below the maximum of permittivity. It can be seen immediately that the reciprocal permittivity given in dotted lines is very helpful in distinguishing the order of phase transition according the relation between T_0 and T_C for the two types of phase transition discussed above.

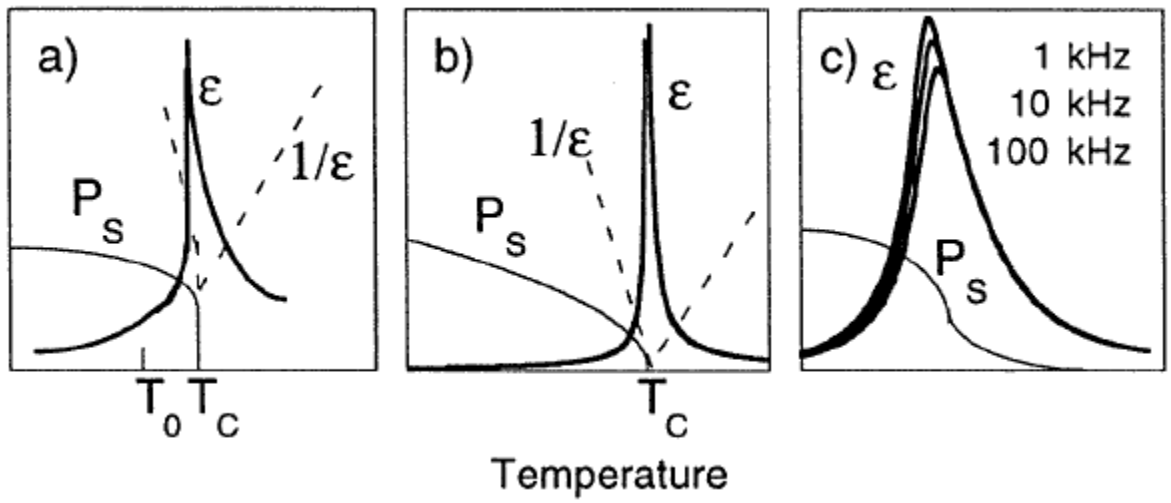

Figure I-26: Schematic temperature dependence of the dielectric permittivity ε and spontaneous polarization P_S for (a) a first- and (b) a second-order ferroelectric and (c) for a relaxor ferroelectric. Permittivity data in (c) is measured on a $Pb(Mg_{1/3}\ Nb_{2/3})O_3$ ceramic [40].

I.3.4. Ferroelectric Domains and Hysteresis:

The regions with uniform spontaneous polarization in a ferroelectric crystal are called domains. In general polarization is not uniformly aligned in one direction throughout the crystal. For the case of perovskite ferroelectrics like $BaTiO_3$ the spontaneous polarization lies along c –axis when the crystal

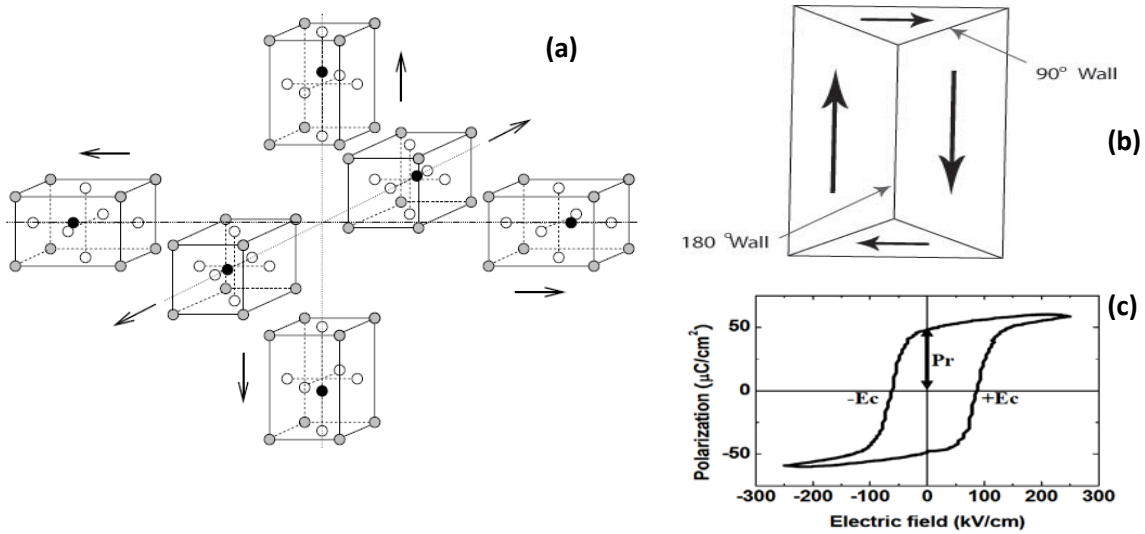

Figure I-27: (a) Six different spontaneous polarization direction in $BaTiO_3$ when cooling from paraelectric to ferroelectric state [42], (b) Schematic representation of 90° and 180° domain walls, arrows show the direction of spontaneous polarization, (c) Typical hysteresis loop observed in ferroelectrics.

undergoes transition from cubic to tetragonal (figure I-24). There are six equivalent directions in the cubic phase of the crystal and the spontaneous polarization may arise with equal probability along any of them when the crystal is cooled through the phase transition figure I-27 (a). Ferroelectric

domains form to minimize the depolarizing fields and elastic energy which develops in the ferroelectric phase [31] [43]. The appearance of spontaneous polarization during the phase transition leads to formation of surface charge. This surface charge produces an electric field called depolarizing field, which is oriented opposite to polarization. Hence the formation of single-domain state is inhibited due to presence of depolarizing field which makes the single-domain state energetically unfavorable. This energy can be minimized by a) splitting of ferroelectric into domains of oppositely oriented polarization or b) compensating depolarizing field by electrical conduction through the crystal, c) charges from the material surroundings like the charges from external circuit [40]. Mechanical stress also leads to splitting of ferroelectric domains. The boundary between two domains is called domain wall. These walls differ from perfect crystal hence they carry an energy called domain wall energy W_{dw} along with the elastic energy W_e. Domain wall energy is considered in detail in the book by Lines and Glass [31]. The type of domain walls that are formed depends on the symmetry of both the non-ferroelectric and ferroelectric phase of the crystal [44]. To minimize the electrostatic energy the neighboring domains should have orientation such that div $P \sim 0$ at the domain boundary. This is condition is satisfied for 90° and 180° domain walls in perovskites [31]. A schematic of 90° and 180° domain walls are shown in figure I-27 (b). Domains can be observed by various methods like optical birefringence, optical rotation, second-harmonic rotation, transmission electron microscopy, chemical etching and powder X-ray Diffraction to name but a few. Each of these methods has its own advantages and disadvantages and they are dealt with in detail by Lines and Glass [31]

When an electric field is applied in direction opposite to the polarization, the polarization can be reoriented in the direction of the electric field [45]. This is because it is much easier for the domain to remain in the direction of electric field since it is energetically favorable. This process of reversal of polarization along the direction of the electric field is called polarization switching. The net polarization of the spontaneous polarized ferroelectric material is small. At low electric field the polarization starts to increase linearly, upon removal of field polarization will revert back to its initial state. However if the electric field is increased beyond the linear regime then the domains with opposite orientation to the electric field will start to switch in the direction parallel to the applied field. The switching continues until all the domains are aligned with the electric field and then polarization of the material reaches saturation. Now if the electric field returns to zero all the domains wont switch back to their initial position and there will be remnant polarization P_r at zero field. This remnant polarization can be brought to zero by applying electric field in the opposite direction. Then strength of electric field needed to bring the remnant polarization to zero is called

coercive field E_C. A complete cycle of the plot of polarization versus electric field then displays a hysteresis loop as shown in figure I-27 (c).

I.3.5. Piezoelectricity:

Piezoelectricity is called ability of certain material to develop an electric charge proportional to applied stress [39]. This is called direct piezoelectric effect. It was discovered by Pierre and Jacques Curie in 1880 while studying crystals such as tourmaline, quartz etc [46]. Generally all ferroelectrics are piezoelectric but vice versa are not true. ZnO and quartz are good piezoelectric materials but they are not ferroelectrics. These materials also show a converse effect where a geometrical strain is produced when a voltage is applied. The direct and converse effect are expressed as

$$P_i = d_{ijk}\sigma_{jk} \quad \text{(direct piezoelectric effect)} \qquad \textbf{Eq 28}$$

$$X_{ij} = d_{kij}E_k \quad \text{(converse piezoelectric effect)} \qquad \textbf{Eq 29}$$

Where P_i is the polarization generated along i-axis in response to the applied stress σ_{jk} and d_{ijk} (= d_{kij}) is the piezoelectric coefficient. X_{ij} is the strain generated in particular orientation in response to the application of electric field E_k along the k-axis. The piezoelectric coefficients are third rank tensors and hence the piezoelectric response is anisotropic. The number of non-zero coefficients is governed by crystal symmetry [47]. Piezoelectric response of a ferroelectric material increases as the transition temperature is approached due to the high polarizability of the lattice close to the transition [48]. Hence piezoelectric coefficient is a strong function of temperature. It also depends on the domain state of the material for example 90° degree domain walls are both ferroelectric and ferroelastic in nature, frequency, excitation field, time and domain wall motion [49].

I.4. Magnetoelectrics and Multiferroics:

I.4.1. Definition and Historical background:

The mutual control of electrical polarization and magnetization is sought after in materials due to its potential applications and also because of the rich underlying physics associated with it. Ever since the prediction of intrinsic magnetoelectric effect by Curie in 1894 much progress has been made in this field [50]. Magnetoelectric effect (ME) in general is the induction of magnetization by an electric field or of polarization by a magnetic field. Landau and Lifshitz suggested that ME effect is only allowed in time asymmetric media [51] . In 1960's it was shown theoretically that Cr_2O_3 violates time-reversal symmetry [52] followed by experimental observation of electric field induced magnetization [53] and magnetic field induced polarization in Cr_2O_3 [54]. Although the effect observed was very small in magnitude to be useful for any practical application. Within a decade

many compounds exhibiting ME effect sprung up and they can be found in reference [55]. After a period of inactivity there is recent surge in this field partly owing to the better understanding of the microscopic behavior of such materials which is made possible by advancements in the theory and experimental techniques [56]. On the other hand 'multiferroics' are materials which have two or more primary ferroic order (ferroelectricity, ferromagnetism and ferroelasticity) coexisting in the same phase [56]. The notion is extended nowadays to include antiferroelectric and antiferromagnetism. This title is fairly new and these materials were initially called ferroelectromagnets by Smolenskii et al [57].

A schematic representation of coupling between order parameters is given in figure I-28 (a) where P is the polarization, M is the magnetization and ε is the strain which is the order parameter for ferroelectricity, ferromagnetic and ferroelasticity respectively [58]. Unlike multiferroics, ME effect may exist whatever the nature of magnetic and electrical order parameters and can for example occur in paramagnetic ferroelectrics. The relation between multiferroic and magnetoelectric materials is shown in figure I-28 (b) [59]. Of these order parameters, ferroelasticity is often overlooked and a fourth order parameter called ferrotoroidic is considered.

Requirements for the all the three order parameter (third one being ferrotoroidic) to coexist puts stringent constraint on the symmetry of the materials. Ferroelectricity needs breaking of spatial inversion symmetry while ferromagnetism needs breaking of time reversal symmetry. About 13 point groups satisfy these requirements and only 9 point groups satisfy requirements for all three order parameter. A detailed account of symmetry requirements is given by Schmid in his pioneering review [60]. Moreover obtaining multiferroic materials is made even more difficult by the condition that ferroelectricity requires ions with d^0 configuration whereas magnetism needs ions with partially filled 'd' orbitals making ferroelectricity and ferromagnetism mutually exclusive [61]. Nevertheless several materials exhibiting multiferroic properties have been reported in recent literature. Most of those reports focus on coupling between spontaneous polarization and magnetization. We will see some examples of multiferroic materials in the section I.4.4. Before that we will consider ME effect in terms of free energy as this will give us the expression for linear and non-linear ME effect and also the limitations of ME effect.

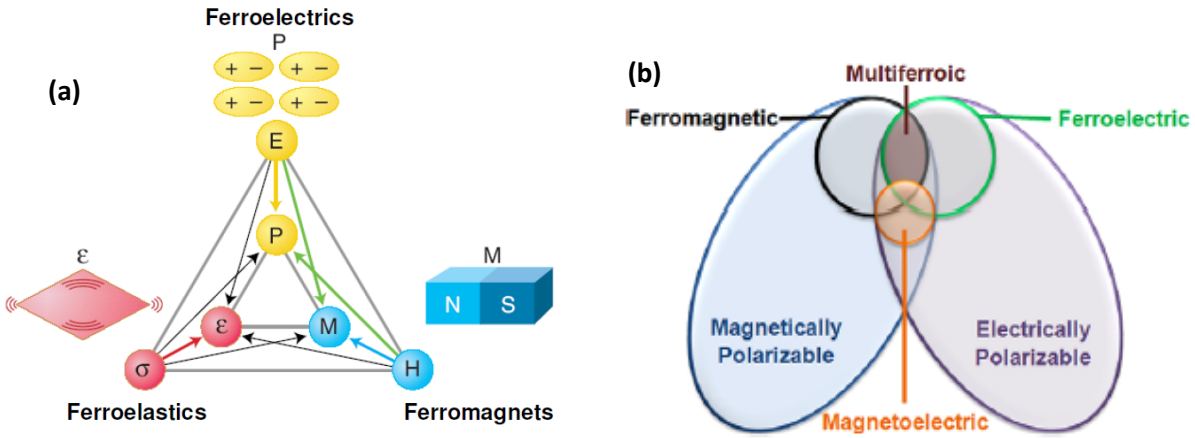

Figure I-28: (a) Schematic representation of coupling between order parameters in multiferroics [58], **(b)** Relation between mutliferroic and magnetoelectric materials [59].

I.4.2. Linear and non-linear magnetoelectric effect:

As we have discussed above linear magnetoelectric is different from multiferroics since they don't have spontaneous polarization (magnetization). However magnetization can be induced by applying electric field or vice versa. Since the electric field E and magnetic field H are vectors, the coupling parameters will be tensors. Then the contribution to the ME effect can be appropriately obtained from the expansion of free energy F.

$$-F(E,H) = \frac{1}{2}\varepsilon_0\varepsilon_{ij}E_iE_j + \frac{1}{2}\mu_0\mu_{ij}H_iH_j + \alpha_{ij}E_iH_j + \frac{\beta_{ijk}}{2}E_iH_jH_k + \frac{\gamma_{ijk}}{2}H_iE_jE_k + \frac{\delta_{ijkl}}{2}E_iE_jH_kH_l \qquad \textbf{Eq 30}$$

Here ε_0 and μ_0 are permittivity and permeability of free space. The relative permittivity ε_{ij} is a second rank tensor and the magnetic equivalent is μ_{ij}, the relative permeability. The third term in the above equation describes the linear ME coupling denoted by α_{ij}. The fourth and fifth term represents the higher order (bilinear) ME coefficients. The last term which is bilinear in both E and H is of particular importance and will be considered in section I.4.3. The derivative of free energy with respect to E gives polarization and magnetization with respect to H. It was further shown that linear ME coupling has a theoretical limit [62] which is given by

$$\alpha_{ij}^2 \leq \varepsilon_0\mu_0\varepsilon_{ii}\mu_{jj} \qquad \textbf{Eq 31}$$

It follows from the above equation that multiferroics (which is both ferroelectric and ferromagnetic possess large permittivity and permeability respectively), display large linear ME effects. If the coupling becomes too strong it might result in phase transition to a more stable state and so the magnetoelectric coefficient will take on a new value [63].

Not all materials have large permittivity and permeability values and hence their linear ME coefficient is small. In those materials high order term denoted by the coefficients β_{ijk}, γ_{ijk} and δ_{ijkl} dominates the linear term. Eerenstein et al. suggested that materials with reduced dimensionality may give magnetoelectric coupling at room temperature through higher order terms and this situation was observed in $BaMnF_4$ at low temperatures [64].

I.4.3. Magnetodielectric Coupling:

Severe symmetry requirements for magnetoelectric and multiferroics has forced researchers to look for coupling which could be observed regardless of the symmetry of the underlying lattice. Such a coupling is indeed possible and can be visualized through the last term in equation 30. This term is bilinear in both electric and magnetic field and hence it is a scalar and can give rise to magnetodielectric (MD) coupling [65]. It describes some kind of coupling between dielectric properties and magnetization in materials which possess neither spontaneous polarization nor symmetry requirements. This coupling can be realized in any insulating magnets and thereby increase the flexibility in designing materials with improved properties. Equation 30 is sufficient to describe MD coupling in ferromagnetic system where there is a non-zero magnetization in the ordered phase. But for anitferromangets where the magnetization remains zero, equation 30 is insufficient. Lawes et al proposed a model to describe the MD coupling in antiferromagnetic system [66]. Their model takes into account spin-phonon coupling and spin-spin correlation to determine the MD coupling. A schematic of MD coupling due to spin-phonon coupling for anitferromagnet is shown in figure I-29 (a). Here q is the wave vector; $\langle M_q M_{-q} \rangle$ is the spin-spin correlation and the g (q) is the MD coupling constant. MD effect will be large if the product of g (q) and $\langle M_q M_{-q} \rangle$ is large. It is apparent from the figure that antiferromagnet has the largest product since the peak in both functions overlap at the maximum whereas for ferromagnet there is no overlap.

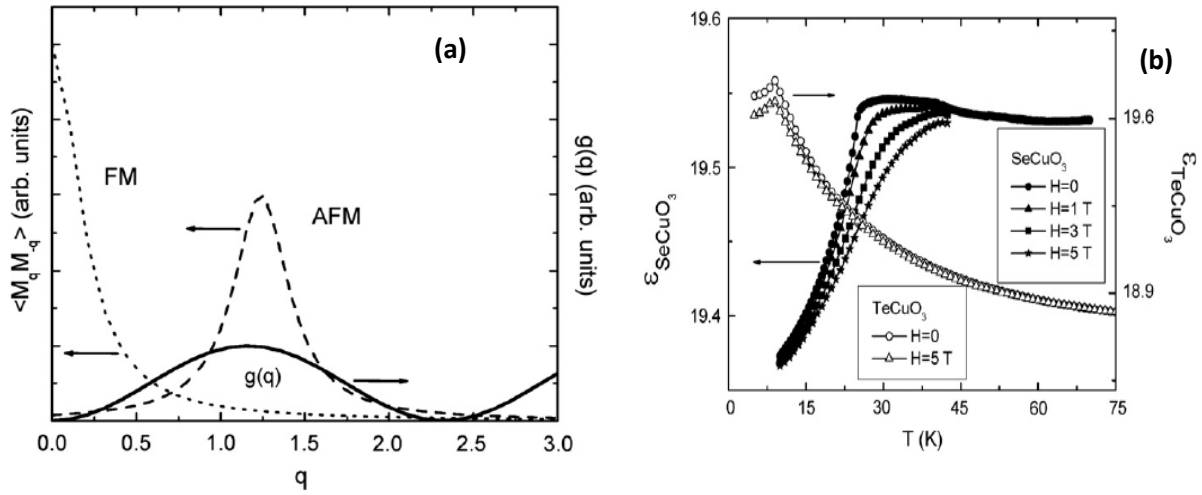

Figure I-29: (a) Schematic curves illustrating the magnetodielectric coupling constant g(q) (solid line), computed assuming spin-phonon coupling, together with the spin-spin correlation functions for ferromagnetic order (dotted line) and antiferromagnetic order (dashed line). **(b)** Temperature dependence of the dielectric constant of SeCuO3 (solid symbols) and TeCuO3 (open symbols) at different fixed magnetic fields. Adapted from ref [65].

Figure I-29 (b) gives the dielectric constant as a function of temperature for $SeCuO_3$ and $TeCuO_3$. $SeCuO_3$ is a ferromagnet with a transition temperature T_C = 25 K and $TeCuO_3$ is an antiferromagnet with a transition temperature T_N = 9 K. Both of these oxides are insulating and they exhibit MD coupling [66]. Above T_C $SeCuO_3$ is a paraelectric and therefore no MD effect is observed. Below T_C spontaneous magnetization appears and the overlap between the MD coupling constant with the ferromagnetic spin-spin correlation goes to zero as described in figure I-29 (a). This leads to a drop in the dielectric constant to its intrinsic value. On the other hand for $TeCuO_3$ due to its antiferromagnetic transition there is a large overlap between MD coupling and the spin-spin correlation leading to maximum in dielectric constant in contrast to the ferromagnetic system. It can also be seen that intrinsic MD coupling is strong close to the magnetic transition temperature which limits its application. The materials which display MD coupling other than the one discussed above are $EuTiO_3$ [67], $TmFeO_3$ [68], Mn_3O_4 [69], $Tb_3Fe_5O_{15}$ [70] etc.

I.4.4. Classification of Multiferroics:

Although multiferroics refers to all three ferroic order parameters, nowadays the term mostly signifies magnetoelectric multiferroics which are ferroelectric and magnetic and not always ferromagnetic. Multiferroics are classified differently by different groups. Van den Brink et al. have classified multiferroics in to two types [71]. In type-I multiferroics ferroelectricity and magnetism have different origins and are often due to different active subsystem of a material. In type-II multiferroics ferroelectricity occurs only in the magnetically ordered state. In this thesis we will classify multiferroics in to two broad classes as intrinsic and extrinsic. The term intrinsic signifies all

the single phase multiferroics. They are further subdivided into four based on the mechanism of ferroelectricity. The extrinsic effects which give rise to multiferroism are (i) mechanical coupling at the interface in composite materials and (ii) heterogeneous conductivity at the interface. We will see both intrinsic and extrinsic multiferroics types in detail in the following.

I.4.4.1. Intrinsic Multiferroics:

Despite vast research in the field of multiferroics over several decades only few materials are promising from the application point of view. Even those are mostly antiferromagnetic ferroelectrics and the combination of ferromagnetism with ferroelectricity can be obtained only as weak coupling. Although the number of point groups which allow the coexistence of ferromagnetism and ferroelectricity are less they alone cannot explain the difficulty in obtaining multiferroics because even in the compound which permit the coexistence, multiferroicity is often not found. Then the natural question which arises is why there are still few multiferroics? Spaldin et al have investigated this very problem and pointed out that in perovskite compounds two kinds of Jahn-Teller distortion can be triggered by transition metal ion [72] [73]. A first-order distortion which retains the center of symmetry and a second-order distortion which breaks the centrosymmetry by off centering of transition metal ion. The latter requires empty 3d orbitals and can only lead to ferroelectricity in a material. For the magnetic order to appear one requires partially filled 3d orbitals which then becomes mutually exclusive with ferroelectricity. Hence efforts have been directed towards finding novel mechanism for ferroelectricity in magnetic materials. Four mechanism were identified which will give rise to spontaneous polarization without the need for cation with empty 3d orbitals and they are (a) lone pair multiferroics, (b) improper geometric multiferroics, (c) charge ordering multiferroics and (d) magnetically driven multiferroics. Accordingly intrinsic multiferroics which are predominantly in single phase system are divided based on these mechanism and they will be described below with an example for each case.

I.4.4.1.1. Lone Pair Multiferroics:

In this kind of multiferroics ferroelectricity and (anti)ferromagnetism have different origins. A lone s^2 pair of electron may hybridize with an empty p orbital to cause a structural distortion and induce ferroelectricity. The compounds which show multiferroism due to this mechanism are $BiFeO_3$ [74], $BiMnO_3$ [75], $BiCrO_3$ [61], Bi_2FeCrO_6 [76] , $PbVO_3$ etc. Here we will discuss only $BiFeO_3$ (BFO). BFO is arguably the most widely studied mutliferroic and also one of the few materials to show ferroelectric and magnetic order above room temperature. It exhibits ferroelectric order below 1100 K and antiferromagnetic ordering at 640 K. The crystal structure of BFO is rhombohedrally distorted perovskite with space group R3C [77]. The ferroelectric order in $BiFeO_3$ is due to the active Bi $6s^2$ lone pair electrons. It exhibits a G-type anitferromagnetic order where the Fe magnetic moments are

aligned ferromagnetically whitin the (111) planes and antiferromagnetically between the adjacent (111) planes. Bulk BFO shows a spiral spin structure with a long wavelength (> 60 nm) spin cycloid propagating along the [1 1 0] direction which cancels out the small ferromagnetic moment due to spin canting. It is schematically shown in figure I-30 [74], [78]. Earlier the value of polarization in bulk BFO was considered to be small with spontaneous polarization on the order of few $\mu C/Cm^2$ [79]. However BFO gained great attention after Wang et al. have shown large ferroelectric polarization of 60 $\mu C/Cm^2$ along with saturation magnetization reaching 150 $emu.cm^{-3}$ in epitaxial thin films [80]. They have found that under the compressive stress in thin films, BFO crystallizes in monoclinic structure and this has enhanced the polarization and magnetization values.

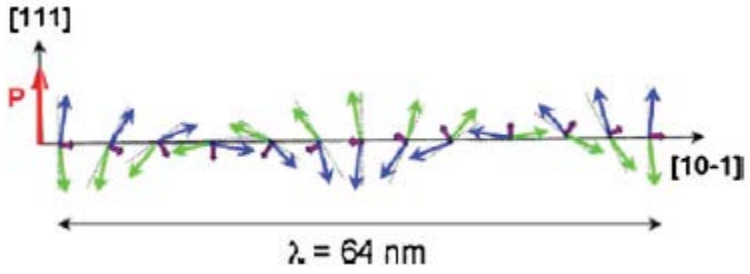

Figure I-30: Schematic representation of the spin cycloid. The canted antiferromagnetic spins (blue and green arrows) give rise to a net magnetic moment (purple arrows) that is spatially averaged out to zero due to the cycloidal rotation. The spins are contained within the plane defined by the polarization vector (red) and the cycloidal propagation vector (black) [78] [74].

However recent studies on high quality BFO single crystal have demonstrated a polarization value of 100 $\mu C/ cm^2$ and this shows that large polarization in BFO is intrinsic and it is not due to the strain as previously shown by Wang et al [81]. On the other hand enhanced magnetic property in BFO was supposed to come from iron oxide based impurity.

Incorporation of BFO films to application faces many challenges of which large leakage is the major factor which degrades the electrical properties of BFO. The large leakage current in BFO films is mostly due to the presence of oxygen vacancies which change the oxidation state of Fe ion in order to compensate for the charge imbalance. The mixed valence of Fe ions (Fe^{2+} and Fe^{3+}) promote charge hopping which leads to conduction and eventually undermines the ferroelectric property of BFO films [82]. It was proposed that substituting some Fe^{3+} ions with Ti^{4+} ions enhances the ferroelectric property of BFO films by decreasing the leakage current [83]. Reduced leakage current is mostly due to the filling of oxygen vacancies by the doping of Ti^{4+} ions and the same effect was found for other dopants like Cr, Mn, Nb. Wang et al. have found improved magnetic properties of BFO by doping it with Ba [84]. Ba doped BFO exhibited spontaneous magnetization and polarization at room temperature. It was stated that magnetization could arise from change in bond angle between Fe –O

– Fe due to the distortion of structure by Ba (large ionic radius) or by the creation mixed valence state of Fe ions (Fe^{3+} and Fe^{4+}).

I.4.4.1.2. Improper Geometric Multiferroics:

The prototype of this type multiferroics is hexagonal rare earth manganite $RMnO_3$. Before 2004 two distinct mechanisms of ferroelectricity was known both of them are based on the second order Jahn-teller effect. The first is the ligand field hybridization of surrounding anions and it is the origin of off center displacement of transition metal cation like in $BaTiO_3$ and $PbTiO_3$ making them ferroelectric [85]. The second is related to the presence of ions with lone pair electrons as we have seen in the case for $BiFeO_3$. Van Aken et al. in their paper reported a new mechanism of ferroelectricity in hexagonal rare earth manganite $YMnO_3$ [86].

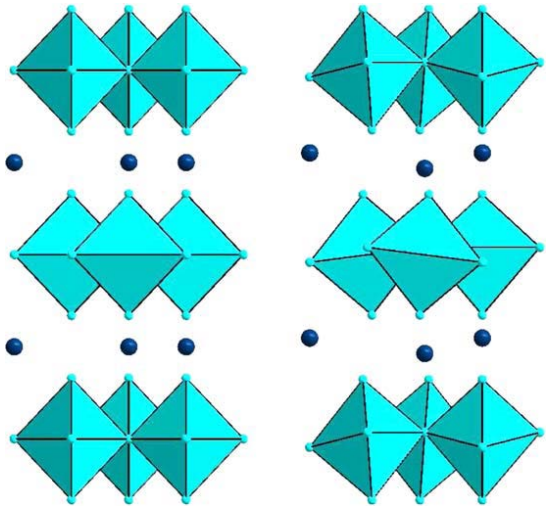

Figure I-31: (Left) High temperature paraelectric and (right) low temperature ferroelectric structure of $YMnO_3$. Note the buckling of MnO_5 polyhedra and the displacement of rare earth Y ion along C-axis in the ferroelectric phase.

They have demonstrated that ferroelectricity in $YMnO_3$ is due to buckling of MnO_5 bi-pyramids and displacement of rare earth ion along c- axis by the collective rotation of MnO_5 polyhedra. It is schematically shown in Figure I-31. This mechanism does not need any hybridization with neighboring orbitals for the ferroelectricity to appear. $YMnO_3$ crystallizes in P63cm hexagonal space group and it is a ferroelectric below 914 K and undergoes antiferromagnetic transition at 80 K. The fundamental interest in this compound was first due to the bulk room temperature ferroelectricity and later on it was greatly considered for electronic application because of the coupling between electric and magnetic orders [87]. One of the advantages of $YMnO_3$ is that polarization can persist to a thickness of only two unit cells even in the absence of screening from metal electrodes [88]. Multiferroic behavior of $YMnO_3$ films were investigated by many researchers. Interestingly Dho et al. demonstrated competing nature of electrical and magnetic orders in $YMnO_3$ [89]. They have shown

that the ferroelectric and magnetic property of $YMnO_3$ depends greatly on the growth direction of the films. Film grown with (0001) orientation was found to be good for ferroelectricity because of their small coercivity and zero exchange bias whereas film grown in (11-21) direction displays large coercivity and exchange bias. Such a dependence on growth direction was attributed to their intrinsic magnetic property due to Mn-Mn spin coupling.

The crystals structure of $RMnO_3$ depends on the ionic radii of the R^{3+} rare earth cations [90] and so does their ferroelectric properties. For R = Ho, Er, Tm, Yb Lu, Sc and Y which have small ionic radii the compound crystallizes in hexagonal P63cm space group and for R = La, Ce, Pr, Nd, Sm, Eu, Gd, Tb and Dy the crystal structure is orthorhombic with Pbnm space group. For the former ferroelectric Curie temperature is well above room temperature and it is far away from magnetic transition temperature and for the latter ferroelectric Curie temperature is below the magnetic transition temperature [33].

I.4.4.1.3. Charge Ordering Multiferroics:

The idea of charge ordering (CO) leading to ferroelectricity was first put forward by Effermov et al. in their pioneering article [91]. The mechanism by which charge ordering leads to ferroelectricity is given explicitly as a schematic in figure I-32 [71]. Figure I-32(a) shows the homogeneous crystal with equal charge on each site or zero charge. Upon CO the site becomes un-equivalent as shown in figure I-32 (b) and dipoles which appear are indicated by black arrows. This does not lead to any net dipole moment since special inversion symmetry is not broken. Figure I-32 (c) gives the bond centered CO, this is due to the dimerization of the lattice. Here the site remains equivalent but the bonds are not, as the strong and weak bonds alternate. Like site centered CO, bond centered CO does not give rise to any dipole moment. Now if we combine site centered and bond centered CO as

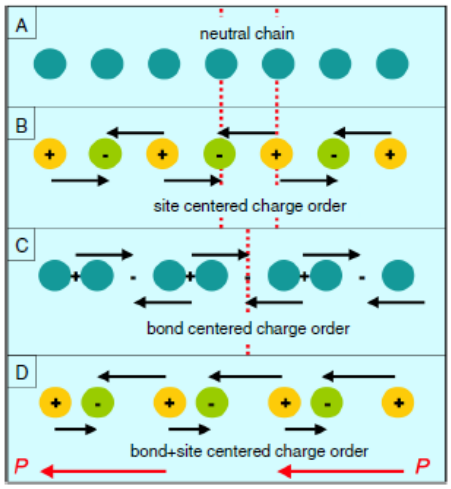

Figure I-32: (A) neutral chain with **(B)** site-centered charge ordering, **(C)** bond-centered charge ordering, and **(D)** combination of B and C leading to ferroelectricity. The red arrows indicate the direction of polarization. [71]

shown in figure I-32 (d), then the situation is totally different and this arrangement breaks spatial inversion symmetry and gives rise to ferroelectricity. Mostly CO is observed in systems with mixed valence cations. Typical examples of compounds that show coupling between electrical and magnetic order due to CO are $Pr_{1-X}Ca_XMnO_3$ [92], Fe_3O_4 [93], $LuFe_2O_4$ (LFO) [94] etc. All of these compounds have mixed valence in their transition metal cation. LFO has a double layer structure with triangular iron lattice within each layer. Here Fe cations are in 2+ and 3+ valence states like in Fe_3O_4. Ferroelectricity in LFO is mainly owing to CO where the charge redistribution of Fe cations between the layers creates a net dipole moment at the CO temperature of 330 K. LFO orders ferrimagnetically at 250 K below which it displays multiferroics behavior [94] .

I.4.4.1.4. Magnetically Driven Multiferroics:

So far we have seen multiferroics whose ferroelectric Curie temperature is different from the magnetic transition temperature. Here we will discuss some systems which give rise to ferroelectricity at the magnetic transition temperature. Therefore the coupling between electrical and magnetic orders is very strong in this class of materials. Such a strong coupling is found in systems of $RMnO_3$ where R = Tb, Gd [95]; RMn_2O_5 where R = Tb,Dy,Y, Ho, Bi etc. [96]; $Ni_3V_2O_8$ [97] and hexaferrite [98]. Especially ferroelectricity appears in these systems in a certain magnetically ordered phase i.e. in the spiral ordered phase. In $TbMnO_3$ antiferromagnetic order sets in at T_N = 41 K with the sinusoid magnetic structure and electrical polarization doesn't appear in this phase. But below 30 K, the magnetic structure of $TbMnO_3$ changes from sinusoidal to helicoidal magnetic structure (or incommensurate to commensurate structure) and a finite polarization appears. Magnetization, dielectric constant and polarization as a function of temperature are shown in figure I-33. It is evident from the figure that dielectric anomaly (middle) and polarization (bottom) appears at magnetic transition indicated by T_{lock} (top) which is nothing but a change in magnetic structure from sinusoidal to helicoidal.

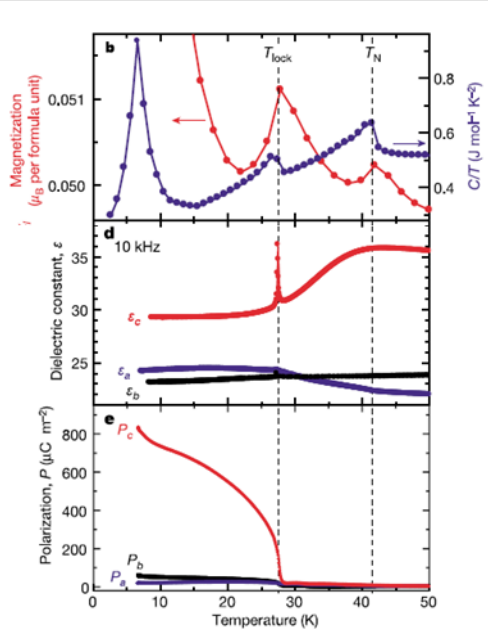

Figure I-33: Magnetization (top), dielectric Constant (middle) and polarization (bottom) as a function of temperature in $TbMnO_3$ single crystal along three crystallographic axis [95]. Notice the change in dielectric constant and appearance of finite polarization at the magnetic transition indicated by T_{lock}.

This polarization can be switched with the external magnetic field. It was further shown by Mostovoy that not all spiral magnetic structure can lead to appearance of ferroelectricity [99]. He stated that if the spin rotation axis 'e' does not coincide with the wave vector of a spiral 'Q' then ferroelectricity can appear. Then we can imagine many multiferroic systems if the above condition is met or even in systems where the wave vector 'Q' coincides with the spin rotation axis 'e' multiferroism can be expected if the external magnetic field can change the direction of the spin [100]. The value of polarization is usually smaller than the classical ferroelectrics like $BaTiO_3$. Nevertheless their coupling between orders parameters are very strong which make them interesting for many applications.

I.4.4.2. Extrinsic Multiferroics:

Although intrinsic single phase multiferroics show interesting properties they are often not suitable for practical application because it is often observed at very low temperature and their magnetoelectric coupling is small. To circumvent this problem research was focused on developing extrinsic multiferroics which might possibly show large magnetoelectric coupling at room temperature. In this respect composite materials made by combining piezoelectric and magnetic substances have attracted lot of attention. In recent years this kind of approach has gained further encouragement due to the progress made in growth of crystallized complex oxide films and heterostructures and in the fabrication of nanostructures [101]. On the other hand recently it was demonstrated in single phase material that magnetocapacitance (i.e. change of capacitance by

magnetic field) can be achieved even without actual magnetoelectric coupling [1]. We will discuss in detail these two approaches in the following section.

I.4.4.2.1. Mechanical Coupling at the Interface:

The property of composite materials is determined by the properties of their constituent phases and their interaction between them. The final composite property can be average or enhancement of the effect of the primary constituents. These composites may also show novel properties which are usually absent in the primary phase. Composite multiferroics are obtained by combining magnetostrictive and piezoelectric compounds. A magnetic field applied to the composite will induce strain in the magnetostrictive phase which is then transferred to the piezoelectric phase and that induces polarization [103]. It is described vaguely by

$$ME\ effect = \frac{electrical}{mechanical} \times \frac{mechanical}{magnetic} \qquad \textbf{Eq 32}$$

The first composite multiferroic using the mechanical coupling at the interface was developed by van Suchtelen and van Boomgard et al [104] [105]. They successfully grew a composite containing ferroelectric piezoelectric $BaTiO_3$ and ferromagnetic piezomagnetic $CoFe_2O_4$. The magnetoelectric effect displayed by these compounds was much larger than the single phase multiferroic one. But their synthesis was complex and cost intensive and hence Harshe et al. developed a particulate ceramic composite of ferrites and $BaTiO_3$ or $PbTiO_3$ by conventional sintering process [106]. This was simple and a very cost effective method. A breakthrough in this field was achieved when a giant magnetostrictive rare earth iron alloy $Tb_{1-X}Dy_XFe_2$ was developed [107]. This compound along with PZT ($PbZr_{0.52}Ti_{0.48}O_3$) which is a good piezoelectric in a composite exhibits a giant magnetoelectric coupling. Generally these bulk composites are usually employed in three connectivity schemes. They are particulate composite, laminate composite and fiber or rod composite and it is shown in figure I-34. Detailed description of the magnetoelectric behavior of these composites is out of scope of the present thesis and can be found in the review by Nan et al. [108]. Apart from strain mediated mechanism discussed here there are other mechanisms which give rise to artificial multiferroic effect. They are (i) charge mediated composite multiferroics, (ii) exchange bias mediated composite heterostructures, (iii) electron transport based multiferroic heterostructures and these are considered in detail in an excellent review by Ramesh et al. [101].

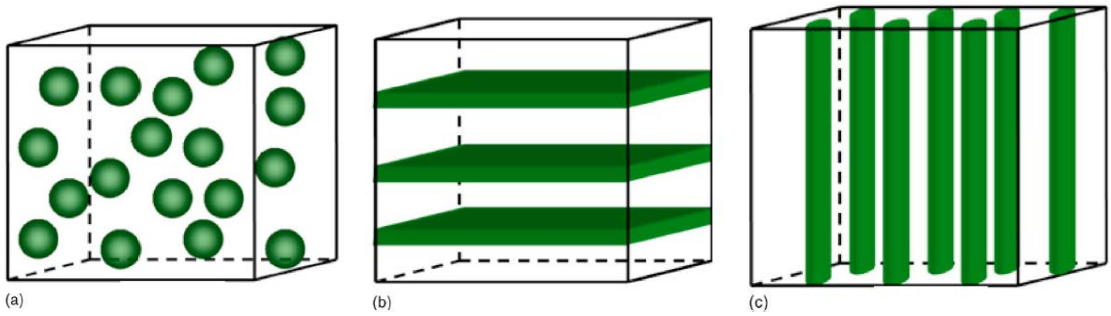

Figure I-34: Schematic illustration of three bulk composites with the three common connectivity schemes: **(a)** particulate composite, **(b)** laminate composite, and **(c)** fiber/rod composite [108].

I.4.4.2.2. Heterogeneous Conductivity at the Interface:

Another possible way of obtaining extrinsic magnetoelectric coupling is by having magneto-resistance (MR) artifacts. This model was first proposed by Catalan [1]. In a capacitor structure with parallel plate electrodes on a dielectric, the response to an electric field contains a capacitive term and a leakage term measured as resistance. At the interface between the electrode and dielectric band bending may occur due to charge injection from the electrode to dielectric or dielectric to electrode (charge depletion). Therefore the density of charge carrier close to the surface layer is different from the bulk of the sample and so is the resistance. This will lead to apparent high dielectric constant based on Maxwell -Wagner effect as seen in section I.2.2.1. Then the equivalent circuit for this process has two leaky capacitor connected in series one representing the bulk and the other one for the interface at the electrode and dielectric. The impedance of this circuit is a complex quantity and it given by the equation 21-24. It is obvious from the equation that if the resistance of any of the layers is changed by magnetic field so does the measured permittivity yielding magnetocapacitance (MC). It is given by

$$MC = \frac{\varepsilon'(H) - \varepsilon'(0)}{\varepsilon'(H)} \times 100 \qquad \textbf{Eq 33}$$

Catalan calculated the contribution of MR to the dielectric permittivity and losses under magnetic field. The results of the calculation are shown in fig I-35. It is easily discernible from the figure that the MR can lead to giant magnetocapacitance even in materials which are not magnetoelectric. A noteworthy feature of this result is that not only capacitance is affected by magnetic field but also the losses. This is the main factor by which one can distinguish the intrinsic MC from the extrinsic one. Additionally MC will be strongly frequency dependent which correlates with the magneto loss. Also the sign of MR changes depending on whether it is due to the core or the interface. Moreover it was further found that MC is more pronounced at the conductivity relaxation time.

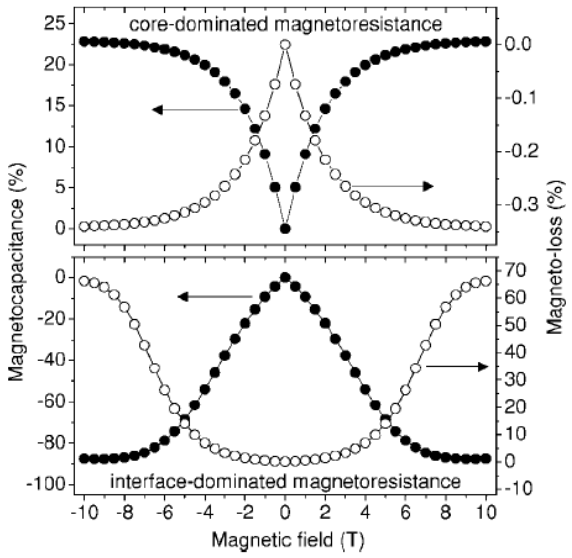

Figure I-35: Calculated magnetocapacitance (full circles) and magnetolosses (empty circles) of a magnetoresistive material with depleted boundary layers when the MR is core-based (e.g., double-exchange mechanism) andinterface-based (e.g., tunneling magnetoresistance) [1].

Parish et al. have proposed magnetic field dependent dielectric constant in an inhomogeneous media even without intrinsic magnetoresistance [109]. They have found theoretically a strong dielectric resonance as a function of frequency and the position of dissipation peak depends on the magnetic field in a composite media of dielectric with pure capacitance sandwiched between electrodes of pure resistance. For such a system they have argued that a large magnetic field can induce dielectric resonance and it is determined by the Hall resistivity. This is achieved inspite of the fact that there is no magnetoresistance. Here the main contributor for the MC is the Hall effect at the metal dielectric interface. Recently Pirc et al. have proposed a model which gives magnetoelectric effect in a single phase or composite media which have both relaxor ferroelectric and relaxor ferromagnetic properties [110]. They point out that magnetostriction plus electrostriction can produce dielectric anomalies when a magnetic field is applied. In relaxor no long range order is possible and hence linear magnetoelectric effect is prohibited therefore higher order magnetoelectric coupling dominates similar to the one we have seen in section I.4.2 and I.4.3. In addition they also showed that sign of the magnetoelectric interaction indicated whether a ferroelectric stated is induced or quenched by magnetic field. Although later two models discuss the possibility of extrinsic magnetoelectric effect we will give examples only for the model proposed by Catalan since it has a direct relation to the present thesis.

Maglione has demonstrated magnetocapacitance in wide range of materials following the Catalan model [2]. He has shown that one cent diodes can give a large MC in applied magnetic field. In a typical p-n junction diode a space charge layer is formed at the interface. The application of magnetic

field alters the free charge trajectories through the Hall effect and favors the recombination thereby reducing the space charge localization and consequently dynamical capacitance. In $CaCu_3Ti_4O_{12}$ (CCTO) a giant permittivity material, MC was found right at the relaxation temperature (100 K) and it is shown in figure I-36(a). It is apparent from the figure that away from dielectric relaxation at 300 K no MC was found and a maximum of 15 % MC was obtained at 100 K, the temperature where CCTO undergoes relaxation. Dielectric relaxation in CCTO is due to the grain boundary layer acting as a dielectric barrier between the conducting grains. Similar to the p-n junction diode free charges are responsible for the observed MC. However Catalan model alone cannot explain why the MC was found only close to dielectric relaxation. Maglione has proposed a model based on the space charge model by Coelho. According to this model the relaxation time τ is given by

$$\tau = d\sqrt{\frac{\sigma}{\varepsilon D}} \qquad \textbf{Eq 34}$$

Where d is the thickness, ε the dielectric permittivity, σ is the conductivity and D the diffusion coefficient of the free charges which localizes at the interface. As we have seen before applied magnetic field interacts with the free charges therefore tunes the σ and D and eventually alters the relaxation time.

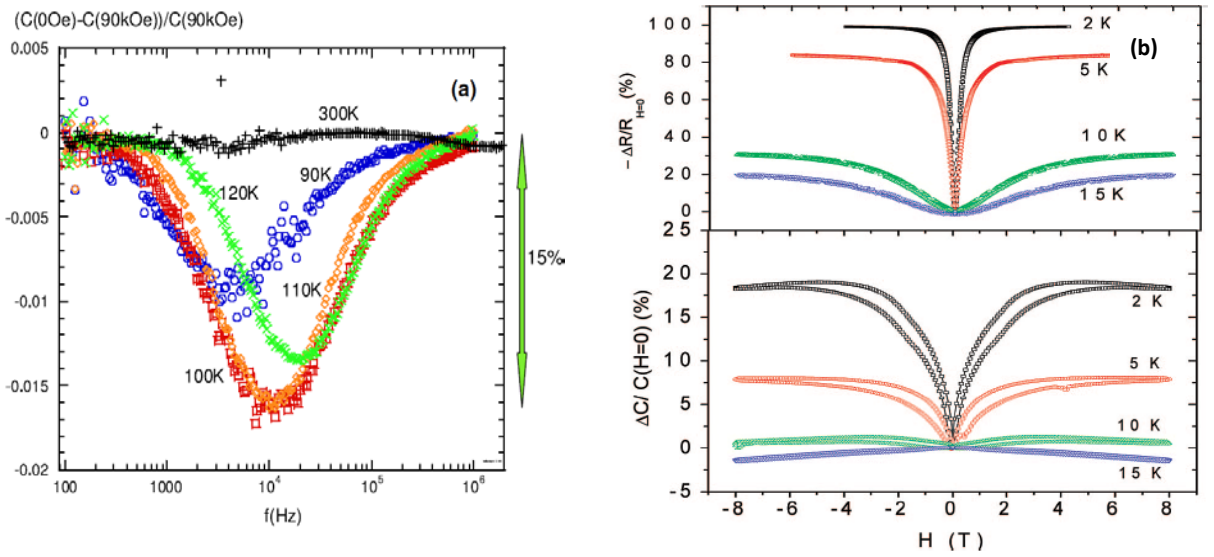

Figure I-36: (a) Relative variation of capacitance under magnetic field of 90 kOe in CCTO [2]**. (b)** Magnetic field dependence of magnetoresistance and magnetocapacitance measured at 100 KHz for $EuNbO_2N$ [112].

The next example is that of polycrystalline $EuNbO_2N$. Jorge et al. have synthesized $EuNbO_2N$ polycrystalline sample and found that it undergoes ferromagnetic transition below 5.1 K [112]. They have also found a large change of resistance at the same temperature. The application of magnetic field above T_C gives a giant magnetoresistance and it becomes colossal in value below T_C

correspondingly MC switches from negative to positive respectively and reaches a maximum value of 20 % at 2 K. These results are shown in figure I-36(b) and note the similarity of the curves as predicted by Catalan. The bulk conductivity related to the grain boundaries increases when a magnetic field is applied gives an additional contribution to the polarization without an intrinsic multiferroic coupling. This is possibly the likely origin of the MC in $EuNbO_2N$ and it is purely extrinsic in nature. MC was also found in nanoparticles of La_2CoMnO_6. Venimadhav et al. have shown that MC in La_2CoMnO_6 arises from both intrinsic and extrinsic factors [113]. Intrinsic factor is due to the coupling of magnetic to the dielectric orders and the magnetoresistance combined with Maxwell-Wagner gives the extrinsic contribution.

Our last example concerns with the thin films of PZT/LSMO bilayers. Dussan et al. have carried out polarization hysteresis measurement with and without magnetic field on PZT/LSMO films with thickness of 1.4 µm and 550 nm PZT on 200 nm LSMO [114]. They found that film with larger thickness shows no hysteresis dependence on magnetic field except for the slight enhancement of the coercive field. On the other hand film with 550 nm PZT shows remarkable effect on the application of magnetic field. The hysteresis voltage width increases with magnetic field up to H =0.33 T and then vanishes completely at H = 0.34 T (figure I-37(a)).

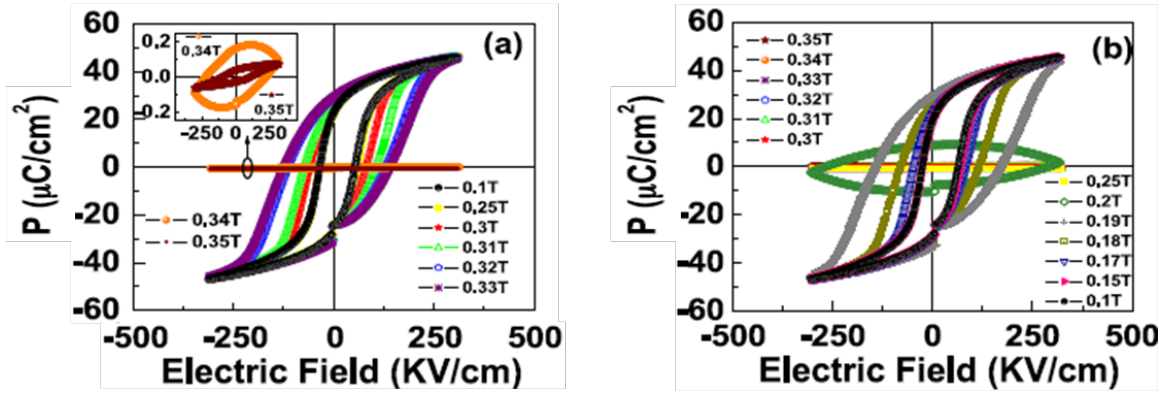

Figure I-37: Ferroelectric hysteresis *P(V)* in PZT films with LSMO electrodes on LAO substrates at different applied magnetic fields for PZT film thickness 0.55 μm. (a) Increasing magnetic field and (b) decreasing magnetic field. A significant magnetic field dependence is observed in the hysteretic loss near a critical field of H = 0.34 T, which is shown more clearly in the inset. This value of H = 0.34 T corresponds closely to the field at which the negative magnetoresistance in LSMO saturates. [114]

Note that hysteresis loop does not switch it but merely reduces to zero above H = 0.34 T. Upon removal of the magnetic field the hysteresis loop is recovered showing reproducibility (figure I-37(b)). They have interpreted this based on the magnetoresistance of the LSMO layer. As the magnetic field increases the LSMO layer becomes more conducting and consequently PZT is subjected to higher net voltage which leads to increases in dielectric losses and therefore widens the hysteresis loop. AT H= 0.34 T the system is shorted and the loop vanishes which is consistent with the

results of Hwang et al. who found that LSMO shows a strong negative magnetoresistance at low fields and becomes flat above H = 0.33 T [115]. They have argued that albeit magnetoresistance plays a major role that alone is not sufficient for the explanation and the striction model by Pric et al. must be taken into account [110].

To summarize we can ascertain two things from the above discussion (1) extrinsic effects may play a major role in realizing multiferroic or magnetodielectric behavior of materials hence utmost care must be taken where intrinsic multiferroic effects are reported. One way to do that is to also probe the dielectric loss along with the capacitance since extrinsic contributions due to magnetoresistance invariably have a consequence on the dielectric loss of the material. (2) Extrinsic effects provide an easy way to realize multiferroic materials which are otherwise more difficult to obtain. Furthermore whatever the morphology of the material extrinsic magnetoelectric or multiferroic can still be achieved as is evident from the above examples.

I.5. Motivation of the Present Thesis:

Application of magnetic field to dielectric or ferroelectric material may give rise to plethora of interesting phenomenon like multiferroicity, magnetoelectricity or magnetodielectric behavior as seen above. One of the major challenge is to identify whether these behavior are due to intrinsic nature of the sample or due to the extrinsic factors. Extrinsic contribution predominantly arises from the conductivity dependence of magnetic field or in other words free charge behavior under applied field. The origin of free charges could be the ubiquitous presence of heterogeneous impurities, oxygen vacancies or intentional as in the case of doped materials. As we have seen above the physical barriers to the motion of free charges affects the capacitance of the materials and these physical barriers could be grain boundaries, electrode – bulk interface etc. Whatever may be the origin of free charges and type of interface the application of external stress like electric field and magnetic field will result in change of dielectric properties extrinsically. So, one of the main objectives of this thesis is to understand the free charges contribution to the dielectric permittivity of materials. We will also study piezoelectric materials and effect of conductivity on the piezo resonance. Finally we turn towards synthesizing and exploring new multiferroic materials since not many good multiferroics are known at the moment. The major questions we will try to answer in this thesis are

- Is it possible to have different interfaces other than grain boundaries and electrode-sample interface?

- What is the influence of external stresses like temperature, electric and magnetic field on this interface and to the dielectric property?
- In the absence of interface how the free charges can influence the dielectric property under magnetic field?
- How the sample conductivity can affect the piezoelectric resonance and why?
- Exploring new magnetically driven ferroelectric materials and how it works?

I.6. References:

[1] R. Coelho. *Physics of dielectrics for the engineer*. Elsevier Scientific Publishing Company, 1978.

[2] D.F. Gibbs and B.W.Jones. *J. Phys. C: Solid State Phys*, 2:1392, 1969.

[3] J.M. Wimmer and N.M. Tallen. *J. App. Phys*, 37:3728, 1966.

[4] W. Kauzmann. *Rev. Mod. Phys*, 14:12, 1942.

[5] P. Debye. *Polar Moelcules*. The Chemical Catalogue Company, 1929.

[6] J.R. Macdonald. *Ann. Biomed. Eng*, 20:289, 1992.

[7] A.K. Jonscher. *Dielectric relaxation in solids*. Chelsea Dielectrics Press, London, 1983.

[8] K.S. Cole and R.H. Cole. *J. Chem.Phys.*, 9:341, 1941.

[9] A.K. Jonscher. *J. Mat. Sci.*, 16:2037, 1981.

[10] R.M. Hill and A.K. Jonscher. *J. Non Cryst. Solids.*, 32:53, 1979.

[11] A.K. Jonscher. *Nature*, 267:673, 1977.

[12] K.L. Deori. PhD thesis, University of London, 1980.

[13] A.K. Jonscher. *Phil. Mag.B.*, 38:587, 1978.

[14] P. Lukenheimer, V. Bobnar, A.V. Pronin, A.I. Ritus, A.A. Volkov, A. Loidl. *Phys. Rev. B.*, 66:052105, 2002.

[15] A.S. Shcheulin, A.K. Kupchikov, A.E. Angervaks, D.E. Onopko, A.I. Ryskin, A.I. Ritus, A.V. Pronin, A.A. Volkov, P. Lunkenheimer, A. Loidl. *Phys. Rev. B.*, 63:205207, 2001.

[16] A. Seeger, P. Lunkenheimer, J. Hemberge, A.A. Mukhin, V.Yu. Ivanov, A.M. Balbashov, A. Loidl. *J. Phys: Condens. Matt*, 11:3273, 1999.

[17] M.A. Subramanian, D. Li, N. Duan, B.A. Reisner, A.W. Sleight. *J. Solid. State. Chem*, 151:323, 2000.

[18] D.C. Sinclair, T.B. Adams, F.D. Morrison, A.R. West. *Appl. Phys. Lett*, 80:2153, 2002.

[19] T.B. Adams, D.C Sinclair, A.R. West. *J. Am. Ceram. Soc*, 89:3129, 2006.

[20] S. Krohns, P. Lunkenheimer, S. G. Ebbinghaus, A. Loidl. *Appl. Phys. Lett*, 91:022910, 2007.

[21] S. Krohns, P. Lunkenheimer, S. G. Ebbinghaus, A. Loidl. *J. App. Phys*, 103:084107, 2008.

[22] V. Bobnar, P. Lunkenheimer, M. Paraskevopoulos, A. Loidl. *Phys. Rev. B.*, 65:184403, 2002.

[23] E. Iguchi, N. Kubota, T. Nakamori, N. Yamamoto, K.J. Lee. *Phys. Rev. B.*, 43:8646, 1991.

[24] O. Bidault, M. Maglione, M. Actis, M. Kchikech, B. Salce. *Phys. Rev. B.*, 52:4191, 1995.

[25] B. Salce, J.L. Gravil, L.A. Boatner. *J. Phys: Coden. Matt*, 6:1977, 1994.

[26] M. Maglione. *Ferroelectrics*, 254:151, 2001.

[27] O. Bidault, P. Goux, M. Kchikech, M. Belkaoumi, M. Maglione. *Phys. Rev. B.*, 49:7868, 1994.

[28] M. Maglione. *Ferroelectrics*, 176:1, 1996.

[29] A. Pimenova, J. Ullrich, P. Lunkenheimer, A. Loidl, C.H.A. Ruscher. *Sol. Stat. Ion*, 109:111, 1998.

[30] R. Gerhardt. *J. Phys. Chem. Sol*, 55:1491, 1994.

[31] M.E. Lines and A.M. Glass. *Principles and Applications of Ferroelectric and Related Materials*. Oxford Classic Text in Physical Sciences, 2001.

[32] F. Jona and G. Shirane. *Ferroelectric Crystals,*. Monograph on Solid State Physics, Pergamon Press, Germany, 1962.

[33] N. Izyumskaya, Ya. Alivov, H. Mokoç. *Crit. Rev. Solid State Mater. Sci*, 34:89, 2009.

[34] J. Valasek. *Phys. Rev.*, 17:475, 1921.

[35] A. Von Hippel. Technical report, US National Defense research Committee Report 300.NDRC, Boston, MA, 1944.

[36] J.C. Slater. *Phys. Rev.*, 78:748, 1950.

[37] V.H. Schmidt. *Ferroelectrics*, 72:157, 1987.

[38] U. Böttger. *Polar Oxides: Properties, Characterization, and Imaging*. WILEY-VCH Verlag GmbH & Co.KGaA, 2005.

[39] B. Jaffe, W.R. Cook, H. Jaffe. *Piezoelectric Ceramics*. Academic Press in London, New York, 1971.

[40] D. Damjanovic. *Rep. Prog. Phys.*, 61:1267, 1998.

[41] W.J. Merz. *Phys. Rev*, 76:1221, 1949.

[42] M. Kamlah. *Contin. Mech. Thermodyn.*, 13:219, 2001.

[43] R.E. Newnham. *Structure-property relations.* Berlin:Springer-Verlag,, 1975.

[44] J. Fousek, V. Janovec. *J. App. Phys*, 40:135, 1969.

[45] Y. Xu. *Ferroelectric Materials and Their Applications*. North-Holland, New York, 1991.

[46] J. Curie P. Curie. *Bull. Soc Min. Fr*, 3:90, 1880.

[47] J.F. Nye. *Physical Properties of Crystals,*. Oxford University Press,, 1957.

[48] D. Wang, Y. Fotinich, G.P. Carman. *J. App. Phys*, 83:5342, 1998.

[49] R.Waser, U. Böttger, and S.Tiedke, editors. *Polar Oxides: Properties, Characterization, and Imaging*. WILEY-VCH Verlag GmbH & Co.KGaA, 2005.

[50] P. Curie. *J. Physi. Théor. App*, 3:393, 1894.

[51] L.D. Landau, E.M. Lifshitz. *Electrodynamics of continuous media*. Oxford: Pergamon, 1960.

[52] I.E. Dzyaloshinskii. *Sov. Phys. JETP*, 10:628, 1960.

[53] D.N . Astrov. *Sov. Phys*, 11:708, 1960.

[54] V.J. Folen, G.T. Rado, E.W. Stalder. *Phys. Rev. Lett*, 607:6, 1961.

[55] H. Schmid. *Int. J. Magn*, 4:337, 1973.

[56] M. Fiebig. *J. Phys. D: App. Phys*, 38:R123, 2005.

[57] G.A. Somlenskii, I.E. Chupis. *Sov. Phys. Usp*, 25:475, 1982.

[58] N.A. Spaldin and M. Fiebig. *Science*, 15:391, 2005.

[59] L.W. Martin, S.P. Crane, Y-H. Chu, M.B. Holcomb, M. Gajek, M. Huijben, C-H. Yang, N. Balke, R. Ramesh. *J. Phys: Condens. Matt*, 20:434220, 2008.

[60] H. Schmid. *J. Phys: Condens. Matt*, 20:434201, 2008.

[61] N.A. Hill, P. Bäettig, C. Daul. *J. Phys. Chem. B*, 3383:106, 2002.

[62] W.F.Jr. Brown, R.M. Hornreich, S. Shtrikman. *Phys. Rev.*, 168:574, 1968.

[63] W. Eerenstein, N.D. Mathur, J.F. Scott. *Nature*, 442:759, 2006.

[64] J.F. Scott. *Phys. Rev. B*, 16:2329, 1977.

[65] G. Lawes, T. Kimura, C.M. Varma, M.A. Subramanian, N. Rogado, R.J. Cava, A.P. Ramirez. *Prog. Sol. Stat. Chem*, 37:40, 2009.

[66] G. Lawes, A.P. Ramirez, C.M. Varma, M.A. Subramanian. *Phys. Rev. Lett*, 91:257208, 2003.

[67] T. Katsufuji, H. Takagi. *Phys. Rev. B.*, 64:054415, 2001.

[68] R. Muralidharan, T-H. Jang, C-H. Yang, Y.H. Jeong, T.Y. Koo. *Appl. Phys. Lett*, 90:012506, 2007.

[69] R. Tackett, G. Lawes. *Phys. Rev. B.*, 76:024409, 2007.

[70] N. Hur, S. Park, S. Guha, A. Borissov, V. Kiryukhin, S-W. Cheong. *Appl. Phys. Lett*, 87:042901, 2005.

[71] J. Van den Brink, D.I. Khomskii. *J. Phys: Condens. Matt*, 20:434217, 2008.

[72] N.A. Hill. *J. Phys. Chem. B*, 104:6694, 2000.

[73] H. Schmid. Magnetoelectric interaction phenomenon in a crsytal. Technical report, 2004.

[74] G. Catalan, J.F. Scott. *Adv. Mater*, 21:2463, 2009.

[75] T. Kimura, S. Kawamoto, I. Yamada, M. Azuma, M. Takano, Y. Tokura. *Phys. Rev. B.*, 67:180401, 2003.

[76] P. Bäettig, N.A. Spaldin. *Appl. Phys. Lett*, 86:012505, 2005.

[77] C. Michel, J-M. Moreau, G.D. Achenbach, R. Gerson, W.J. James. *Sol. Stat. Comm*, 7:701, 1969.

[78] D. Lebeugle, D. Colson, A. Forget, M. Viret, A.M. Bataille, A. Gukasov. *Phys. Rev. Lett*, 100:227602, 2008.

[79] J.R. Teague, R. Gerson, W.J. James. *Sol. Stat. Comm*, 8:1073, 1970.

[80] J. Wang, J.B. Neaton, H. Zheng, V.S. Nagarajan, B. Ogale, B. Liu, D. Viehland, V. Vaithyanathan, D.G. Schlom, U.V. Waghmare, N.A. Spaldin, K.M. Rabe, M. Wuttig, R. Ramesh. *Science*, 299:1719, 2003.

[81] G. Lawes, G. Srinivasan. *J. Phys D: Appl. Phys*, 44:243001, 2011.

[82] V.R. Palkar, J. John, R. Pinto. *Appl. Phys. Lett*, 80:1628, 2002.

[83] X. Qi, R. Dho, R. Tomov, M.G. Blamire, J.L. Macmanus Discroll. *Appl. Phys. Lett*, 86:062903, 2005.

[84] D.H. Wang, W.C. Goh, M. Ning, C.K. Ong. *Appl. Phys. Lett*, 88:212907, 2006.

[85] R.E. Cohen. *Nature*, 358:136, 1992.

[86] B.B. Van Aken, T.M. Palstra, A. Filippetti, N.A. Spaldin. *Nat. Mater*, 3:164, 2003.

[87] Z.J. Huang, Y. Cao, Y.Y. Sun, Y.Y. Xue, C.W. Chu. *Phys. Rev. B.*, 56:2623, 1997.

[88] S. Na, C.J. Fennie, A.A. Demkov. *Phys. Rev. Lett*, 102:107601, 2009.

[89] J. Dho, M.G. Blamire. *Appl. Phys. Lett*, 87:252204, 2005.

[90] H.L. Yakel Jnr, W.C. Koehler, E.F. Bertaut, E.F. Forrat. *Acta. Crystallogr*, 957:16, 1963.

[91] D.V. Effremov, J. Van den Brink, D.I. Khomskii. *Nat. Mater*, 3:853, 2004.

[92] S. Mercone, A. Wahl, A. Pautrat, M. Pollet, C. Simon. *Phys. Rev. B.*, 69:174433, 2004.

[93] Y. Miyamoto, S. Ishihara, T. Hirano, M. Takada, N. Suzuki. *Sol. Stat. Comm*, 89:51, 1994.

[94] N. Ikeda, H. Ohsumi, K. Ohwada, K. Ishii, T. Inami, K. Kakurai, Y. Murakami, K. Yoshii, S. Mori, Y. Horibe, H. Kitô. *Nature*, 436:1136, 2005.

[95] T. Kimura, T. Goto, H. Shintani, K. Ishizaka, T. Arima, Y. Tokura. *Nature*, 426:55, 2003.

[96] N. Hur, S. Park, P.A. Sharma, S. Guha, S.W.P. Cheong. *Phys. Rev. Lett*, 93:107207, 2004.

[97] G. Lawes, A.B. Harris, T. Kimura, N. Rogado, R.J. Cava, A. Aharony, O. Entin-Wohlman, T. Yildirim, M. Kenzelmann, C. Broholm, A.P. Ramirez. *Phys. Rev. Lett*, 95:087205, 2005.

[98] T. Kimura, G. Lawes, A.P. Ramirez. *Phys. Rev. Lett*, 94:137201, 2005.

[99] M. Mostovoy. *Phys. Rev. Lett*, 96:067601, 2006.

[100] D.I. Khomskii. *J. Mag. Mag. Mater*, 306:1, 2008.

[101] C.A.F. Vaz, J. Hoffman, C.H. Ahn, R. Ramesh. *Adv. Mater*, 22:2900, 2010.

[102] G. Catalan. *Appl. Phys. Lett*, 88:102902, 2006.

[103] C.W. Nan. *Phys. Rev. B.*, 60:6082, 1994.

[104] J. Boomgaard, D.R. Terrell, R.A. Born, H.F.J.I. Giller. *J. Mat.Sci*, 9:1705, 1974.

[105] J. van Suchtelen. Technical report, Philips Research Reports, 1972.

[106] G. Harshe, J.P. Dougherty, R.E. Newnham. *Int. J. App. Electromag.Mat*, 4:145, 1993.

[107] J. Ryu, S. Priya, A.V. Carazo, K. Uchino, H.E. Kim. *Ja. J. App. Phys: Part 1*, 49:4948, 2001.

[108] C.W. Nan, M.I. Bichurin, S. Dong, D. Viehald, G. Srinivasan. *J. App. Phys*, 103:031101, 2008.

[109] M.M. Parish, P.B. Littlewood. *Phys. Rev. Lett*, 101:166602, 2008.

[110] R. Pirc, R. Blinc, J.F. Scott. *Phys. Rev. B.*, 79:214114, 2009.

[111] M. Maglione. *J. Phys: Condens. Matt*, 20:322202, 2008.

[112] A.B. Jorge, J. Oro´-Sole´, A.M. Bea, N. Mufti, T.T.M. Palstra, J.A. Rodgers, J.P. Attfield, A. Fuertes. *J. Am. Chem. Soc*, 130:12572, 2008.

[113] A. Venimadhav, J. Krishna Murthy. *J. App. Phys*, 111:024102, 2012.

[114] S. Dussan, A. Kumar, R.S. Katiyar, S. Priya, J.F. Scott. *J. Phys: Condens. Matt*, 23:202203, 2011.

[115] H.Y. Hwang, S-W. Cheong, N.P. Ong, N. P, B. Batlogg. *Phys. Rev. Lett*, 77:2041, 1996.

Chapter 2

II. Experimental Techniques:

In this chapter all the experimental techniques used during the course of this thesis are described in detail. Solid state synthesis and co precipitation methods were adopted to obtain ceramic powders. These ceramics were then analyzed with X- ray diffraction to determine the structure and phase purity. For characterization most widely used experiments are capacitance, piezoelectric and pyroelectric measurements. For certain cases these measurements were carried out under magnetic field in Physical Property Measurement Systems to deduce the material behavior under magnetic field. Additional measurements like magnetization measurements, second harmonic generation mapping were performed as well.

II.1. Sample Preparation:

In this thesis many ceramics with different structures like NASICON type phosphates, spinels and novel phases were obtained by solid state reactions. The principle of the solid state reaction is that the chemical phase that minimizes the free energy is most favorable to nucleate and grow. In general solid state method requires high temperatures and controlled atmosphere for preparation. Figure II – 1 describes the process involved in solid state reaction in the form of flow chart. Firstly the entire precursor were thoroughly mixed in stoichiometric ratio and ground well in an agate mortar. To achieve good mixing and grinding, ethanol is added to the precursor and further mixed in a planetary mill. Proper grinding is very important to reduce the particle size to facilitate the diffusion process and to increase the rate of the reaction. Precursors are then dried overnight in an oven at 100° C to remove ethanol. The dried precursors are then pressed into pellets and placed in a platinum boat which is then put in an alumina crucible. In some cases instead of pellets powders are directly placed in the crucible. The crucible is then introduced into the tube furnace and it is heated under air or controlled atmosphere depending on the final phase required. At every step the powders are analyzed by X – ray diffraction to follow the phase formation and purity of the sample. Intermediate grinding and pelletizing were carried out several times to get pure phase. For the final sintering step the calcined powders are pressed again into pellets and heated to a temperature sufficiently above the phase formation temperature. If binders are used to make pellets then the sample was made to dwell at a temperature where all the traces of binders were removed and then heated to the final sintering temperature. During the sintering process the most of the pores close and grains grow larger in size and the final ceramics are highly dense. It is important to have high dense ceramic for ferroelectricity since it is a long range phenomenon any discontinuity in the sample will affects its property.

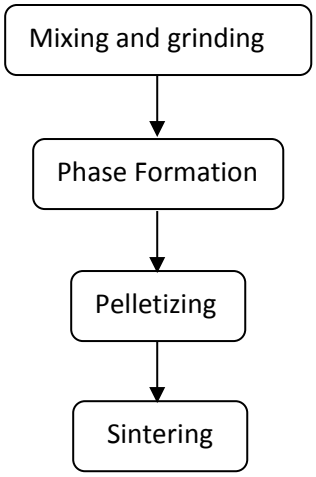

Figure II-1: Schematic representation of typical solid state reaction process

Apart from solid state reactions, coprecipitation was employed for the preparation of some NASICON type phosphates. One of the main advantages of liquid phase synthesis is that they have high reaction rate and also reactions can take place at considerably lower temperature compared to solid state reactions. In this method all the stoichiometric amount of precursors are dissolved in a solvent. Solvent could be either water or some strong acids. All the dissolved precursors are mixed together in a beaker and then it was slowly heated in a sand bath over night to remove the solvent. The precipitate which was obtained after the removal of solvent was given thermal treatment with intermittent mixing and grinding to attain the final phase.

II.2. Structural Characterization:

X – Ray diffraction is one of the most important techniques to determine the phase and the atomic structures of the material and also it is a non-destructive method to characterize the material. With the discovery of X – rays by Röntgen, enabled scientist to investigate the crystalline structure at the atomic level since X – rays are basically electromagnetic radiation of wavelength about 1 A°. X – ray powder pattern is unique for every crystalline solids which can be used as a fingerprint for its identification. In addition it is also possible to find out about the lattice parameter, atomic structural arrangement etc. Diffraction of X – rays in crystalline solids happens if the wavelength λ, interplanar distance d and scattering angle θ satisfies the Bragg law, which is given by

$$n\lambda = 2dsin\theta \qquad \textbf{Eq 35}$$

This leads to constructive interference of the incident rays and the diffracted rays and it appears as peaks in the X – ray pattern. Typically in powdered sampled small crystallites are oriented in every direction and by scanning the sample through a range of 2θ all possible diffractions lines can be obtained. The Full Width at Half Maximum (FWHM) and shape of the diffracted peaks has contribution from both the measurement parameters and the sample properties. Measurement

parameters are beam divergence, focus, resolution, grid width etc and the sample properties are area, size, structure and dispersion of grains. As mentioned earlier that X – rays are electromagnetic radiation they interact strongly with electrons of the atom. More electrons an atom or ion has stronger are the reflection. The influence of the magnetic structure of the sample on the laboratory X – rays is very low and can be neglected. The samples with heavy atoms like bismuth or lead give rise to very strong intense peaks compared to light elements like hydrogen or oxygen and therefore they are difficult to see in the pattern.

In this work X-ray diffraction (XRD) patterns were collected on a PANalitycalX'pert MPD Bragg-Brentano θ-θ geometry diffractometer equipped with a secondary monochromator over an angular range of 2θ = 8-80°. Each acquisition lasted for 34 minutes. The Cu-Kα radiation was generated at 40 KV and 40 mA (λ = 0.15418 nm). The samples were put on sample holders made of aluminum alloy and flattened with a piece of glass.

II.2.1. The Rietveld Refinement Method:

In this method the refinement of powder diffraction pattern is done by the mathematical model developed by H.M.Rietveld [1] [2]. According to his method a crystallographic model is refined by minimizing the difference of the points of the measured diffraction pattern and the calculated pattern using least squares.

$$\chi^2 = \sum_i \frac{\left|Obs_i^2 - Calc_i^2\right|}{Obs_i^2} \qquad \textbf{Eq 36}$$

First a model has to be chosen in the beginning and then the theoretical values for several angles θ_i is computed based on the above model. Then the measured and calculated intensities on each angle θ_i is compared and the quality of fit χ^2 is deduced. On the basis of this value the assumed model can be optimized by varying the structural parameters like size and symmetry of the unit cell as well as reflection multiplicities and peak shape functions.

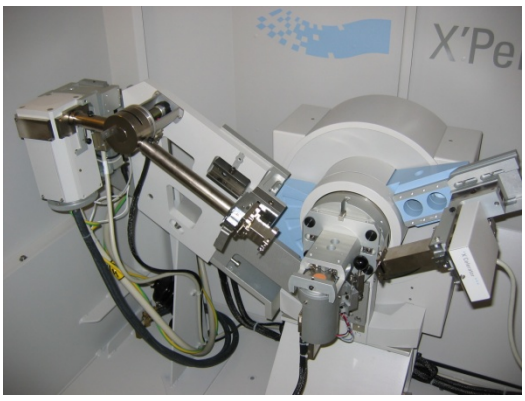

Figure II-2: Set up of X- ray diffractometer equipped with monochromator.

In this work X-ray diffraction (XRD) patterns were collected on a PANalitycalX'pert MPD Bragg-Brentano θ-θ geometry diffractometer equipped with a germanium monochromator (which ensures perfect monochromatic radiation) and a spinner over an angular range of 2θ = 10-130°. The Cu-Kα radiation was generated at 40 KV and 40 mA (λ = 0.15418 nm). The setup is shown in the figure II -2

II.3. Bulk Characterization:

II.3.1. Capacitance Measurement:

To study the ferroelectric and dielectric property of the material it is necessary to investigate their electrical polarization and permittivity. Moreover one of the focuses of this thesis is to understand the coupling between electrical polarization and magnetization. It can be done by probing the electrical polarization during the application of magnetic field or alternatively to study the permittivity at the magnetic ordering temperature. The relative permittivity of the material is a complex quantity and it is given by $\varepsilon_r^* = \varepsilon_r' - i\varepsilon_r''$. It is related to the absolute permittivity of the material by the expression $\varepsilon = \varepsilon_0\varepsilon_r$ where ε_0 is the permittivity of the free space and it is a constant (8.854 X 10^{-12} F.m^{-1}). In general ε depends on temperature, frequency and to a lesser extent, pressure. But the real and imaginary part of permittivity cannot vary independently since they are related to each other by Kramers-Krönig relation. The ratio of imaginary part to the real part of permittivity (ε''/ε') is called dielectric loss.

Throughout this thesis capacitance and dielectric losses are measured in parallel plate capacitor geometry which is shown in figure II.3. Then the capacitance is given by

$$C = \varepsilon_r \varepsilon_o \frac{A}{d} \qquad \textbf{Eq 37}$$

where ε_r is the relative permittivity of the sample, ε_o permittivity of free space, A the area of the electrode overlap on both sides and d the thickness of the sample. Using the above formula real part of permittivity can be deduced from the measured capacitance and the imaginary part from the dielectric loss.

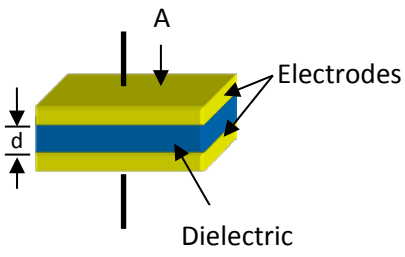

Figure II-3: Schematic of parallel plate capacitor with electrodes on both sides of the dielectric**.**

II.3.1.1. Capacitance Measurement in PPMS:

The capacitance measurement at low temperature and under magnetic field was carried out using Physical Property Measurement System (PPMS) by Quantum Design Model 6000. PPMS can perform temperature scans from 1.8 K to 400 K and 0 to 9 Tesla in magnetic field. The set up consists of a flange with four BNC connectors which are then connected to the steel coaxial wires. The Steel wires are then attached to the sample holder which is at the bottom of the probe. The sample holder can be rotated which is useful to perform parallel and perpendicular magnetic measurements. A picture of the probe and the sample holder is shown in figure II – 4. The samples were gold sputtered to make electrodes on the largest surface and thin silver wires glued with silver paste to the center of the electrodes were used for electrical contact and then mounted on the sample holder. The probe was then connected to the HP 4194 A impedance/ gain phase analyzer in the range of 100 Hz – 10 MHz for the frequency dependent capacitance measurements. The measurement was done assuming a parallel RC circuit since there is always some dielectric loss in the sample.

(a)

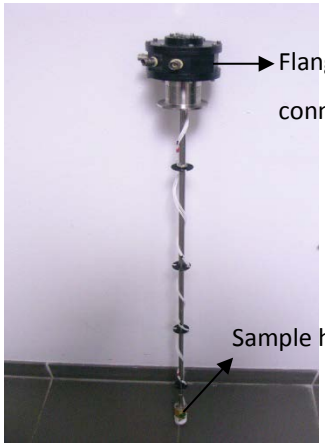

(b)

Figure II-4: (a) PPMS dielectric measurement probe with sample holder; (b) sample holder with horizontal rotator

II.3.2. Piezoelectric Measurement:

In this work the piezoelectric characterization was done using the resonance frequency method. A body of solid has a characteristic frequency at which mechanical resonance occurs. Piezoelectric materials have the specific feature to be driven to their mechanical resonance through an electrical excitation. The sample will resonate freely with greater amplitude than at other frequency when excited at the resonant frequency f_r. There is an anti-resonance frequency f_a where the impedance of the sample is at maximum and the oscillation amplitude minimum. These characteristic frequencies provide the means to evaluate the piezoelectric and the elastic property of the material.

At the resonance, a piezoelectric material can be modelled by the equivalent circuit shown in figure II -5 [3]. It consists of a capacitor in parallel to the series combination of

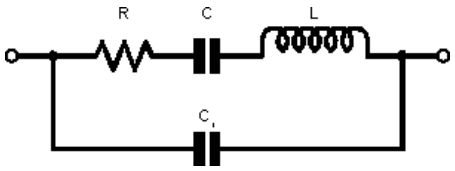

Figure II-5: Equivalent for the resonating piezoelectric material

resistor, capacitor and inductor. In general a piezoelectric material can vibrate in several modes depending on the geometry of the material. Some of the common vibration modes for different geometries are given in figure II -6. It is very important to have well defined geometry of the material in order to avoid mode mixing. In this thesis converse piezoelectric effect is used to probe the sample i.e. application of electric field to the material creates stress. Typical oscillating voltage of 1 V is used.

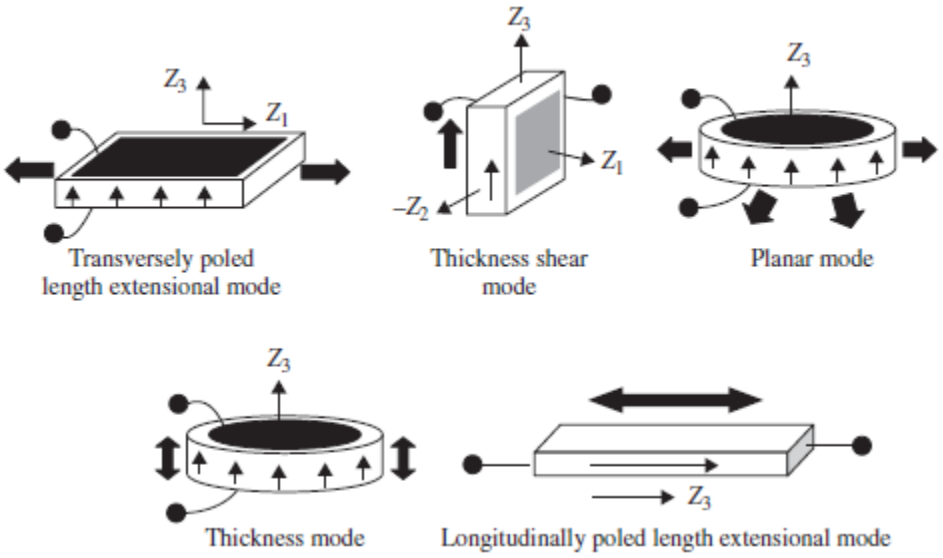

Figure II-6: Common piezoelectric vibrating modes in different geometries and electric field.

The resonance frequency was identified by scanning the frequency in steps throughout the available frequency range. In general length mode of the sample appears at much lower frequency (in the range of few hundred kilo hertz) than the thickness mode which occurs above 1 MHz. Only these two modes were measured in light of the present thesis. The obtained resonance frequency was assigned as length or thickness mode by comparing with the obtained theoretical value according to the formula

$$f_r = \frac{1}{2l\sqrt{\rho S_{ij}}} \qquad \textbf{Eq 38}$$

Where l is the length or thickness of the sample, ρ is the density of the material and S_{ij} is the elastic compliance of the sample material. If there is no reliable estimate of the compliance available then the length mode was identified by decreasing the length of the sample which led to an expected increase in the resonance frequency. While measuring the piezo resonance the sample should not be constrained in any way or else the resonance will be damped. Hence all the measurements were done by suspending the sample between the contact wires. For measurements under controlled temperature and atmosphere a homemade piezoelectric cell was used. It consists of a four BNC connectors connected to two thick copper wires which act as electrodes on which the sample was suspended. The suspended sample was then encapsulated inside a cell which maintains temperature and atmosphere (figure II – 7).

Figure II-7: Set up of piezoelectric cell.

II.3.3. Pyroelectric Measurement:

Appearance of electric charges due to a change in temperature of the material is called pyroelectric effect. For the pyroelectric effect to be present in a material, it has to possess polar point symmetry. Therefore all ferroelectrics exhibit pyroelectric effect. Under equilibrium condition the depolarization field due to polarization discontinuity at the surface is compensated by free charges. But when the material temperature changes spontaneous polarization also changes due to which an excess of free charges flow in the material and external circuit. The sense of current depends on the direction of the polarization change. For the pyroelectric measurement of the material it has to be supported in a manner where it can expand freely. In a typical pyroelectric current measurement involves poling of the sample while cooling under an applied electric field through the transition to align the dipoles parallel to the poling direction. It is shown schematically in figure II – 8. The random orientation of dipoles is not sufficient to give rise to pyroelectric current.

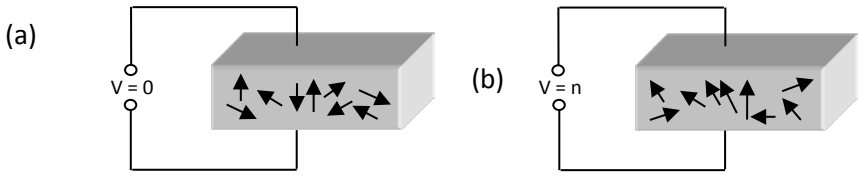

Figure II-8: (a) Before poling, (b) after poling.

After the sample reaches the desirable low temperature, electric field is removed and the pyroelectric current is measured on heating at a constant rate. At the ferroelectric transition a maximum in the pyroelectric current is usually observed which is then integrated in time to give the electrical polarization. Polarization is given by charge on the surface divided by the surface area

$$P = \frac{Q}{A} \qquad \textbf{Eq 39}$$

Where p is the polarization, Q is the charge on the surface and A the area of the sample electrode surface. Now we know

$$i = \frac{\partial Q}{\partial t} \qquad \textbf{Eq 40}$$

Substituting Eq 5 in Eq 6 we have

$$i = A * \frac{\partial P}{\partial t} \qquad \textbf{Eq 41}$$

Then polarization is obtained by integrating the pyroelectric current

$$P = \frac{1}{A}\int i * \partial t \qquad \textbf{Eq 42}$$

Some of our investigated samples display linear coupling between electric and magnetic field. For those samples it is necessary to investigate pyroelectric current under magnetic field since the application of magnetic field will affect the polarization. Here the sample was heated above the magnetic ordering temperature and then both the electric field for poling and magnetic field applied simultaneously. Then the sample was cooled to a temperature much below the transition temperature (in our case the sample was cooled down to 5K) and then the electric field was removed leaving the magnetic field intact. This procedure is called magnetoelectric (ME) cooling. Before the electrodes were shorted in order to remove surface charges. The pyroelectric current was measured while warming at a constant rate with the magnetic field on. If the sample is magnetoelectric then a maximum of pyroelectric current should be observed at the magnetic ordering temperature under magnetic field and above the transition the polarization should vanish. A Stanford Research Systems PS 350 high voltage DC power supply was used to pole the sample and a Keithley 6517B electrometer was used to measure the pyroelectric current.

II.3.4. Magnetic Measurements:

Investigation of magnetic properties is essential to understand the multiferroic materials. The macroscopic magnetization in general depends on the magnetic field H and the temperature. It is given by

$$M = \chi_m H \qquad \textbf{Eq 43}$$

Where M is the magnetization, H is the magnetic field and the proportionality constant χ_m is the susceptibility of the material. This is equation holds for diamagnetic and paramagnetic materials but not for ferromagnetics since they have hysteresis. According to Curie law the susceptibility of the pure paramagnetic material is given by

$$\chi = \frac{C}{T} \qquad \textbf{Eq 44}$$

But if the material is antiferromagnetic or ferromagnetic, then the susceptibility at the paramagnetic temperature range is better described by Curie – Weiss law

$$\chi = \frac{C}{T - \theta} \qquad \textbf{Eq 45}$$

Here θ is the Weiss constant and for ferromagnetic material it is replaced by T_C.

The temperature dependence of the susceptibility and the inverse susceptibility for paramagnetic, antiferromagnetic and ferromagnetic materials is shown in figure II – 9.

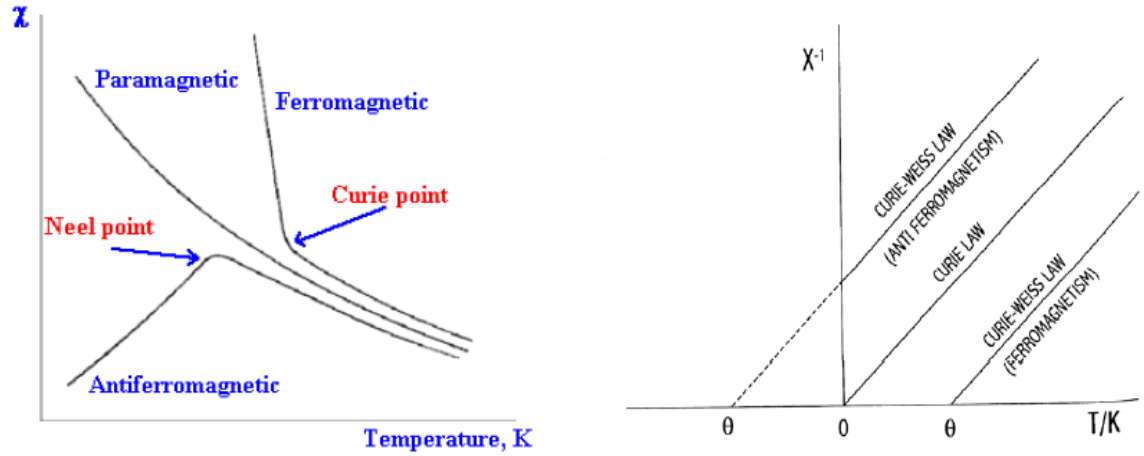

Figure II-9: (a) Susceptibility and (b) inverse susceptibility as a function of temperature for paramagnetic, antiferromagnetic and ferromagnetic materials

For paramagnetic material there is no transition down to zero Kelvin on the other hand for ferromagnetic and antiferromagnetic materials have characteristic temperature called Curie temperature (T_C) and Neel temperature (T_N) at which there is a transition. The inverse susceptibility

of the paramagnetic material has an intercept with temperature axis at the origin whereas the ferromagnetic and antiferromagnetic materials have positive and negative intercept with temperature respectively.

The Magnetic properties were measured using a Magnetic Property Measurement System (MPMS) by Quantum Design. This apparatus is a highly sensitive magnetometer because it has a Super Conducting Quantum Interface Device (SQUID) to measure changes in the magnetic flux as the sample moves through the detection coil. The set up can reach upto 5 Tesla in magnetic field and has a temperature range of 1.8 K to 400 K. The same set up can be used to measure hysteresis loops. Although this equipment can perform AC magnetic measurements most of the measurement is done in DC mode during my thesis. The samples are generally powders or pellets inserted in the gelatin capsule which are then mounted to the transparent plastic straw. The gelatin and the straw have a small diamagnetic contribution. Most of the measurements were performed in Zero-Field cooling (ZFC) mode where the sample is cooled through the magnetic ordering temperature without the application of external field and then the required magnetic field is switched on at the lowest temperature and the magnetization was measured during warming. The subsequent measurement of magnetization while cooling under magnetic field is called Field – Cooled (FC) mode.

II.3.5. Magnetoelectric Characterization:

II.3.5.1. Calibration of PPMS for Magnetoelectric Experiment:

Characterization of magnetoelectric effect with the application of electric and magnetic field to dielectric or semiconducting materials needs caution. Hence a detailed calibration of the experiment under magnetic field and electric field is necessary so as to identify the spurious effect arising from the sample holder and the set up at the same time to have a reference value. Here we calibrate our experimental set up in open circuit and short circuit condition under electric and magnetic field.

II.3.5.1.1. Open Circuit Calibration:

For the open circuit calibration of PPMS, a Teflon disk sputtered with gold on both sides was used as a sample. Teflon is a very low loss material and therefore the circuit can be considered to be open. Figure II -10 (a) & (b) gives the capacitance and dielectric losses as a function of temperature

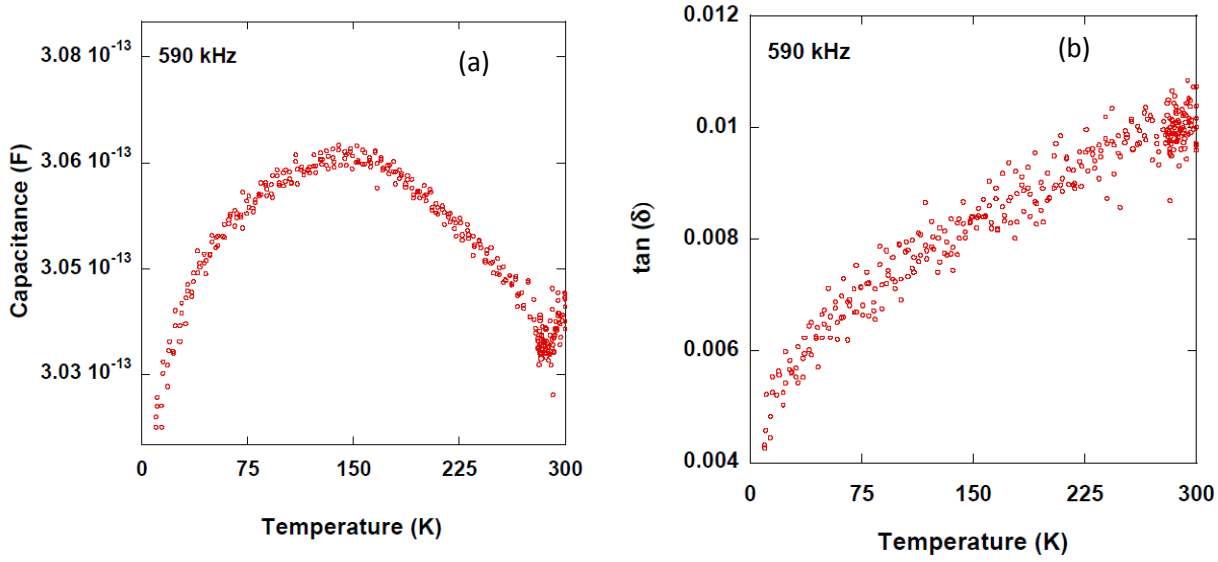

Figure II-10 : (a) & (b) capacitance and dielectric loss as a function of temperature for a Teflon sample at 590 kHz.

for the

heating and cooling cycles at 590 kHz. It is evident from the plot that there is no difference in capacitance and losses between heating and cooling. In the capacitance plot there is an anomaly close to 150 K but the difference between the maximum at 150 K and minimum of capacitance is 0.004 pico farad which is much below all capacitances measured in this work (always higher than 1pF) and moreover this anomaly is not accompanied by a change in the dielectric losses. In addition the dielectric losses stay well below 1 percent. At all temperatures both the capacitance and dielectric losses of Teflon were independent of the magnetic field up to 90kOe. Therefore we can consider that the Teflon sample is highly insulating and hence the measurement on Teflon gives a good estimate on the open circuit calibration of PPMS.

II.3.5.1.2. Short Circuit Calibration:

To calibrate PPMS in short circuit, the sample was removed and the two contact wires were glued together with the silver paste finally to the impedance analyzer. Resistance and reactance was measured as a function of frequency with (45 kOe) and without magnetic field from 300 – 10 K. Figure II – 11 (a) & (b) shows the plot of resistance and reactance as a function of frequency

respectively at 10 K. Without magnetic field resistance and reactance is almost flat below 1 MHz frequency.

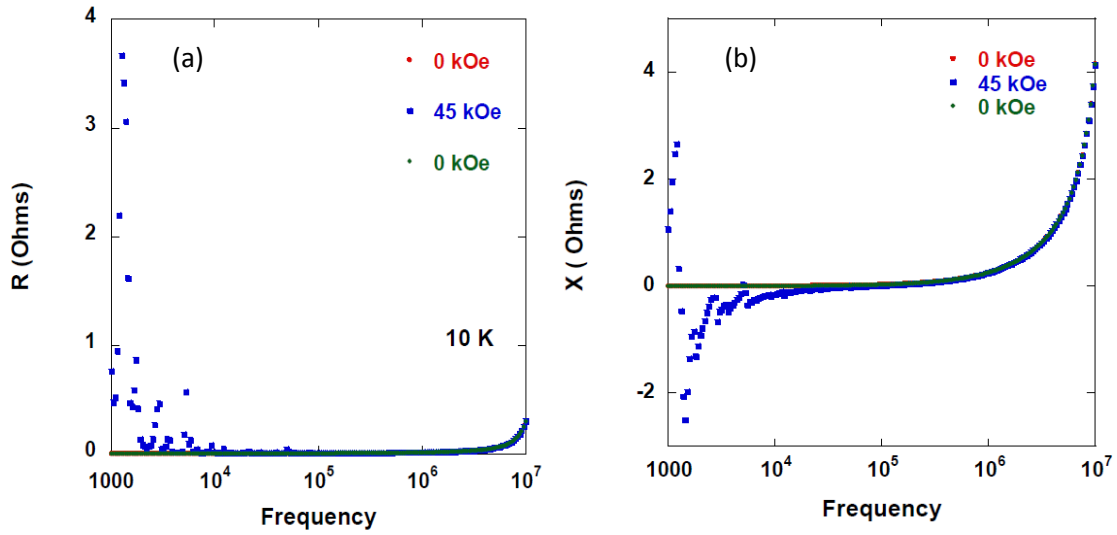

Figure II-11: (a) & (b) Resistance and reactance as a function of frequency respectively at 10 K in short circuit mode with and without magnetic field.

The increase in the resistance and reactance above 1 MHz is due to the contribution of inductance. With magnetic field both the resistance and reactance are highly disturbed below 10 kHz. Magnetic field increases the resistance whereas it causes resonance in the reactance. This is observed in all the temperature range. It is very important in the light of this thesis because most of the time semiconducting and conducting samples are probed for dielectric properties under magnetic field. For example we measured sodium cobaltite which is a high conducting sample under magnetic field for resistance and reactance. We found the same kind of magnetic field induced effect. Without this calibration one could misinterpret that the effect is originating from the sample. Henceforth if there is an effect of magnetic field only at low frequency in conducting samples it has to be analyzed keeping in mind that the sample holder and contact wires are also contributing.

II.3.6. Equivalent Circuits:

An ideal capacitor has only the capacitance associated with it but in reality capacitors always have a conducting element which is represented as a resistance in the equivalent circuit. This conducting element can be presence of free charges due to defects or impurities in the material. Under the application of electric field these conducting elements start to flow leading to dielectric loss. In the parallel plate capacitors we have a parallel arrangement of capacitor and the resistance. Now if we apply external stresses like electric field and magnetic field to this circuit then depending on the response of the material we can classify them as pure magnetodielectric, magnetocapacitance or multiferroics. Figure II – 12 describes these effects in the form of equivalent circuit.

R

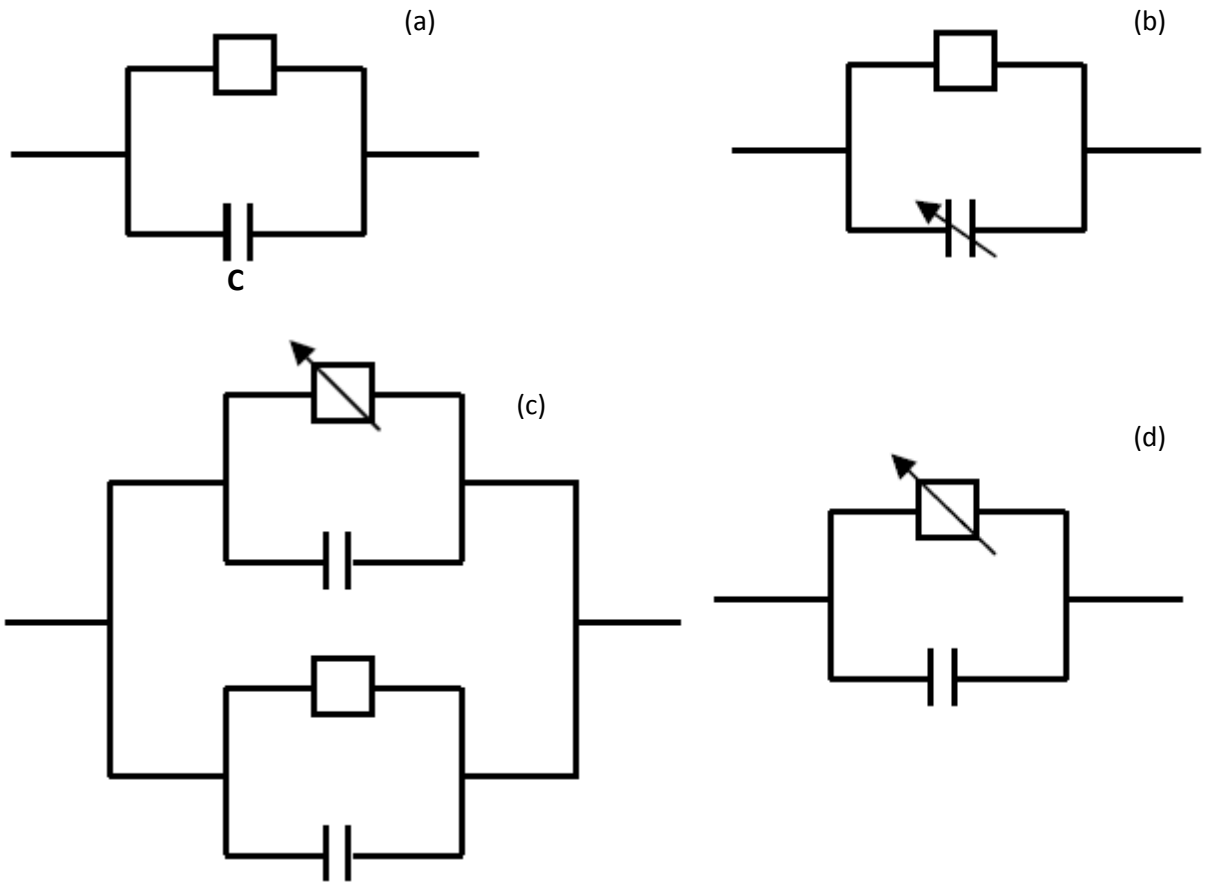

Figure II-12: Equivalent circuit for (a) normal capacitor, (b) pure magneto dielectric, (c) interface effect leading to magnetocapacitance and (d) magnetolosses. Here R is the resistance and C is the capacitance.

Figure II – 12 (a) is for a real dielectric with a capacitor and a resistance in parallel, now if we apply magnetic field to such a system and the response of material is such that there is a change in capacitance due to magnetic field without the induction of ferroelectricity and also there is no considerable change in the dielectric loss then the effect can be considered as magnetodielectric. This effect is represented as the changeable capacitance under magnetic field in figure II -12 (b). If there are several interfaces in dielectric like electrode-sample interface, grain boundary – grain interface etc then the dielectric behavior can be represented by the series combination of two parallel RC circuits as shown in figure II -12 (c). Now if the conducting element of one of the circuit is responsive to external magnetic field then a change in the capacitance can be induced according to equation 24 of chapter 1. This is mostly due to interface effect and it is called magneto capacitance though not intrinsic to the sample material. If only the conducting element is affected by magnetic field then it can only lead to change in the dielectric loss without change in the permittivity or capacitance of the material. It is shown schematically in figure II-12 (d).

II.4. References:

[1] H. Rietveld. *Acta. Crystallogr. A*, 22:151, 1967.

[2] H. Rietveld. *J. Appl. Crystallogr.*, 2:65, 1969.

[3] Ieee standards on piezoelectricity, 176 - 1987.

Chapter 3

III. Chapter 3: Localization of free charges and its influence on the dielectric properties of Fe doped $BaTiO_3$ single crystals.

III.1. Introduction:

Pure barium titanate has a band gap of 3 eV and so it is an insulator with a room temperature resistivity of more than 10^{10} Ω cm [1]. This is very good for capacitor application but because of the ferroelectric transition temperature (T_c = 130°C) the temperature stability of BaTiO3 properties does not meet the devices requirements. To reach temperature independent dielectric properties T_C must be shifted away from ambient temperature or the dielectric peak should be strongly depressed. This is achieved mostly by doping isovalent cations (Pb, Zr, Ca, Sr, Sn etc) [39]. These isovalent impurities influence only the ferroelectric behavior but they do not significantly affect the electrical conductivity of the material. On the other hand off valent impurities affect both the ferroelectric transition as well as the electrical conductivity of $BaTiO_3$ [3]. These off valent impurities are Fe, Mn, Mg, Sb, Nb, Cu, La etc. Conductivity in $BaTiO_3$ (BTO) can also be altered by specific annealing procedure. For example reduced BTO ceramic usually show n- type conductivity due to partially reduced Ti^{4+} and it can be written according to the Kroger – Vink notation [4]

$$Ti^{4+} + e^- \rightarrow Ti^{3+} \qquad \textbf{Eq III-1}$$

Reduction of titanium occurs mostly due to the creation of oxygen vacancies by the loss of oxygen during the reduction process.

$$2O^{2-} \rightarrow O_2 + 4e^- \qquad \textbf{Eq III-2}$$

$$O_O^x \rightarrow \frac{1}{2}O_2 + V_o^{\cdot\cdot} + 2e^- \qquad \textbf{Eq III-3}$$

Where $V_0^{\cdot\cdot}$ is the vacant oxygen site which carries a double positive charge.

Depending on the doping site of the heterovalent impurities, ionic or electronic compensation takes place. In La doped BTO major charge compensation mechanism is the creation of the barium vacancies [5] and these vacancies are immobile whereas in the Fe doped BTO, Fe is incorporated at the Ti sites [6] and the charge compensation is through the above mentioned creation of oxygen vacancy. Since the valence of Fe (3+) is smaller than Ti (4+) these kinds of doping are acceptors on the other hand doping with Nb (5+) is called donor due to the high valence of the doped cation on

the Ti sites. The creation of oxygen vacancy due to the doping of trivalent 3d transition metal cation at the Ti^{4+} site can be written as [7]

$$A_2O_3 \xrightarrow{(2TiO_2)} 2A'_{Ti} + 3O_0 + V_0^{\cdot\cdot} \qquad \textbf{Eq III-4}$$

The acceptor oxide (A = Mn, Fe, Co etc) replaces the host oxide shown in parentheses above the arrow. It is well known from ESR measurements of Fe doped $SrTiO_3$, Mn doped $SrTiO_3$ and Mn doped $BaTiO_3$ that the transition metal dopants are associated with charged oxygen vacancies [8] [9]. Furthermore Hagemann [10] calculated the concentration of oxygen vacancy V_0 quantitatively based on the model proposed by Daniels et al [5] for Fe and Mn doped BTO. The results of the calculation are shown in figure III – 1.

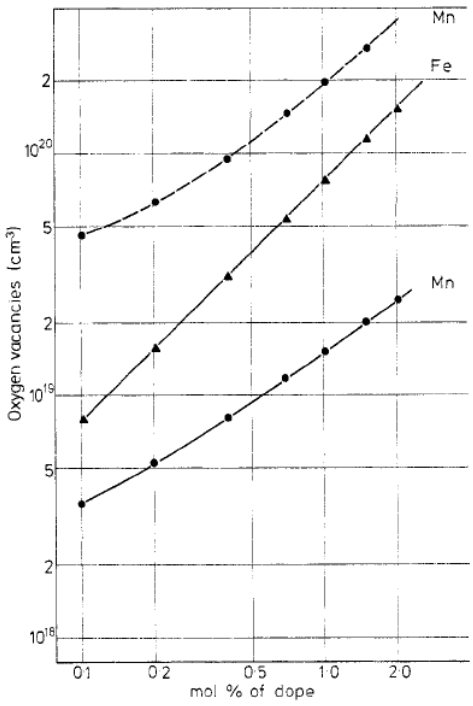

Figure III-1: Oxygen vacancy dependence on the doping percentage of Fe and Mn in BTO as calculated by Hagemann [10] under different annealing conditions. Solid lines – oxidizing conditions, broken lines – reducing conditions.

It is evident from the above plot that oxygen vacancy increases with increase in acceptor type impurities like Fe and Mn. Depending on the annealing conditions whether it is reducing or oxidizing number of oxygen vacancy varies in Mn doped BTO. Under reducing conditions there is a lack of oxygen availability which leads to creation of more oxygen vacancies. The doping of Fe in BTO leads to creation of free charges following the same principle as for doped semiconductors [11] [7]. In some cases these free charges are due creation of oxygen vacancies. The localization of these free charges can happen at the unit cell scale which lead to creation of polarons or at the macroscopic scale at the electrode-sample interface or domain walls. Whatever the type of localization they

eventually affect the dielectric property of Fe doped BTO. This will be studied under the application of magnetic field. Before we begin describing the results let's look at how domain walls and polarons can affect the dielectric property of the ferroelectric material.

III.1.1. Domain wall contribution to the dielectric property of ferroelectrics:

Domains and domain walls play a major role in determining the dielectric property of the ferroelectrics. The well-known hysteresis effect of the ferroelectrics is due to the nucleation and growth of domains during the reversal of polarization at large electric fields. This involves considerable motion of domain walls. One of the earliest studies on domains in $BaTiO_3$ single crystals is done by Merz where he studied the domain formation and domain wall motion [12]. Since then vast number of articles appeared in the literature on the nature of domains and domain walls in BTO in the form of single crystals, ceramics and thin films. Several studies have been devoted to understand the effect of domain walls on the dielectric permittivity and the losses at small and large electric fields. At the same time frequency dependent measurement are very useful as well. There are several contributions to the complex permittivity of ferroelectric crystal below the Curie point and it is given by [13]

$$\varepsilon = \varepsilon_\infty + \varepsilon_i + \Delta\varepsilon_w \qquad \textbf{Eq III-5}$$

Where ε_∞ is the optical permittivity, ε_i is the contribution of the ionic polarization to the permittivity and $\Delta\varepsilon_w$ the contribution of the displacements of the domain walls. It is obvious from Equation 5 that domain walls have significant influence on the complex permittivity.

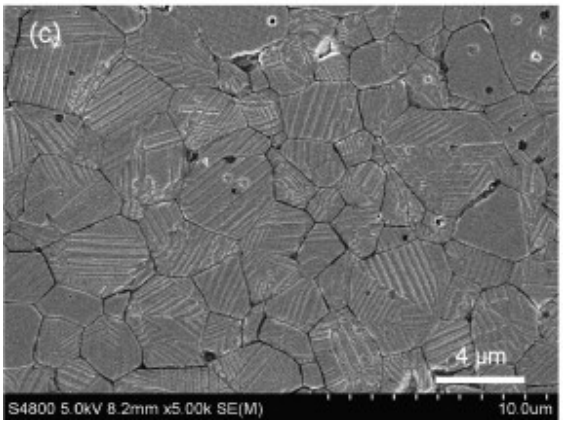

Figure III-2: Scanning electron microscopy image of the domains in $BaTiO_3$ ceramics sintered at 1250°C. Adapted from ref [14].

Indeed at very high fields polarization reversal occurs and the contribution of domain walls at these fields are very high. Hagemann has measured permittivity and the loss factor of $BaTiO_3$ ceramic as a function of electric field and doping concentration [10]. An example of domains in $BaTiO_3$ ceramics is

shown in fig III – 2 for reference [14]. He found that permittivity and loss factor has a threshold field E_0 above which both parameters start to increase as a function of field. Below the threshold field E_0 the parameters are independent of the external electric field. Moreover with increase in Fe doping concentration threshold field also increases. This shows that doping of Fe in BaTiO3 induces a pinning effect on the motion of domain walls and stabilizes it. The stabilization of domains may be due to three different mechanisms [15] [16] [17] (i) Orientation of anisotropic defects by the local electrical moments which favors existing direction of spontaneous polarization P_S within each domain (bulk effect); (ii) lattice defects like oxygen vacancy diffuse to the regions near domain walls and reduce its mobility (wall effect); (iii) Diffusion of charged defects towards grain boundary and fix the overall domain structure (grain boundary effect). In general there are two kinds of contribution to the permittivity and losses by domain walls. When the electric field is below the threshold field then the contribution is dominated by reversible or oscillating domain walls. Above the threshold field E_0 irreversible (hysteretic) domain switching effects dominate the dielectric response. Generally these two contributions can be distinguished by plotting real part of permittivity ε_r' as a function of imaginary part of permittivity ε_r'' at different field amplitudes (Arlt, 1993) (D.A. Hall, 1998). It is shown in the figure III – 3.

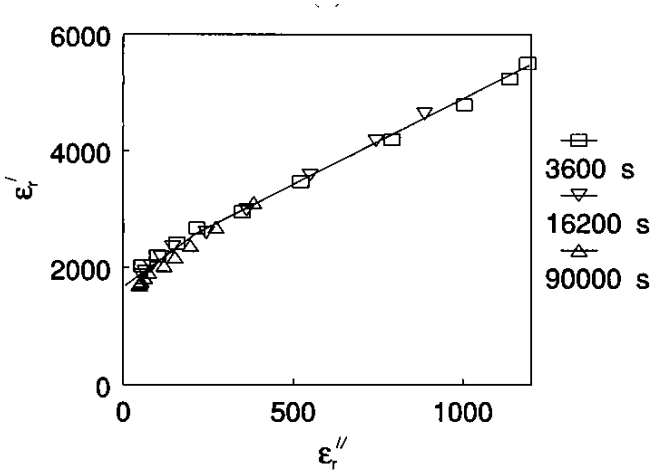

Figure III-3: Plot of real part of permittivity $\boldsymbol{\varepsilon_r'}$ as a function of imaginary part of permittivity $\boldsymbol{\varepsilon_r''}$ at different field amplitudes for Co doped BTO. Note the two linear components in the plot. Adapted from ref. [18]

Two linear portions can be distinguished, at lower values the linear part corresponds to the reversible domain wall effect and at higher values it is due to the irreversible domain wall contribution. Throughout this thesis only small electric field of about 10 V. Cm^{-1} is applied therefore only the contribution of reversible or oscillating domain walls is important and it is discussed in detail below. The effect of irreversible domain switching which involves long range motion of domain walls can be ignored.

To understand the influence of the domain wall motion on the dielectric properties combined measurements by mechanical spectroscopy and dielectric spectroscopy are useful. From mechanical spectroscopy we can obtain mechanical loss factor Q^{-1}. In any ferroelectric, the presence of mechanical loss can indicate the motion of domain walls since they can move under the applied stress. In general the applied stress is small hence no deformation of the sample occurs. And then with the help of dielectric spectroscopy at high frequencies one can make correlation between the domain walls and the observed changes in the dielectric property of the ferroelectric. B.L. Cheng et al have studied undoped coarse grained ceramic using flexural mode of vibration [19]. They found that each phase transition in BTO gives rise to peak in mechanical loss Q^{-1} (P) and a corresponding sharp anomaly in the elastic modulus (A). In addition to this, an extra mechanical loss peak was observed in each of the ferroelectric crystalline phase (R). This R peak was thought to originate from domain walls similar to the one observed in Sr doped lead zirconate titanate (PZT) [20], potassium dihydrogen phosphate (KDP) [21], triglycine sulphate (TGS) [22]. Several models were proposed regarding how domain walls can give rise to the loss peak. Postnikov et al. [20] have said that loss peak may be due to the interaction of the immobile 90° domain wall with the charged point defect. Getner et al. also proposed model based on interaction of point defects and the 90° domain wall where the energy level arrangement of point defects is controlled by order parameters which vary continuously within the walls. There are other models proposed by Arlt et al. [23] and Snead et al [24] although the model by Huang et al [25]and B.L. Cheng et al [26] has been widely accepted.

According to B.L. Cheng et al R peaks are due to the interaction of domain walls and the diffusion of oxygen vacancies in each crystalline ferroelectric phase. They have done mechanical and dielectric measurements on coarse grain and fine grain BTO ceramics [27]. Apart from the sharp anomalies in shear modulus and mechanical loss related to phase transition they also found broad anomalies at each ferroelectric phase due to relaxation (R peaks). They found that only coarse grain samples clearly show relaxation peaks (R peak) in each of the ferroelectric phase. This shows microstructure is of prime importance for the appearance of the relaxation peak. Moreover this relaxation can be fitted by Arrhenius equation. Similarly in dielectric spectroscopy, dielectric losses peaks were found only with large grain samples in each of the ferroelectric phase. These peak shift to higher temperature with increase in frequency and are therefore considered to be relaxation peaks. The relaxation peaks and sharp anomalies by mechanical and dielectric measurements are shown in Figure III – 4 (a) & (b) respectively. The activation energy of the relaxation peak found by mechanical and dielectric spectroscopy fall on the same slope indicating that the basic mechanism is the same. Furthermore the activation energy of mechanical and dielectric loss peak are very similar to the activation energy for the diffusion of oxygen vacancies. The strength of the mechanical loss peak was

also found to depend on oxidizing or reducing atmosphere. These facts indicate that interaction between domain walls and oxygen vacancy is at the origin of these relaxation peaks and the same relaxation process exists at different ferroelectric phases. The disappearance of relaxation peak in fine grained sample is due to the pinning effect of grain boundaries on the motion of domain walls. The samples used in thesis are all single crystals therefore we should be able to observe the relaxation due to domain walls. To conclude motion of domain walls and its interaction with oxygen vacancy lead to relaxation in all ferroelectric phase.

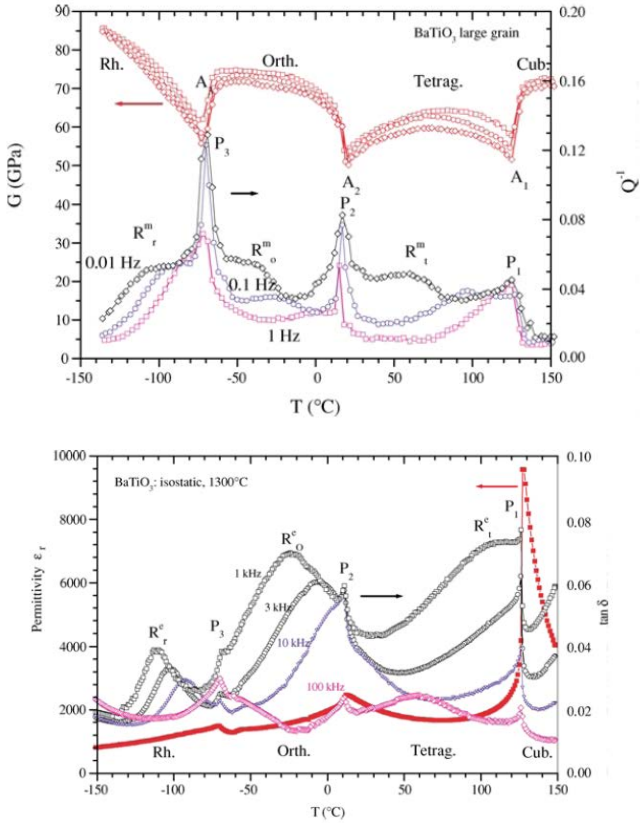

Figure III-4: (a) Temperature dependence of shear modulus G and mechanical loss Q^{-1} at low frequencies in large grain BTO ceramic, (b) temperature dependence of permittivity and loss for the same BTO sample. The peak indicated as R shifts to higher temperature in both mechanical and dielectric measurements. [27]

III.1.2. Polaron contribution to dielectric response of ferroelectrics:

Polarons and its influence on dielectric properties were discussed in great detail in Chapter 1. Here I will briefly summarize some of the important points concerning polaron contribution to dielectric response in light of the following results. Polarons have been gaining attention due to their relevance in the field of giant magnetoresistance [28] [29] and high temperature superconductors [30]. Typically in these kinds of materials the polaron density is very high in the range of 10^{23} cm^{-3}. But in our material of interest especially in Fe doped $BaTiO_3$ the polaron density is appreciably low of about 10^{17} cm^{-3} [31]. The usual way of probing polarons is by local spectroscopies such as EPR and

optical spectroscopy as well as by macroscopic measurement such as conductivity measurements, thermocurrents and Hall experiments. Recently dielectric measurements were used to identify polarons in the materials. Salce et al. found the evidence for extremely low dielectric losses in very high purity KTaO3 single crystals [25]. These losses cannot be fitted to usual dielectric relaxation equation but their activation energy obtained by Arrhenius plotting of loss maximum is about 100 meV. This was followed by Bidault et al. who showed such loss peak was not only limited to $KTaO_3$ single crystals but they were found in many other perovskite samples of different composition, impurity level, morphology and lattice properties [24]. All these materials had the same activation energy in the range of 100 meV and it is shown in figure III – 5 [26].

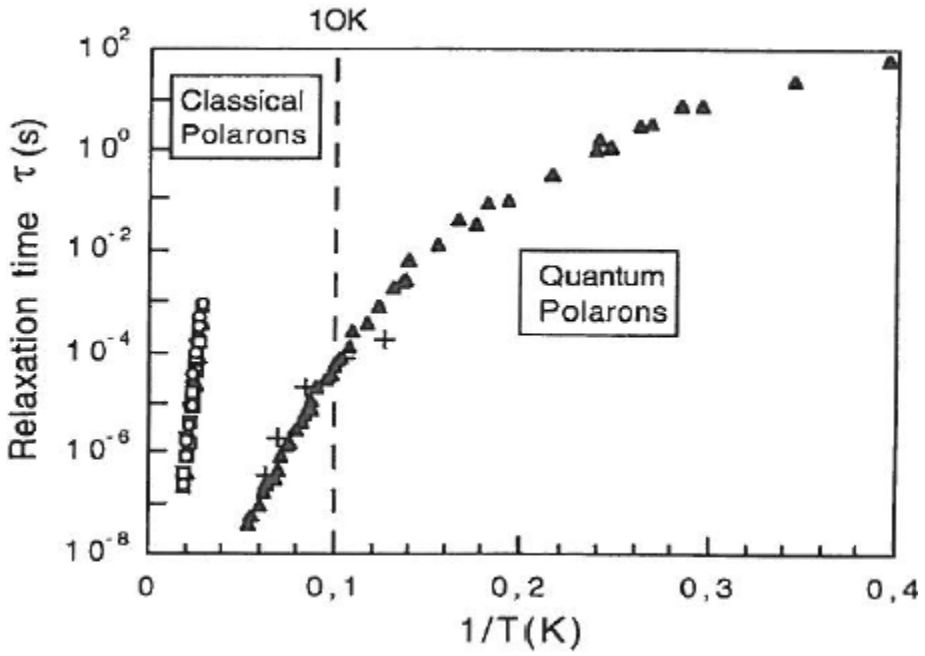

Figure III-5: Arrhenius plot of several pure and doped ferroelectric perovskite shown on the left. Case of pure and doped $SrTiO_3$ is on the right. Note the saturation for $SrTiO_3$ showing quantum behavior [26]

This activation energy is similar to the one found by resistivity and Hall measurements in $BaTiO_3$ single crystals [35] [36]. This show that the observed dielectric relaxation at low temperature in several perovskite is related to the polarons especially the reorientation of dipoles when the free charges hop through the lattice. The favorable sites for the free charges to hop in the lattice are defect centers such as unwanted iron impurity or oxygen vacancies. The case of quantum polarons is typical for $SrTiO_3$ which has low activation energy and tendency for saturation at low temperatures.

In the present chapter we focus on the following studies on Fe doped $BaTiO_3$ single crystals for possible magnetocapacitance effect. Accordingly i) domain wall relaxation discussed above at high

temperature will be probed under magnetic field, ii) the polaron relaxation at low temperatures will also be probed under magnetic field, iii) preliminary studies on $SrTiO_3$ will be described as well.

III.2. Experimental Techniques:

Single crystals of $BaTiO_3$ with two different concentrations of iron (0.075 at. % , 0.135 at % and 0.3 at. %) were investigated and also preliminary studies on $SrTiO_3$ (STO) single crystals have been conducted. Typical sample dimensions were 4 x 4 x 2 mm^3 for BTO and 2 X 2 X 1 mm^3 for STO. Gold was sputtered on the major faces to make electrodes and silver wires glued to the center of the electrode with silver paste were used for electrical contact. The samples were then put in a Quantum Design Physical Properties Measurement System (PPMS) connected to four coaxial cables linked to an HP4194 impedance analyzer through BNC connectors. Capacitance and dielectric losses were measured as a function of temperature from room temperature down to 10 K in the frequency range of 100 Hz-10 MHz. For measurements under magnetic field, the field was raised at a rate of 200 $Oe.s^{-1}$ from 0 to 90 kOe; this field was then fixed throughout the temperature cycle. ESR measurements were performed using an X-band Bruker spectrometer operating at 9.4 GHz. An Oxford Instruments ESR 9 He cryostat operating in the temperature range 4 – 300 K was used for temperature dependence studies of ESR spectra intensities.

III.3. Results and Discussion:

Fe doped $BaTiO_3$ single crystals have been investigated with dielectric spectroscopy under magnetic field for extrinsic multiferroic effects. Recently Maglione has reported magnetocapacitance in one cent diodes as well as in $CaCu_3Ti_4O_{12}$ so called giant permittivity material [2]. Magnetocapacitance in diode stems from interaction of external magnetic field with free charges accumulated at the p-n interface. In case of $CaCu_3Ti_4O_{12}$ free charges arise from incomplete compensation of Cu related defects and the interfaces are grain boundaries which under magnetic field generates magneto capacitance. In $BaTiO_3$, it was also shown that ferroelectric domain walls can be the necessary interfaces where to locate free charges. In this present thesis we go one step further to study in detail the domain walls contribution to the magnetocapacitance in three different Fe doping concentrations in barium titanate at the same time to probe for polaron relaxation.

III.3.1. Magnetic field influence on the domain wall relaxation in Fe doped $BaTiO_3$ single crystals:

In the following Fe doped $BaTiO_3$ single crystals are probed for artificial magnetocapacitance (AMC). Magnetocapacitance is the change in capacitance under magnetic field. Figure III-6 (a) & (b)

shows capacitance and dielectric losses as a function of frequency in the temperature range of 140 to 180 K for BTO doped with 0.135 at % Fe. It is evident from the plot that both the capacitance relaxation and dielectric losses (tan δ) peak shift to higher frequency with increase in temperature. The relaxation of capacitance is reflected as a large maximum in the dielectric losses. This is a typical signature of Debye type relaxation. The activation energy obtained from the Arrhenius plotting of the loss peak maximum gives a value of 0.22 eV. This value is similar to the one obtained by B.L. Cheng et al. and they attributed it due to the domain wall relaxation [27]. We will now look for possible magnetic field effect on this relaxation.

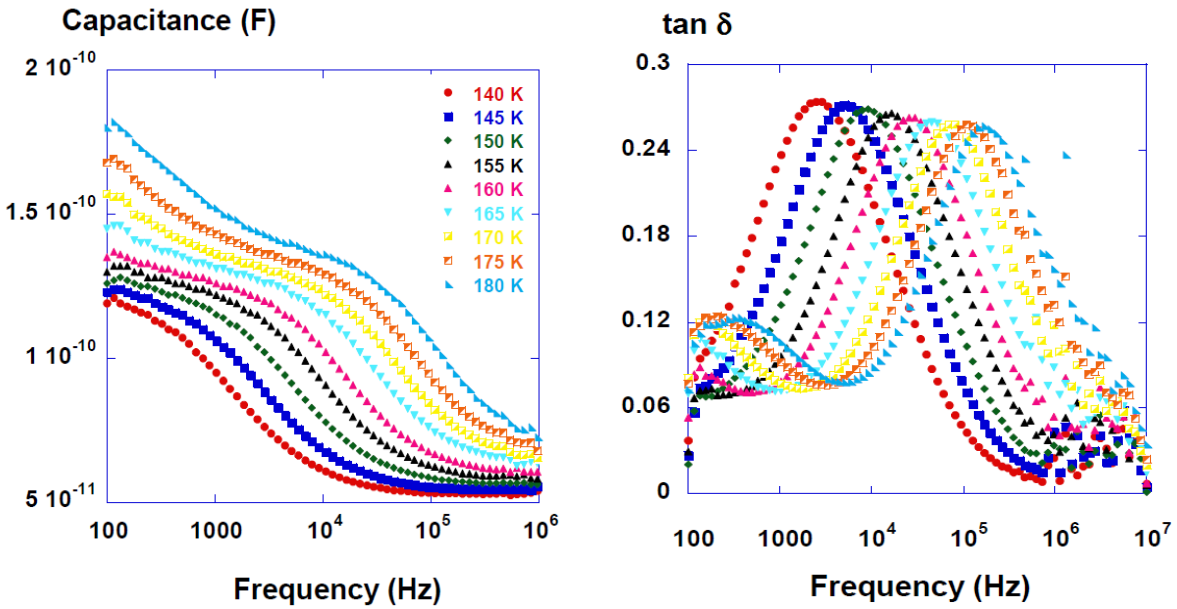

Figure III-6: Frequency dependence of (a) capacitance, (b) dielectric losses at different temperatures for BTO doped with 0.135 at% Fe.

Reliable measurement of AMC needs caution so as to avoid spurious results since even a small amount of magnetic impurities will give AMC which may not have its origin in the sample. As a necessary precaution care should be taken to ensure that external factors (sample holders, connections etc.) do not contribute to the observed relaxation especially at low temperatures. Since our single crystals of BTO and STO have very low loss, it is required to calibrate our experiment with a low loss sample for dielectric anomaly in the temperature range of interest. Hence a piece of Teflon was chosen for our measurement due to its very low dielectric loss and the capacitance and losses are described in chapter 2. No relaxation or other dielectric anomaly was found and no effect of a magnetic field up to 90 kOe was observed. Since Teflon is a very low permittivity sample it is also necessary to perform calibration using samples with permittivity and losses similar to $BaTiO_3$ single crystals. For this purpose we chose $KTaO_3$ single crystals. On figure III-7, in agreement with former

reports, we find a continuous increase of the capacitance on cooling and a slight increase of losses at about 50 K [25]. On this figure, the errors bars denote the long term isothermal evolution of the capacitance and losses when the magnetic field was swept from 0 to 90 kOe. This fixes the detection threshold of the dielectric parameters under magnetic field to 3 %.

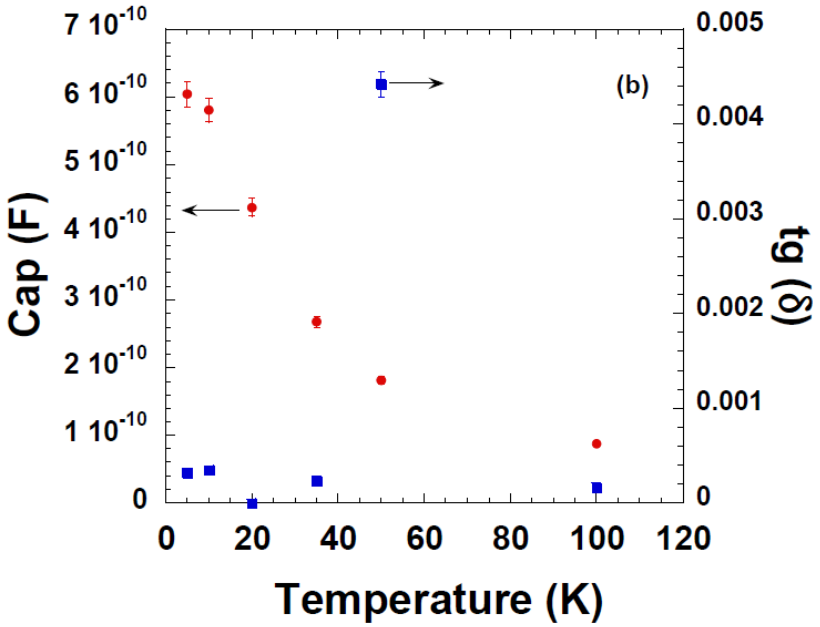

Figure III-7: Temperature dependence of capacitance and dielectric losses (tan δ) for pure $KTaO_3$ single crystal. The long term isothermal evolution of capacitance and losses when the magnetic field was swept from 0 to 60 kOe is denoted by the error bars.

Figure III-8 (a-c) shows dielectric losses as a function of temperature for BTO doped with 0.075 at%, 0.135 at% and 0.3 at% Fe at a spot frequency of 10 kHz with 0 and 90 kOe magnetic fields respectively. Figure III -8 (d) shows capacitance under the same condition as above for BTO doped with 0.135 at% Fe.

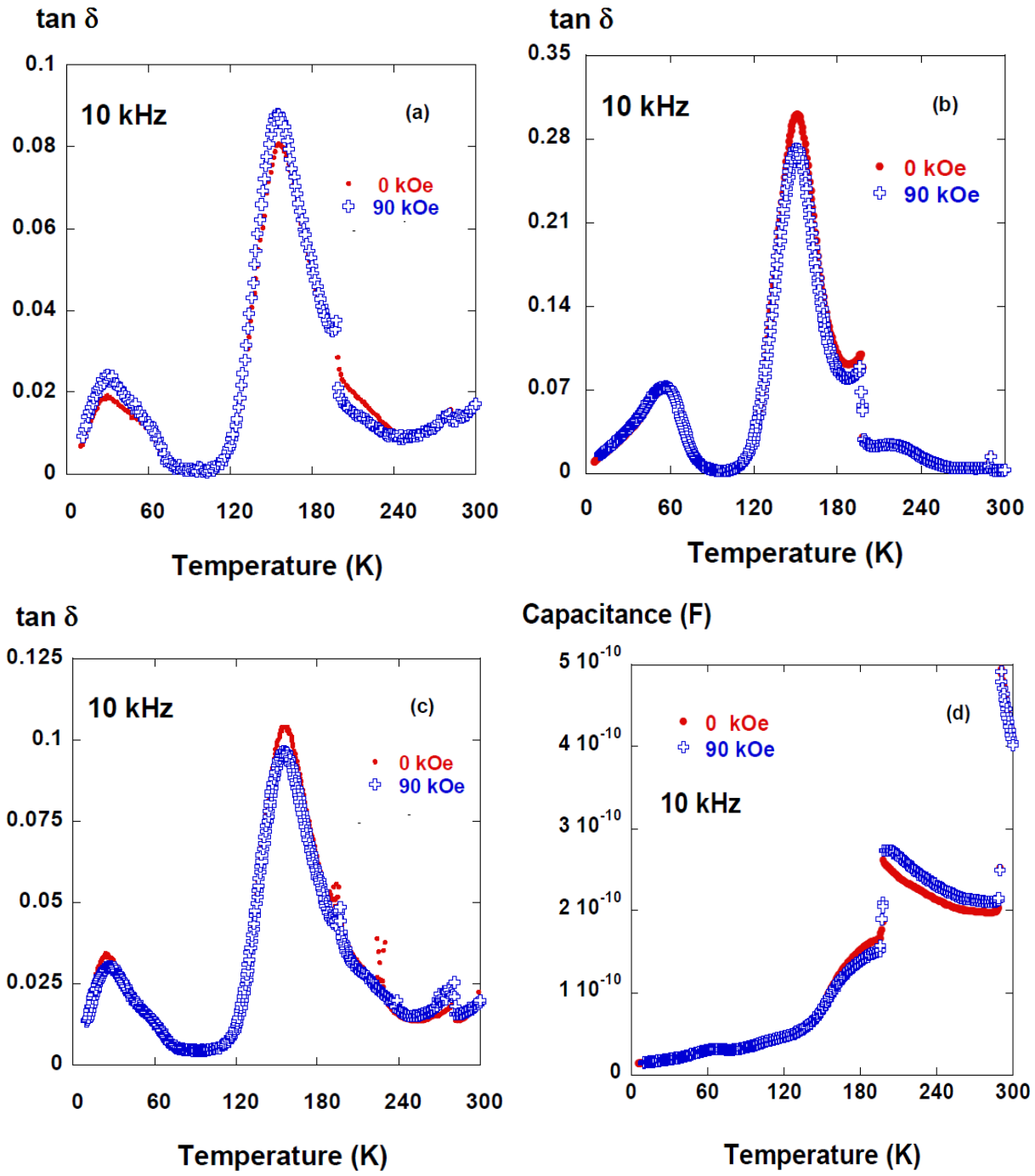

Figure III-8: (a-c) Dielectric loss as a function of temperature for BTO doped with 0.075 at%, 0.135 at% and 0.3 at% Fe respectively with and without magnetic field at a single spot frequency of 10 kHz; (d) Temperature dependence of capacitance for BTO doped with 0.135 at% Fe at the same frequency and magnetic field. Notice the effect of magnetic field on both capacitance and dielectric losses.

The sharp anomalies at 281 K and 198 K are phase transition from tetragonal to orthorhombic and orthorhombic to rhombohedral respectively. The transition temperatures are not the same as pure BTO due to effect of doping Fe [38]. Now it is clear that the broad maximum noticed close to 155 K is due to domain wall relaxation whereas the maximum seen around 30 K can be ascribed to polaronic relaxation arising from the presence of Fe^{2+} and Fe^{3+} ions. Low temperature polaron relaxation will be discussed in detailed later; here we will focus on magnetic field on high temperature relaxation. It is

evident from the fig III-8 (a) that for BTO with 0.075 at% Fe application of magnetic field has enhanced the amplitude of relaxation maximum whereas for BTO with0.135 at % and 0.3 at% Fe magnetic field has depressed the amplitude of relaxation (fig III-8 (b & c)). In addition not only dielectric losses which are affected by magnetic field even the capacitance are equally affected which is clearly seen in fig III-8 (d). From these observations we can say that there is no systematic link between the Fe content and the effect of magnetic field. This confirms that the domain walls which are highly sensitive to thermal cycling are major contributors to the observed effect on this temperature range.

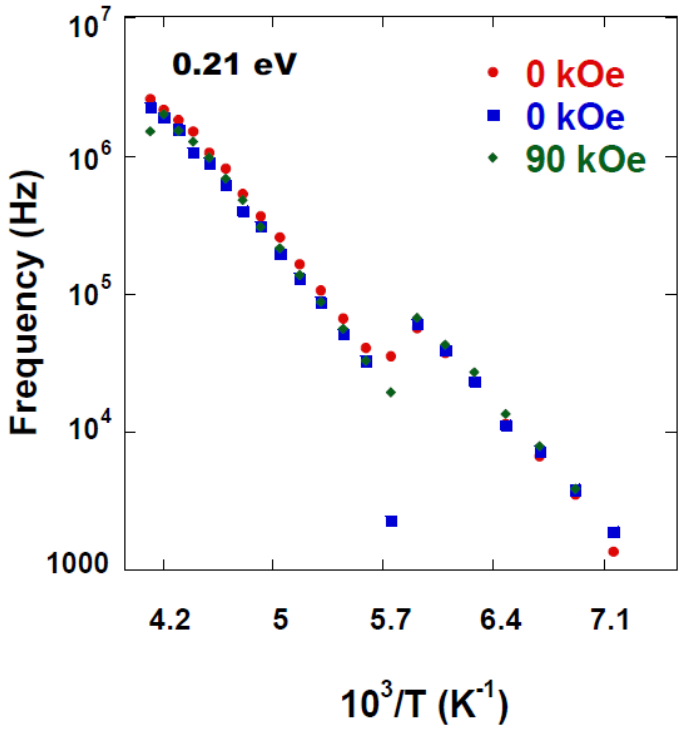

Figure III-9: Log frequency as a function of inverse temperature for domain wall relaxation in BTO with 0.3 at% Fe under 0 and 90 kOe magnetic field.

Furthermore temperature dependence of relaxation was plotted as conventional log fr versus $10^3/T$ which could be fitted with Arrhenius law and activation energy of 0.21 eV was found for both 0 and 90 kOe indicating no influence of magnetic field on the barrier energy (see Figure III-9). Another interesting thing to note here is that the magnetic field effect is more pronounced at the relaxation maximum, away from the maximum there is no effect of magnetic field on the dielectric losses.

III.3.2. Magnetic field effect on the polaron relaxation in Fe doped $BaTiO_3$ single crystals:

Now let's look at the low temperature relaxation due to polarons. Before going in detail we would like to stress again that it is important to confirm the observed relaxation indeed stems from

the sample. Teflon experiment which we have described earlier assures that sample holder or other external factors do not contribute to the relaxation at low temperatures and it stems only from the sample. If the relaxation comes from external factors which respond to magnetic field then it will give a false AMC.

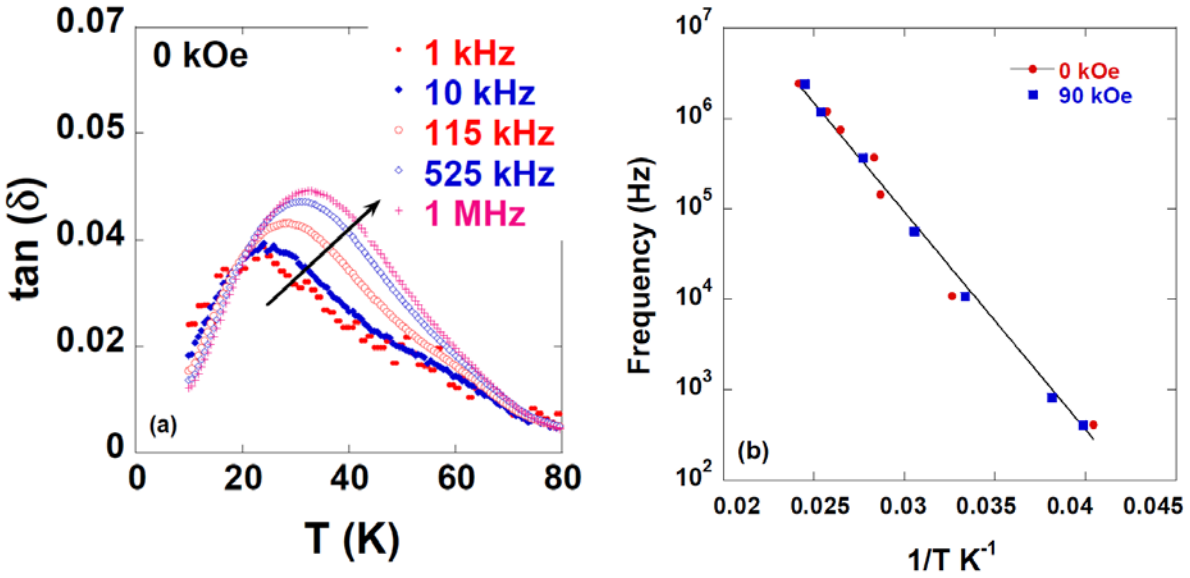

Figure III-10: (a) Dielectric loss as a function of temperature at several frequencies for BTO doped with 0.3 at% Fe. (b) log frequency as a function of reciprocal temperature for BTO doped with 0.075 at% Fe.

Fig III – 10 (a) gives the temperature dependence of dielectric losses for BTO doped with 0.3 at% Fe between 0 to 80 K at several frequencies. A clear maximum is seen around 30 K at 1 kHz. This maximum shifts with frequency and temperature showing relaxation. The Arrhenius plot obtained by plotting the log frequency and reciprocal temperature of the loss maximum gives an activation energy of 47 meV for BTO doped with 0.075 at% Fe (fig III – 10(b)) under 0 kOe. We find the same for BTO doped with 0.3 at% Fe. The temperature range and the activation energy have led us to infer the observed relaxation as polaron relaxation [24]

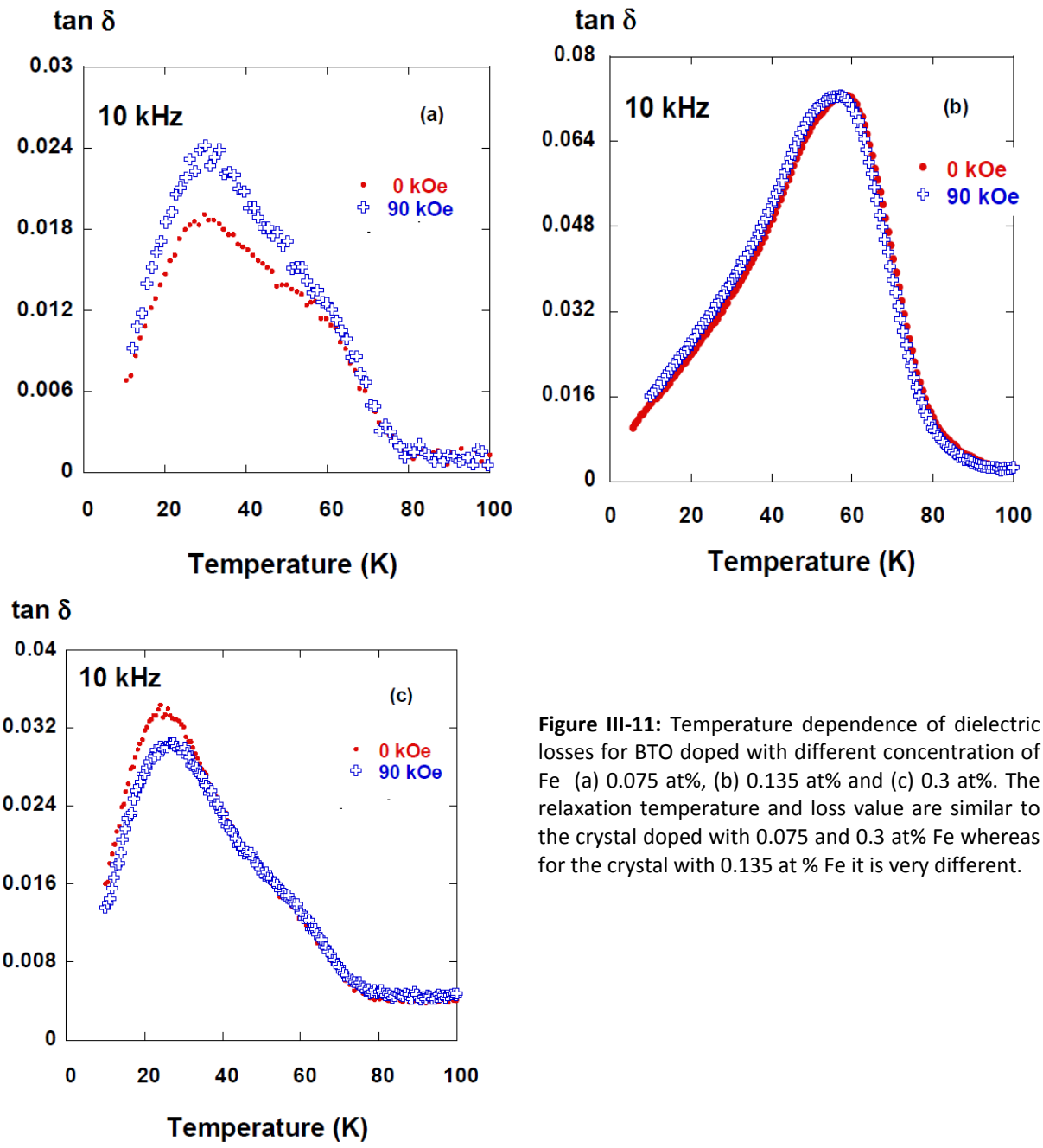

Figure III-11: Temperature dependence of dielectric losses for BTO doped with different concentration of Fe (a) 0.075 at%, (b) 0.135 at% and (c) 0.3 at%. The relaxation temperature and loss value are similar to the crystal doped with 0.075 and 0.3 at% Fe whereas for the crystal with 0.135 at % Fe it is very different.

Fig III- 11 (a - c) gives dielectric losses as a function of temperature for BTO doped with 0.075 at%, 0.135 at% and 0.3 at% Fe at a spot frequency of 10 kHz under 0 and 90 kOe magnetic field. The maximum of relaxation is around 30 K for 0.075 at % and 0.3 at % Fe doped crystals and it is around 50 K for 0.135 at% Fe doped crystal. This indicates that BTO with 0.135 at % Fe is not the same as the other two crystals. Furthermore the losses are very high in 0.135 at% Fe doped BTO around 6 % compared to the other two crystals where the losses are close to 2 to 3 %. Under the application of magnetic field of 90 kOe, amplitude of the relaxation is enhanced for BTO with 0.075% Fe and depressed for BTO with 0.3 at% Fe whereas for crystal with 0.135 at% Fe no magnetic field effect is seen. In all the cases, the temperature of the dielectric losses maximum was not shifted under

magnetic field (see fig III – 10(b)). This shows that the activation energy of 47 meV obtained from crystals with 0.075 at% and 0.3 at% Fe is not altered by the magnetic field.

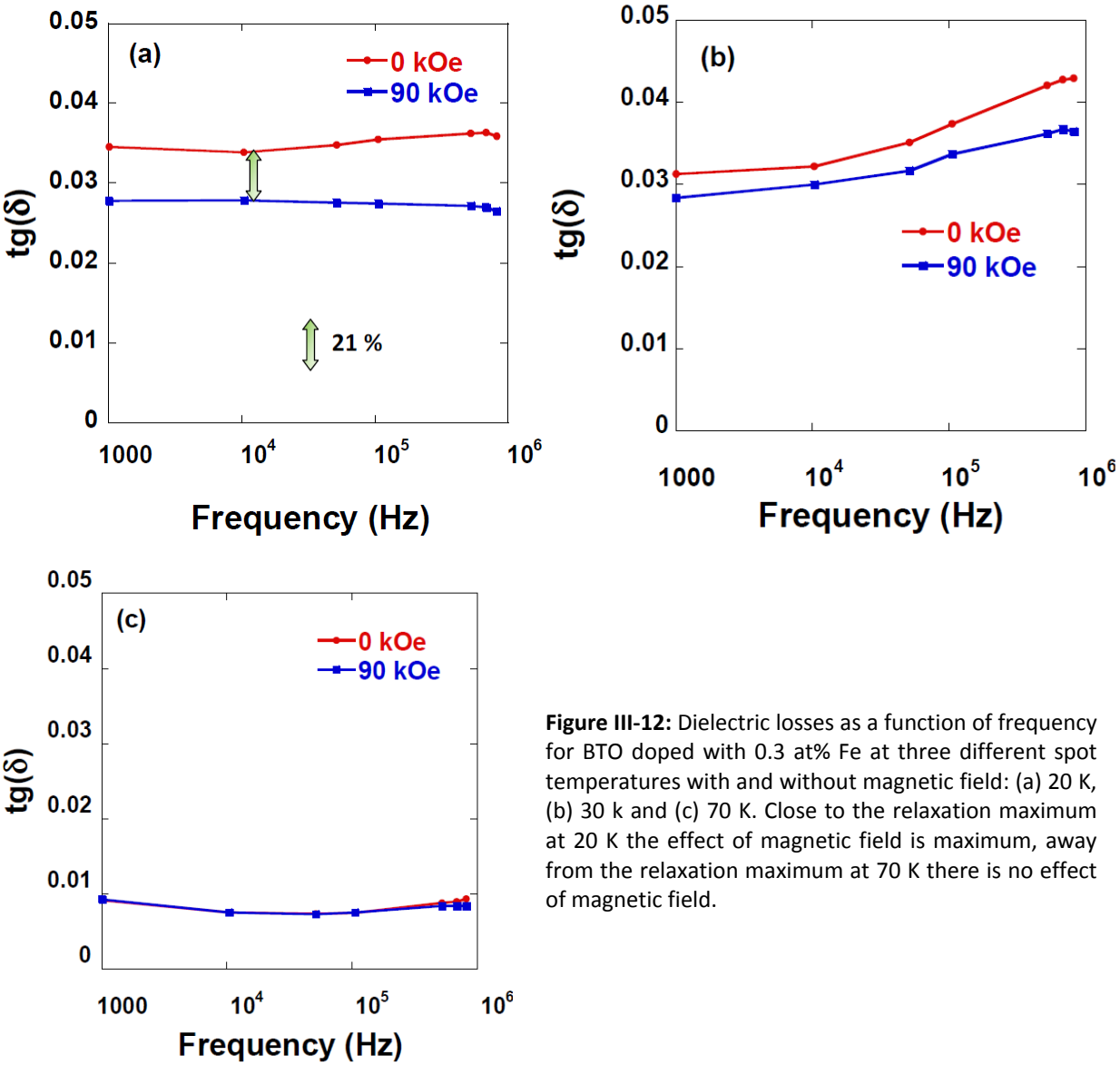

Figure III-12: Dielectric losses as a function of frequency for BTO doped with 0.3 at% Fe at three different spot temperatures with and without magnetic field: (a) 20 K, (b) 30 k and (c) 70 K. Close to the relaxation maximum at 20 K the effect of magnetic field is maximum, away from the relaxation maximum at 70 K there is no effect of magnetic field.

The activation energy of the crystal with 0.135 at% Fe is unexpectedly very high (in the range of eV) which does not correspond to activation energy of polaron relaxation. Therefore only the results from crystals with 0.075 at% and 0.3 at% Fe will be considered. In these two crystals only the magnitude of dielectric losses is affected. It can be seen from fig III – 8(d) that capacitance is not affected by magnetic field at temperatures below 80 K. To appreciate the amplitude variation by magnetic field on the relaxation, dielectric losses was plotted as a function of frequency for BTO with 0.3 at% Fe at three different spot temperatures (20, 30 and 70 K) with and without magnetic field as shown in fig III-12 (a)-(c). It appears from fig III-12 (a) & (b) that the effect of magnetic field is more pronounced at 20 and 30 K respectively; it reaches 21% at a frequency of 10 kHz for 20 K where the

maximum of polaronic relaxation occurs. At higher temperatures (70 K) sufficiently away from the relaxation maximum, the magnetic tuning of dielectric losses disappears (fig III-12 (c)).

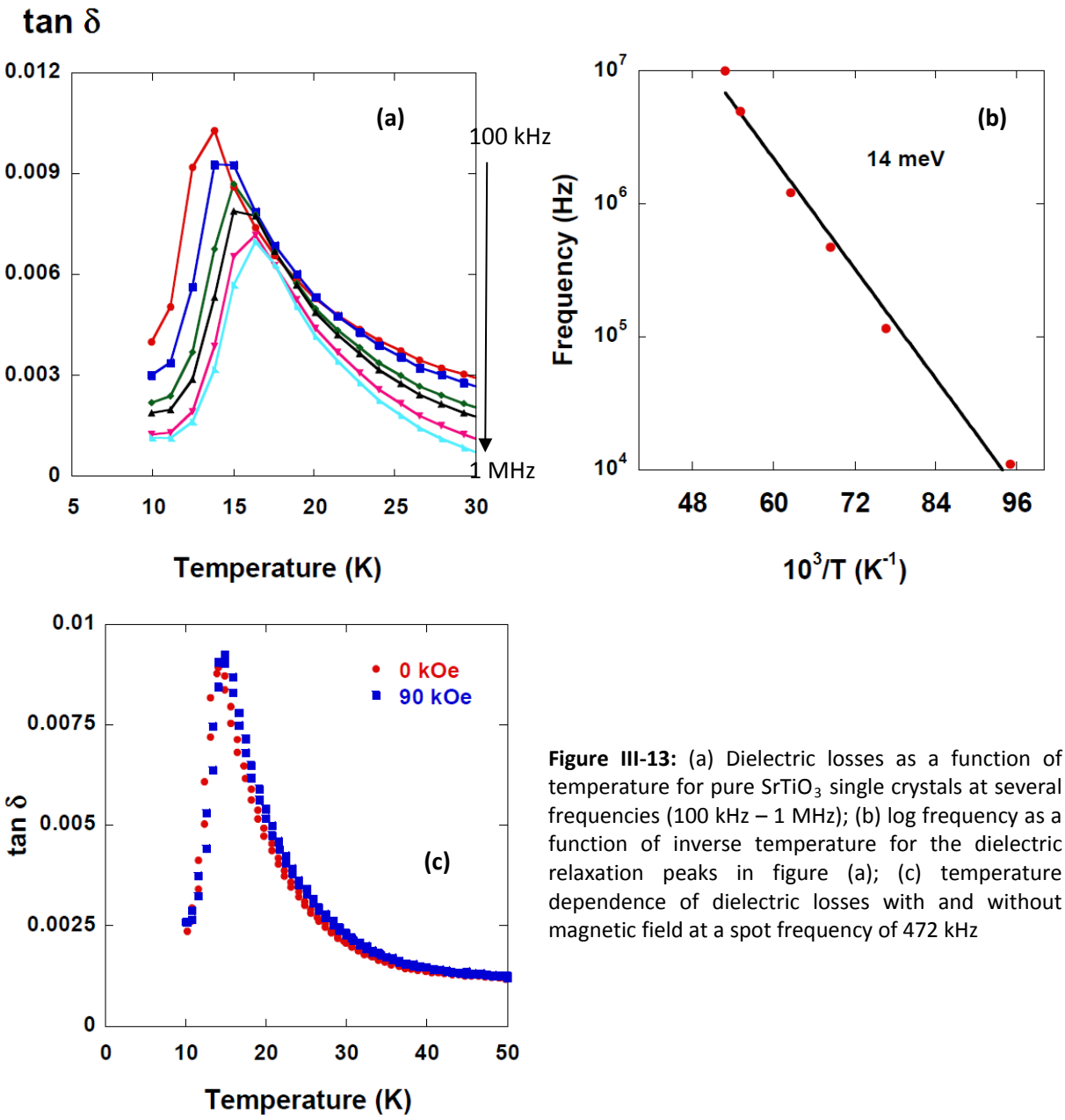

Figure III-13: (a) Dielectric losses as a function of temperature for pure $SrTiO_3$ single crystals at several frequencies (100 kHz – 1 MHz); (b) log frequency as a function of inverse temperature for the dielectric relaxation peaks in figure (a); (c) temperature dependence of dielectric losses with and without magnetic field at a spot frequency of 472 kHz

Similar to BTO single crystals, $SrTiO_3$ single crystals have a relaxation at very low temperature with very small activation energy prompting to look for AMC. Fig III-13 (a) presents dielectric loss as a function of temperature for pure strontium titanate single crystal at several spot frequencies in the range of 100 kHz to 1 MHz. Maximum in the dielectric loss was observed below 20 K and within the measured frequency range the observed maximum shifts in temperature from 13 K to 16 K with increase in frequency, indicating relaxation phenomenon. Activation energy of 14 meV (Fig III – 13 (b)) for this relaxation agrees very well with earlier reported one for strontium titanate [24]. It is also interesting to note that dielectric losses are less than 1% confirming purity of the crystal. Fig III-13 (c)

shows the dielectric loss as a function of temperature for pure STO at an attempt frequency of 472 KHz with and without magnetic field (90 kOe). It is evident from the figure that magnetic field has no influence on the maximum of the relaxation.

III.3.3. Magnetic field effect on piezoresonance in Fe doped $BaTiO_3$ single crystals:

Finally we describe here the piezoresonance of $BaTiO_3$ with 0.135 at% Fe under magnetic field of 90 kOe. The method for identifying the piezo resonance frequency is described in detail under section II.3.2 of chapter 2. In Fig III-14 (a) & (b) dielectric loss is plotted versus frequency under isothermal condition at 10 K with and without magnetic field. The two zero field resonances represent measurements taken before (red peak) and after (green peak) the application of magnetic field and the blue peak gives the piezo resonance under magnetic field of 90 kOe. In Fig III-14 (a) where thick silver wire (Φ - 0.12 mm) was used for contacts, piezo resonance shows a shift of 3 KHz from 3.76 10^5 Hz under zero field to 3.79 10^5 Hz with 90 kOe magnetic field. Recovery of zero field piezo resonance (green peak) upon removal of the magnetic field is to be noted importantly. Fig III-14 (b) is plotted for the same sample measured with thin silver wire (Φ - 0.05 mm) for contacts. No shift of piezo resonance like the one obtained upon using thick wire under magnetic field was found.

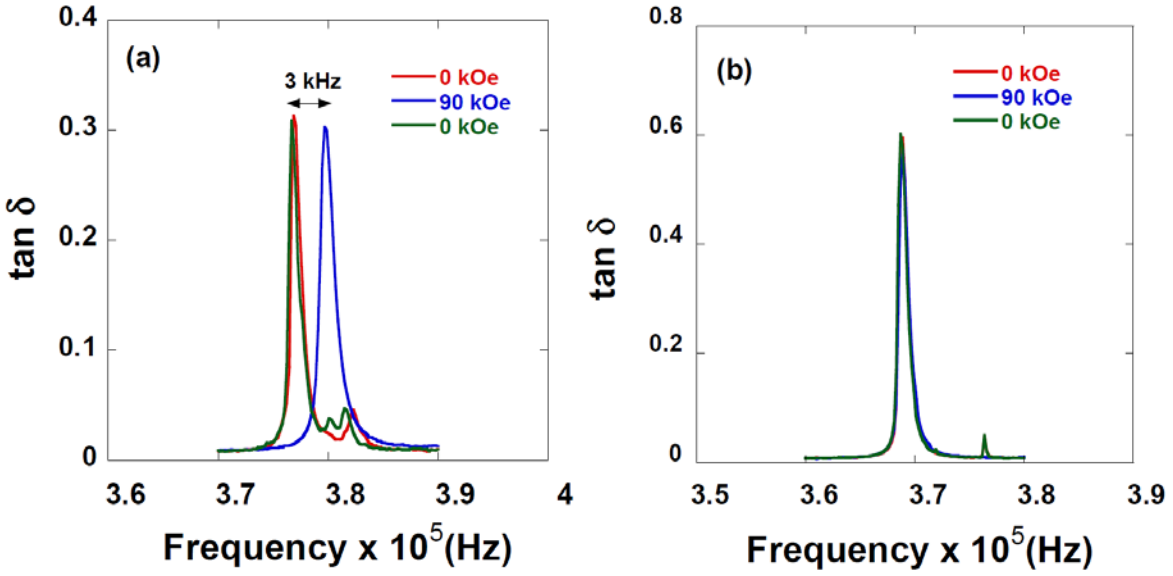

Figure III-14: Dielectric loss as a function of frequency with and without magnetic field at 10 K for BTO doped with 0.135 at% Fe: (a) thick silver wire, (b) thin silver wire. Red peak and green peak represents piezo resonance for 0 kOe before and after the application of magnetic field respectively. A shift of 3 kHz in piezo resonance obtained when thick silver wire was used for contacts.

III.3.4. Microscopic investigation of the magnetic field effect on relaxation:

According to Catalan model, the interface between electrode and dielectric has a resistance different from the core of the dielectric due to the difference in charge carrier density that give rise

to Maxwell - Wagner effect and eventually to magnetodielectric effect caused by change of resistance at the interface under magnetic field [1]. The essential ingredient in obtaining AMC is interfaces and free charges. Following his model, Maglione has observed magnetocapacitance in one cent diodes and as well as in $CaCu_3Ti_4O_{12}$ so called giant permittivity material [2]. Magnetocapacitance in diode stems from interaction of external magnetic field with free charges accumulated at the p-n interface. In case of $CaCu_3Ti_4O_{12}$ free charges arise from incomplete compensation of Cu related defects and the interfaces are grain boundaries which under magnetic field generates magneto capacitance. He also showed that this kind of tuning of dielectric properties by magnetic field is not only observed in ceramics but also in single crystals of $BaTiO_3$ doped with Fe. The doping of Fe^{3+} in site of Ti^{4+} creates charged oxygen vacancies and these vacancies act as the source of free charges in the crystal. Localization of free charges at such interfaces was held responsible for the tuning of macroscopic impedance versus the magnetic field. Furthermore it was also shown that such tuning under magnetic field is more pronounced at the relaxation frequency $f=1/(2\pi\tau)$ according to

$$\tau = d\sqrt{\frac{\sigma}{\varepsilon D}} \qquad \textbf{Eq III-6}$$

where d is the thickness, σ is the conductivity, ε is the dielectric permittivity and D the diffusion coefficient of the free charges which localize at the interface. Having found AMC in Fe doped BTO, in this work we looked for dependency of AMC on doping concentration *i.e.* concentration of free charges. It is clear from fig III-8 that artificial magneto capacitance observed shows no consistent trend with the doping concentration. Surprisingly the effect tends to vary between two different experiments of the same sample indicating non-reproducibility. This can be interpreted by means of kinetics of domain walls with temperature. The number of domain walls changes (i.e. interfaces) when the sample is subjected to several temperature cycles as it goes through phase transition many times. Since artificial magneto capacitance depends on both interfaces and charged defects, changing one of them would consequently change the magneto capacitance. We have no way of controlling the number of domain walls since it depends on the temperature, which makes the magnitude of this magneto capacitance effect highly irreproducible.

The low temperature dielectric relaxation is a more reliable way of achieving artificial magneto capacitance because this relaxation does not stem from domain wall dynamics. As mentioned earlier in this chapter that the same kind of dielectric losses anomaly arising from polarons was reported in many perovskites around 40 K due to different valence states of dopants. In $BaTiO_3$ doped with Fe we found a relaxation at low temperatures in the temperature range of 20 to 50 K which is ascribed

to polarons that appears due to existence of Fe^{2+} and Fe^{3+} in the crystal [40]. Our polaron model was further supported by the activation energy of 47 meV obtained for the relaxation which very well agrees with the previous results [24]. In fig III-11 (a) for BTO doped with 0.075 at% the magnetic field enhances the relaxation amplitude while it depresses for BTO doped with 0.3 at% Fe (fig III-11 (c)), showing contradiction. To understand the effect of magnetic field on the amplitude of this relaxation it is necessary to look deeply into the microscopic process happening in the crystal at low temperatures. The relaxation under discussion is due to hopping of free charges and it can happen in number of ways (i) by purely lattice related defects where there is a charge transfer between Ti^{4+} and Ti^{3+} centers or oxygen vacancy related centers; (ii) by extrinsic charged defects, in our case it is the hopping of free charges between different oxidation states of iron owing to doping of Fe. Such hopping process leads to dipoles reorientation which could then undergo relaxation. Importantly hopping of free charges induces a change in lattice elastic energy and the application of magnetic field does not affect this energy; this is confirmed by our finding of same activation energy for low temperature relaxation with 0 and 90kOe magnetic field (Fig III-9). In contrast, magnetic field could affect the way these electrons are hopping provided the temperature and frequencies are favorable. This could explain why the magnetic field influences the amplitude of relaxation. It is immediately seen in Fig III-12 (a) & (b) where the magnetic field effect on the maximum of the dielectric losses is strongly marked at 20 K and 30 K along with high losses which points out the transfer of electron between different oxidation states of iron ions. On the other hand, at 70 K both no magnetic field effect and low dielectric losses were observed showing that the frequency and temperature are not favorable for hopping or polaron relaxation (fig III-12 (c)). Interestingly low temperature relaxation was found even in undoped $BaTiO_3$ but no magnetocapacitance was noticed (not shown) and the same holds for pure $KTaO_3$. It is known that iron is ubiquitous which could lead to relaxation at low temperatures following the same process described earlier but the concentration of free charges are very low which precluded us from obtaining magnetocapacitance in pure $BaTiO_3$ and $KTaO_3$ crystals.

Our interest in probing pure $SrTiO_3$ under magnetic field was inspired from the low temperature relaxation seen in un-doped $BaTiO_3$. $SrTiO_3$ is an incipient ferroelectric and there is a strong increase of capacitance below 50 K accompanied by dielectric loss anomaly around 15K in the form of relaxation (fig III-13 (a)). The origin of this relaxation peak is thought to arise from domain dynamics at low temperatures although it is still speculative (K.A. Muller, 1991). Observation of internal friction below 40 K in $SrTiO_3$ by O.M. Nes et al supports domain dynamics scenario [41]. In spite of these observations an important thing to be noted here is that the activation energy of 14 meV (fig III-13 (b)) for low temperature relaxation agrees very well with the literature [42], yet it is very small and close to our observation of low temperature relaxation in $BaTiO_3$ (40meV). Fischer *et al.* have

studied local disorder in pure $SrTiO_3$ at low temperature and found a strong maximum in oxygen Debye Waller factor at 31 K which they attributed to unwanted impurities [43]. Chen Ang *et al.* investigated dielectric relaxation in Fe doped $SrTiO_3$ at low temperatures and stated that dielectric relaxation behavior is due to trap controlled ac conduction [44]. Polaronic nature of dielectric relaxation in $SrTiO_3$ was pointed out by Bidault *et al.* [24]. Based on the previous arguments and proximity of the dielectric relaxation in $SrTiO_3$ to BaTiO3 with very small activation energy lead us to infer that the relaxation stems from localized dipoles that arise from unwanted impurities. Consequently application of magnetic field to this relaxation should give us magneto capacitance yet no such effect was noticed (fig III-13(c)). This is because free charges which are responsible for the tuning of dielectric losses under magnetic field are very small in concentration which forbade us in realizing any magnetic field induced effect on the dielectric property of $SrTiO_3$ reflecting the same situation as in the case of pure $BaTiO_3$.

To find microscopic evidences of free charge hopping between Fe ions in $BaTiO_3$ doped with Fe, we performed ESR studies in the nominally pure and the Fe-substituted $BaTiO_3$ single crystals. We point out that the crystals that were used for ESR studies are the same as the ones used for the dielectric experiments reported just above. Figure III-15 (a) gives the ESR spectra as a function of magnetic field for pure and 0.075 at% Fe doped BTO at 4 K. For both the crystals there is an intense resonance located at g = 2.0005 (3350 Oe) due to the central ±1/2 transition of Fe^{3+}.

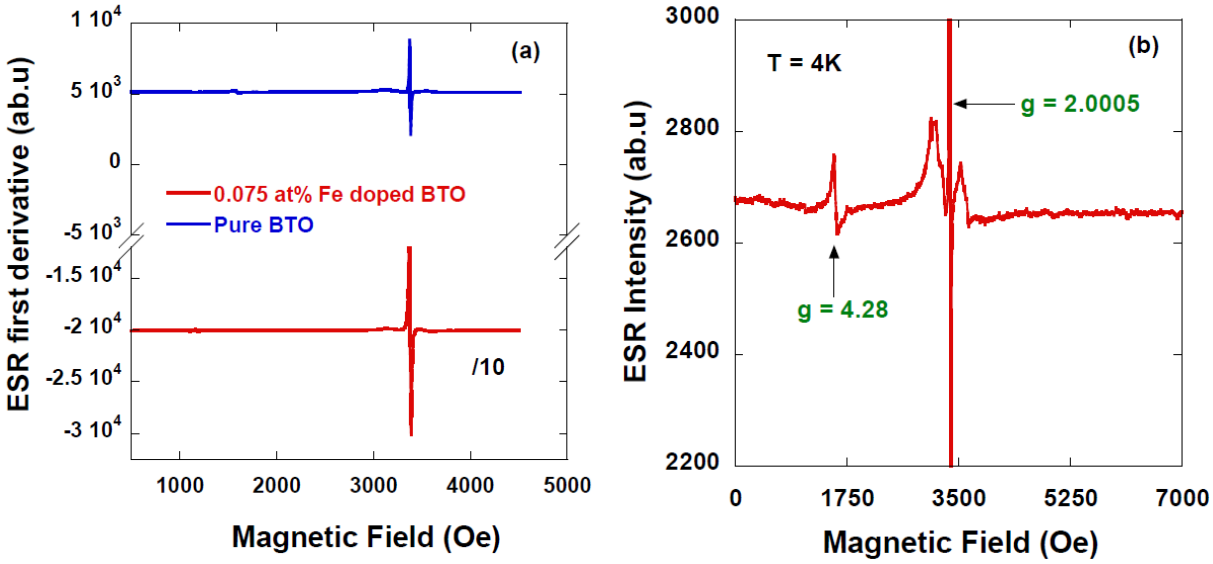

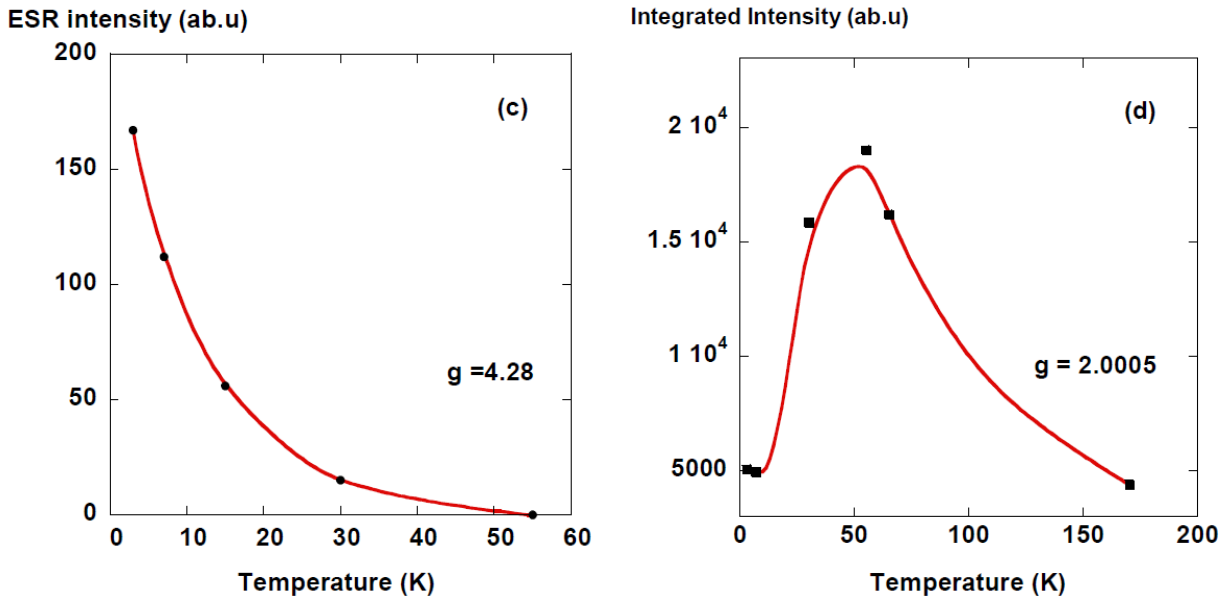

Figure III-15: (a) ESR spectra for pure and 0.075 at% Fe doped $BaTiO_3$ single crystals. Note the line intensity of Fe doped BTO is divided by the factor of 10 for plotting; (b) Zoom of ESR spectra for pure BTO shown in figure (a). Notice the two symmetric resonance located at 3350 Oe (g =2.0005) and 1580 Oe (g = 4.28); (c) temperature dependence of the integrated intensity for the line at 1580 Oe; (d) temperature dependence of the integrated intensity of the line at 3350 Oe. (solid lines are guide to eyes)

It can also be noticed that the resonance of Fe doped BTO is at least 15 times more intense than the pure BTO crystal even after dividing the intensity of Fe doped BTO ESR spectra by factor of 10 indicates that the line's intensity is proportional to iron concentration. Because of the very low detection limit of ESR and the unavoidable presence of iron in the nominally pure $BaTiO_3$, the ESR spectra recorded at 4 K look the same in all crystals. The full analysis of these spectra including the rotation plots is out of the scope of the present thesis and the Fe doped BTO crystals show many overlapping resonance in their ESR spectrum therefore for the sake of clarity only ESR spectra on the pure BTO crystals will be described. Here we only underline the Fe^{3+} related lines and their behavior as a function of temperature. Figure III- 15 (b) shows the zoom of ESR spectra of pure BTO showed in fig III-15 (a) and in agreement with previous reports, the line located at g=2.0005 (3350 Oe) is ascribed to Fe^{3+} ($3d^5$ ion, with electron spin S=5/2) in the six-fold environment of oxygen. In the same way, the line at g=4.28 (1580 Oe), smaller in intensity, stems from Fe^{3+} centers linked to 2 oxygen vacancies with random relative position. Because of their symmetry, these centers do not entail any change in the spectra on rotating the crystals versus the magnetic field (not shown). For both these lines, the intensity displays very distinct anomaly at *ca* 40 K. The VO-Fe^{3+}-VO line intensity decreases from 4 K and fully vanishes above 40 K (fig III-15 (c)) and in contrast the six-fold oxygen coordination of Fe^{3+} line grows from 20 K up to a large maximum at *ca* 40 K (fig III-15 (d)). Both these features can be ascribed to electron exchanges between Fe^{2+} and Fe^{3+} centers. Keeping in mind that Fe^{2+} ion ($3d^6$

ion, S=0) is not ESR active, then the decrease of the VO-Fe^{3+}-VO intensity above 40 K can result from the electron delocalization from this charged Fe^{3+} center. This was also confirmed by magnetic measurement as a function of temperature in which the magnetization goes to zero above 30 K in both zero field cooled and field cooled condition (fig III-16). Above 30 K the signal is very noisy because the magnetization is below the detection limit of the standard SQUID magnetometer.

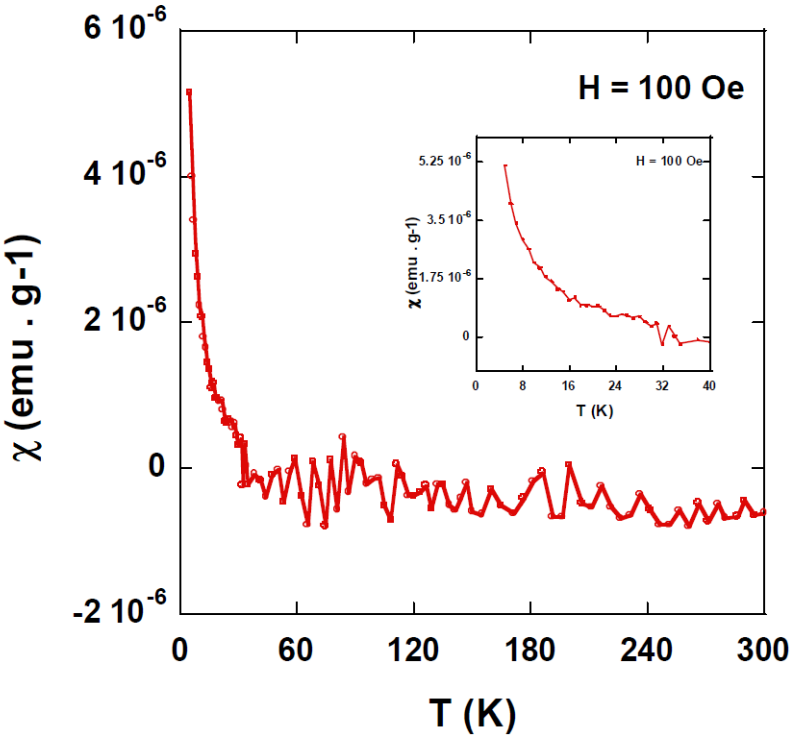

Figure III-16: Susceptibility as a function of temperature under Zero field cooled condition. We find the same in field cooled conditions well. Inset shows the zoom of the same plot from 0 to 40 K.

The disappearance of this charged Fe^{3+} center follows an Arrhenius law with activation energy of 0.13 eV which is in agreement with a shallow trap located close to the bottom of the conduction band. On the other hand, we ascribe the 40 K maximum of the octahedral Fe^{3+} center to the optimal electron exchanges among Fe^{2+}/Fe^{3+} sites which reflects in the thermally activated losses. In such a case, the ESR maximum is signing the high electron hopping rate in this temperature range. More precisely, it is in this temperature range that the electron trapping on Fe centers is counter-balanced by the thermal activation of long range electronic motion. This also led to an optimal interaction of these hopping electrons with the applied magnetic field. Our temperature dependent ESR results are thus a strong support for the magnetic field induced losses without magneto-capacitance modulation.

We have seen possible artificial magnetocapacitance effect at the domain wall relaxation and tuning of losses at the low temperature. Interestingly there is yet another well-known means of obtaining magnetoelectric coupling that is by strain which could be internal (lattice mismatch,

magnetostriction etc) or external (clamping of the sample) [103] [46]. Composites of $BaTiO_3$-$CoFe_2O_4$ display huge magnetoelectric coupling which is several times larger than single phase magnetoelectrics. In this composites application of electric field causes the sample to develop strain which is then passed on to the magnetic layer then eventually magnetic property of the composite is changed due to magnetostriction [18]. In our sample BTO doped with 0.135 at% Fe, applying external strain lead to a shift of piezoresonance by 3 KHz although the applied strain was unintentional (Figure III-14 (a)). When thick silver wire was used for electrical contacts there was a buildup of residual strain in the sample during the application of magnetic field due to restricted motion of the sample which eventually induces shift in the piezoresonance. After the removal of the field concomitantly strain decreases and the normal position of the sample is recovered along with piezoresonance. In contrast when thin silver wire was used, the sample is free to move under magnetic field and no shift in piezoresonance was obtained (fig III-14 (b)). Albeit the application of strain was uncontrolled and unintentional it presents us with a reliable way for inducing artificial magnetoelectric coupling even in single phase materials if the sample is put as a cantilever under magnetic field.

III.3.5. Conclusions:

Artificial coupling of a magnetic field with dielectric parameters of ferroelectric single crystals can happen in several ways. Close to the ferroelectric domain wall relaxation range, in agreement with the Catalan model, a large artificial magneto capacitance effect has been confirmed in Fe doped $BaTiO_3$ crystals. However, due to the lack of control of the domain wall density, such effect is unreliable. In the low temperature range T<50 K, the magnetic field has no effect on the capacitance but it can tune the dielectric losses. This tuning can be more than 15% under 90 kOe in Fe-doped $BaTiO_3$ while it stays below the detection threshold in pure $BaTiO_3$ and $SrTiO_3$ single crystals. We suggest that such efficient tuning of losses results from the interaction between the magnetic field and hopping polarons that affect the dielectric losses. When the density of such polarons is small like in pure crystals, no macroscopic effect can be measured. Unlike domain walls relaxation, this polaronic contribution does not need interfaces to happen which in turns explain why no magneto capacitance could be observed. Finally in our observation of shift in the piezoresonance due to unintentional strain in BTO doped with Fe under magnetic field show the importance of strain in achieving AMC. Strain engineering may provide us with controlled application of strain to materials which are on their own either ferroelectric or ferromagnetic and transform them into multiferroics. At this juncture it is important to focus on magnetic field dependent conductivity and strain engineering to achieve artificial coupling between dielectric parameters and external magnetic field as a possible way for circumventing the intrinsic multiferroics in single phase materials.

III.4. References:

[1] R.C. Casella and S.P. Keller. *Phys. Rev*, 116:1469, 1959.

[2] B. Jaffe, W. R. Cook, H. Jaffe. *Piezoelectric Ceramics*. Academic Press in London, New York, 1971.

[3] M.E. Lines, A.M. Glass. *Principles and Applications of Ferroelectric and Related Materials*. Oxford Classic Text in Physical Sciences, 2001.

[4] F.A. Kroger and H.J. Vink. *Physica B*, 20:950, 1954.

[5] J. Daniels, K.H. Hardtl, D. Hennings and R. Wernicke. *Philips Res Reports*, 31:487, 1976.

[6] A.W. Hornig, R.C. Rempel, H.E. Weaver. *J. Phys. Chem. Solids*, 10:1, 1959.

[7] M.V. Raymond and D.M. Smyth. *J. Phys. Chem. Solids*, 57:1507, 1996.

[8] E.S. Kirkpatrick, K.A. Muller and R.S. Rubins. *Phys. Rev*, A136:86, 1964.

[9] M. Nakahara and T. Murakami. *J. Appl. Phys*, 45:3795, 1974.

[10] H-J. Hagemann. *J. Phys. C: Sol. Stat. Phys*, 11:3333, 1978.

[11] S.M. Sze and K. K. Ng. *Physics Semiconductor Devices*. John Wiley & sons, Inc, Hoboken, New Jersey, 2007.

[12] W.J. Merz. *Phys. Rev*, 95:690, 1954.

[13] J. Fousek. *Czech. J. Phys.*, 15:412, 1965.

[14] P. Zheng, J.L. Zhang, Y.Q. Tan and C.L. Wang. *Acta Materialia*, 60:5022, 2012.

[15] H.G. Unruh and H.E. Müser. *Z. Angew. Physik*, 14:121, 1962.

[16] G.H. Jonker. *J. Am. Ceram. Soc*, 55:57, 1972.

[17] K. Okada. *J. Phys. Soc. Jp*, 16:414, 1961.

[18] D.A. Hall, M.M. Ben-Omran and P.J. Stevenson. *J. Phys: Conden. Matt*, 10:461, 1998.

[19] B.L. Cheng, M. Gabbay, G. Fantozzi and W. Duffy Jr. *J. Alloys. Comp*, 211:352, 1994.

[20] P.V. Postnikov, V.S. pavlov, S.A. Gridev and S.K. Turkov. *Sov. Phys: Sol. Stat*, 10:1267, 1968.

[21] L.N. Kamyasheva and S.N. Drozhin. *Ferroelectrics*, 71:281, 1987.

[22] X.H. Chen, Y.N. Wang, H.M. Shen, Z.M. Niu and P.C.W. Fung. *Proceedings of ICIFUAS-9, Beijing, china July 1989,*, page 153, 1989.

[23] G. Arlt and H. Dederiches. *Ferroelectrics*, 29:47, 1980.

[24] C.L. Snead Jr and D.O. Welch. *J. Physique*, 46 (C10):589, 1985.

[25] Y.N. Huang, Y.N. Wang and H.M. Shen. *Phys. Rev. B*, 46:3290, 1992.

[26] B.L. Cheng, M.Gabbay and G. Fantozzi. *J. Mat. Sci*, 31:4141, 1996.

[27] B.L. Cheng, M. Gabbay, M. Maglione and G. Fantozzi. *J. Electroceramics*, 10:5, 2003.

[28] J. M. De Teresa, M. R. Ibarra, P. A. Algarabel, C. Ritter, C. Marquina, J. Blasco, J. García, A. del Moral and Z. Arnold. *Nature*, 386:256, 1997.

[29] P. B. Allen and V. Perebeinos. *Phys. Rev. Lett*, 43:4828, 1999.

[30] J. G. Bednorz and K. A. Müller. *Rev. Mod. Phys*, 60:585, 1988.

[31] M. Maglione. *arXiv:1006.3719v1*, 2010.

[32] B. Salce, J.L. Gravail and L.A. Boatner. *J. Phys: Conden. Matt*, 6:4077, 1994.

[33] O. Bidault, M. Maglione, M. Actis, M. Kchikech, B. Salce. *Phys. Rev. B*, 52:4191, 1995.

[34] M. Maglione. *Ferroelectrics*, 254:151, 2001.

[35] T. Kolodiazhnyi and S.C. Wimbush. *Phys. Rev. Lett*, 96:246404, 2006.

[36] C. Gillot, J.P. Michenaud, M. Maglione and B. Jannot. *Sol. Stat. Comm*, 84:1033, 1992.

[37] M. Maglione. *J. Phys: Conden. Matt*, 20:322202, 2008.

[38] M. Maglione, R. Bohmer, A. Loidl and U.T. Hochli. *Phys. Rev. B*, 40:11441, 1989.

[39] G. Catalan. *Appl. Phys. Lett*, 88:102902, 2006.

[40] G. E. Peterson, A. M. Glass, and T. J. Negran. *Appl. Phys. Lett*, 19:130, 1971.

[41] O. M. Nes, K. A. Muller, T. Suzuki and F. Fossheim. *EuroPhys. Lett*, 19:397, 1992.

[42] R.Viana, P. Lunkenheimer, J. Hemberger, R.Bohmer and A. Loidl. *Phys. Rev. B*, 50:601, 1994.

[43] M. Fischer, A. Lahmar, M. Maglione, A. San Miguel, J. P. Itic, A. Polian and F. Baudelet. *Phys. Rev. B*, 49:12451, 1994.

[44] Chen Ang, J. R. Jurado, Zhi Yu, M. T. Colomer, J. R. Frade and J. L. Baptista. *Phys. Rev. B*, 57:11858, 1998.

[45] C.W. Nan. *Phys. Rev. B*, 60:6082, 1994.

[46] Y. Ni and A. G. Khachaturyana. *J. Appl. Phys*, 19:130, 2007.

Chapter 4

IV. Chapter 4: Influence of Ionic conductivity on the piezoelectric resonance of $KTiOPO_4$ single crystals:

IV.1. Introduction:

In the previous chapter we have seen how electronic conductivity in the material can lead to some interesting phenomenon on the dielectric properties due to localization. Here we will consider ionic conductivity and its effect on the ferroelectric properties. For that purpose ideal test material would be potassium titanyl phosphate. Potassium titanyl phosphate ($KTiOPO_4$ (KTP)) is one of the major non linear optical materials for visible and infrared generation. The conversion efficiency reaches 50 – 70 % for KTP crystals 3-5 mm long in other words a KTP crystal of 3mm long can replace KH_2PO_4 (KDP) crystal which is 40 cm long. Zumsteg et al. were the first to discover the excellent non linear properties of KTP crystals [1]. KTP is a very interesting material particularly because it has combination of ferroelectric and superionic conduction properties in which the phenomenon of electrical ordering is combined with an anomalously high mobility of cations [2]. In the following we will see in detail the structure, conductivity, dielectric and nonlinear optical properties of KTP.

IV.1.1. Crystal Structure of $KTiOPO_4$:

The properties displayed by any crystalline material are undoubtedly related to their underlying structure. Therefore it is imperative to study the structure of KTP in detail in order to understand its properties. Tordjman et al. determined the crystal structure of KTP and they found that the KTP crystals belong to mm2 class of orthorhombic systems with non centrosymmetric space group $Pna2_1$ [3]. The lattice parameters are a = 12.814 A° (6), b = 6.404 A° (2) and c = 10.616 A° (5). The KTP structure has a 3D rigid framework of vertex sharing titanium – oxygen octahedra TiO_6 and phosphorus – oxygen tetrahedral PO_4 and it shown in figure IV – 1(a). The neighboring octahedra of titanium are linked by PO_4 tetrahedra to form infinite chains in the structure. The structure is characterized by wide helical channels that extend along the c crystal axis and are occupied by large monovalent potassium cations. These helical channels provide the means for the mobility of potassium cations in the crystal. Another important structural feature of KTP is that there are long and short Ti – O bonds. There are two independent crystallographic position for titanium cations Ti(1) and Ti(2) due to displacement of titanium from the center of octahedra such that long (2.00-2.10 A°) and short (1.72-1.74 A°) Ti – O bonds alternate in the - O(9) – Ti(1) – O(10) – Ti(2) – O(9)- chains

(Figure IV – 1(b)) [4]. These chains of TiO_6 octahedra a rigidly held together by undistorted PO_4 tetrahedral groups. It was shown that these chains are responsible for the non linear optical properties observed in KTP crystals [1].

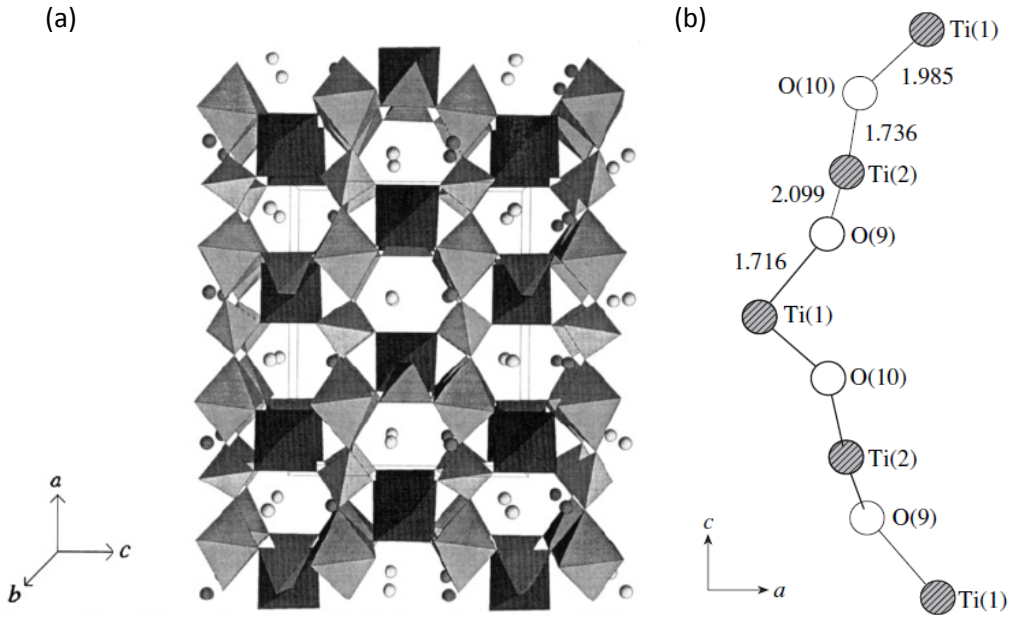

Figure IV-1: (a) KTP crystal structure along [0 1 0] direction; the octahedra represents TiO_6 anions and tetrahedral represents PO_4 anionic group and the potassium ions sitting in the cavities are represented by spheres. (b) Alternating long and shot Ti – O bonds forming chains in KTP structure.

The potassium cations occupy crystallographically two independent positions at room temperature with respect to the coordination with oxygen. These positions are K(1) and K(2) with nine and eight oxygen atoms surrounding them respectively. The high mobility of potassium ions observed in KTP is not only due to the presence of helical channels in the structure but also due to the creation of potassium vacancies during the growth of crystals at high temperatures. It was found that when the KTP crystals were grown at temperatures higher than 900°C then it is usually accompanied by the formation of vacancies at the potassium positions [5] [6]. The creation of vacancy at high temperatures can be written as

$$KTiOPO_4 \rightarrow K_{1-x}TiOPO_{4-x/2} + \left(\frac{x}{2}\right)K_2O \qquad \textbf{Eq IV-1}$$

Where x is the vacancy concentration in the potassium sublattice. The Curie temperature of the crystal increases with an increase in the K/P ratio in the melt particularly at low KTP concentration [6].

IV.1.2. Conduction Mechanism of $KTiOPO_4$:

From the crystal structure of KTP discussed above it can be seen that mobility of potassium ions is preferably along C axis. For this reason KTP is known as a quasi one dimensional superionic conductor of K^+ ions [7] [8]. The migration of the potassium ions requires the presence of potassium vacancies which are formed during the high temperature crystal growth. The room temperature ionic conductivity of KTP is around $10^{-4} – 10^{-8}$ S/cm [9] [10]. Furusawa et al. under took a detailed study regarding the conductivity of KTP crystals in the temperature range of 300 – 1200 K at different frequencies [11]. They explained the highly anisotropic conductivity of KTP along c axis based on the crystal structure. They found that conductivity along c axis is at least four orders of magnitude higher than the other two directions and also frequency independent above 1000 K. The conduction mechanism in KTP is through hopping of mobile K^+ ions to the neighboring vacant site along the conduction paths. These conduction paths have bottlenecks which the mobile ions have to pass through for hopping. In other words there is an energy barrier which must be overcome in order for the conduction to take place. Furusawa et al. defined four kind of conduction paths <A>, <B>, <C> and <D> from the crystal structure. The schematic of these conduction paths are shown in figure IV-2. The efficiency of these conduction paths for the K^+ ions to pass through them is defined by the ratio of size of the bottleneck and the ionic radius of mobile K^+ ions. They found that the ratio for the conduction path <A> and <B> is higher than the other two paths. This means the conduction along <A> and <B> is easier than the

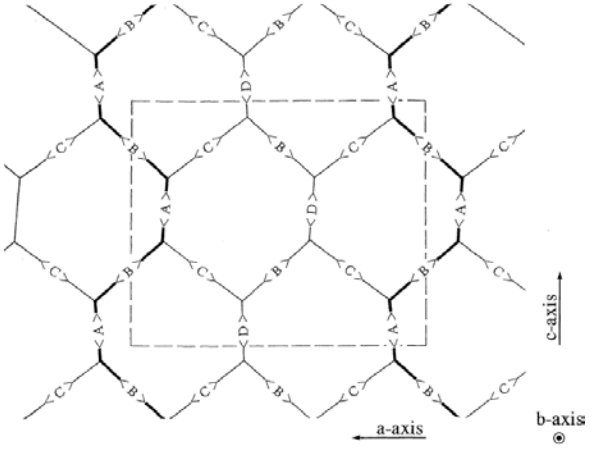

Figure IV-2: The schematic of the chains of conduction paths for K^+ ions in KTP projected along b direction. Note the chains of easy conduction path <A> and <B> along c axis.

other two paths. From figure IV-2 it can be seen that c axis contains only the highly conducting paths leading to one dimensional conduction in KTP. The other parts contain at least one of the difficult paths. Through put the whole temperature range the conductivity in KTP is a thermally activated

process and can be described by Arrhenius equation with a 1/T term in the pre-factor which is usual in ionic conductors

$$\sigma = \left(\frac{\sigma_0}{T}\right) \exp(-\frac{E}{kT}) \qquad \textbf{Eq IV-2}$$

Where E is the activation energy of the charge carriers but there are two temperature regions. For high temperature region activation energy is relatively high at about 0.21 – 0.36 eV [9] [10] whereas at low temperature activation energy is 2 – 3 times lower at about 0.16 eV [12].

IV.1.3. Ferroelectric and dielectric properties of $KTiOPO_4$:

The ferroelectric phase transition in KTP is identified by means of anomaly in the permittivity or in the second harmonic generation signal. Both these parameters undergo a specific change at the ferroelectric phase transition. The phase transition of KTP is around 1207 K but Angert et al. stated that the Curie temperature of KTP is very sensitive to potassium non stoichiometry i.e. K/P ratio during the growth [6]. They found that the change in the ratio of K/P can significantly change the Curie temperature of about 100 K wide temperature range. It is shown in figure IV – 3.

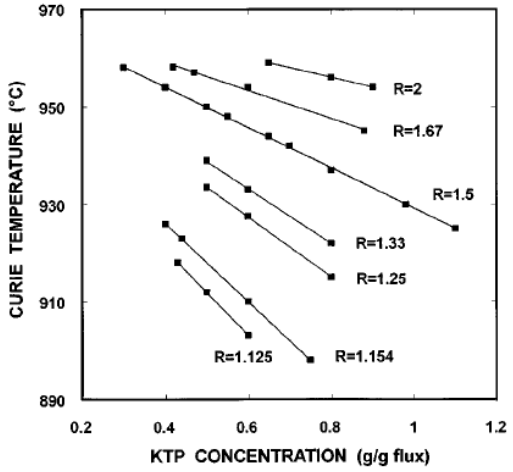

Figure IV-3: The Curie temperature dependence on KTP concentration for different self fluxes with varying K/P ratio (R). Notice that with increase in potassium in the flux (high R value) there is an increase in Curie temperature and also at low KTP concentration in the flux the Curie temperature is higher. Adapted from ref. [6]

Moreover the permittivity anomaly observed at the transition were not observed when the permittivity measurements is done along x and y axes. This shows that KTP crystal is a uniaxial ferroelectric with a change in symmetry from paraelectric Pnan to ferroelectric $Pna2_1$ space group [13] [14]. The substitution of thallium in place of potassium in KTP reduces the Curie temperature to 854 K. This decrease in Curie temperature made it possible for the researcher to study the dynamics of ferroelectric phase transition in detail. Harrison et al. have shown using $TlTiOPO_4$ (TTP) crystals that the displacement of alkali cations along the c axis plays a major role on the spontaneous

polarization of crystals in KTP family [15] [16]. It was also shown in $TlSbOGeO_4$ compound that the displacement of thallium is about 0.8 A° during the phase transition at 272 K and it occupies crystallographically two independent positions in the structure [17]. The displacement of other atoms is about one or two orders of magnitude smaller. These facts confirm that potassium cations are responsible for the ferroelectric nature of KTP. In fact potassium cations have large spatial distribution in the paraelectric state and in ferroelectric state they are displaced from their regular position which gives rise to noncentrosymmetry and spontaneous polarization (see figure IV – 4) [18].

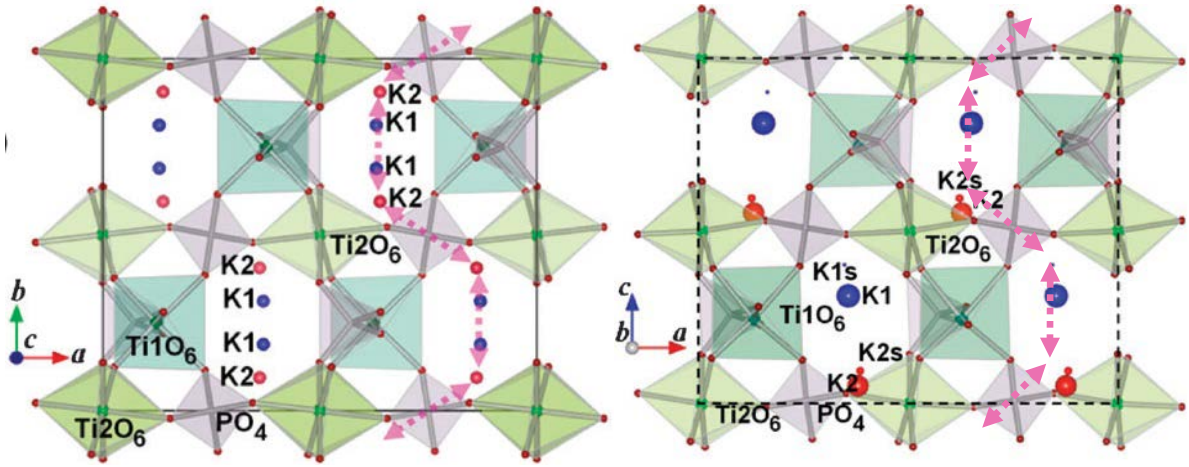

Figure IV-4: structure of KTP in (a) paraelectric state (b) in ferroelectric state. Notice is the difference in spatial distribution of K^+ ions in the paraelectric and ferroelectric state. The pink arrows represent the helical channels for the mobility of K^+ ions. The solid and dashed line in (a) and (b) denotes the corresponding unit cell. Adapted from ref [18].

The displacement of K^+ ions decreases with increase in temperature and at T_C it goes to zero indicating displacive nature of ferroelectric – paraelectric phase transition. At the same time the evolution of average K^+ ions displacement and spontaneous polarization with temperature follows the power law $(1- T/T_C)^{1/2}$ which is the characteristics of second order ferroelectric phase transition.

IV.1.3.1. Dielectric Studies on $KTiOPO_4$:

The dielectric studies on KTP are usually combined with conductivity measurements to ascertain the nature of conductivity in KTP at low temperatures. There are several reports on temperature and frequency dependence of permittivity and losses available in the literature. All these reports indicate on the possible superionic transition at low temperature the exact range of temperature is still debated. The dielectric studies on KTP were first carried out by Kalesinkas et al. [9]. They suspected that at 280 K there is a superionic phase transition in KTP due to the presence of low broad dielectric loss peak at this temperature range. This was followed by Rosenman et al. who found that at room temperature dielectric permittivity is characterized by strong dispersion. This dispersion disappears

at around 170 K. The same was observed for dielectric loss peak. This indicates that the high value of permittivity observed at high temperature and low frequency are mainly due to the contribution from conductivity of KTP. Urenski et al. measured dielectric, dc and ac conductivity of several families of $MM'OXO_4$ (where M = Rb, K; M' = Ti; X = P, As) crystals [12]. They found that plotting of dc and ac conductivity as a function of inverse temperature show two straight lines for all the studied family crystals which indicate two quite different temperature regions (see figure IV – 5). The deflection point T_d separates these regions. At the same deflection point dispersion in the permittivity and dissipation factor disappears. The dissipation factor is at least 2 orders of magnitude lower than the high temperature value. For KTP the deflection point is around 200 K. J.H. park et al. observed same kind of dielectric behavior around 190 K [19]. Both the permittivity and dissipation factor are very low below 190 K. Furthermore Jiang et el. found that at 180 K an increasing thermal absorption and an abnormal change in thermal expansion in a wide temperature range in the vicinity of 180 K. Shaldin et al. reported that pyroelectric effect suddenly reduces at around 200 K. These facts clearly indicate that KTP does show superionic phase transition around 200 K.

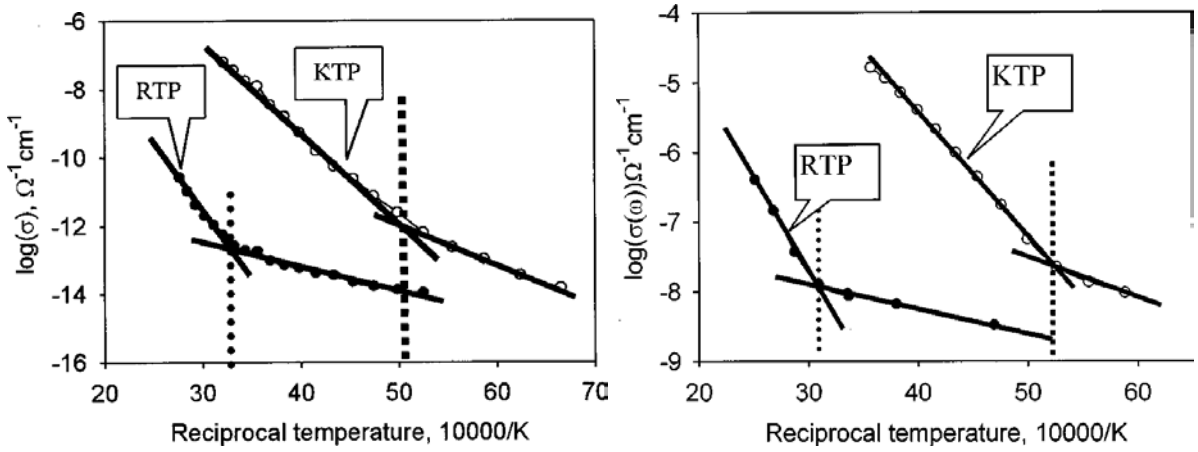

Figure IV-5: Log conductivity as a function of inverse temperature (a) dc conductivity, (b) ac conductivity (f= 20 KHz). Note the change in slope for both $RbTiOPO_4$ and KTP crystals at about 305 K and 200 K respectively. Adapted from ref [12]

The dissimilarity in the results available in the literature indicates that the superionic phase transition takes place over a broad temperature range. This is the typical characteristics of second order phase transition and it is very much within the consideration of theory of superionic conductors. At room temperature K^+ ions are highly mobile, as the temperature is lowered the mobility of K^+ ions drastically decreases and potassium ions start to localize at the lattice site. This happens at around 180 – 200 K leading to superionic to insulator phase transition. Note that this phase transition is not accompanied by any structural transition but only that above the transition K^+ ions gains sufficient energy and become mobile.

IV.1.4. Domains in $KTiOPO_4$:

The KTP crystals are the preferable material of choice for nonlinear optical convertors because of their large optical nonlinearity, high optical damage resistance and broad optical transparency [20]. Domain structures in KTP are important due to their influence on the nonlinear optical conversion efficiency. For better efficiency a quasi phase matched (QPM) condition is necessary which involves spatial variation of the sign of the nonlinear optical coefficient which is linked to the direction of the spontaneous polarization P_S [21]. QPM condition is needed for the compensation of the natural optical dispersion in the crystal [22].

The KTP crystals are collinear ferroelectrics possessing only 180° ferroelectric domain structure [23]. Mostly periodically poled KTP (PPKTP) is used for practical application which has alternating 180° domains of opposite sign placed in regular interval. The domain width can be in the range of tens of micrometer [24]. Recently Canalias et al. demonstrated a submicron periodically poled domains in flux grown KTP using electron beam lithography [25]. Stolzenberger et al. [26]proposed that during the domain inversion process K^+ ions shift in the -c direction, i.e., the nine coordinated cations becomes eight coordinated and vice versa. Due to this TiO_6/PO_4 framework is forced to adjust then the short Ti – O bonds become long and the long ones short while the PO_4 tetrahedra and TiO_6 undergo only a slight rotation with respect to each other [27]. Rejmankova et al. investigated PPKTP using optical interferometry and Bragg-Fresnel imaging to understand the structure of domain walls in KTP crystals. They proposed a domain structure based on their results and calculations and said that the P(1) atom is the linking or pivot atom for connecting the inversion domains across the wall. The schematic view of domain wall in PPKTP is given in figure IV – 6. The continuity of major structural chains of $P(1)O_4 – Ti(2)O_6$ polyhedra along [100] is maintained across domain walls.

Their findings are consistent with Urenski et al. [23] who found that domains in KTP are highly anisotropic. They argued that domain growth in KTP should occur in the direction of the crystalline b axis where the nucleation step is minimal. The lattice constant of KTP is smaller for b parameter and therefore domains prefer to grow in this direction. They observed that even when the switching electrode strips are oriented along x axis, the domains continue to grow along y axis.

Even though there are several articles discussing the physical property of KTP crystals there are only few articles discussing the piezoelectric properties of KTP [28] [29] [30]. In fact we find that there are no reports on the temperature dependent studies on piezoelectric resonance in KTP as far as we know. In this thesis we made a sincere attempt to study the piezoelectric resonance as a function of external stresses like temperature and electric field. We believe that a coupling between ionic conductivity and piezoelectric resonance in KTP can be anticipated due to the fact that potassium

ions are at the origin of these two properties. In what follows we describe the results on piezoelectric resonance of KTP and second harmonic generation mapping to visualize the domains as a function of temperature.

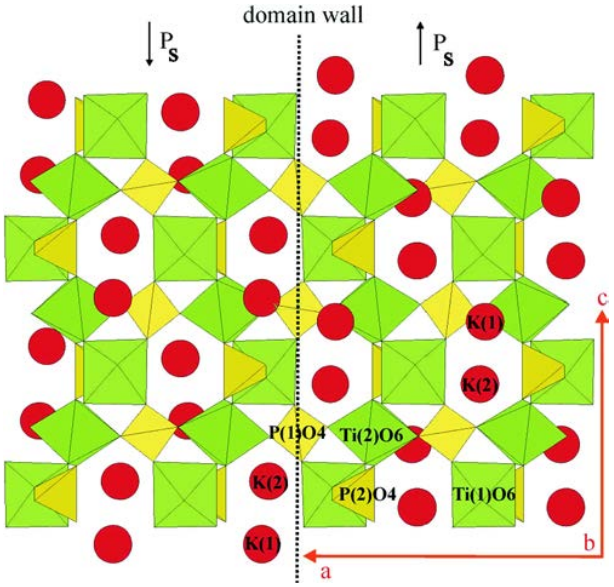

Figure IV-6: Schematic view of domain wall in PPKTP. Note the P(1) atom which is the link between the inverted domains. Also note the position of potassium atoms in the cavities between the two domains. In the domain on the left, the two potassium ions are slightly shifted downwards compared to the right domain where the potassium ions are shifted upwards. It is clear from this picture that domain walls in KTP are perpendicular to a axis and parallel to c axis.

IV.2. Experimental methods:

Several bars and plates of KTP single crystals with electrodes coated on (100), (010) and (001) faces were used for the measurements described below. The dimensions were 4 x 4 x 1 mm^3, 0.5 x 2 x 2 $mm^3$and 1 x 4 x 4 mm^3 for the plates; 4 x 1 x 1 mm^3, 7.89 x 2.79 x 1.02 mm^3 and 5.09 x 1.22 x 1.78 mm^3 for the bars. Gold was sputtered to make electrodes, and thin silver wires were glued with silver paste to the center of the electrode were used for electrical contact.

The ac resistivity of KTP was measured from room temperature to 120K using a HP 4194 A Impedance/ Gain Phase Analyzer in the range 100 Hz - 1 MHz. The samples were left for 10 min at each temperature in order to reach the thermal equilibrium.

Piezo resonances were obtained by measuring the conductance G and susceptance B as a function of frequency with an Impedance/ Gain Phase Analyzer. The measurement of G and B were carried out with a 1V sinusoidal voltage. Small frequency steps were applied in order to find the piezo resonance frequencies; then the selected length and thickness modes of each sample were measured between

room temperature and 120 K. The methods for identification of the length and thickness modes can be found in the reference [31]. All measurements were done under helium atmosphere. Bias electric fields upto 400 V. cm^{-1} were applied in both positive and negative directions to study the influence of bias on KTP single crystals.

IV.3. Results and discussion:

IV.3.1. Resistance Measurements:

Fig IV – 7 (a - e) gives the plot of reactance X versus resistance R over the frequency range 100 Hz - 1 MHz measured in a KTP crystal with electrodes perpendicular to [001] direction at several temperatures. The ionic conductivity of KTP is strongly anisotropic hence it could be measured only along [001] [11]. At 298 K the trace of the semicircle is seen at high frequency (left side) followed by a large linear increase at low frequency (right side). The intercept of the semicircle to the x axis then gives the resistance. As the temperature is decreased, resistance increases exponentially and below 200 K resistance can no longer be measured within the range of our impedance bridge. Additionally, the temperature dependence of resistivity was plotted as conventional log R versus 10^3/ T that can be fitted with Arrhenius law, which is shown as an inset in Fig IV – 7 (a) and the activation energy was found out to be 0.45 eV.

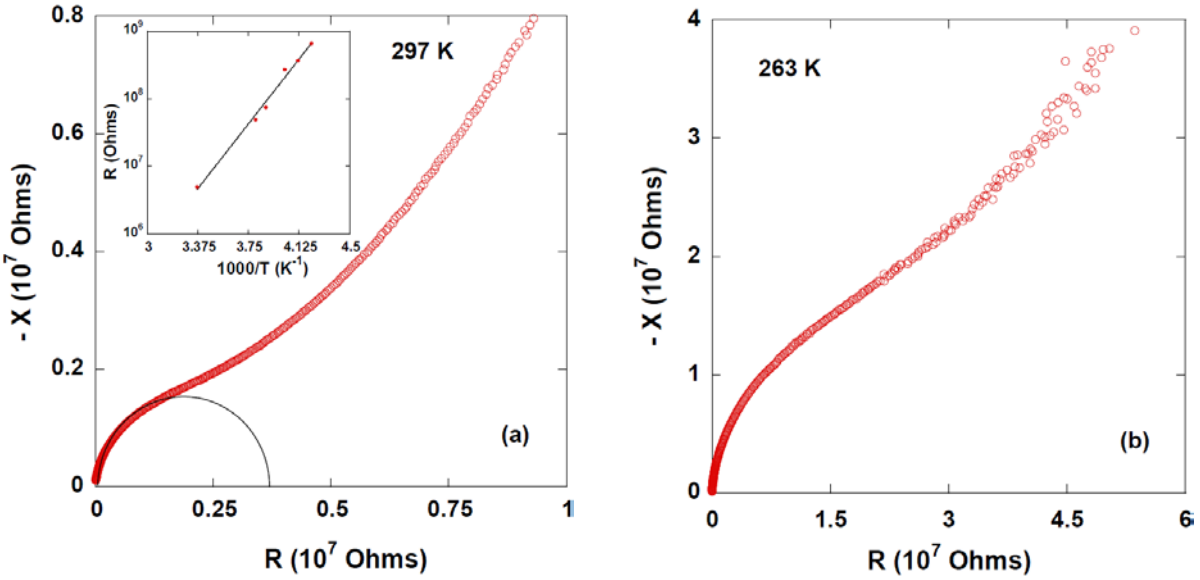

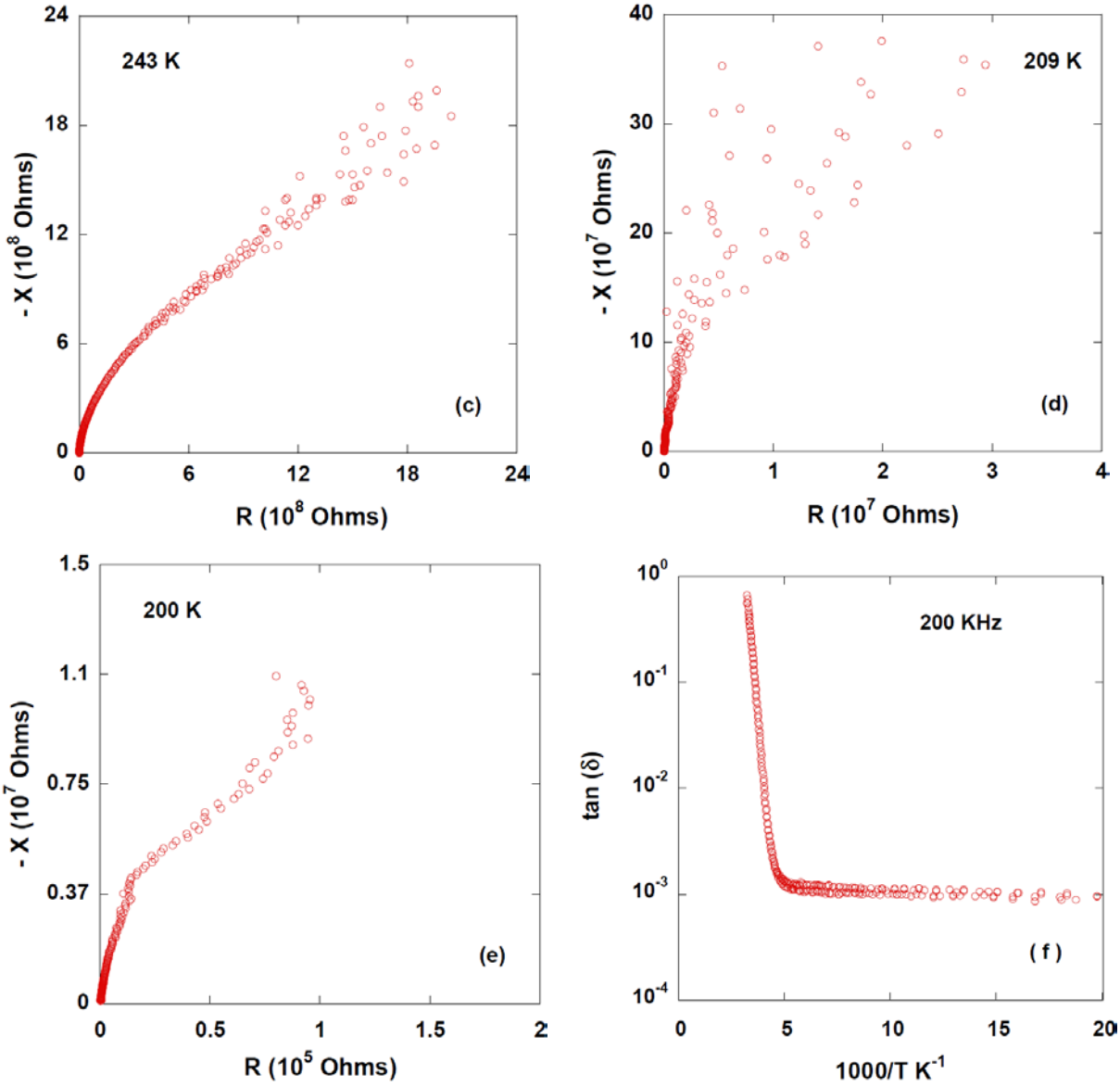

Figure IV-7: (a – e) Reactance (–X) as a function of Resistance (R) at several temperatures measured along [001] direction of a KTP. The trace of semicircle can be seen at room temperature. Inset to figure (a) gives log resistance as a function of inverse temperature. Figure (f) shows dielectric loss Vs inverse temperature measured along [001] direction at 200 kHz of KTP. The Presence of a steep slope from room temperature to 200 K indicates the drastic decrease in ionic conductivity.

The difference between the previously reported activation energy of 0.2eV [19] and the one we measured 0.45 eV lies in the different temperature ranges that were investigated. The literature data dealt with high temperature ionic conductivity (T>300K) while we focused on low temperatures (T<300K). While a purely Arrhenius behavior with low activation energy was evidenced in the former case, the proximity to superionic transition temperature may artificially increase the activation energy in our experiments. The increase in resistance at low temperatures is apparent in the plot of log dielectric loss as a function of inverse temperature at 200 KHz (see Fig IV – 7 (f)). When the temperature decreases, the dielectric loss decreases drastically from room temperature, which can be evidenced from the steep slope until 200K followed by a plateau at low temperature. A sudden

change of slope indicates a superionic transition around 200 K since dielectric losses are proportional to conductivity.

IV.3.2. Pyroelectric Measurements:

Pyroelectric measurements were done on KTP single crystals with electrodes perpendicular to [001]. At high temperature the ionic conductivity of KTP is very high which prevents the observation of pyrocurrent at high temperature. Hence at low temperature when the ionic conductivity becomes negligible, pyrocurrent can be measured. Integration of pyrocurrent with temperature then gives the polarization. Since the polarization of KTP is along [001], only crystals with electrodes on (001) were used. Fig IV - 8 gives the polarization as a function of temperature for both heating and cooling cycle and it is the same for all temperature rates, confirming that the pyroelectric currents indeed stem from the polarization appearance. Temperature rates of 2, 4 and 6 K min^{-1} were used and pyrocurrent increased respectively.

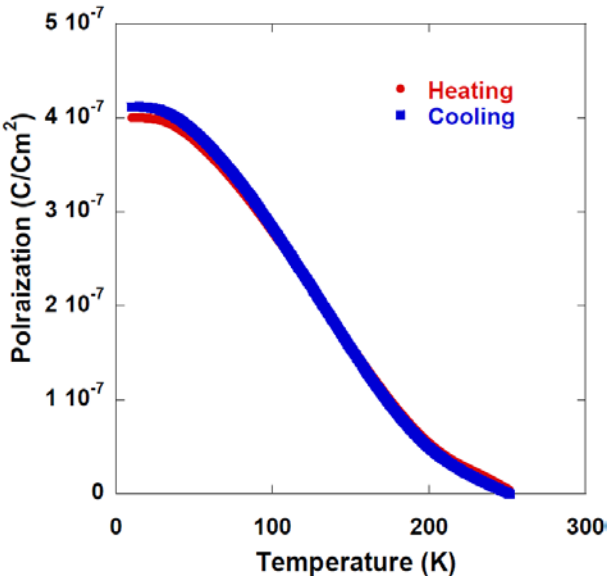

Figure IV-8: Polarization as a function of temperature on KTP along [0 0 1] direction for both heating and cooling cycles.

Furthermore direction of the current changed during heating and cooling cycles confirming what we were observing was indeed pyrocurrent. An important feature to be noted here is that above 200 K polarization is negligible, only below 200K polarization starts to appear indicating that polarization occurs at this temperature. This is not to say that KTP is ferroelectric only below 200K, it simply means that potassium ions which are responsible for ionic conduction starts to localize leading to reduction in screening of polarization by ionic conductivity. Hence the temperature of deflection T_d is around 200 K. All the samples reach maximum pyrocoeffcient of 2.3 nC cm^{-2} K^{-1} which is in agreement with the literature [32].

IV.3.3. Piezoelectric Measurements:

Fig IV – 9 (a - e gives the plots of conductance G at room temperature and 200 K as a function of frequency for a KTP bar sample with the electrode coated on (001) face. We interpret the observed peak of conductance as a transverse piezoelectric resonance for which the ultrasound vibrations occur along [100] while the generating electric field is applied along [001]. The corresponding resonance frequency f_r, can be expressed as

$$f_r = \frac{1}{2l\sqrt{\rho S_{11}}} \qquad \textbf{Eq IV-3}$$

where l is the bar length, ρ the crystal density and s_{11} the inverse elastic compliance along [100] . The lack of reliable estimate of s_{11} precluded a quantitative computation of the f_r. However, we checked this mode assignment by decreasing the bar length, which lead to an expected behavior of increase of the resonance frequency f_r. A single piezo resonance peak was observed at room temperature around 896 KHz. It is very clear from Fig IV – 9 that the peak shifts to higher frequency at low temperature, close to 210 K a second peak appeared and a full splitting being observed at 200 K. But no splitting was observed in thickness mode, *i.e.* along [001] recorded at 2.9 MHz. By plotting the resonance frequency before and after the splitting as a function of temperature makes the splitting to be seen more readily. AVANTAGE software developed by Thermo Fisher Scientific was used to fit the splitting and to deconvolute the peaks. The frequency of splitting was then taken from these deconvoluted peaks. The peak at room temperature is named Resonance Fr 1 and the new peak that appears is Resonance Fr 2. From fig IV – 10 it can be seen that at higher temperature, there is only one resonance frequency, while the splitting happens around 210 K.

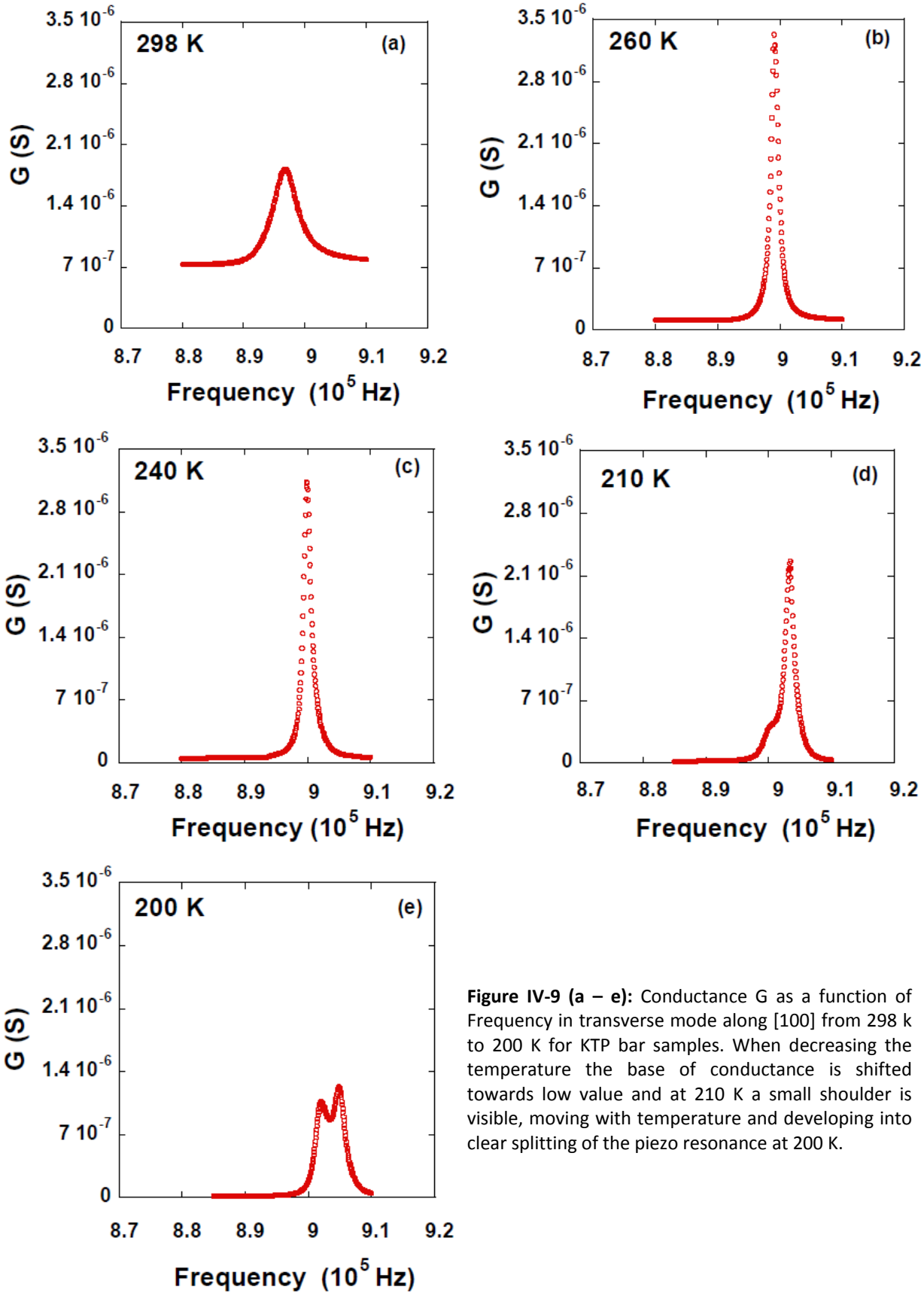

Figure IV-9 (a – e): Conductance G as a function of Frequency in transverse mode along [100] from 298 k to 200 K for KTP bar samples. When decreasing the temperature the base of conductance is shifted towards low value and at 210 K a small shoulder is visible, moving with temperature and developing into clear splitting of the piezo resonance at 200 K.

The overall decrease of frequencies by increasing the temperature is expected since it results from the thermal expansion of the crystals. It can be also noted from Fig 3 that Resonance Fr 1 disappears below 160 K.

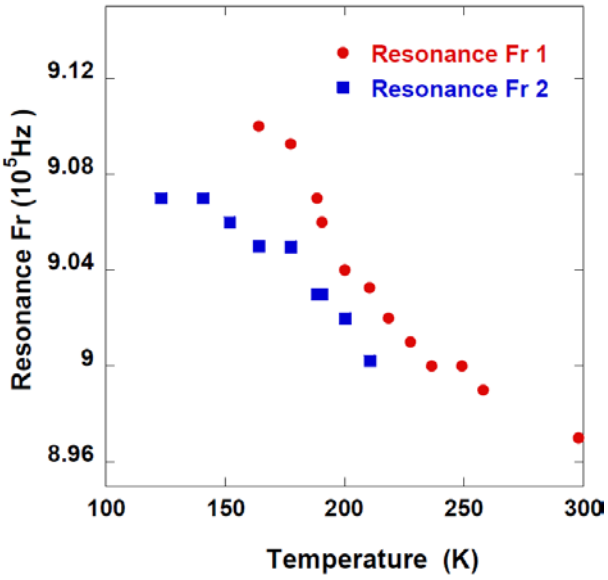

Figure IV-10: Resonance frequency before (Fr 1) and after splitting (Fr 2) as a function of temperature. With decrease in temperature, the resonances move to high frequency and Fr 1 disappears below 160 K.

Similarly, the conductance G of a KTP plate with electrode coated onto the (100) faces was measured as a function of frequency. Fig IV – 11 (a) and (b) give the corresponding plots at 298 K and 170 K in transverse mode along b and c respectively. Here the peak at room temperature splits at 170 K exhibiting similar behavior as KTP bar sample. It is difficult to assign this piezo resonance to one particular direction *i.e.* b or c, since the contribution for resonance comes from both [010] and [001] directions, the dimensions being the same in these directions. A splitting was observed for this sample in thickness mode along [100], which is given in Fig IV – 11 (a) and (b).

The results obtained for all the measured samples are summarized in Table 1. The theoretical resonance frequency was calculated with the help of elastic compliance data taken from reference [29]. It appears that the splitting occurs in all directions and there is no anisotropy in the splitting of piezo resonance peak. For samples 2 and 3 the length mode cannot be calculated since it involves two directions in length mode. Note that in KTP, the ionic conductivity decreases drastically due to the localization of the potassium ions and pyroelectric current starts to appear around 200 K [33] [11] [19]. As a consequence, we can assume that the potassium ions are at the origin of these splitting through their conductivity. This could be understood with the space charge model as described by Coelho [1]. For this purpose, the effect of dc bias on the splitting of the piezoelectric resonance was probed which lead to the results that are described hereafter.

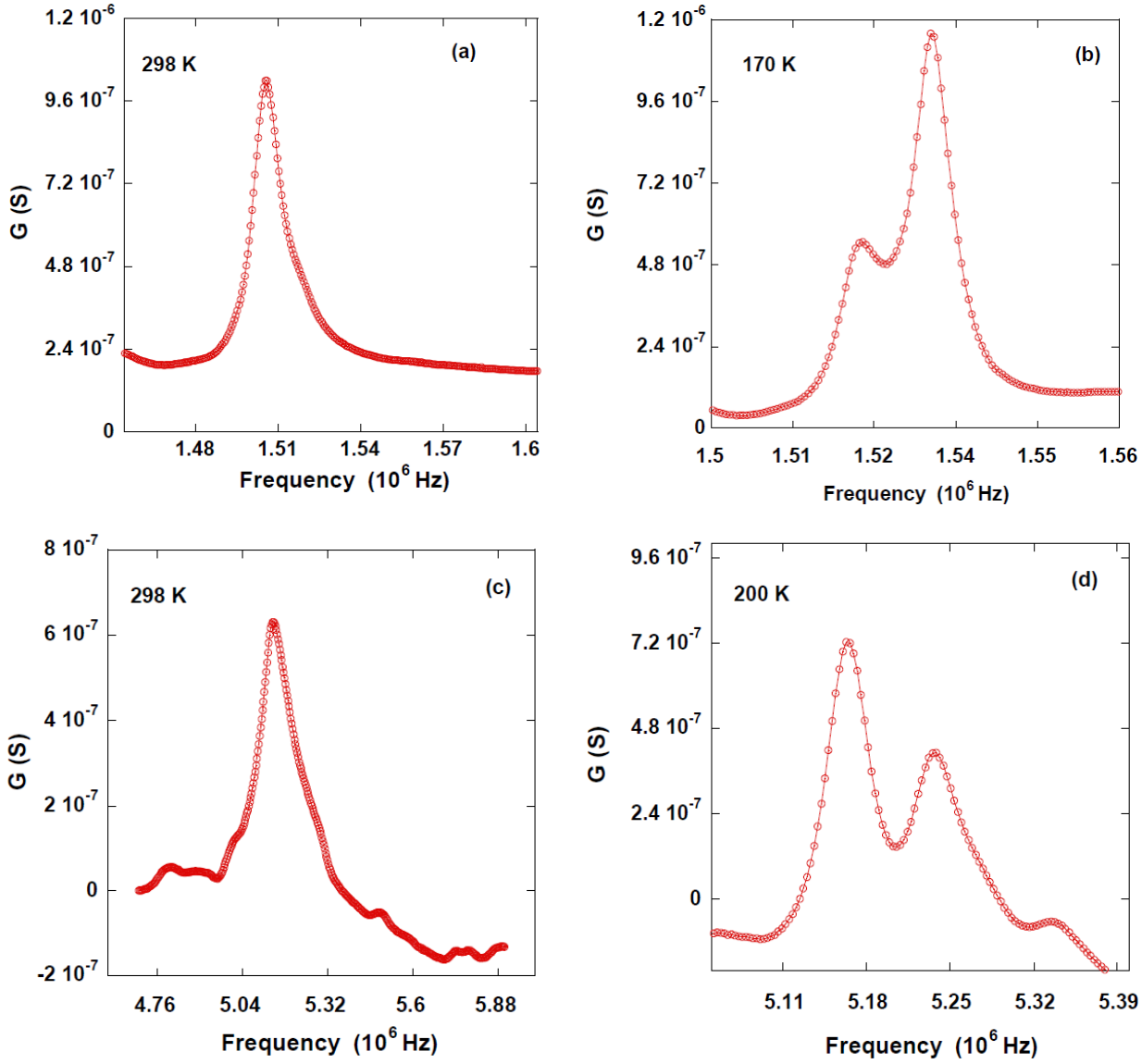

Figure IV-11: (a – b) Conductance G versus frequency for KTP plate sample in transverse mode along [0 1 0] and [0 0 1] at 298 K and 170 K. (c – d) Splitting of thickness mode along [1 0 0] at 298 K and 200 K on the same sample.

Fig IV – 12(a)-(d) gives the conductance as a function of frequency for the KTP bar sample with electrodes perpendicular to [001]. Both positive and negative electric fields upto 400 V.cm^{-1} were applied by step. Fig IV – 12(a) shows that there is no effect of the bias on the splitting at 180 K under isothermal conditions. Thus when the bias is applied after achieving splitting, we conclude that the potassium ions become rigid in their local position so that it cannot have any effect on splitting. Hence, the bias was applied before achieving splitting while cooling. Fig IV – 12 (b) shows the splitting for two piezo resonances: one without bias (0 V.cm^{-1} fields) at 180 K and the other after applying a field of 400 V.cm^{-1}during cooling at the same temperature. It is evident from the plot that there is an effect of the bias on the splitting which is irreversible. Fig IV – 12 (c) show the same kind of plot at 150 K indicating that the bias has considerable influence on the splitting, which is more

pronounced than that at 180 K. As expected at higher temperature (240 K), the splitting disappears and there is no discernible difference before and after the application of the bias, as shown in fig IV – 12 (d). According to these measurements we can deduce the three following features: there is no effect of the bias on the splitting under isothermal condition; a field cooling has an effect on the splitting with an enhancement at lower temperature, the bias has no influence on the piezo resonance at higher temperature when the splitting vanishes.

Table IV-1: Piezo measurements on several KTP samples with different orientation and dimensions**.**

Sample Number	Orientation	Dimensions (mm)	Electroded Face	Mode	Theoretical Resonance Frequency	Measured Resonance Frequency	Splitting
1		4 x 1 x 1	(0 0 1)	Length	454 KHz	890 KHz	Yes
				Thickness	3.51 MHz	2.9 MHz	No
				Length harmonics	1.36 MHz	2.7 MHz	Yes
2	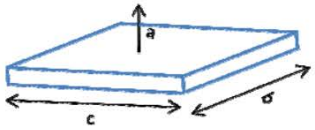	1.08 x 4.18 x 4.18	(1 0 0)	Length		810 Khz	Yes
				Thickness	3.46 MHz	2.1 Mhz	No
3	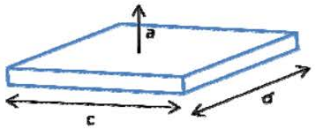	0.5 x 2 x 2	(1 0 0)	Length		1.5 MHz	Yes
				Thickness	7.49 MHz	5 MHz	Yes
4	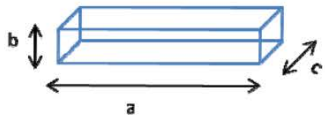	5.09 x 1.22 x 1.78	(0 1 0)	Length	333 KHz	325 KHz	No
				Thickness	3.1 MHz	1.8 Mhz	Yes
5		7.87 x 2.79 x 1.02	(0 0 1)	Length	230 KHz	450 KHz	No
				Thickness	3.4 MHz	3.5 MHz	Yes
6		7.87 x 2.79 x 1.02	(0 0 1)	Length	230 KHz	450 KHz	No
				Thickness	3.4 MHz	3.7 MHz	Yes

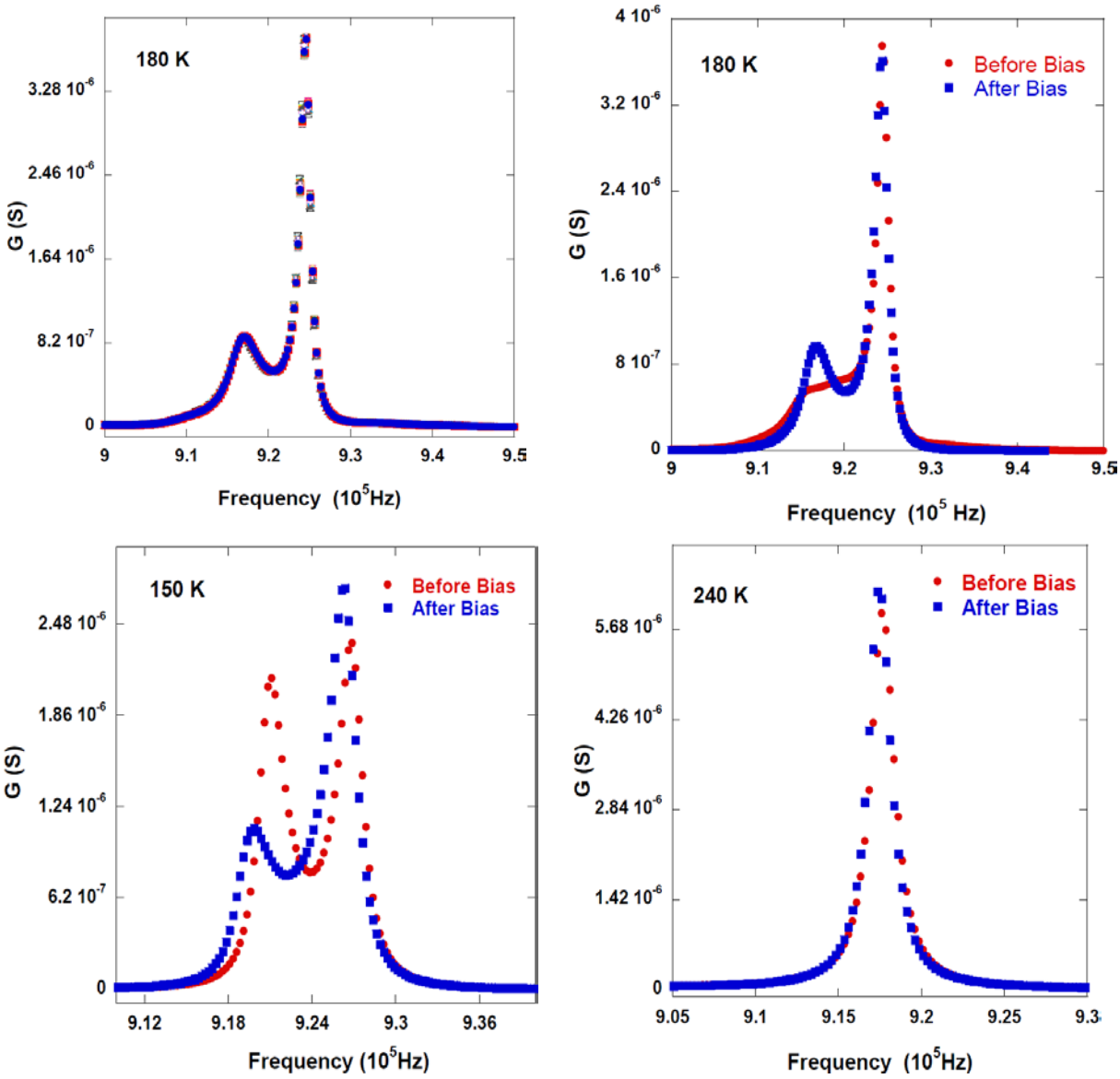

Figure IV-12(a – d): Conductance G vs Frequency in a KTP bar sample in transverse mode along [100] at 180 K, 150 K and 240 K under 400 V.cm-1 and without bias. (a) The bias was applied after splitting at 180 K under isothermal conditions and no effect was observed; (b) noticeable influence of the bias observed when it is applied during cooling before the actual splitting, (c) Enhanced bias effect at 150 K under field cooling; (d) at 240 K, far away from the temperature where the actual splitting start to appear, the bias has no influence on the piezo resonance.

Our observation of a large decrease of the dc conductivity and of a strong cusp in the ac dielectric losses, both at about 200 K, is consistent with previous reports on the superionic transition of KTP at 200 K. Actually the ionic conductivity of KTP decreases with temperature, and Jiang *et al.* reported that KTP undergoes a superionic transition at 180 K [35]. They also showed that thermal absorption takes place at the same temperature which indicates a phase transition. Noda *et al.* and J-H. Park *et al.* observed dielectric dispersion at 223 K and 193 K respectively [36] [19]. Shaldin *et al.* reported that pyroelectric current in KTP appears at 200 K and that a possible superionic phase transition can occur

at the same temperature [37]. In addition, Rosenman *et al.* found that KTP becomes a superionic conductor at 170 K according to the Seebeck effect that gradually undergoes a transition from ionic conductivity to electronic conductivity below 200 K as reported by V.D. Antsigin et al. [38] [39]. Non uniformity in these results for defining the superionic phase transition is not surprising since two different types of phase transitions generally occur in superionic conductors: In the first type, the transition happens sharply at a given temperature while transition occurs over a range of temperatures in the second type [40]. From these reports we can conclude that the transition in KTP is of second order, the mobile potassium gradually becomes immobile over a wide range of temperatures. Interestingly, Angert et al. have found that the Curie temperature seems to vary over a range of 100 K depending on the potassium concentration [6]. Potassium stoichiometry then affects the superionic phase transition, since the ionic conductivity of KTP is by vacancy mechanism involving potassium sites. As a first step for establishing a link between the ionic conductivity and lattice related properties, we thus confirmed that all of the KTP single crystals we used have a standard ionic conductivity along the c-axis. The first consequence of such ionic conductivity disappearance below 200 K is the increase of the pyroelectric current which can be integrated to lead to the polarization [37]. Note that it does not mean that the KTP ferroelectric transition takes place at 200K, but only that the ferroelectric polarization is screened by the ionic conductivity at high temperatures. This confirms the previous observations of ferroelectric hysteresis loop on reducing the conductivity [37] and on the birefringence onset below 200 K [41].

The original point we put in emphasis here is that the elastic parameters are affected by the conductivity suppression at 200K. Indeed, the mechanical resonance frequency of any solid material involves the sample dimension that is resonating, as well as the density and the elastic compliance S_{ij} as indicated by equation 1. It is important to note that such a mechanical resonance can be excited through a small ac electric field, *i.e.* less than 10V/cm in the case of KTP. Following equation 1, the splitting of the KTP piezoelectric resonance at 200 K can only result from a splitting of elastic parameters since the sample dimensions and density have no specific evolution at 200 K. Our investigation of several sample geometries and domain states (table 1) confirmed that there is no correlation between the crystal polarization state and the resonance splitting. This is also seen on figure IV – 10 that the splitting is just superimposed to the continuous increase of the resonance frequency on cooling which stems from the thermal dilatation. We thus can conclude that the inverse elastic compliance which is single at high temperatures becomes split at T<200 K. This feature seems to indicate that the crystal behaves like 2 slabs in the low temperature state. It is important to note that the superposition of many ferroelectric domains will not result in a resonance splitting but rather lead to a broadening of the resonance peak. We thus assume that a space charge

bi-layer is built in KTP upon decreasing the temperature below 200 K (figure IV-13). . Within a single ferroelectric domain and for temperatures higher than 200 K, K^+ ions are homogeneously distributed in all directions, in particular along the thickness that is parallel to the c-axis and below 200 K, K^+ ions localize in a way that is schematically shown in the figure IV – 13. This heterogeneous localization results from the electrical continuity at the electrode/crystal interfaces and from the built in potential resulting from the polarization orientation. The extension of such space charge along the c-direction is not known; however, since the polarization of KTP is directly resulting from the K^+ ions localization, the sample maybe considered as a superposition of 2 slabs having the same elastic properties in the ab plane but not along c. This may explain the splitting of piezoelectric resonances below 200K.

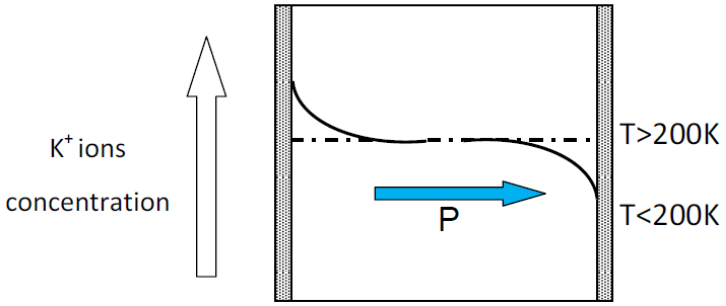

Figure IV-13: Schematic view of the space charge distribution above and below the superionic transition temperature (200 K) in KTP within a single ferroelectric domain.

So this space charge model thus provides a link between the ionic conductivity and the lattice elastic properties [1]. This is further confirmed by the poling experiments reported on figure IV – 12 where using a slight electric field of 400V/cm during the sample cooling through the 200K temperature range; we were able to tune the amplitude of the split resonances. When the samples were cooled without this dc electric field (ZFC), a subsequent isothermal poling is not efficient for changing the resonance splitting. Translating this in terms of the space charge model, we thus state that the dc electric field can alter the building of space charge only when its application starts before full localization and trapping of the mobile K ions. Conversely, once the splitting has been altered under field cooled conditions, the only way to recover the original resonance shape is to rejuvenate the sample under heating in the temperature range where ionic conductivity is efficient. The way to cancel the dc field effect on the space charge is to remove the potassium gradients by thermally activating the hopping of individual ions. Additionally, splitting happens at different temperatures for the same sample depending on the sample thermal history which corroborates the presence of space charge. In figure IV – 9 this splitting occurs at 200 K when the sample was cooled by steps of 20 K where the sample was left at each step for several minutes until it reached a thermal equilibrium, and for the same sample splitting appears at 180 K (figure IV – 12) when it was cooled continuously

without any steps. Furthermore, dependence of space charge with temperature also affects the dc field influence on the splitting. Fig IV – 12(b) shows that the dc field enhances the amplitude of the split resonance at 180 K whereas it suppresses the resonance amplitude at 150 K. These facts emphasize the space charge effect which was created during the localization of K^+ ions at low temperature on the ferroelectric properties of KTP. The space charge is only an assumption up to this point and it needs further probing.

IV.3.4. Second Harmonic Generation Mapping:

In this section we probe the space charge with the help of second harmonic mapping technique. In second harmonic generation (SHG) the frequency ω of the incident light is doubled (2ω) or in other words the specific wavelength of the light is converted into half its original i.e. $\lambda_1 \rightarrow 1/2\ \lambda_1$.The optical response of a linear material is expressed in terms of the induced polarization P. For a linear material the relationship between the polarization and the electric field E of the incident radiation is linear. With high power source the induced polarization due to the large optical fields can be written as Taylor expansion.

$$P_i = \chi_{ij}E_j + \chi_{ijk}E_jE_K + \chi_{ijkl}E_jE_KE_l + .. \qquad \textbf{Eq IV-4}$$

Where χ_{ij} is the linear susceptibility, χ_{ijk} is the second order nonlinear susceptibility and χ_{ijkl} is the third order nonlinear susceptibility. An important point to note here is that, for $\chi_{ijk}$to be non zero the crystal structure should be non centrosymmetric whereas the odd linear $\chi_{ij}$and nonlinear χ_{ijkl} contributions are always active whatever the symmetry of the material. Note that for the specific case of a space charge in a material, the combination of the static electric field E_{DC} resulting from the space charge and the third-order nonlinearity χ_{ijkl} gives an effective second-order nonlinear contribution and this is given by the equation below

$$P_{2\omega} = \chi^2_{eff}(-2\omega;\omega,\omega)\cdot E^2(\omega) = [\chi^3(-2\omega;\omega,\omega,0)\cdot E_{Dc}]\cdot E^2(\omega) \qquad \textbf{Eq IV-5}$$

This contribution is currently called Electric Field Induced Second Harmonic (EFISH) and corresponds to an electro-optic Kerr effect (four waves mixing). Hence, for polar materials with χ_{ijk} it is possible to visualize 180° domains in a noncontact and non-destructive way, which has been considered unfeasible before the works of Uesu and co-workers on SHG microscope for ferroelectric domain observation [42] [43] [44]. The 180° domains which are optically equivalent were previously studied by acid etching which uses the difference in etching rates for domain characterization. However this destroys the quality of the sample making it inefficient for quasi phase matching applications. Below

we describe the μ-SHG microscope set up used to study the domains and domain walls and in this particular case for KTP we also use it to study the space charges.

IV.3.4.1. Second harmonic generation imaging set up:

In this nonlinear microscopy technique, an intense laser field induces a nonlinear polarization of the medium, confined to the focal center of the beam waist (depth of focus: DOF), resulting in the production of a wave at exactly twice the incident frequency. The interaction of collimated beams onto interfaces radiates coherent SHG in well-defined transmission and reflection directions. If we now intend to provide microscopic SHG images, the incident laser beam must be focused to a small spot size and the driving fields can no longer be considered as simple plane waves. The structure of the radiating SHG becomes critically dependent on the distribution of the input fields near the focal center. Thus, in focused beam the phases of the input fields play a crucial role: there is an axial phase shift of the focal field which is known as the Gouy phase shift. Since the phase of the excitation beam is phase-delayed by the Gouy shift close to the focal point, the axial effective incident wave vector is diminished and the phase-matching condition for SHG can be revised. Conservation of the transfer moment along the axial direction drives a coherent SHG signal within two well-defined off axis lobes with an angle θ peak that depends on many parameters [45] [46]. Since forward SHG is most intense than backward SHG because of the coherent nature of the process, SHG is most currently detected in the forward direction for imaging purposes using mirror scanning see eg. Chapter 5 of reference [47]. A main advantage of SHG microscopy is its unique capability to provide 3D images of the materials with micrometer resolution.

The micro-SHG setup we used for this study is based on a modified micro-Raman spectrometer (Horiba HR800) allowing the analysis of backscattered light. This original setup gives the opportunity to perform μ-Raman and μ-SHG to get a direct link between physical properties and local structure [48] [49] [50].

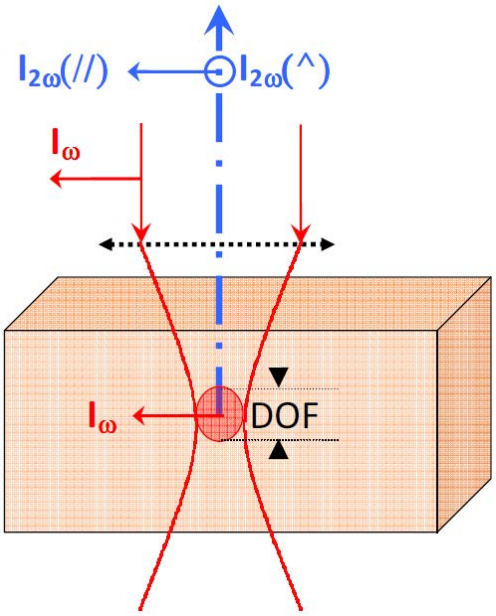

Figure IV-14: Orientation conventions for the backscattered parallel (//) and perpendicular (^) polarized light intensity $I_{2\omega}$ with respect to the incident light intensity I_{ω}. Note here that the depth of focus (DOF) corresponds to the axial resolution estimated to 2-3 µm using an 100X objective with NA=0.50

The source is a diode-pumped picosecond laser (EKSPLA PL2200: pulse duration 65 ps, repetition rate 2kHz) operating at λ=1064 nm focused at the surface of the sample with a NIR objective 100X (NA=0.50). The energy per pulse is adjusted by a power unit composed of a rotating half-wave plate in front of a GLAN Taylor prism and it can be tuned (from 10 µJ to less than 10 nJ) notably at low energy to avoid eventual sample photodegradation. The incident pulse power is monitored by a fast InGaAs photodiode for quantitative power calibration purposes. The measurement of the SHG intensity $I_{2\omega}$ can be realized using two different light polarization configurations, namely the dubbed parallel (//) and perpendicular (⊥) configurations, corresponding to incident and scattered lights with collinear or orthogonal polarizations respectively (Figure IV-14). Since the polarization of KTP is predominantly along z direction we used the // polarization configuration. The µ-SHG signal at high NA (NA > 0.50), i.e. the present experiment and that of Uesu et al will not give any phase information but only the magnitude of the polarization. Here, the lateral spatial resolution is estimated to be 0.5 µm from the far field resolution limit. The depth of focus was estimated to be ca. 2-3 µm. If the probed thickness is defined by the depth of focus (DOF) of the focused beam which is lower than the coherence length (L_c ~ 4-5µm for KTP along c axis) of the material (thin layer approximation where no oscillatory behavior is expected), the SHG intensity (I2ω) is related to the NLO susceptibility d_{eff} as follows.

$$(I_{2\omega}) \propto DOF^2 * (d_{eff})^2 * (I_{\omega})^2 \qquad \textbf{Eq IV-6}$$

IV.3.4.2. SHG mapping results on KTP:

It is important to have a reference sample without ionic conductivity to compare with KTP. For that purpose reduced $BaTiO_3$ (BTO) single crystals was chosen. Generally $BaTiO_3$ does not have any ionic conductivity however reduced BTO have electronic conductivity. Now it will be interesting to probe Fe doped BTO for any space charge and then compare it with KTP. Figure VI -15 (b & c) gives the 2D SHG map of the cross section shown in figure (a) at room temperature for BTO single crystals. The dark lines seen in fig (a) is due to domain walls. It can be seen from xz cross-sectional SHG image (surface map) that domain walls appear dark (figure IV – 15 (b)). This is because the domain walls cancel the polarization component from each domain and therefore no SHG signal is generated at the domain walls. Within the domains there is considerable SHG intensity due to the polarization of the domains. The xy cross-sectional SHG image (depth map) obtained after rotating the sample to 45° clearly show that there are no space charge layer at the surface since the SHG intensity at y =0 μm (top surface of the material) is very low compared to the two bright spots at y = 70 μm (see figure IV – 15 (c)). It can be safely assumed that the two bright spots are due to the polarization of the domains which are parallel to the polarization of the incident light. Since both the surface (xz) and depth (xy) maps are available it is possible to construct domain wall orientation within the bulk and it is shown as a schematic in figure IV – 15 (d). Here the red double headed arrow represents the laser light polarization direction; blue arrows show the domains with polarization perpendicular to the initial laser polarization. They do not give any SHG signal however the domains which have polarization parallel to the laser's represented as circles display strong SHG signal seen as two bright spots. However the sign of polarization cannot be determined here since this SHG signal does not contain any phase information.

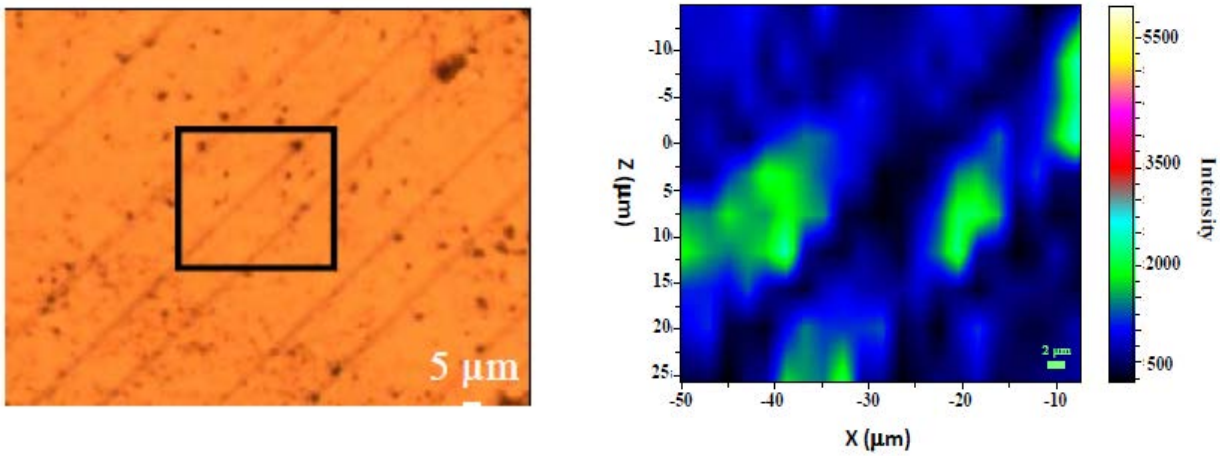

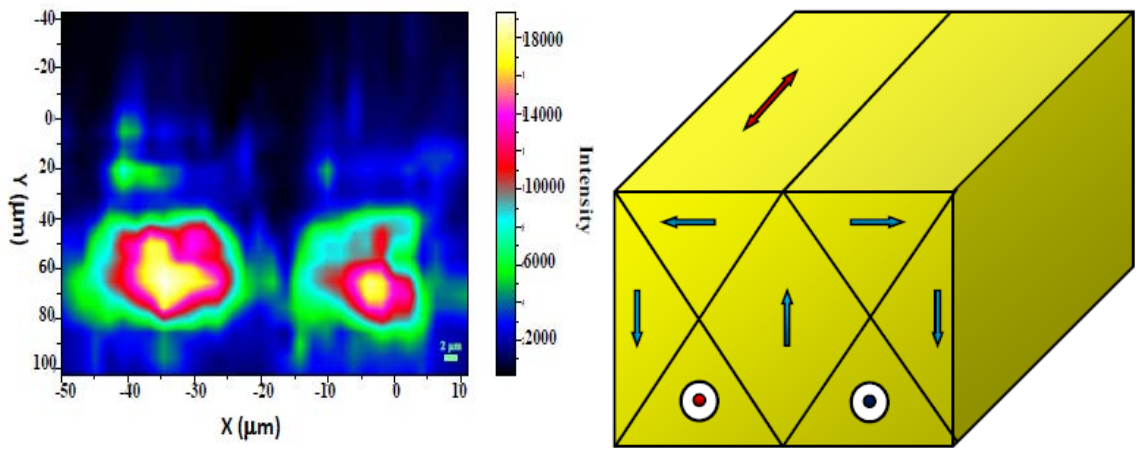

Figure IV-15: (b) & (c) gives the xz and xy SHG map for the cross section shown in (a) for $BaTiO_3$ single crystals. (d) Gives the schematic of the domain wall orientation within the bulk interpreted from (b) & (c). Red arrow here represents the incident laser polarization direction. Circles represent domain with polarization parallel to the incident laser.

Similarly KTP single crystals were probed with μ-SHG to identify the space charge. The orientation of the single crystal is shown in fig IV – 16(a). Here the laser is passed along y-direction and then scanned to obtain xy (depth) or xz (surface) map. Fig IV – 16 (b – e) gives the xz cross-sectional SHG map of KTP single crystals 10 μm below the surface (z = 0) at different temperatures. The excitation and response fields are oriented along z since we aim to probe the ionic conductivity (space charge). It can be seen from the figures that with decrease in temperature SHG intensity decreases and at 170 K the SHG intensity is low. This is in agreement with previous results that conductivity decreases drastically and below 200 K, KTP behaves as an insulator as seen from resistance measurements. When the conductivity is higher, the potassium ions are mobile and they tend to localize at the surface which gives rise to high SHG signal at the surface. It is also important to perform in depth SHG map to see the space charge layer if any due to localization of potassium close to the surface. Figure IV – 17 (a – d) shows the xy (depth map) cross-sectional SHG image for the same KTP single crystal and at the same spot. Remarkably at room temperature the SHG intensity is very high close to the surface and below y = 40 μm there is no SHG signal indicating that the bulk SHG intensity is much lower than the one at the surface of the sample. This is in contrast to BTO single crystals which did not show any space charge layer at the surface (see fig IV – 15 (c)). The very low SHG signal within the bulk indicates that the structural second-order response (bulk response) is at least two order of magnitude lower than the effective EFISH response which is the product of the third order non linearity (χ^3), expected to be high in that material, and the embedded electric field due to the space charges. Since the third order non linearity (as the 2nd- order one) is expected to be homogeneous in the crystal, the SHG maps reveal the distribution of the square of the amplitude of the electric field where we can see hot points notably at room temperature, indicating large inhomogeneity of the distribution of K^+ in the crystal.

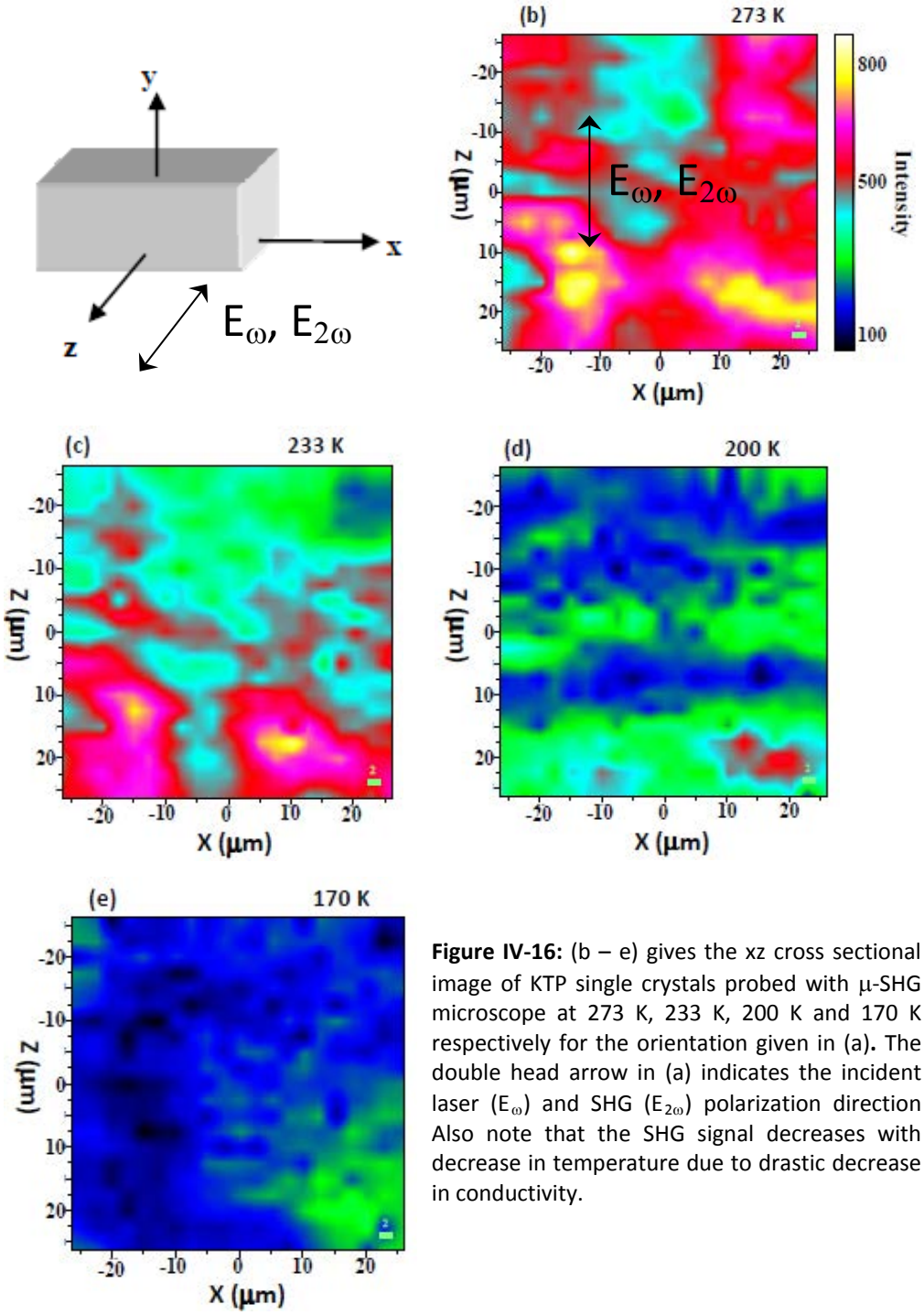

Figure IV-16: (b – e) gives the xz cross sectional image of KTP single crystals probed with μ-SHG microscope at 273 K, 233 K, 200 K and 170 K respectively for the orientation given in (a)**.** The double head arrow in (a) indicates the incident laser (E_ω) and SHG ($E_{2\omega}$) polarization direction Also note that the SHG signal decreases with decrease in temperature due to drastic decrease in conductivity.

The space charge layer in KTP is about 20 to 30 μm at the surface. It is difficult to interpret the effect of temperature on the intensity of SHG from the images. Nevertheless it can be seen immediately by plotting the corresponding profile of SHG for all the temperatures close to the surface. Figure IV – 18 shows the profile of average SHG intensity along y direction (depth) obtained from the xy cross-sectional images shown in figure IV – 17. The SHG intensity at the surface i.e. y = 0 μm is high for all temperatures and width of the peak gives the thickness of the space charge layer. At room temperature the SHG intensity is high and at 233 K it reaches a minimum. This minimum coincides

exactly with the decrease in conductivity which starts to happen at this temperature range. At 200 K and 170 K the SHG intensity increases again, this can be explained on the basis of intrinsic polarization of KTP which becomes more pronounced at low temperatures as seen from the pyroelectric measurements. . Here it is worth noting that at those optical frequencies of the fundamental and harmonic waves 1064-532 nm, SHG is sensible to electronic fluctuations (in the range of fs to ps) mostly due to the Ti-O bonds (fs range) in KTP. These electronic fluctuations relate not only the instantaneous electronic polarization but also fluctuations of nucleus motions (ps range) that induce also electronic fluctuations as it happens in Raman scattering for example. Then, the overall high EFISH intensity at the surface is a consequence of the static inhomogeneous distribution of potassium ions (static space charge) but also of their dynamical hopping (dynamical contribution not solved at optical frequencies) which give rise to electron density fluctuation. This kind of static space charge layer due to migration of ions has been observed even in glasses [48].

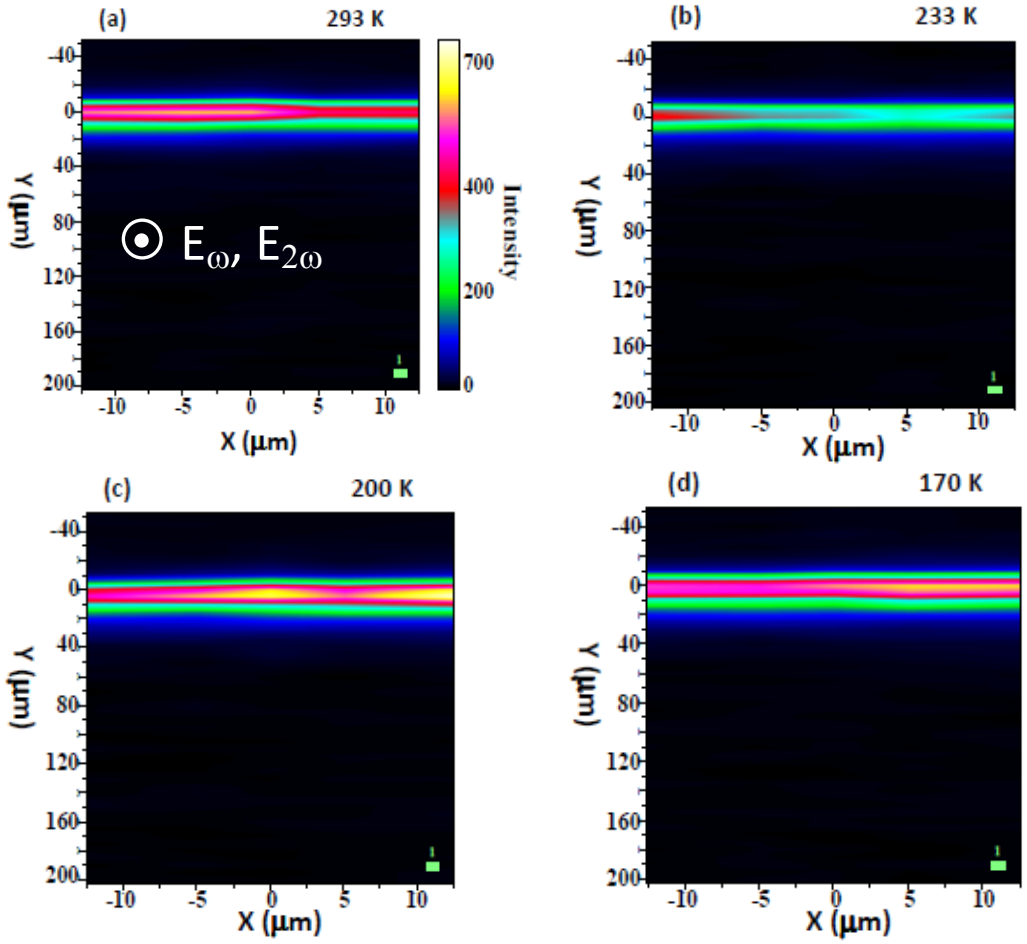

Figure IV-17: xy (depth map) cross-sectional SHG image for the same KTP single crystals used in fig IV – 16 at different temperatures. Note the high SHG intensity at the surface i.e. y = 0 μm indicating space charge layer.

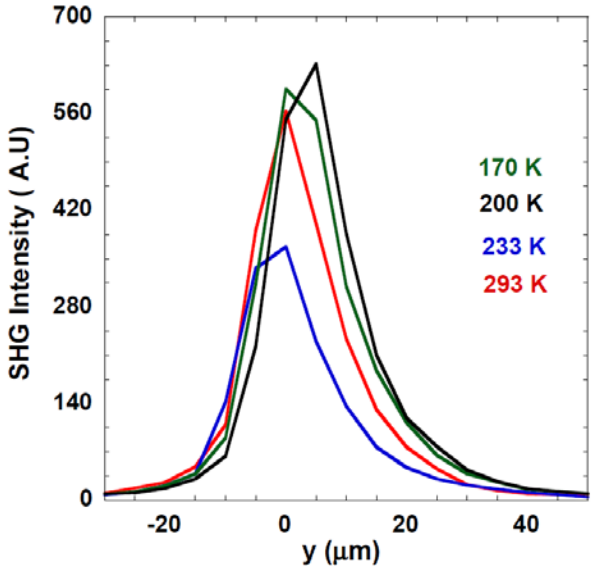

Figure IV-18: The profile of average SHG intensity along y direction (depth) obtained from the xy cross-sectional images shown in fig IV – 17.

Similar experiment was done on periodically poled KTP (PPKTP). In PPKTP the domains are arranged in regular and alternative fashion. All the domains are oriented parallel to z direction since it is the principal polarization direction. It is also interesting for nonlinear optics as PPKTP are often used for quasi phase matching. The orientation of the PPKTP for μ-SHG mapping is the same as fig IV – 16 (a). Fig IV – 19 (a – d) gives the xz cross-sectional SHG image of PPKTP at several temperatures. Images reveal regular domains and domain walls. In PPKTP domains are reversed alternatively but it appears same in the images because backscattered SHG signal does not contain phase information. Domain walls appear dark due to the local cancellation of polarization. Fig IV – 19 (e) shows the profile of average SHG intensity along x direction obtained from fig (a – e). The regular drop in SHG intensity represents domain walls and the distance between them gives the width of the domain and it is about 17 μm. At 333 K the SHG intensity is very low showing apparent contradiction to the expectation. This drop down of effective SHG at high temperature may be triggered by a loss of spatial extent of the static/dynamic space charge. However further experiments and detailed investigation is needed to clarify our hypothesis.

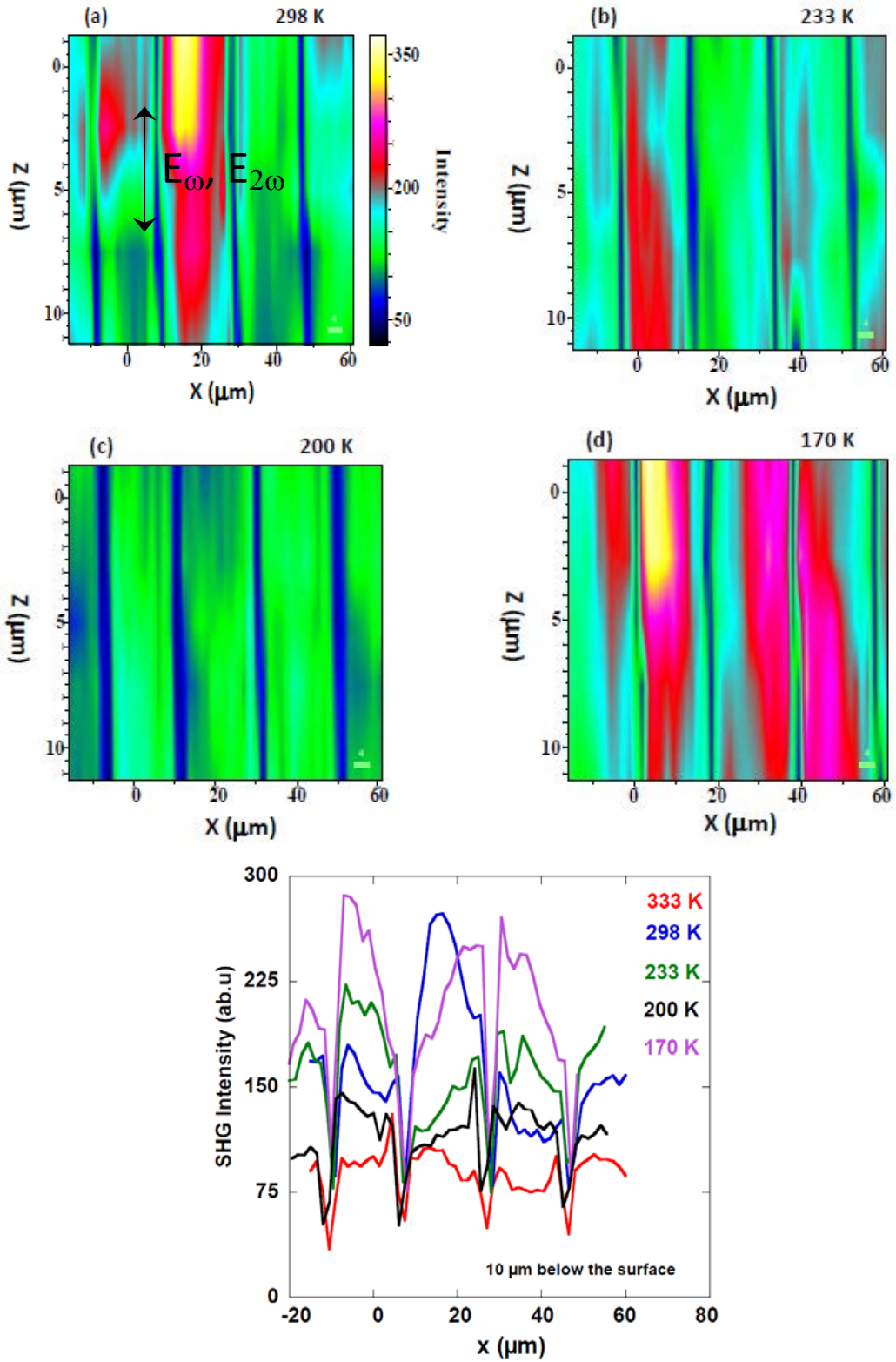

Figure IV-19: (a – d) xz cross-sectional SHG image of PPKTP at different temperatures with the orientation of the crystal same as fig IV – 17 (a). Fig (e) gives the profile of average SHG intensity along x direction obtained from images (a – d). The sharp drop in intensity represents domain walls and the distance between them gives the width of the domains.

Below 333 K the trend similar to the one observed in normal KTP (i.e. with decrease in temperature SHG intensity decreases and it reaches a minimum after which it increases again) was observed in

PPKTP. However the temperature of the minimum in normal KTP (233 K) is different from PPKTP (200 K). Infact it was found that the minimum temperature changes with thermal cycling of the sample indicating that the SHG intensity at the surface is due to space charge layer at the surface of the sample.

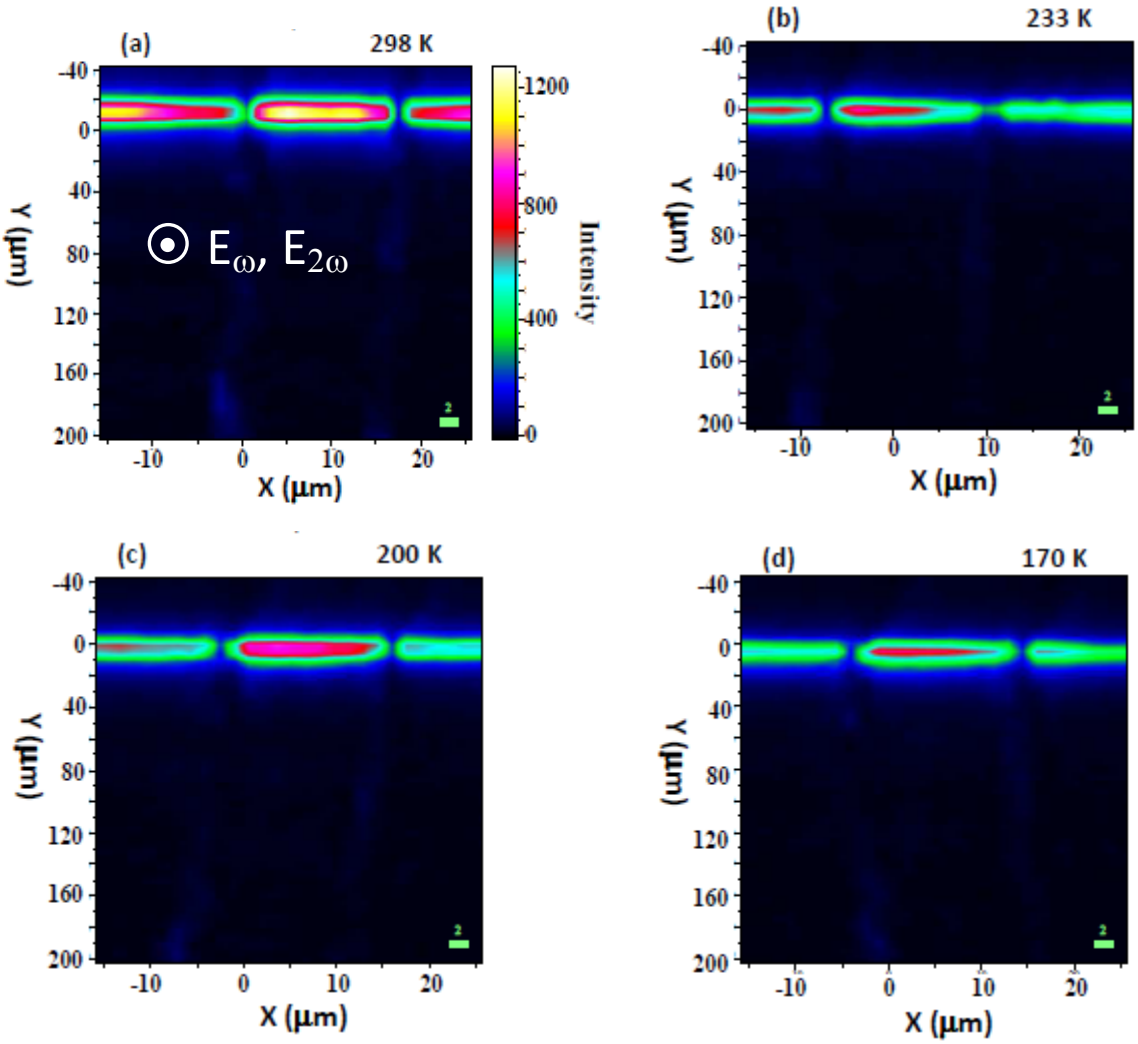

Figure IV-20: (a – d) presents the xy (depth) cross-sectional SHG image for PPKTP at different temperatures. Both the domains and domain walls are clearly seen along with the space charge layer at the surface.

The space charge layer is formed due to the localization of potassium ions at the electrode-sample interface. In PPKTP we have domain walls which can also act as an interface. To probe whether there is any localization of potassium ions at the domain walls, in depth μ-SHG mapping has been done. Fig IV – 20 (a – d) shows the xy (depth map) cross-sectional SHG image of PPKTP at different temperatures. Resembling normal KTP, PPKTP also display space charge layer at the surface y = 0 μm. In addition both domain and domain walls can be clearly seen. The SHG intensity inside the domains is maximum whereas at the domain walls it is minimum for reasons explained previously. Remarkably it can also be seen that there is some SHG intensity within the bulk at the domain walls seen as blue

lines in the images in contrast to normal KTP where the SHG intensity within the bulk is very low. This can be immediately seen by plotting the profile of the SHG intensity along a line parallel to y direction at the domain walls for all temperatures (figure IV – 21 (a)). There is a large SHG intensity close to the surface and within in the bulk the intensity is low however small peaks are visible at 40 and 120 μm inside the bulk (i.e. along y direction). These peaks may be due to the strong fluctuations or inhomogeneities at the domain. The profile obtained by plotting SHG intensity along a line passing through the center of the domains shows that the SHG intensity within the domain is much larger in comparison to the domain walls (see figure IV – 21 (b)). Furthermore no peaks within the bulk are visible since there are no interfaces inside the domain for the potassium to localize. The SGH intensity at the surface is higher at room temperature and decreases with temperature. This is in agreement with the previous results in normal KTP.

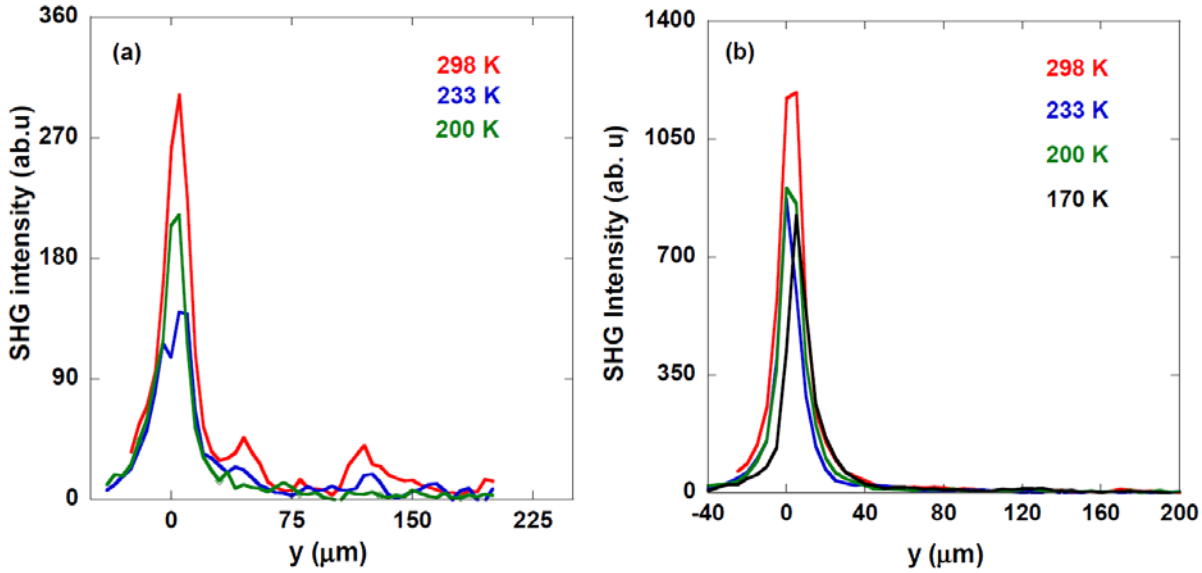

Figure IV-21: (a) The profile of SHG intensity along y direction at the domain walls and (b) the profile of SHG intensity along y direction for a line passing at the center of domains. Both the profiles are drawn for the SHG images shown in fig IV – 20.

IV.3.5. Conclusion:

We have shown that the mechanical resonances of KTP single crystals undergo a well-defined splitting at about 200 K, which corresponds to the temperature where the ionic conductivity ends and pyroelectric currents as well as birefringence start to increase. This splitting of the piezoelectric resonance occurs for many crystal orientations and resonance modes whatever the ferroelectric domain state is. In most of the cases, it is observed when the probing ac voltage is applied parallel to the c-axis, which is the main path for the ionic conductivity. We ascribed the splitting to the building up of ionic space charges in the single crystal. We thus suggest that the piezoelectric resonance is relevant parameter in order to track the space charge as a function of several external stresses using

a very small applied voltage which is not perturbing the spontaneous balance between the ferroelectric polarization and the ionic conductivity in KTP, which is maybe true in other ferroelectric ionic conductors. The space charge creation was then probed with the help of μ-SHG microscope in reflection mode on normal and periodically poled KTP. This clearly revealed the localization of potassium ions at the surface and creates space charge. This was compared with the BTO single crystals were no such space charge was evidenced. We thus conclude that the ionic mobility of potassium is the major factor behind the development of space charge in KTP confirming the results by piezoelectric measurements. We also demonstrated that domain walls can also act as an interface for the potassium ions to localize in PPKTP. From μ-SHG images other useful information such as width of the domains and domain walls can be obtained. Therefore this technique is a powerful to probe space charges as well domain characterization.

IV.4. References:

[1] F. G. Zumsteg, J. D. Bierlein, and T. E. Gier. *J. Appl. Phys*, 47:4980, 1976.

[2] V.I.Voronkova and V.K. Yanovskii. *Neorg. Mater*, 24:2062, 1988.

[3] I. Trodjman, R. Masse and J-C. Guitel. *Z. Kristallogr*, 139:103, 1974.

[4] N.I. Soronkina and V.I. Voronkova. *Crystallogr. Rep*, 52:80, 2007.

[5] P.A. Morris, A.Fretti, J.D. Bierlein and G.M. Loiacono. *J. Cryst. Growth*, 109:367, 1991.

[6] N.Angert, M. Tseitlin, E. Yashin and M. Roth. *App. Phys. Lett*, 67:1941, 1995.

[7] J.D. Bierlein and C.B. Arweiler. *Appl. Phys. Lett*, 49:917, 1986.

[8] V.K. Yanovskii and V.I. Voronkova. *Fiz. Tverd. Tela*, v:2183, 1985.

[9] V.A. Kalesinkas, N.I. Pavlova, I.S. Rez and I.P. Grigas. *Lit. Phys. Papers*, 22:87, 1982.

[10] V.K. Yanovskii and V.I. Voronkova. *Phys. Stat. Sol A*, 93:665, 1986.

[11] S. Furusawa, H. Hayasi, Y. Ishibashi, A. Miyamoto and T. Sasaki. *Jou. Phy. Soc. Jpn*, 62:183, 1993.

[12] P. Urenski, N. Gorbatov and G. Rosenman. *J. Appl. Phys*, 89:1850, 2001.

[13] P.A.Thomas, A.M.Glazer and B.E.Watts. *Acta. Crystallogr. Sec B: Struc. Sci*, 46:333, 1990.

[14] V.I. Voronkova, S.Yu. Stefanovic and V.K. Yanovskii. *Kavantovaya Elektron*, 15:752, 1988.

[15] W.T.A. Harrison, T.E. Gier, G.D. Stucky and A.J. Schultz. *J. Chem . Soc: Chem. Comm*, 7:540, 1990.

[16] W.T.A. Harrison, T.E. Gier, G.D. Stucky and A.J. Schultz. *Mat. Res. Bull*, 30:1341, 1995.

[17] L. Belokoneva, F.M. Dolgushin, M.Y. Antipin, B.V. Mill, Y.T. Struchkov. *Rus. J. Inorg. Chem*, 38:584, 1993.

[18] M.Yashima and T. Komatsu. *Chem Comm*, page 1070, 2009.

[19] J.H. Park, B.C. Choi, J.B. Kim. *Sol. Stat. Comm*, 130:533, 2004.

[20] J. Birelein and H. Vanherzeele. *J. Opt. Soc. Am. B*, 6:622, 1989.

[21] M.M. Fejer L.M. Myers, R.C. Eckardt and R.L. Byer. *J. Opt. Soc. Am. B*, 12:2102, 1995.

[22] J. Armstrong, N. Blombergen, J. Ducuing and P. Pershan. *Phys. Rev*, 127:1918, 1962.

[23] P. Urenski, M. Lesnykh, Y. Rosenwaks, G. Rosenman and M. Molotskii. *J. Appl. Phys*, 90:1950, 2001.

[24] C. Canalias. *Domain engineering in KTiOPO4*. PhD thesis, Royal Institute of Technology, Stockholm, Sweden, 2005.

[25] C. Canalias, V. Pasiskevicius, R. Clemens, and F. Laurell. *App. Phys. Lett*, 82:4233, 2003.

[26] R. Scripsick, M. Stolzenbergerand. *Proc. SPIE*, 3610:23, 1999.

[27] J.D. Bierlein and F. Ahmed. *Appl. Phys. Lett*, 51:1322, 1987.

[28] I.M. Sil'vestrova, V.A. Maslov, and Yu.V. Pisarevskii. *Sov. Phys. Crystallogr*, 37:660, 1992.

[29] D.K.T. Chu, J.D. Bierlein and R.G. Hunsperger. *IEEE. Trans. Ultrason. Ferroelect. Freq. Control.*, 39:683, 1992.

[30] H. Graafasma, G. W. J. C. Heunen, S. Dahaoui, A. EL Haouzi, N. K. Hansen and G. Marnier. *Acta. Cryst.*, B53:565, 1997.

[31] *IEEE Standards on Piezoelectricity, Trans. On Sonics and Ultrasonics, SU 31, 2 Part II, (1984) and 176, 1987*.

[32] P. Urenski, G. Rosenman. *J. Phys. D: Appl. Phys*, 33:2069, 2000.

[33] S. Dahaoui, N.K. Hansen, J. Protas, H.G. Krane, K. Fischer and G. Marnier. *J. Appl. Crys*, 32:1, 1999.

[34] R. Coelho. *Physics of Dielectrics for the Engineer*. Elsevier Scientific Publishing Company, 1978.

[35] Q. Jiang, M.N. Womersley, P.A.Thomas, J.P. Rourke, K.B. Hutton and R.C.C. Ward.. *Phy. Rev. B*, 66:094102, 2002.

[36] K. Noda, W. Sakamoto, T. Yogo and S. Hirano. *J. Mat. Sci. Let.*, 19:72, 2000.

[37] Yu. V. Shaldin and R. Poprawski. *J. Phys. Chem. Solid.*, 51:101, 1990.

[38] G. Rosenman, A Skliar, D. Eger, M. Oron and M. Katz.. *Appl. Phys. Lett.*, 73:3650, 1998.

[39] V.D. Antsigin, V.A. Gusev, V.N. Semenenko and A.M. Yurkin.. *Ferroelectrics*, 143:223, 1993.

[40] J.B. Joyce and T.M.Hayes. *Physics of Superionic Conductors, edited by M.B. Salamon*. Springer, New York, 1979.

[41] R.V. Pisarev, S.A. Kizhaev, J.P. Jamet and J. Ferré. *Sold. Stat. Comm.*, 72:155, 1989.

[42] Y. Uesu, S. Kurimura, and Y.Yamamoto. *Ferroelectrics*, 169:249, 1995.

[43] Y.Uesu, S. Kurimura, and Y.Yamamoto. *Appl.Phys.Lett*, 66:2165, 1995.

[44] S. Kurimura, Y. Uesu. *J. Appl. Phys*, 369:81, 1997.

[45] L. Moreaux, O. Sandre, J.Mertz. *J. Opt. Soc. Am. B.*, 17:1685, 2000.

[46] J. Mertz, L. Moreaux. *Opt. Comm*, 196:325, 2000.

[47] V. Rodriguez T. Verbiest, K. Clays. *Second-Order nonlinear optical caharacterization techniques: An Introduction,*. CRC Press, Taylor & Francis Group, 2010.

[48] M. Dussauze, V . Rodriguez, A. Lipovskii, M. Petrov, C. Smith, K. Richardson, T. Cardinal, E. Fargin, E.I.Kamitsos. *J. Phys. Chem.C*, 114:12754, 2010.

[49] V. Rodriguez, D. Talaga, F. Adamietz, J.L. Bruneel, M. Couzi. *Chem. Phys. Lett*, 190:431, 2006.

[50] H. Vigouroux, E. Fargin, S. Gomez, B. Le Garrec, G. Mountrichas, E. Kamitsos, F. Adamietz, M. Dussauze, V. Rodriguez,, E. Fargin. *Adv. Func. Mater.*, 2012.

Chapter 5

V. Synthesis, Structure determination and characterization of new phosphates

V.1. Introduction:

In the previous chapter we have established a clear link between the ionic conductivity and polarization of $KTiOPO_4$. Furthermore some phosphates like $LiCOPO_4$, $LiNiPO_4$ have been found to show interesting multiferroic behaviour [1] [2] [3]. Motivated by this we chose to investigate Nasicon (Sodium (Na) Super (S) Ionic (I) Conductor (Con)) type phosphates since they can accommodate vast number of cations into their structure and also show interesting magnetic property. However no spontaneous polarization has been found in this type of phosphates yet. Our goal is to synthesize new phosphates of Nasicon type structure looking for ferroelectricity along with interesting magnetic property.

To this aim we have decided to synthesize phosphates of formula $BaFeTi(PO_4)_3$ and $BiFe_2(PO_4)_3$ which is derived from well-known Nasicon type phosphate $Na_3Fe_2(PO_4)_3$. The reason for substitution of barium and bismuth in place of sodium is twofold. First, bismuth due to its lone pair ($6s^2$) electrons may induce ferroelectricity similar to $BiFeO_3$. Second, ionic radius of barium is big compared to sodium therefore conductivity of barium substituted compound is anticipated to be much lower than NFP which otherwise may screen the polarization if there is any.

The general formula of Nasicon composition can be written as $AM_1M_2P_3O_{12}$ where the site 'A' can be occupied by alkali ions (Li^+, Na^+, K^+, Rb^+ and Cs^+), alkali earth ions (Mg^{2+}, Ca^{2+}, Sr^{2+} and Ba^{2+}), Cu^+, Ag^+, Pb^{2+}, Cd^{2+}, Mn^{2+}, CO^{2+}, Ni^{2+}, Zn^{2+}, Al^{3+}, Ln^{3+} (Ln = rare earth), Ge^{4+}, Zr^{4+}, Hf^{4+} or it can also be vacant. The M_1 and M_2 sites can be occupied by divalent cations (Zn^{2+}, Cd^{2+}, Ni^{2+}, Mn^{2+}, Co^{2+}), trivalent cations(Fe^{3+}, Sc^{3+}, Ti^{3+}, V^{3+}, Cr^{3+}, Al^{3+}, In^{3+}, Ga^{3+}, Y^{3+}, Lu^{3+}), tetra valent cations (Ti^{4+}, Zr^{4+}, Hf^{4+}, Sn^{4+},Si^{4+}, Ge^{4+}) and penta valent cations (V^{5+}, Nb^{5+}, Ta^{5+}, Sb^{5+}, As^{5+}) [4]. This shows that Nasicon framework is highly flexible and can accommodate different cations in different atomic sites. The Nasicon structure was first described by Hagman et al for the phosphate $NaZr_2(PO_4)_3$ (NZP) which has a trigonal symmetry belonging to the space group $R\bar{3}c$ [5]. Alamo et al. have studied NZP structure in detail and proposed a model concerning the accommodation of different valence cation in to the structure [6]. According to them the skeleton is made up of PO_4 tetrahedra and ZrO_6 octahedra that share vertices so the bonds are strong and stable. These bonds while inserting a cation can bend and therefore the polyhedral shows small rotations without breaking the structure. When the phosphate

group rotates the chains along c-axis move closer and so the structure contracts in a direction and the zirconium octahedra rotate alternatively as shown in Fig V -1. Hong et al found that by substituting Si^{4+} for P^{5+} in NZP, the structure exhibits super ionic conductivity [7]. They also showed that how structure can suffer a monoclinic distortion without breaking any bonds. For the present thesis however we are concerned only with $Na_3Fe_2(PO_4)_3$ since it is directly related to the phosphate of our interest. Understanding of its structure and property will make the understanding of $BaFeTi(PO_4)_3$ and $BiFe_2(PO_4)_3$ easier.

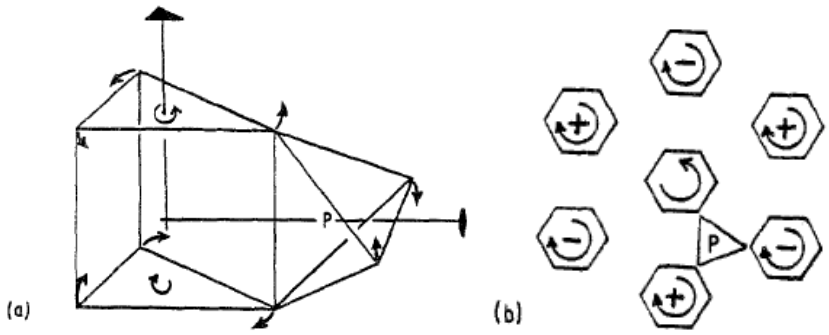

Figure V-1: (a) & (b) Rotation of PO_4 tetrahedra and ZrO_6 octahedra in NZP. This rotations lead to change in lattice parameters. Adapted from ref [6]

$Na_3Fe_2(PO_4)_3$ (NFP) was first synthesized by Pintard –Scrépel et al as well as Delmas and coworkers [8] [9]. It has been shown by different methods that with increasing temperature there are two structural phase transition in NFP [10] [11]. The α phase corresponds to monoclinic distortion of the rhombohedral structure with space group C2/c and lattice parameters a = 15.13 Å, b = 8.72 Å, c = 8.80 Å and β = 125.16° [12]

$$\boldsymbol{\alpha \xrightarrow{368\,K} \beta \xrightarrow{418\,K} \gamma - Na_3Fe_2(PO_4)_3}$$

The γ phase corresponds to hexagonal axes in rhombohedral symmetry with space group $R\bar{3}c$ and lattice parameters a = 8.73 Å, c = 21.79 Å [10]. The monoclinic distortion in the α phase is due to the direct consequenc of PO_4 tetrahedra distortions caused by regular but asymmetrical distribution of sodium ions on the sites surrounding the tetrahedral.

The distribution of ions and vacancies in the sodium sublattice has a long range order in the monoclinic phase. In fact the monoclinic phase can be described in the pseudo-hexagonal cell with lattice parameters a' = 8.73 Å, c' = 21.57 Å, β' = 90.14°, γ' = 120.07°. Fig V – 2 (a –b) shows the monoclinic and rhombohedral structure of NFP. The structure of NFP consists of the basic $Fe_2(PO_4)_3$ repeating unit called as 'lantern' which is made of three PO_4 tetrahedra connected to two FeO_6

octahedra. Each of these lanterns is connected to six other lanterns which generate a large interstitial space that accommodates sodium ions. The sodium ions sits in two distinct sites named Na1 and Na2. Na1 sits in an octahedral coordination forming infinite ribbons of O_3FeO_3 – Na1 – O_3FeO_3 parallel to c-axis and connected by PO_4 tetrahedra. The Na2 is situated between the ribbons and it is 8 coordinated [13]. The occupation factor for Na1 and Na2 sites are 1 and 2/3 respectively.

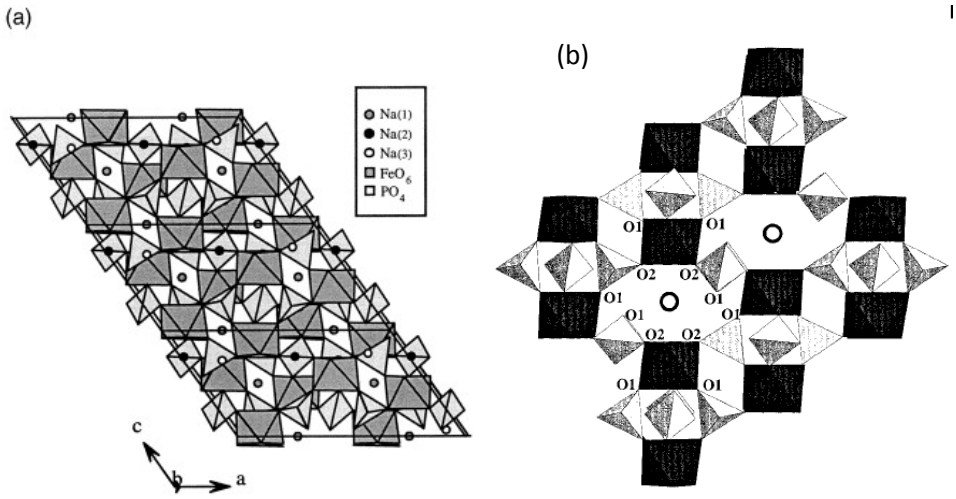

Figure V-2: (a) α monoclinic phase and (b) γ rhombohedral phase of $Na_3Fe_2(PO_4)_3$ along [0 0 1] direction. Adapted from reference [14] [12]**.**

The partial occupation of Na2 site is the major factor determining the Na^+ mobility [15]. The transfer of Na^+ ions in the Na1 site to Na2 sites through the bottleneck is aided by the partial occupation at the Na2 site. At low temperatures distributions of Na^+ ions is ordered which lead to low conductivity. As the temperature is increased the allotropic transformations lead to disorder in the structure and the conductivity increases [13]. The magnetic susceptibility measurements on NFP have been done by several researchers which show a para to antiferromagnetic transition at a Neel temperature (T_N) of 47 K with a weak ferromagnetic moment due to spin canting [16] [17] [18] [19]. The magnetic structure obtained from the neutron diffraction on the monoclinic cell indicated that the spins lying on the ab plane at 29° from the 'a' axis direction with a magnetic moment of 2.9 μ_B [18] but the study by Greaves et al assuming rhombohedral symmetry indicates antiferromagnetic arrangement of Fe moments aligns at 42° to the hexagonal c-axis with the moment of 4.5 μ_B [19]. A recent study of NFP gave an effective moment of 5.95 μ_B [20] which is close to the already reported 5.84 μ_B in ref [17]. This value of effective magnetic moment agrees with the theoretical calculated value of 5.91 μ_B.

In the following we will describe the synthesis, structural and physical properties characterization of $BaFeTi(PO_4)_3$ and $BiFe_2(PO_4)_3$.

V.2. Experimental:

V.2.1. Synthesis of $BaFeTi(PO_4)_3$ and $BiFe_2(PO_4)_3$:

Solid state reaction was adopted to perform synthesis of the desired phosphate. Stoichiometric ratio of $BaCO_3$ (Cerac, 99.9 %), TiO_2 (Cerac, 99.9 %), Fe_2O_3 and $(NH_4)_2HPO_4$ (Sigma Aldrich, > 99.0%) were taken and mixed thoroughly in the agate mortar for $BaFeTi(PO_4)_3$ (BFTP). Fe_2O_3 was prepared by heating iron nitrate at 450°C for 5 hrs to remove nitrogen and water. The XRD pattern of the resulting powder was identical to pure Fe_2O_3. A 2% excess of $(NH_4)_2HPO_4$ was added to the starting mixture due to the unavoidable presence of water in $(NH_4)_2HPO_4$. The mix was then put in a 3D planetary mill along with ethanol to form uniform slurry. The slurry was then placed in an oven and maintained at a temperature of 110°C for 12 hrs to remove ethanol and water. The resulting mixture was progressively heated under air to 400°C, 600°C and 1000°C for 15 hrs with intermediate grinding. The synthesis conditions were same as the Nasicon $Na_3Fe_2(PO_4)_3$ [21]. The reaction mechanism is given in the following

$$\mathbf{BaCO_3} + \left(\frac{\mathbf{1}}{\mathbf{2}}\right)\mathbf{Fe_2O_3} + \mathbf{TiO_2} + \mathbf{3(NH_4)_2HPO_4} \rightarrow \mathbf{BaFeTi(PO_4)_3} + \mathbf{CO_2} \Uparrow + \mathbf{6NH_3} \Uparrow + \left(\frac{\mathbf{9}}{\mathbf{2}}\right)\mathbf{H_2O} \Uparrow$$

The first two steps ensure the removal of water, ammonium and carbon dioxide and the phase forms at 1000°C. The final powder is white in color. It was then pelletized and then fired again at 1050°C for sintering. The sintered pellet was slightly pale due to oxidation. These sintered pellets were used for dielectric measurements.

For $BiFe_2(PO_4)_3$ (BiFP) stoichiometric ratio of Bi_2O_3 (Cerac, 99.999%), Fe_2O_3 and $(NH_4)_2HPO_4$ (Sigma Aldrich, >99.0%) were taken. The mixing procedure same as that of BFTP was followed and then the resulting mixture was progressively heated under air to 400°C, 600°C and 975°C for 15 hrs with intermediate grinding. The reaction which takes place during the heat treatment is shown below.

$$\left(\frac{\mathbf{1}}{\mathbf{2}}\right)\mathbf{Bi_2O_3} + \mathbf{Fe_2O_3} + \mathbf{3(NH_4)_2HPO_4} \rightarrow \mathbf{BiFe_2(PO_4)_3} + \mathbf{6NH_3} \Uparrow + \left(\frac{\mathbf{9}}{\mathbf{2}}\right)\mathbf{H_2O} \Uparrow$$

For all the temperature steps the heating rate was 2°C min^{-1}. After the final heat treatment the sample was quenched in air to room temperature. The final powder was pale white in color. It was then pelletized by uniaxial pressing and then fired at 1000°C for sintering. The sintered pellet was red in color.

V.2.2. X-ray powder diffraction measurements:

X-ray powder diffraction patterns were measured with a Philips Xpert diffractometer using Bragg-Brentano geometry with $CuK\alpha_1$ and $CuK\alpha_1$-α_2 radiations. The X-ray data were collected in the 2θ range from 10° to 120° with a step of 0.02°. The X-ray diffraction data were refined by a Le Bail

Profile analysis [22] using the FULLPROF program package [23]. The background was estimated by a Legendre polynom and the peak shapes were described by a Pseudo-Voigt function varying five profiles coefficients. For Rietveld refinement, X-ray powder diffraction patterns were measured with PANalitycalX'pert MPD Bragg-Brentano θ-θ geometry diffractometer equipped with a germanium monochromator which ensures a perfect monochromatic radiation and a spinner over an angular range of 2θ = 10-130°. The generated Cu Kα radiation had a wavelength of $\lambda = 0.15418$ nm.

V.2.3. Physical property measurements:

The sintered pellets were gold sputtered to make electrodes and thin silver wires were glued to the electrodes with the help of silver paste to make electrical contacts. The sample was put in the sample holder of Physical Property Measurement System (PPMS) Quantum Design which was then connected to the Wayne Kerr 6500B impedance/gain phase analyzer operating in the range of 100 Hz to 10 MHz for frequency dependent measurement. PPMS can regulate temperature from 2 K to 380 K and magnetic field upto 90 kOe or 9 Tesla. Magnetic measurements on the samples were done using Magnetic Property Measurement System (MPMS) Quantum Design. This instrument can reach upto 50 kOe (or 5 Tesla) in magnetic field and temperature in the range of 1.8 K to 400 K. The same set up can be used to perform hysteresis and ac magnetic measurements as well. Heat capacity measurements were performed by a relaxation method with the PPMS and using two tau model analysis. Data were taken in the temperature range 2 – 90 K. For these measurements samples were a plate obtained from compressing the powder samples.

V.3. Results and discussion:

V.3.1. Crystal structure determination of $BaFeTi(PO_4)_3$ using powder diffraction:

The first step in determining the crystal structure of a new phase is to identify space group and for that we used TREOR software which gave us a solution without any extinction conditions on hkl indices. The profile matching was performed with this space group. Since the suggested space group is very general without any reflection conditions all the peaks could be indexed. Therefore it is necessary to check for other space groups by studying the observed peaks and the extinction conditions. Careful examination of the hkl indices shows that the Bravais lattice is rhombohedral. It is also noted that the conditions on h-h0l; l=2n. Then the possible space group is $R\bar{3}c$ which is the usual space group for NASICON structure. The compound $BaFeTi(PO_4)_3$ was first synthesized by Masse in 1972 and indexed the XRD pattern in the rhombohedral space group $R\bar{3}c$ [3]. He gave the XRD pattern only from 0 - 58° 2θ. Figure V-3 gives the profile matching of the XRD pattern with the space

group $R\bar{3}c$ with initial lattice parameter taken from [3]. Most of the peaks match the pattern given by Masse but there are two additional peaks observed at 19.5° and 22.7° in the 2θ region which does not match with the pattern given by Masse. But these peaks were profile matched within the same space group (see inset to figure V-3).

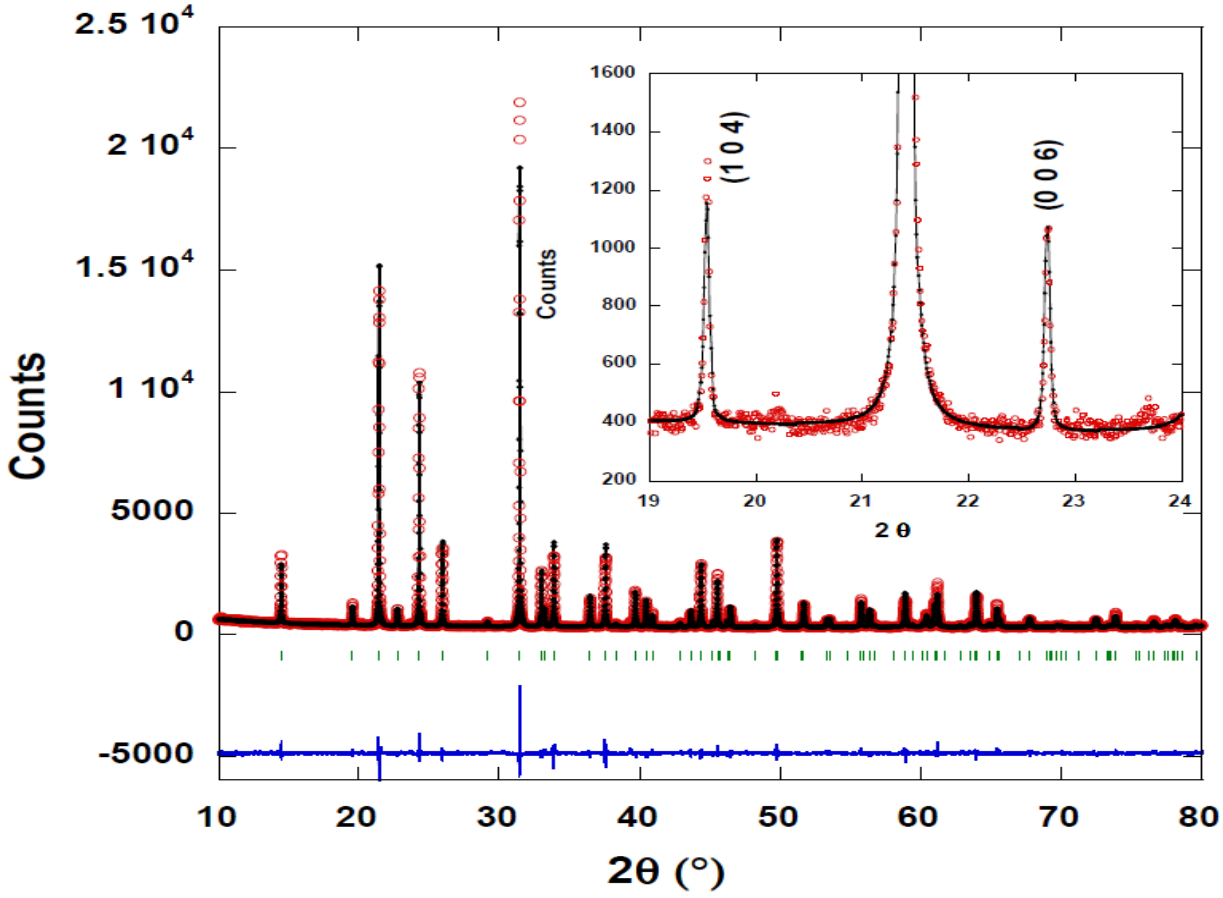

Figure V-3: Experimental XRD pattern of $BaFeTi(PO_4)_3$. For the sake of clarity only data until 80° 2θ are shown here. The observed, calculated (profile matching), difference profiles and Bragg positions as red, black, blue and green lines respectively. The inset focuses on two additional peaks observed at 19.5° and 22.7° 2θ region to highlight the indexation and profile matching with space group $\mathbf{R\bar{3}c}$.

The fact that these peaks were not observed earlier may be due to the low resolution of X-ray diffraction instrument. In addition no impurities could be found for those peaks therefore we concluded that those peaks belong to the compound under investigation. At 39.3° 2θ region there is a small peak which could not be indexed by the space group $R\bar{3}c$ (see figure V- 4 (a)). No impurities correspond to this peak. Furthermore we investigated the chemical composition of the compound using Electron Probe Micro Analyzer (EPMA) coupled with Wavelength Dispersive spectroscopy and Scanning Electron Microscopy (SEM). The result on the qualitative and quantitative analysis of the sample is given in figure V -5. The overall cation composition determined by EPMA was Ba 0.83, Fe 0.87(5), Ti 0.85(6) and P 3.00(1); note that oxygen is not determined accurately by this method and was assumed on the basis of cation stoichiometry. The results indicate off stoichiometry in the

compound but there is no sign of any impurity phase in the sample. This suggests that the actual space group might be different from $R\bar{3}c$. In fact this peak can be indexed with the same unit cell parameters but without the condition h-h0l; l=2n. Note that the indexation of this peak is (3 0 3) which satisfies the general reflection condition of rhombohedral symmetry. Therefore the possible space group is $R\bar{3}m$ but the exact determination of the space group might need high intensity sources like synchrotron or neutron. Nevertheless for the present purpose the space group $R\bar{3}c$ is enough to describe the average structure. Hence for Rietveld refinement on BFTP only $R\bar{3}c$ was considered and the results will be presented below.

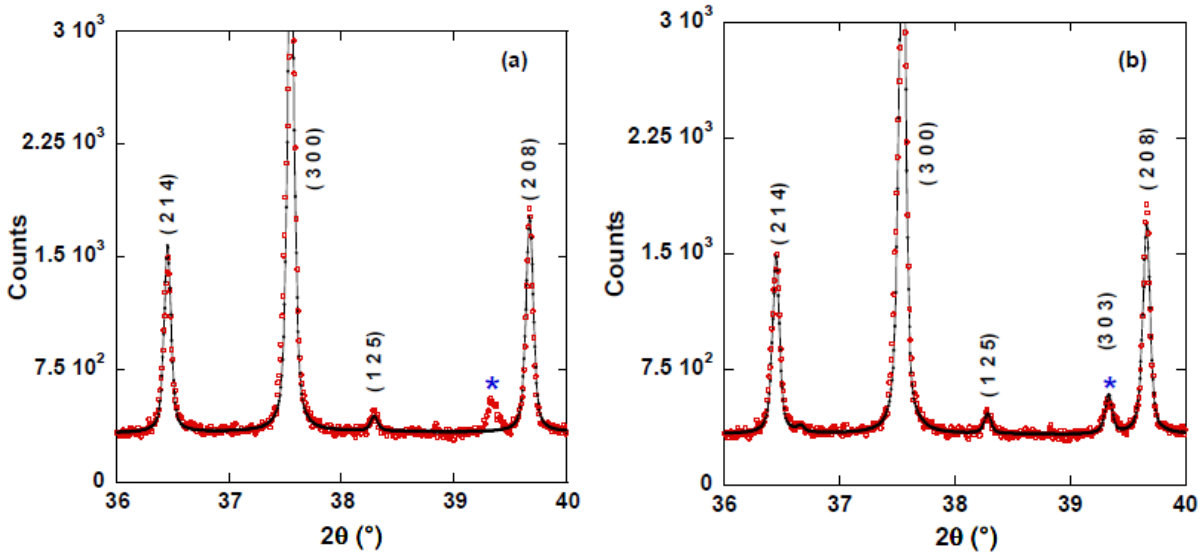

Figure V-4: Experimentally observed (red circles) and calculated profile (black lines) of XRD pattern on $BaFeTi(PO_4)_3$, (a) profile matching with $\mathbf{R\bar{3}c}$ space group, (b) profile matching with general rhombohedral symmetry. Notice the peak at 39.3° 2θ in both the figures indicated by (*). This peak is not taken into account by $\mathbf{R\bar{3}c}$ space group.

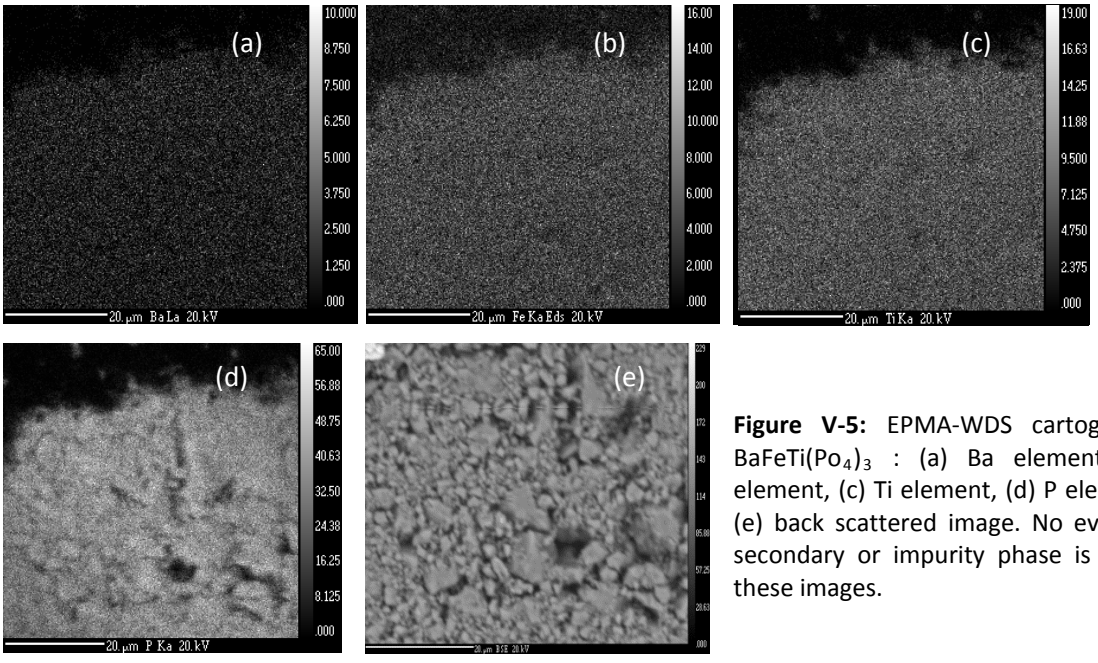

Figure V-5: EPMA-WDS cartography of $BaFeTi(Po_4)_3$: (a) Ba element, (b) Fe element, (c) Ti element, (d) P element and (e) back scattered image. No evidence of secondary or impurity phase is visible in these images.

The atomic coordinates of $Ba_{0.5}FeNb(PO_4)_3$ in space group $R\bar{3}c$ were used as starting model for Rietveld refinement [25]. Barium was introduced statistically with full occupancy whereas Iron and Titanium occupy Fe and Nb position with a total occupancy factor of 1. The crystallographic data, profile and structure refinement parameters obtained by Rietveld refinement using FullProf software is given in Table V-1 and the list of fractional coordinates is given in Table V-2.

Table V-1: Crystallographic data, profile and structure refinement parameters for $BaFeTi(Po_4)_3$:

Formula	$BaFeTi(PO_4)_3$	Formula	$BaFeTi(PO_4)_3$
Temperature	Room temperature	Background noise	
Radiation	CuKα (λ = 0.154056 nm)	Zero	0.0025(1)
Data collection range		Profile Functions	
2θ(°)	10 – 130°	U	0.05995(7)
2θ Step	0.008	V	-0.02026(7)
Scan speed	0.00066°/sec	W	0.00539(4)
Analytical function for	Pseudo Voigt (PV)	Profile Parameters	
profile shape		η	0.627(4)
Space group	$R\bar{3}c$	Asymmetry	
Lattice Parameters		P_1	0.043(1)
a (Å)	8.2905(3)	P_2	0.011(1)
c (Å)	23.4419(1)	Reliability factors	
Z	6	R_P	5.28%
Volume/Z ($Å^3$)	232.558(1)	R_{Wp}	6.88%
Density (g/cm^3)	3.79	R_B	4.50%
		χ^2	2.01

The occupation of all the elements was kept constant in order to improve the refinement. The refinement converged rapidly to a satisfactory agreement factors as it is evident from the table V-1. The isotropic temperature factor of barium is unusually high (Table V-2) and the same was observed in $Ba_{0.5}FeNb(PO_4)_3$ [25]. This might be due to the presence of disorder at the barium site or the true space group of the structure is different from $R\bar{3}c$. It is necessary to have single crystal to confirm disorder in the structure. It is also interesting to note that the occupation factor of Ti is slightly higher than Fe leading to an off stoichiometric composition.

Table V-2: Atomic coordinates of $BaFeTi(PO_4)_3$

Atoms	Wyck. Pos	x	y	z	B_{eq} (Å ^{2})	Occ
Ba	6b	0	0	0	2.075(5)	1.020(2)
Fe	12c	0	0	0.1520(2)	0.040(1)	0.47(2)
Ti	12c	0	0	0.1520(2)	0.034(1)	0.56(3)
P	18e	0.2852(1)	0	0.25	0.636(6)	0.5
O1	36f	0.1561(4)	0.9438(4)	0.1976(12)	1.567(101)	1
O2	36f	0.1850(3)	0.1609(3)	0.0974(12)	2.815(103)	1

The overall cation composition obtained by Rietveld refinement is Ba 1.020, Fe 0.93, and Ti 1.12. The composition of phosphorous and oxygen cannot be determined by the Rietveld refinement using routine X-ray techniques

Table V-3: Selected Interatomic distances in $BaFeTi(PO_4)_3$

Cation	Anion	Distance (Å)
Ba	O_2 x 6	2.702(2)
Fe(Ti)	O_1 x 3	1.899(3)
	O_2 x 3	1.925(1)
P	O_1 x 2	1.548(1)
	O_2 x 2	1.578(1)

Cation	Cation	Distance (Å)
Ba	Fe(Ti)	3.563(4)
	P	3.565(1)
Fe(Ti)	P	3.298(1)

The average structure can be described in the space group $R\bar{3}c$ using 5 independent atomic positions of the NASICON structure The structure of $BaFeTi(PO_4)_3$ consists of three dimensional framework of PO_4 tetrahedra and $Fe(Ti)O_6$ octahedra sharing common corners(FigureV-6). The barium ions are surrounded by 6 oxygen and forms octahedra. This octahedra is elongated along c axis and shares a common face with Fe(Ti) octahedra. The presence of large barium ion is the main reason for high c value of the structure. The barium ion in a six fold coordination is rather unusual but was earlier found in similar phosphates $Ba_{0.5}FeNb(PO_4)_3$, $BaTi_2(PO_4)_3$ [25] [26] [6]. Furthermore the barium-oxygen distance of 2.702 Å (see Table V-3) found in our refinement is close to 2.713 Å and 2.724 Å found in $Ba_{0.5}FeNb(PO_4)_3$ and $BaTi_2(PO_4)_3$ [25] [26]. From table V-3 it can be said that the local symmetries around Fe(Ti) and P are 3 and 2 respectively with Fe(Ti)-O and P-O bond lengths characteristics of Fe^{3+} and P^{5+} in octahedral and tetrahedral coordination and they are close to the similar phosphates found in the literature [25] [27].

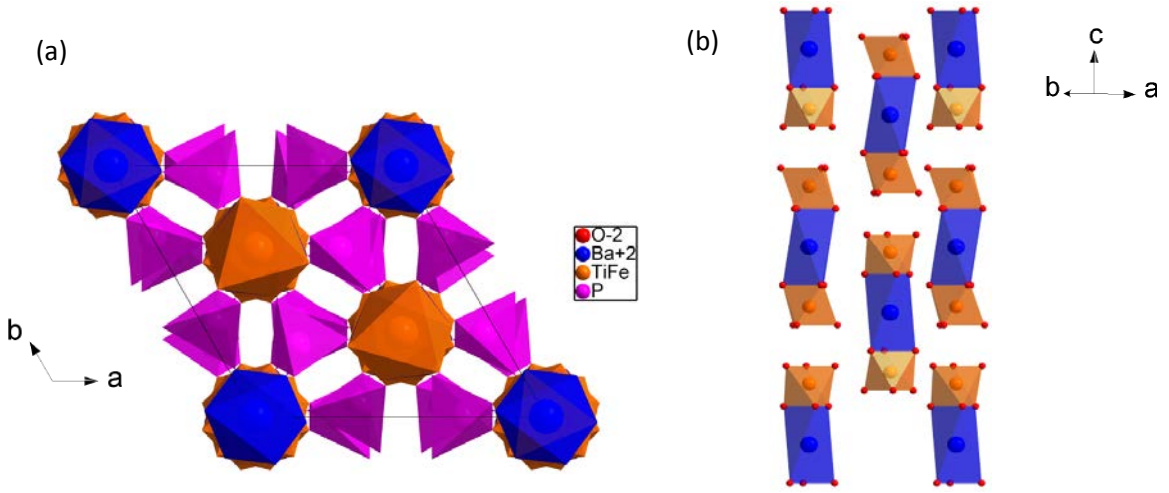

Figure V-6: (a) Structure of $BaFeTi(PO_4)_3$ evidencing the rhombohedral unit cell, (b) Representative structure along [1 1 0] direction. Barium octahedra share faces with Fe(Ti) octahedra. Along c axis there are

V.3.2. Crystal structure determination of $BiFe_2(PO_4)_3$:

Figure V – 7(a) & (b) gives profile matching of two different powder X-ray pattern obtained on $BiFe_2(PO_4)_3$.(BiFP) They are named pattern 1 and pattern 2 respectively. The space group and lattice parameters used for profile matching will be discussed later. The chemical composition of the pattern 1 sample after sintering was investigated using EPMA coupled with WDS and they did not show any impurities in the sample. The results are shown in figure V – 8 and the overall cation stoichiometry determined by EPMA method is Bi 0.96(3), Fe 1.96(5) and P 3. The standard peak search using TREOR suggests a hexagonal symmetry with unit cell parameters a = 14.2882 Å, c = 7.4101 Å. But pattern 2 displays three additional peaks at 26.4°, 29.3° and 36.6° 2θ region compared to pattern 1. Almost all the time pattern 2 was observed but sometimes pattern 1 was also observed under the same synthesis conditions as pattern 2. These three additional peaks are shown in the inset marked by stars in fig V – 7(b) and can be clearly distinguished by comparing with pattern 1 in inset to fig V – 7(a). No impurities or parasitic phases are found to correspond to those 3 peaks. As it will be shown later in the structure determination, these three peaks can be indexed by doubling the 'a' parameter. We would like to highlight that the current structure is new since compounds with similar global composition have parameters different from $BiFe_2(PO_4)_3$.

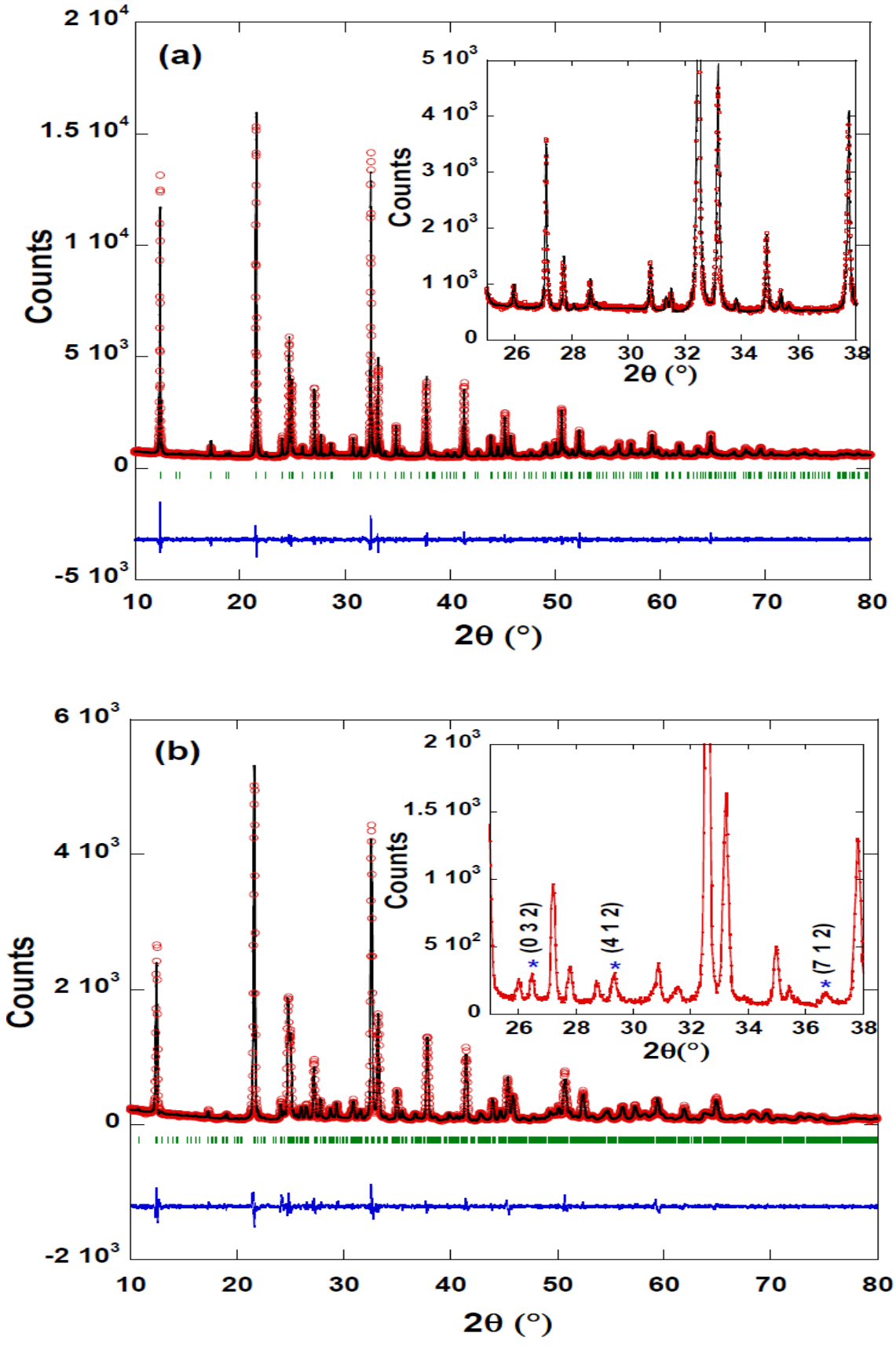

Figure V-7: The observed (red circles) and calculated (black lines) pattern of Powder X – ray diffraction in $BiFe_2(PO_4)_3$; (a) pattern 1, (b) pattern 2. The inset to (b) shows 3 additional peaks (marked by *) observed in pattern 2 (black lines) in comparison with pattern 1. (red circles).

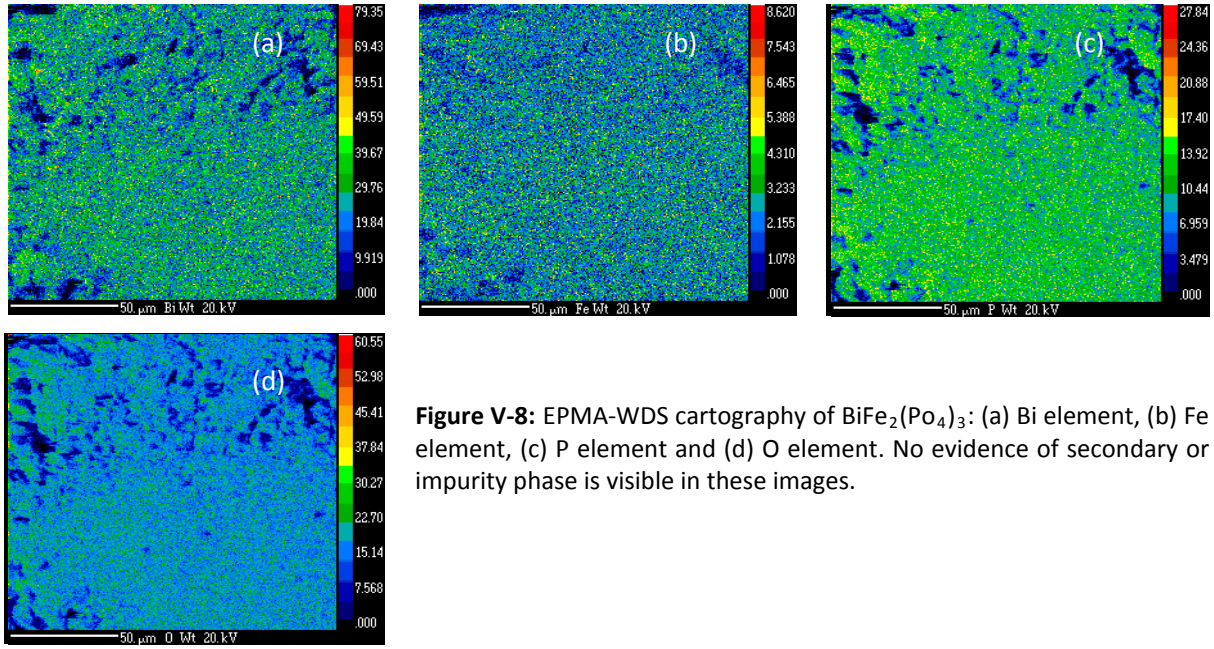

Figure V-8: EPMA-WDS cartography of $BiFe_2(Po_4)_3$: (a) Bi element, (b) Fe element, (c) P element and (d) O element. No evidence of secondary or impurity phase is visible in these images.

V.3.2.1. Single crystal growth and unit cell parameters:

V.3.2.1.1. Condition of single crystal growth:

The single crystals of $BiFe_2(PO_4)_3$ were grown by slowly cooling the furnace to ensure the growth of big crystals. First the stoichiometric composition of BiFP was synthesized in the form of powder. The XRD on the obtained powder did not show any impurity. This powder was then placed in a platinum crucible and heated to complete melting at 1125°C under air for 6 h at a rate of 2° C/min. Then the melt was slowly cooled to 1000°C at a rate of 1.8° C/hr. The sample was then cooled to room temperature in 24 hrs. The crystals grown were mostly less than millimeter size and were in the shape of needles. Figure V – 9 shows the image of the grown needle. The structural characterization of the crystals was done in collaboration with J. Darriet and they are described in the following section.

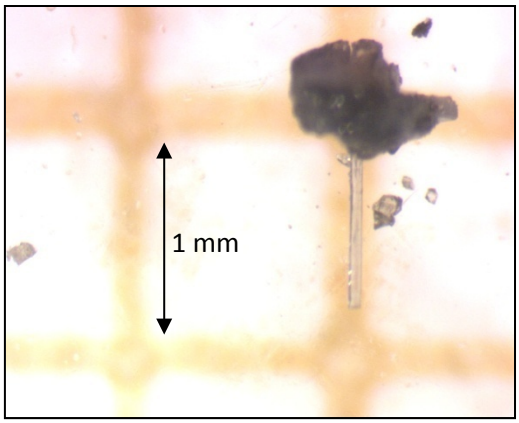

Figure V-9: Single Crystal of $BiFe_2(PO_4)_3$ in the form of needle.

V.3.2.1.2. Unit cell parameters:

Transparent crystals in the form of thin needles were extracted from solidified material and these single crystals of $BiFe_2(PO_4)_3$ were glued on a glass fiber and mounted on a Bruker Enraf – Nonius Kappa CCD four circle diffractometer using MoKα radiation (λ= 0.7101 Å) with graphite monochromator.

Several single crystals were tested and their quality assessed on the size and sharpness of diffraction spots. Using the Jana2006 version the search of the unit cell confirm the hexagonal symmetry with doubling of the a-parameter (a = 28.4000 Å, c = 7.4005 Å). The reconstructed reciprocal (hk0), (h0l) and (hk1) planes clearly show that the strongest peaks can be indexed using the sub cell with a =b=14.2373(1) Å, c =7.4005(2) Å (Fig V -10). It is also noticed that the intensity of the additional spots change from crystal to crystal. As it is shown in the figure V – 10 (d) diffusion streaks are observed indicating some disordered in the structure. This observation will be checked for all the studied single crystals. Therefore as a first step we solve the structure using the sub cell.

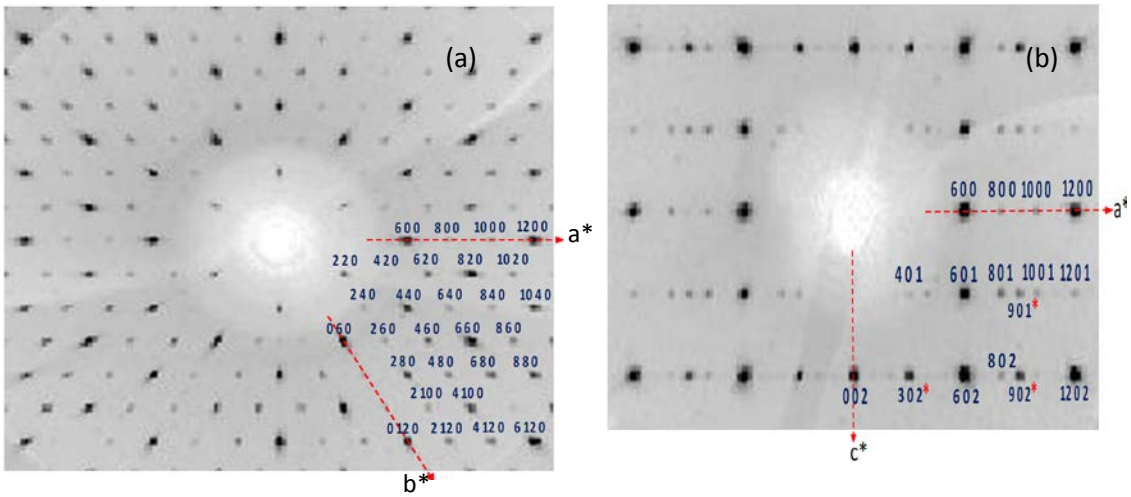

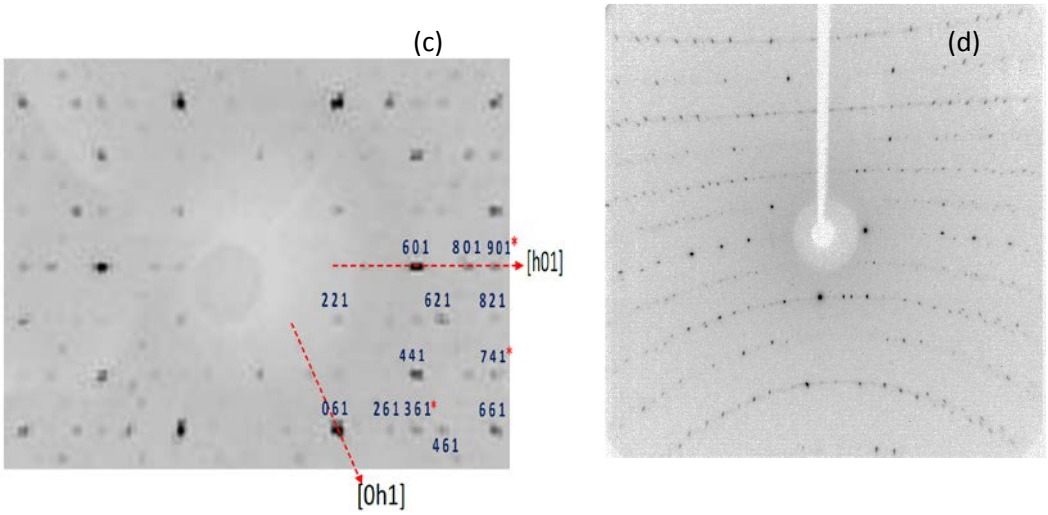

Figure V-10: Reconstructed reciprocal space images of $BiFe_2(PO_4)_3$ (a) (h k 0) plane, (b) (h 0 l) plane, (c) (h k 1) plane and (d) diffusion streaks. In image (a) only even number planes were observed whereas in image (b) & (c) odd number (hkl) planes marked by * were also observed. Observation of diffusion streaks in (d) indicates disorder in the structure.

V.3.2.2. Crystal structure of the sub cell (a=b= 14.237 Å, c = 7.4005 Å):

Data were corrected for Lorentz and polarization effects with the Eval–CCD package [28]. The structure refinement was done using Jana2006 program package. The $P6_3/m$ or $P6_3$ were found to be the possible space group. Gaussian correction, based on the shape of the crystal determined via the video camera of the Kappa CCD, was applied. The crystal data for $BiFe_2(PO_4)_3$ are given in Table V-4.

The structure was resolved using the centrosymmetric space group P63/m.The atomic positions of the bismuth atoms were determined using the superflip algorithm included in Jana2006 program. The bismuth atoms occupy three independent positions, one 4e position (0 0 z with z ≈0.04) and two 4f positions (1/3 2/3 z with z ≈±0.05).These positions are half occupied in order to respect the Bi composition of the phase (Z = 6). The atomic positions of the other atoms were determined by successive difference Fourier synthesis. All these positions are fully occupied.With isotropic atomic displacement parameter (ADP), the residual factors converged to R(F) ≈ 0.12 and $wR(F^2)$ ≈ 0.24 for 46 refined parameters. The use of anisotropic displacement parameter for all positions lowered them to R(F)=0.0686 and $wR(F^2)$= 0.1351 for 101 refined parameters. However the difference Fourier synthesis shows clearly electron residue around the Bi1 position (≈ $5e^-$/ Å 3) with x ≈ -0.01, y ≈ 0.01 and z ≈ 0.04.

Table V-4: Crystallographic data and structure refinement for $BiFe_2(PO_4)_3$:

Formula	**$BiFe_2(PO_4)_3$**
Crystal color	transparent
Crystal size (mm)	needle 0.15x0.036x0.036
M($gmol^{-1}$)	605.6
Crystal system	hexagonal
Space group	$P6_3/m$
Parameters	a = 14.2373 (0.007)Å c = 7.4005(0.0004)Å
V($Å)^3$	1299.11(9)
Z	6
Density calc. (gcm^{-3})	4.64
F(000)	1656
Temperature (K)	293
Diffractometer	Enraf-nonius
Monochromator	Oriented graphite
Radiation	MoKα (λ = 0.71069 Å)
Scan mode	CCD scan
h k l range	±25, ±25, ±13
$\theta_{min}\theta_{max}$	5°, 40°
Linear absorption coeff.(mm^{-1})	25.587
Absorption correction	Gaussian
T_{min}/T_{max}	0.180/0.616
R_{int}	0.186
No. of reflections	24642
No. of independent reflections	2868
Reflections used [I> 3s(I)]	1678
Refinement	F^2
No. of refined parameters	107
R factors R(F)/wR(F^2)	0.0600/0.1293
g.o.f.	1.73
Weighting scheme	$w = 1/(s^2(I)+0.0009I^2)$
Diff. Fourier residues ($e^-Å^{-3}$)	-1.87, + 2.09

Table V-5: Atomic position and equivalent isotropic displacement parameters for $BiFe_2(PO_4)_3$ (S.G $P6_3/m$)

Atom	Wyckoff Position	Occupancy	x / a	y / b	z / c	U [Å^2]
Bi1	12i	1/6	0.984(2)	-0.001(3)	0.0376(2)	0.012(2)
Bi2	4f	1/2	1/3	2/3	-0.0531(2)	0.0143(2)
Bi3	4fi	1/2	1/3	2/3	0.0509(2)	0.0140(2)
Fe1	12i	1	0.31503(7)	0.96841(7)	0.04818(12)	0.0081(3)
P1	6h	1	0.5619(2)	0.7914(2)	3/4	0.0061(6)
P2	6h	1	0.4887(2)	0.9076(2)	1/4	0.0054(6)
P3	6h	1	0.0790(2)	0.8498(2)	1/4	0.0061(6)
O1	12i	1	0.5667(4)	0.7348(4)	0.9202(6)	0.013(2)
O2	6h	1	0.1994(4)	0.8819(4)	1/4	0.006(2)
O3	12i	1	0.5548(4)	0.9489(4)	0.4205(6)	0.016(2)
O4	6h	1	0.4483(5)	0.7818(5)	1/4	0.013(2)
O5	12i	1	0.0207(4)	0.7879(4)	0.4200(6)	0.017(2)
O6	6h	1	0.4344(5)	0.7831(5)	1/4	0.015(2)
O7	6h	1	0.3977(5)	0.9364(5)	1/4	0.008(2)
O8	6h	1	0.3500(4)	0.0874(4	1/4	0.007(2)
O9	6h	1	0.0432(5)	0.1212(5)	1/4	0.023(3)

Table V-6: Anisotropic displacement parameter (Å^2) for $BiFe_2(PO_4)_3$

Atom	U_{11}	U_{22}	U_{33}	U_{12}	U_{13}	U_{23}
Bi1	0.01839(1)	0.01839(1)	0.00664(7)	0.00919(5)	0	0
Bi2	0.02006(0)	0.02006(0)	0.00544(8)	0.01003(0)	0	0
Bi3	0.04931(4)	0.04931(4)	0.00401(9)	0.02465(7)	0.00000	0.00000
Fe1	0.00977(1)	0.00946(0)	0.00506(2)	0.00416(4)	0.00024(7)	-0.00028(9)
P1	0.00638(8)	0.00544(9)	0.00637(0)	0.00279(4)	0	0
P2	0.00686(7)	0.00439(0)	0.00609(3)	0.00292(2)	0	0
P3	0.00550(9)	0.00738(3)	0.00889(1)	0.00418(9)	0	0
O1	0.01353(7)	0.01611(2)	0.00920(9)	0.00652(9)	0.00413(6)	0.00759(9)
O2	0.00729(4)	0.00900(2)	0.00549(2)	0.00503(0)	0	0
O3	0.013(2)	0.01550(8)	0.02246(7)	0.01164(7)	0.01001(5)	0.00783(1)
O4	0.01007(3)	0.01193(2)	0.00781(6)	0.01009(0)	0	0
O5	0.01318(6)	0.02841(8)	0.00969(9)	0.00851(5)	-0.00366(0)	-0.00768(1)
O6	0.00506(4)	0.01468(2)	0.02051(1)	0.00550(9)	0	0
O7	0.00902(8)	0.00865(3)	0.00521(2)	0.00347(3)	0	0
O8	0.01055(9)	0.01079(5)	0.02391(7)	0.00556(1)	0	0
O9	0.01390(0)	0.01040(2)	0.05199(2)	0.01043(7)	0	0

Table V-7: Interatomic distances (Å) and bond valence for $BiFe_2(PO_4)_3$

Cation	Anion	Distance [Å]	BVS (a.u)
Bi1	O9	2.18(3)	
	O9	2.067(10)	
	O9	2.33(3)	3.15(8)
	O9	2.64(3)	
	O9	2.723(9)	
	O9	2.50(2)	
Bi2	O4 x 3	2.192(7)	2.83(2)
	O6 x 3	2.732(5)	
Bi3	O6 x 3	2.146(7)	3.10(2)
	O4 x 3	2.764(5)	
Fe	O1	1.949(7)	
	O2	2.105(3)	
	O3	1.879(5)	
	O5	1.923(8)	3.14(2)
	O7	2.088(6)	
	O8	2.122(4)	
P1	O1 x 2	1.515(5)	
	O4	1.554(8)	5.04(4)
	O8	1.545(5)	
P2	O3 x 2	1.506(5)	
	O6	1.539(7)	5.15(4)
	O7	1.542(9)	
P3	O5 x 2	1.522(4)	
	O2	1.537(6)	5.09(4)
	O9	1.531(9)	

Using this new 12i position for Bi1, the R factors decrease to R(F)≈ 0.0600 and wR(F^2)≈ 0.1293 for 107 refined parameters and 1678 observed reflections with non –significant difference Fourier residues (see Table V -4). The resulting atomic positions and anisotropic displacement parameters are given in Tables V – 5 and V – 6. Tables V – 7 gives the interatomic distances and bond valence sum of BiFP.

The structure of $BiFe_2(PO_4)_3$ is shown in figure V – 11 (a & b). The Bi1 atom is close to the center of BiO6 octahedron and these octahedra share faces forming chains parallel to the c – axis (Figure V – 11 (b). Within in the Bi1O6 octahedron there is three Bi-O distances close to 2.2 Å and three longer distances ≈ 2.7 Å (Table V – 7). Therefore, the coordination number of Bi1 is CN = 3 which is characteristic of Bi^{3+} where the lone pair $6s^2$ is active. Considering the lone pair, the environment of Bi1 is a tetrahedron constituted by three oxygen plus the lone pair along the c – axis. The environment of Bi2 and Bi3 is BiO6 trigonal prism where the bismuth is delocalized from the center of the prism along the c – axis. This trigonal prism share faces and form chains parallel to the c – axis (figure V – 11(b)).The Bi2 and Bi3 atoms are in fact bonded to three oxygen atoms with short distance (Bi-O ≈ 2.2 Å) and to other three oxygen atoms with long distance (Bi-O ≈ 2.7 Å) like in the case of Bi1 position (Table V – 7).One can also notice the activity of the $6s^2$ lone pair for Bi2 and Bi3 atoms. The stereoactivity of the $6s^2$ lone pair is usual in bismuth compounds like Bi_2O_3, $Bi_2Sr_2CaCu_2O_8$ with nearest Bi – O distances of 2.14 to 2.29 Å [29] [30]. This value is closer to the observed value of 2.2 Å for $BiFe_2(PO_4)_3$ structure.

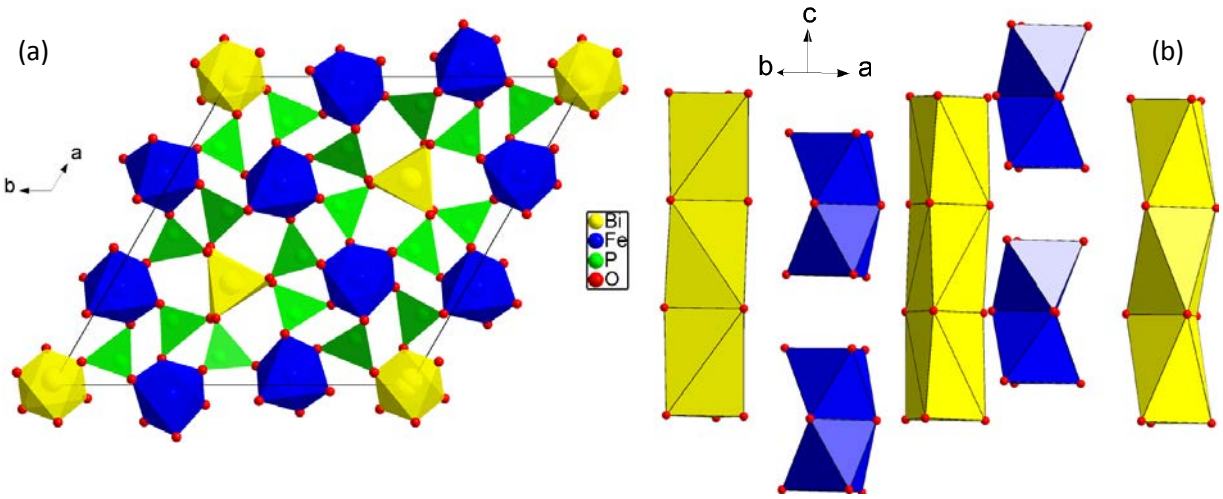

Figure V-11: Projection of hexagonal unit cell of $BiFe_2(PO_4)_3$ ab plane, note two different environment of bismuth in octahedra (extreme right) and trigonal prism and the iron (blue) are located in the octahedral holes. (b) View of the structure along c - axis. The face sharing octahedra and prism of bismuth form columns along c axis. The face sharing octahedra of iron also forms columns along c axis. After every two octahedra there is a void space

The framework of the structure of BiFP is very similar to that of nasicon (compare figure V – 4(a) and fig V -11 (a)). The similarity is obvious regarding the connection of the chains by the PO_4 tetrahedra. The difference is only on the nature of the chains formed by Ba-Fe-Ti in BFTP and Bi-Fe in BiFP (figure V -4(b) and figure V – 11 (b)). It results in a relationship between the lattice parameters of these two phases.

$$a_1 = \frac{a_2}{\sqrt{3}}$$

$$c_1 = c_2 * 3$$

where a1, c1 and a2, c2 are lattice parameters of $BaFeTi(PO_4)_3$ and $BiFe_2(PO_4)_3$ respectively. One can expect that the precise determination of structure considering the doubling of a and b parameter will imply a perfect ordering of the bismuth in the [BiO6] chains. Therefore it is necessary to select a single crystal where many additional spots are obvious and well defined. This work is currently in progress.

V.3.3. Magnetic Property of $BaFeTi(PO_4)_3$ and $BiFe(PO_4)_3$:

V.3.3.1. Temperature dependence of magnetic susceptibility in $BaFeTi(PO_4)_3$:

The reciprocal magnetic susceptibility ($1/\chi$) as a function of temperature between 5 and 300 K with a step of 5K is shown in figure V -12. The reciprocal susceptibility show a deviation of the Curie – Weiss law indicating a magnetic order phenomenon. However the chosen temperature step (5 K) is not enough to clearly identify the nature of transition. The linear behavior of the curve above 60 K can be fitted by the modified Curie-Weiss law.

$$\chi(T) = \chi_0 + \frac{C}{T - \theta_W} \qquad \textbf{Eq V-1}$$

Where χ_0 is the temperature independent susceptibility, C is the Curie constant and θ is the paramagnetic Curie – Weiss temperature. The fit for χ(T) curve using Eq (V – 1) over the temperature range above 60 K yields θ_W = -32 K±2, χ_0 = 1.2 X 10^{-4} emu/(mol –Oe) and C = 4.39±0.4 K emu/(mol Fe^{3+}).

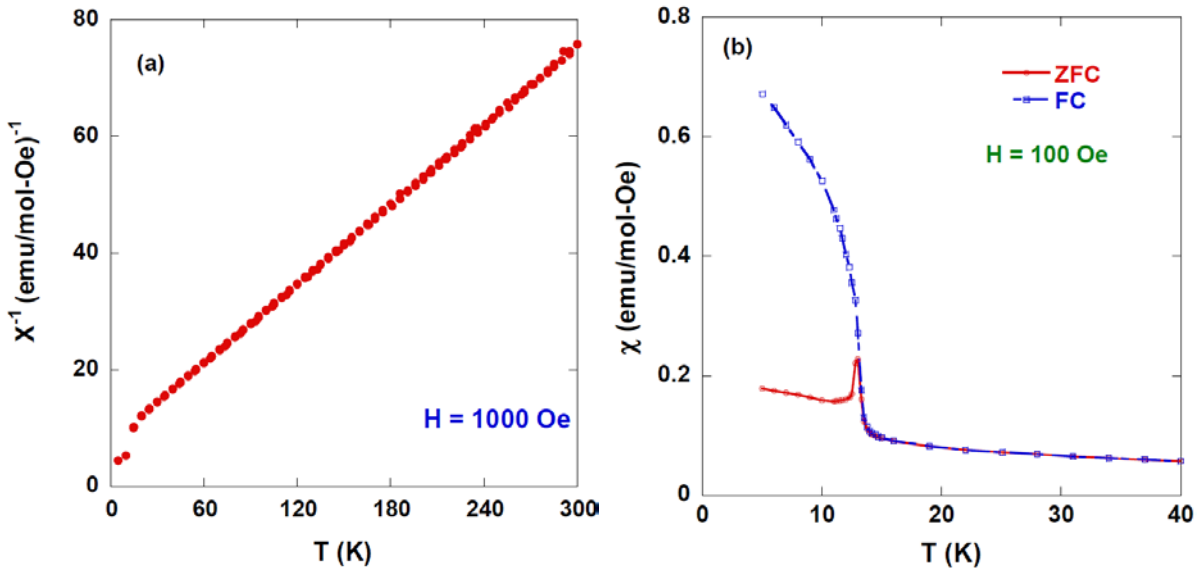

Figure V-12: Reciprocal susceptibility as a function of temperature for $BaFeTi(PO_4)_3$ at a field of 1000 Oe. Between 10 to 15 K a step in the reciprocal susceptibility is seen indicating magnetic order. (b) Shows ZFC and FC mode on the same sample. A very sharp transition is seen at 13 K in ZFC mode whereas FC mode shows bifurcation.

The effective magnetic moment per mol Fe (μ_{eff}) is calculated by using the formula

$$C = N\mu_{eff}^2/3k_B \qquad \textbf{Eq V-2}$$

where N is the number density of Fe^{3+} ions pr mol and k_B is the Boltzmann constant. We obtain μ_{eff}=5.92(2) μ_B where μ_B is the Bohr magneton which is close to the value obtained on similar phosphates like $Na_3Fe_2(PO_4)_3$ and $Li_3Fe_2(PO_4)_3$ [20]. This indicates that the valency of titanium and iron are Ti^{4+} and Fe^{3+} and the magnetic property of BFTP is only due to Fe^{3+} ions.

To study the nature of magnetic transition in detail the magnetic susceptibility was measured between 5 to 40 K with a step of 0.25 K. The figure V – 12 (b) show magnetic susceptibility versus temperature under zero field cooled (ZFC) and field cooled (FC) mode. For the zero field cooled case, the sample was cooled from 40 to 5 K and then a magnetic field of H = 100 Oe was applied and magnetic measurements were done after ensuring stabilization at each temperature. Upon reaching 40 K, the data were similarly collected with decreasing temperature (FC mode) keeping the same applied field.

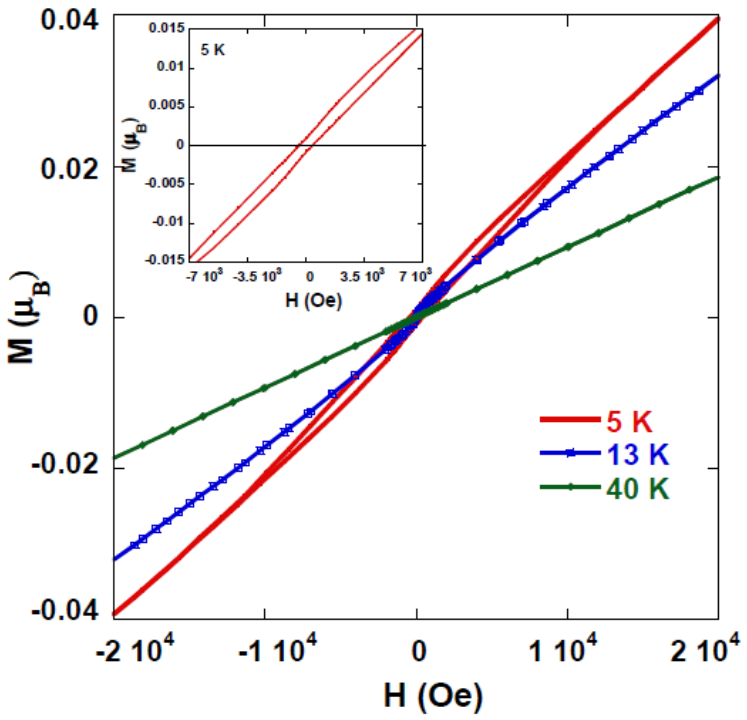

Figure V-13: Magnetization as a function of applied field for BFTP at 5, 13 and 40 K. At 5 and 13 K the curve deviates from linearity and a clear opening is seen at 5 K. Inset gives the zoom of the 5 K curve showing the opening.(Lines are drawn to guide the eyes)

The susceptibility exhibits a very sharp peak at T_S=13 K under ZFC with FWHM of about 1.3 K whereas in FC mode a clear bifurcation from ZFC behavior is seen exactly at the transition temperature

showing irreversibility. The behavior under ZFC mode is antiferromagnetic but under FC mode it is more like ferromagnetic or ferrimagnetic. These two set of data coincide above 13 K. It is also possible that the irreversibility in the ZFC and FC may be due to spin glass behavior.

The magnetization versus applied field curve for BFTP is shown in figure V – 13. Above the T_S at 40 K M versus H curve is linear exhibiting paramagnetic behavior. At T_S deviation from linearity is seen and at 5 K a clear opening is visible in the curve. This opening is clearly seen in the inset and gives a coercive field of H_C = 400 Oe. Therefore BFTP shows complex magnetic behavior related to canted antiferromagnetic, clusters or spin glass behavior. The complexity in the magnetic behavior can be easily understood by studying the structure in detail. From figure V – 6(a & b) it can be seen that every metal octahedra is linked to each other via PO_4 tetrahedra. Furthermore the octahedra form chains along c- axis. This leads to complex exchange path mediated by the oxygens in PO_4 tetrahedra. Therefore as a first step we probed the spin glass behavior by frequency dependent susceptibility measurements and they are described in the following section.

V.3.3.2. Frequency dependence of susceptibility:

To examine the presence of spin glass behaviour temperature dependent ac susceptibility measurements were carried out between 5 and 20 K as frequencies from 0.33 to 1 KHz. The applied ac driving field was 2 Oe and the external dc field was 5 Oe.

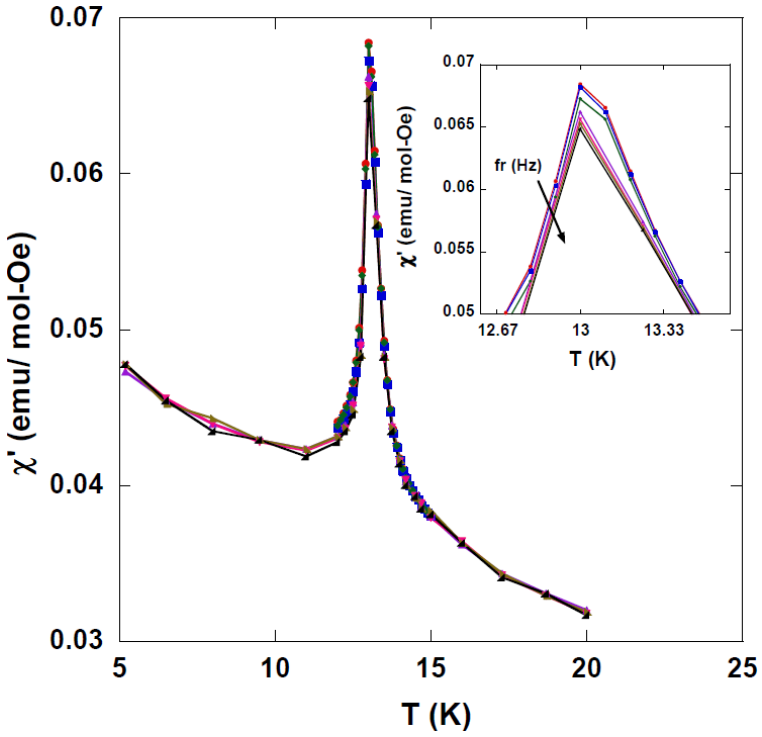

Figure V-14: The real part of ac susceptibility as a function of temperature between 5 and 20 K at several frequencies from 0.33 Hz to 1.12 KHz. Inset focuses on the zoom of the same plot. The peak temperature is not

affected by the frequencies but the magnitude of ac susceptibility shows strong frequency dependence. (Lines are drawn to guide the eyes)

Results in figure V – 14 show temperature dependence of real part of the ac susceptibility (χ') under ZFC mode for several frequencies and a sharp peak is seen at T_S=13 K similar to dc magnetic measurement. It seems the peak temperature does not depend on the frequency of the ac field which is clearly shown in the inset. This clearly indicates the presence of long range antiferromagnetic order. However the magnitude of ac susceptibility is frequency dependent below T_S, being higher at lowest frequency than at higher frequencies. The frequency dependence disappears above and below the peak temperature where all the curves merge. The same behaviour is observed on the imaginary part of ac susceptibility (not shown).

V.3.3.3. Field dependence of susceptibility:

The dc susceptibility was probed under different fields between 1000 to 5000 Oe to study the effect of applied field on the magnetic transition at 13 K. Figure V – 15 show the susceptibility as a function of temperature for different applied fields under ZFC condition. Both the peak temperature and the magnitude of the peak decrease with increase in field.

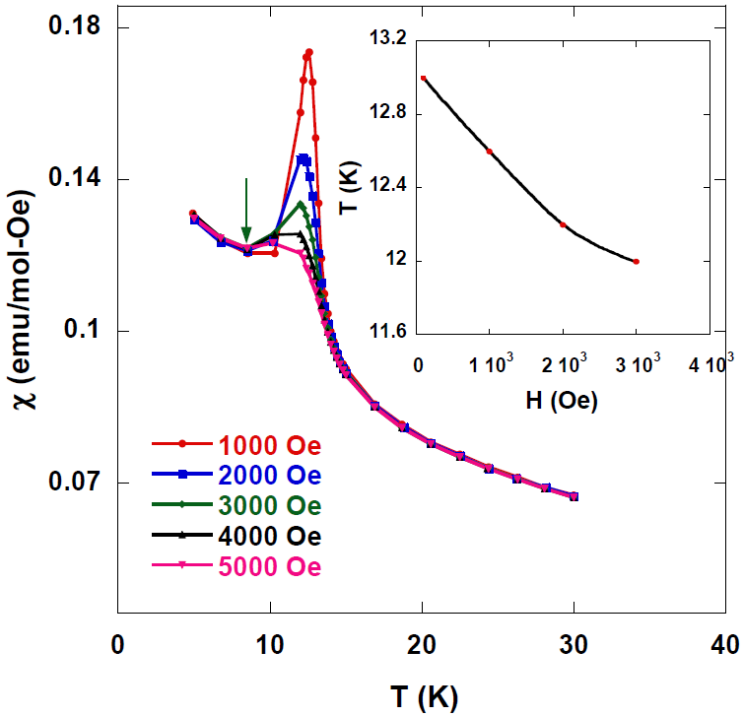

Figure V-15: Temperature dependence of dc susceptibility under ZFC condition at different fields. Inset shows the dependence of peak temperature obtained from ZFC curves as a function of applied field. (Solid lines are guide to eyes)

The sharp peak seen at low field becomes much broader and low in magnitude with high field. Above the peak temperature there is a sharp drop of susceptibility for all H and moreover all the curves

tend to merge below about 8.5 K (marked by the arrow) for all the values of H marked by the arrow. Inset to the figure V – 15 shows the field dependence of the peak temperature. It can be seen that there is sharp decrease in the peak temperature with field's upto 2000 Oe, above this field the peak temperature does not change much as evident from the beginning of the plateau.

Figure V – 16 gives the susceptibility as a function of temperature under field cooled (FC) and field cooled warming (FCW) condition. On comparing this figure with the previous one a strong irreversibility between ZFC and FC curves is visible. In the FC curve no peak is seen instead it rises monotonously below 13.5 K which is close to T_S. Upon increase in the field the magnitude of the curve decreases furthermore between 4000 and 5000 Oe the decrease is much less indicating saturation. In addition thermal hysteresis is seen between FC and FCW curves. The curve opening decreases with increase in the field and totally merges at 5000 Oe. Above 13.5 K the curves for all H values merges

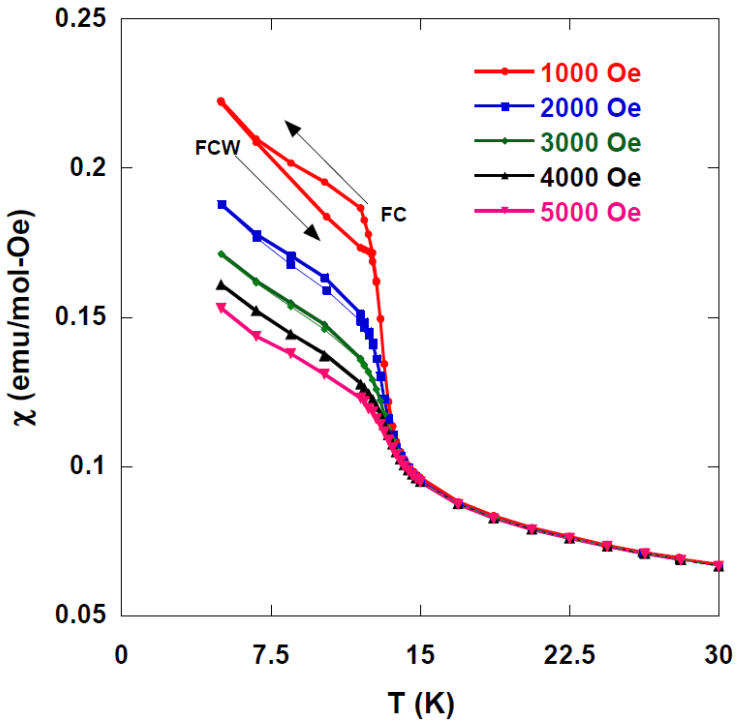

Figure V-16: Susceptibility as a function of temperature under field cooled (FC) and field cooled warming (FCW) mode. Notice the monotonous increase of susceptibility below 13.5 K. There is also a thermal hysteresis between FC and FCW curves as seen from the opening between them.

V.3.3.4. Nature of magnetic transition in $BaFeTi(PO_4)_3$:

The strong irreversibility observed below T_S between ZFC and FC is due to complex magnetic behavior as discussed above. Considering the results above it is apparent that there must be different short range and long range order. The peak in dc and ac susceptibility along with frequency independence indicates long range magnetic order. However the field dependence of dc

susceptibility shown in fig V – 15 is a signature of spin glass type behavior. It is also corroborated by the observation of a strong monotonous increase seen in fig V – 12(b) which is similar to spin glass $LiMn_2O_4$ [31]. This shows the presence of several competing exchange interactions in the structure and it may be due to complex exchange paths and the actual distribution of FeO6 and TiO6 octahedra which is not known. Giot et al have demonstrated similar type of behaviour in $Bi_{0.67}Ca_{0.33}MnO_3$ [32]. They found a very small frequency dependence of the real part of the susceptibility along with a weak depression of the peak with frequency. More importantly they found collapse of dissipation peak for moderate applied field. This is exactly the situation for BFTP however the collapse was found in dc susceptibility and also the susceptibility is frequency independent. The frequency dependence of the magnitude of susceptibility peak seen in BFTP was also found in $LiMn_2O_4$ and was interpreted as spin glass by Y-I. Jang [31]. These fact shows that there is a presence of magnetic order and magnetic disorder at the same temperature similar to the case of $Bi_{0.67}Ca_{0.33}MnO_3$ [32]. To be able to comment more on the nature of transition further magnetic measurements along with neutron diffraction is needed.

V.3.3.5. Temperature dependence of magnetic susceptibility in $BiFe_2(PO_4)_3$:

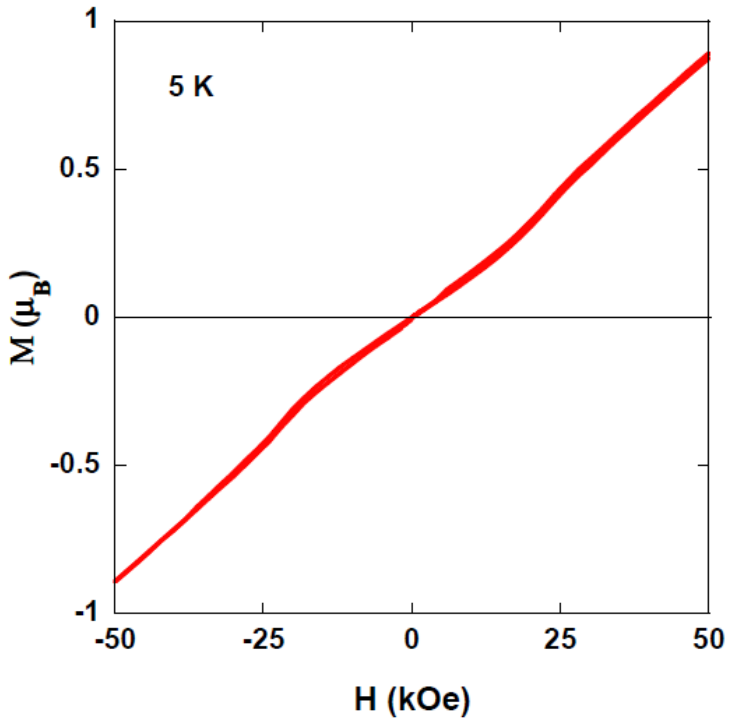

Figure V-17: Magnetization versus field at 5 K. The curve is mostly linear except for a small deviation around 2 kOe.

The variation of the magnetization versus the applied field at T = 5 K is given in Fig V – 17. The magnetization is almost linear with the applied field except a small deviation observed around H = 2

kOe (Fig V – 17). The magnetic susceptibility of a polycrystalline BiFP sample was measured in ZFC and FC mode with H = 100 Oe at temperatures from 300 K to 5 K. Figure V – 18 shows temperature dependence of reciprocal susceptibility χ^{-1} under ZFC and FC conditions. With decrease in temperature χ^{-1} decreases monotonically and at about 25 K shows a broad minimum indicating a possible magnetic order transition. The solid straight line indicates the fit to equation 1 and extrapolates to negative temperature. The parameters extracted from the fit gives Curie – Weiss temperature θ_W = - 54 K (2), χ_0 = 1 X 10^{-4}(emu/mol) and C = 4.42 $\pm$ 0.2 (emu K/ Fe^{3+}). The effective magnetic moment deduced from equation 2 is 5.94(2) μ_B which is close to the theoretically expected spin only value of 5.91 $\mu_B$per Fe^{3+}.

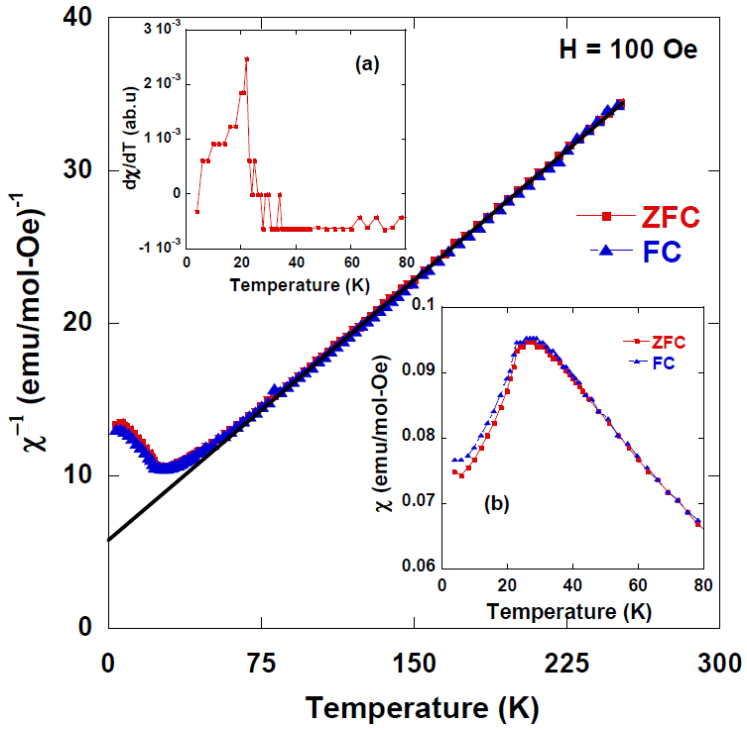

Figure V-18: Reciprocal susceptibility χ^{-1} as a function of temperature under ZFC and FC mode. The solid line indicates the fit using Curie – Weiss law. Inset (a) shows the derivative of susceptibility as a function of temperature with a peak at 22 K indicating T_N. Inset (b) gives the χ as function of temperature under ZFC and FC conditions.

The specific heat measurements at low temperatures between 2 K to 90 K show clearly a typical lamba peak characteristic of an ordering temperature. Therefore BiFP is antiferromagnetic with a Neel temperature T_N = 22 K (figure V – 19). The Neel temperature is very close to the maximum of the susceptibility observed at T = 25 K. An exact determination of the Neel temperature from the susceptibility measurement can be done by plotting $d\chi/dT$ versus T (inset to figure V -18).

The maximum of the slope is observed at T = 22 K which corresponds exactly with the Neel temperature obtained by specific heat measurements.

As it was shown before, the crystal structure of the BiFP shows clearly that the iron constitute isolate dimers with an intra Fe – Fe distance of 2.99 Å (fig V – 11(b)) which is longer than the facing sharing octahedra observed in Fe_2O_3 (2.896 Å) [33]. The inter – dimer Fe – Fe distance in BiFP along the c – axis is 4.41 Å and the inter-chain distance is 4.78 Å. Therefore, in first approximation one could expect that at high temperature the magnetic behaviour of BiFP should be antiferromagnetic from isolated dimers. This is characterized by a large maximum in the susceptibility, the temperature of which depends on the strength of exchange interactions. However the magnetic behaviour of BiFP is characteristics of three dimensional antiferromagnetic systems. No anomaly in the susceptibility is observed above the Neel temperature which indicates that the inter-dimer exchange interaction along the chains and between the chains are significant compared to the intra-dimer exchange interaction. This is another example where the strength of the Fe – Fe exchange interactions is not only governed by the metal – metal distance but also by the orientation of the atomic orbitals in the super – superexchange interaction.

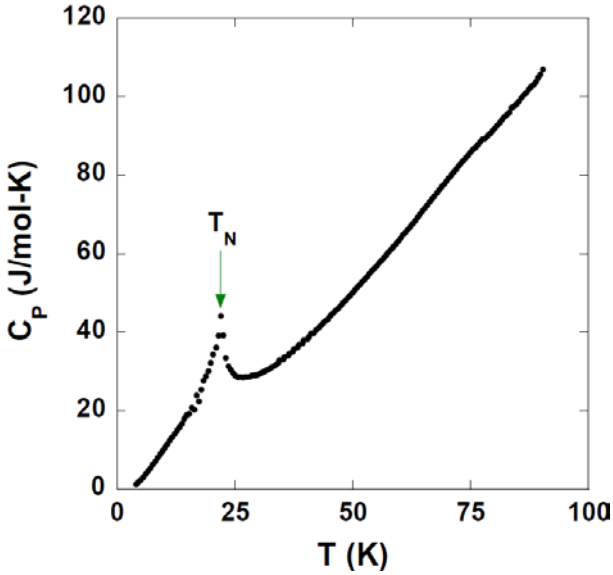

Figure V-19: Low temperature data of specific heat for $BiFe_2(PO_4)_3$

V.3.4. Dielectric properties of $BiFe_2(PO_4)_3$:

The compound $BaFeTi(PO_4)_3$ could not be sintered into high density pellets therefore no dielectric property measurements were carried out on this compound. We will discuss only the dielectric property of $BiFe_2(PO_4)_3$ from here on. To make high density pellets of BiFP, the sample powder was uniaxially pressed in to a circular disc pellet. The pressed pellet was then fired at 1050°C

for 15 hrs. After sintering, the pellet was red in color subsequent X – ray diffraction did not show any impurities and was similar to the powder X –ray pattern. The obtained density was 4.29 g cm^{-3} which is 93% of theoretical X – ray density. Figure V – 20 (a) & (b) gives the capacitance and dielectric losses of BiFP sintered ceramic respectively as a function of temperature during heating and cooling at three different frequencies. It can be seen from the plots that there is no thermal hysteresis during heating and cooling cycles. The capacitance decreases monotonically from room temperature to 10 K. With increase in frequency, capacitance decreases at high temperatures and at low temperatures this decrease is less pronounced. The dielectric constant deduced from equation 2 in chapter 2 is about 35 at room temperature. In the range from 100 to 200 K a broad shoulder is visible. It looks like this shoulder moves to higher frequency with increase in temperature. In general dielectric losses stay lower than 5% in all frequency range. A broad peak is observed in the range 100 – 200 K which corresponds to the shoulder observed in the capacitance. This broad peak shifts in frequency with increasing temperature which is a sign of relaxation process in the material.

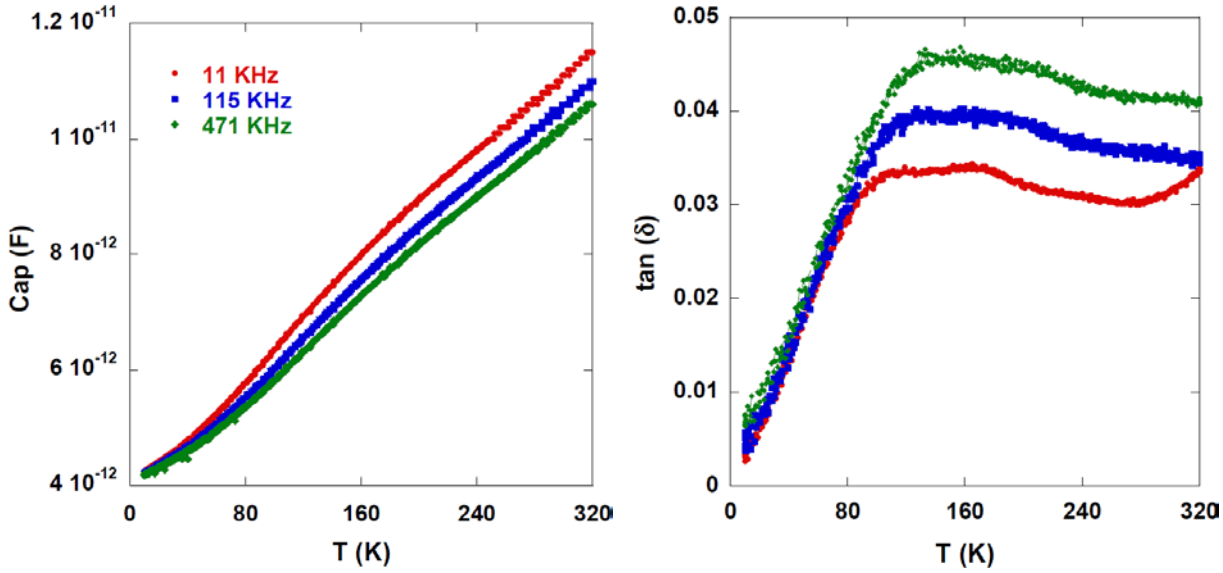

Figure V-20: Dielectric property of $BiFe_2(PO_4)_3$. Temperature dependence of (a) capacitance, (b) dielectric losses at different frequencies during heating and cooling cycles. No particular anomaly is found in capacitance expect for a very broad shoulder in the range of 100 to 200 K. At the same temperature range dielectric losses display a broad peak.

The activation energy determined by plotting log frequency as a function of inverse temperature of the peak maximum is about 0.13 eV (see figure V – 21). Below the broad peak about 130 K dielectric losses drops rapidly until the lowest temperature and it is much less than 1% at 10 K indicating that the material behaves as an insulator at low temperatures. Measurement under magnetic field of 90 kOe did not show any effect of magnetic field on both capacitance and dielectric losses (not shown).

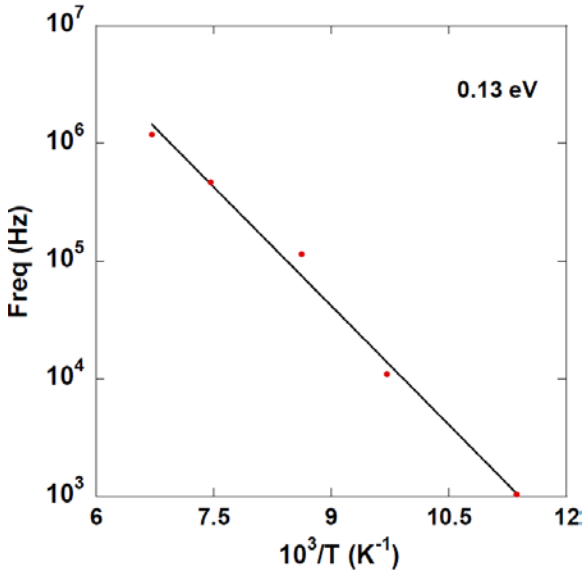

Figure V-21: Log frequency as a function of reciprocal temperature for $BiFe_2(PO_4)_3$. The temperature and frequency are taken from the maximum in the dielectric losses. The solid line is the fit to Arrhenius law.

The absence of ferroelectricity in BiFP can be explained on the basis of their structure. BiFP crystallizes in centrosymmetric space group P 6_3/m. In the structure bismuth sits in three independent positions, octahedra and two prisms. Bismuth in prism coordination is shifted along c – axis this gives rise to a dipole moment. This shift can be positive or negative with respect to c – axis however the distribution of this shift is not known at the moment. Nevertheless it could be possible to induce long range order by forcing the bismuth to shift in a cooperative manner by suitable substitution.

V.4. Conclusion:

New phosphates of formula $BaFeTi(PO_4)_3$ and $BiFe_2(PO_4)_3$ have been successfully synthesized using solid state reaction. The lattice parameters, atomic coordinates, interatomic distances and occupancy factors have been determined for both phosphates using Rietveld refinement. BFTP crystallizes in approximate space group of $R\bar{3}c$ and for the exact determination of space group requires single crystal. On the other hand single crystals of BiFP were grown successfully by slow cooling method which resulted in millimeter size needle shape crystals. The x – ray diffraction on these single crystals gave a space group of $P6_3$/m with hexagonal symmetry. Magnetic measurement of BFTP exhibits an antiferromagnetic type peak at 13 K in ZFC whereas FC curve shows strong irreversibility. Nature of magnetic transition is still ambiguous which calls for further detailed experiments whereas BiFP shows typical antiferromagentic type behavior below 22 K in both ZFC and FC which is taken as the transition temperature. Dielectric measurement of BiFP on ceramics did not show any ferroelectric type anomaly but they undergo relaxation and the origin of which is still not

clear. X –ray diffraction versus temperature in the range of occurrence of dielectric relaxation could be used to link this relaxation to the Bi dynamics. By making suitable substitution in BiFP it might be possible to induce long range order which may invoke ferroelectricity. To summarize these new phosphates holds some promise in the light of their interesting magnetic and dielectric properties.

V.5. References

[1] B. B. Van Aken, J.P. Rivera, H. Schmid, M. Fiebig. *Nature*, 449:702, 2007.

[2] T. B. S. Jensen, N. B. Christensen, M. Kenzelmann, H. M. Rønnow, C. Niedermayer, N. H. Andersen, K. Lefmann, J. Schefer, M. V. Zimmermann, J. Li, J. L. Zarestky, and D. Vaknin. *Phys. Rev.B.*, 79:092412, 2009.

[3] H. Schmid. *Ferroelectrics*, 161:1, 1994.

[4] N. Anantharamulu, K. KOteswara Rao, G. Rambabu, B. Vijaya Kumar, V. Radha. M. Vithal. *J. Mat. Sci.*, 46:2821, 2011.

[5] L. Hagman and P. Kierkegaard. *Acta Chem. Scan*, 22:1822, 1966.

[6] J. Alamo, R. Roy. *J. Mat. Sci*, 21:444, 1986.

[7] H.Y. Hong. *Mat. Res. Bull*, 11:173, 1976.

[8] M. Pintard -Scrépel, F.D' Yvoire, F. Remy. *Comp.Rend.*, 286, Serie C:381, 1978.

[9] C. Delmas, R. Olazcuaga, F. Cherkaoui, R. Brochu, G.L. Flem. *C.R. Acad, SC. Paris*, 287, Serie C:169, 1978.

[10] F. d'Yvoire, M. Pintard- Scrépel, E. Bretey, M. de la Rochere. *Sol. Stat. Ionics*, 9/10:851, 1983.

[11] F. d'Yvoire, M. Pintard- Scrépel, E. Bretey. *Sol. Stat. Ionics*, 18/19:502, 1986.

[12] C. Masquelier, C. Wurm, J. Rodriguez-Cavajal, J. Gaubicher, L. Nazar. *Chem. Mater*, 12:525, 2000.

[13] C. Delmas, F. Cherkaoui, P. Hagenmuller. *Mat. Res. Bull*, 21:469, 1986.

[14] A.S Andersson, B. Kalska, P. Eyob, D. Aernout, L. Haggstrom, J.O. Thomas. *Sol. Stat. Ionics.*, 140:63, 2001.

[15] G. Lucazeau, M. Barj, J.L. Soubeyroux, A.J. Dianoux, C. Delmas. *Sol.Stat.Ionics.*, 18/19:959, 1986.

[16] D. Beltan-Porter, R. Olazcuaga, L. Fournes, F. Menil, G.Le. Flem. *Rev.Phys. Appl.*, 15:1155, 1980.

[17] D. Beltan-Porter, R. Olazcuaga, C. Delmas, F. Cherkaoui, R. Brochu, G.Le. Flem. *Rev. Chim. Minéral.*, 17:458, 1980.

[18] N. Fanjat, J.L. Soubeyroux,. *J. Mag. Mag. Mat.*, 104-107:933, 1992.

[19] C. Greaves, P.R. Slater, M. Slaski, C.M. Muirhead. *Physica B*, 194-196:199, 1994.

[20] A.S. Anderson, B. Kalska, P. Jonsson, L. Haggstrom, P. Norblad, R. Tellgren, J.O. Thomas. *J. Mat. Chem*, 10:2542, 2000.

[21] F. Cherkaoui. *Etude cristallo-chimique et physique de nouvelles familles de mate?riaux de type nasicon*. PhD thesis, University of Bordeaux 1, 1985.

[22] A. Le Bail, H. Duroy, J.L. Fourquet. *Mat. Res. Bull*, 23:447, 1998.

[23] J. Rodriguez-Carvajal. Technical report, ILL internal report, FULLPROF computer program, 1993.

[24] R. Masse. *Bull. Soc. Fr. Minéral. Cristallogr*, 95:405, 1972.

[25] A. Housni, I. Mansouri, A.El. Jazouli, R. Olazcuaga, L. Fournes, G.LE. Flem. *Ann. Chim.Sci.Mat*, 23:73, 1998.

[26] A. Leclaire, M.M. Borel, A. Grandin and B. Raveau. *Eur. J. Sol. Sta. Inorg. Chem*, 26:561, 1989.

[27] L. Hagman and P. Kierkegraad. *Acta. Chem. Scand*, 28:1822, 1968.

[28] A.J.M.Duisenberg, L.M.J. Krron - Batenburg, A.M.M. Schreurs. *J. Appl. Crystallogr*, 36:220, 2003.

[29] R. Retoux, F. Studer, C. Michel, B. Raveau, A. Fontaine and E. Dartyge. *Phy. Rev. B*, 41:193, 1990.

[30] S. A. Sunshine, T. Siegrist, L. F. Schneemeyer, D. W. Murphy, R. J. Cava, et al. *Phys. Rev.B.*, 38:893, 1988.

[31] Y-I. Jang, F.C. Chou, Y.M. Chiang. *APP. Phys. Lett*, 74:2504, 1999.

[32] M. Giot, A. Pautrat, G. André, D. Saurel, M. Hervieu, J. Rodriguez-Carvajal. *Phys.Rev.B.*, 77:134445, 2008.

[33] L.W. Finger, R.M. Hazen. *J. App. Phys*, 51:5362, 1980.

Chapter 6

VI. Magnetic field induced polar state at the antiferromagnetic transition in Co_3O_4:

VI.1. Introduction:

Geometrically frustrated magnets are gaining a lot of attention due to their display of interesting array of phenomenon like spin glass, spin liquids, spin ice and cooperative paramagnets to name a few [1] [2]. Apart from the above mentioned phenomenon many geometrically frustrated magnets have been found to show multiferroic behavior which has coexistence of more than one order parameter (ferroelectricity, ferromagnetic and ferroelasticity) in a single phase [3] [4]. Frustration is usually found in lattice with triangular or tetrahedral arrangement but not restricted to only these two. Typical lattice which display geometric frustration are delafossite, pyrochlore, kagome and spinels. Accordingly many delafossites like $CuFeO_2$ [5], $CuFe_{1-X}Al_XO_2$ [6], $ACrO_2$ (A= Cu, Ag) and rocksalt structure $ACrO_2$ (A=Li, Na) [7] show spin driven ferroelectricity and antiferroelectricity respectively due to the frustration in the triangular lattice. Recently many spinels like ACr_2O_4 (A=Fe, Co, Mn), $CdCr_2S_4$and CdV_2O_4 were shown to possess ferroelectricity in the magnetically ordered state [4], [9], [10]. Thus spinels are a good candidate for finding novel multiferroics in contrast to the earlier belief that spinels scarce display ferroelectricity [11]. However the ferroelectricity here is not an independent phenomenon (occurs concomitantly with magnetic ordering) therefore its strength is several orders smaller than the conventional ferroelectrics like $BaTiO_3$ or PZT. Nevertheless the magnetoelectric coupling in spinels is very strong which is unlike $BiFeO_3$ which show weak magnetoelectric effect since the ferroelectricity and magnetic order appears at different temperature.

First we will see how geometric frustration can arise in a real crystalline material followed by the description for the specific case of spinels. Later on we will discuss the mechanism for the induction of polarization by the magnetic order. Magnetic frustration appears when a large fraction of magnetic sites in a lattice is subject to competing or contradictory constraints [12]. If the frustration is essentially due to the geometry or topology of the lattice then it is called geometric frustration [13]. This usually occurs in lattice based on triangles geometry [1]. Figure 1 gives some of the lattice arrangement which lead to geometric frustration. If the magnetic ions are arranged in a triangular manner in the lattice (fig 1 (a)) they order antiferromagentically due to the minimum in energy. If the first two spins align antiparallely then the third spin is frustrated because it has two possible orientations with the same energy. This type of frustration is also seen in tetrahedral arrangement of

magnetic ions (fig 1(b)). Here only two of the four equivalent nearest neighbour (n.n) interactions are satisfied leading to frustration. If only n.n interactions are considered in square planar plaquette (fig 1(c)) then there is no frustration as all the spins are antiparallel to each other. In three dimensions corner and edge shared triangular and the corner and edge sharing tetrahedral lattices are typical examplesof frustrated lattices. The former is called Kagome lattice and the corner shared tetrahedra lattice occurs in pyrochlore and spinel structures.

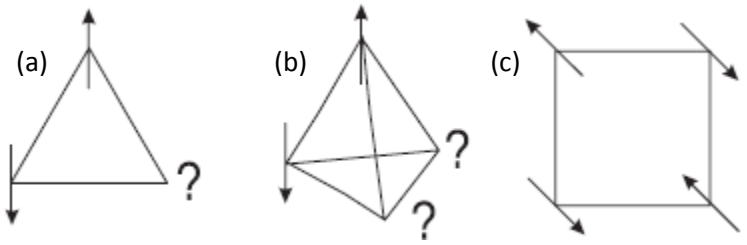

Figure VI-1: Frustrated geometries (a) triangular, (b) tetrahedral, (c) square planar. Adapted from ref [14].

From here on only the spinel compounds will be discussed: The ones which have the chemical formula AB_2X_4 (X = O, S, Se). The spinel oxide structure consists of two structural units, AO_4 tetrahedra and BO_6octahedra as shown in fig VI -2(a). The A site ions form a diamond lattice which can be viewed as two interpenetrating face centred cubic (fcc) sublattices shifted by one quarter along the space diagonal which is shown in fig VI -2(b). The B site ions form three dimensional networks of corner sharing tetrahedra as shown in fig VI -2(c) and it is known as pyrochlore lattice. The base of these tetrahedral forms Kagome lattice (fig VI -2(d)). The antiferromagnetically coupled spins placed on the pyrochlore lattice give rise to very strong frustration because of the triangle based tetrahedral geometry. Furthermore diamond sublattice formed by A site ions can also give rise to appreciable frustration. This is because here the next nearest neighbour coupling becomes important because the magnetic coupling between A ions are mediated by complex exchange path including O-B-O links. Some examples of A site frustrated spinel compounds are MAl_2O_4 where A = CO, Fe, Mn [15]

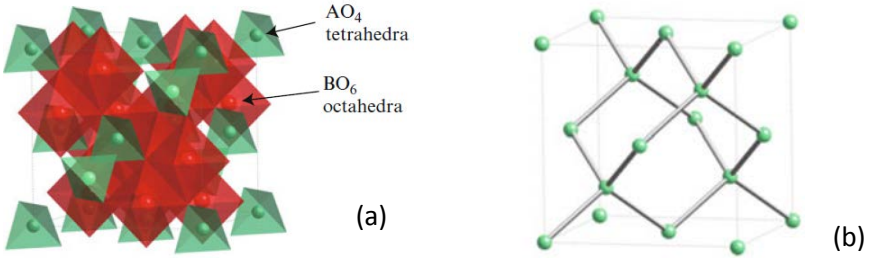

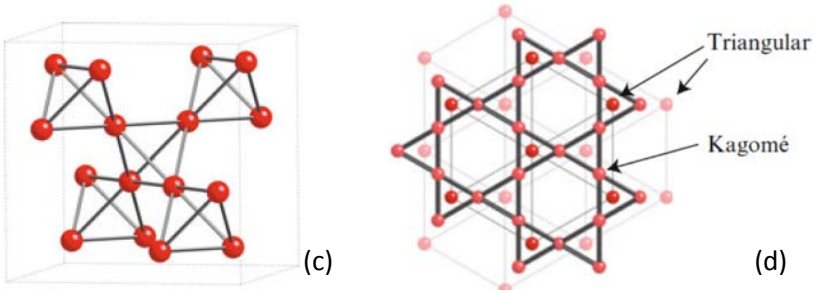

Figure VI-2: (a) Framework of spinel structure with AO_4tetrehedra and BO_6octahedra, (b) Diamond lattice as sublattice of A ions, (c) Pyrochlore lattice as B sublattice, (d) Kagome lattice as part of B sublattice when viewed in <111> direction. Adapted from reference [2].

Several types of spin arrangement can bring about induction of ferroelectricity and they are shown in fig VI – 3 (a-f) [16]. The collinear magnetic order (fig VI – 3(a)) observed in up-up-down-down spin arrangement along the atomically alternating A-B lattice can break inverse symmetry and induce polarization due to exchange striction. In non collinear magnetic order, polarization is induced following the spin current or inverse Dzyaloshinskii – Moriya (DM) model (fig VI – 3(b)) [17] [18].

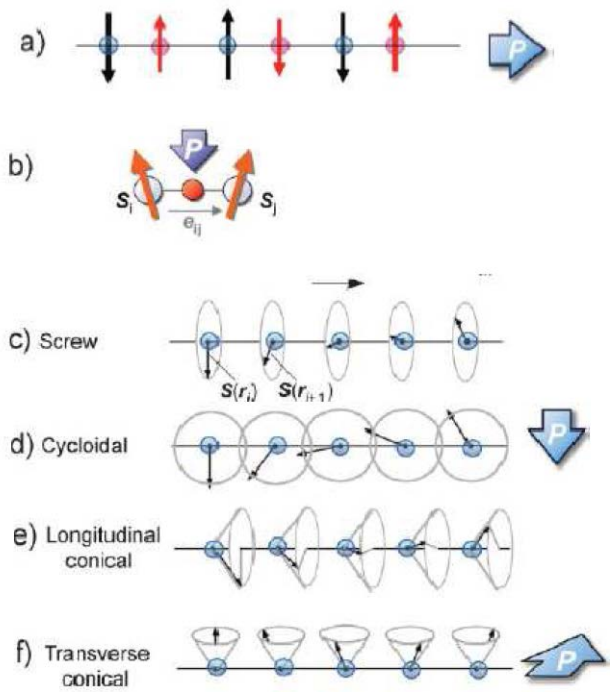

Figure VI-3: Different spin arrangement which give rise to polarization (a) Collinear, (b) non collinear, (c) proper screw type (d) cycloidal, (e) longitudinal conical and (f) transverse conical. The spin arrangements from c to f are part of spiral magnetic structures. The blue arrows give the direction of induced polarization. Adapted from reference [16].

According to spin current model the overlap of electron wave function between the two atomic sites with canted spins generates electronic polarization via the spin –orbit interaction. Analogous to charge current producing the magnetic field spin current produces an electric field or electric

polarization. Therefore a spontaneous spin current flows between the mutually canted spin sites. The direction of polarization is given by

$$P = a \sum_{<ij>} e_{ij} \times (S_i \times S_j) \qquad \textbf{EqVI-1}$$

Here e_{ij} is the unit vector connecting the neighbouring spins S_i and S_j and the proportional constant 'a' is determined by the spin – orbit and spin – exchange interactions as well as the possible spin – lattice coupling term. The sign of P depends on the clockwise or counter clockwise rotation of spin along the spin propagation axis. Inverse DM interaction is based on the conventional DM interaction according to that non centrosymmetric bond causes canting of interacting spins. In contrast to this in inverse DM model states that canted spins may displace the intervening ions connecting the magnetic ions leading to generation of polarization. The spiral magnetic structures shown in fig VI – 3 (c –f) like proper screw type, cycloidal and conical can give rise to electrical polarization based on these models. There are also other spin arrangements which do not follow these models yet give rise to polarization. A complete discussion of all these mechanism is out of scope of this present thesis.

With respect to the present chapter we will see an example of magnetically induced ferroelectricity in $CoCr_2O_4$. The structure of $CoCr_2O_4$ is cubic with space group Fd-3m. Co^{2+} ions are tetrahedrally coordinated by oxygen ions at A (8a) site and Co^{3+} ions are octahedrally coordinated by oxygen ions at B (16d) site [19]. The frustration factor defined by θ_{CW}/T_N is about 7 and therefore frustration becomes important here [20]. This spinel undergoes a ferromagnetic transition at T_C = 93 K; upon further lowering temperature a transition to transverse conical spin state with an incommensurate propagation vector of [q q 0] (q = 0.63) takes place at 26 K. With further decrease in temperature a lock –in transition occurs without much change to the q value.Yamasaki et al found spontanoues polarization (P) along with spontaneous magnetization (M) in $CoCr_2O_4$ [4]. Here the spontaneous magnetization directs along [0 0 1] while the spontaneous polarization was expected to be along [1-1 0] which is perpendicular to the spontaneous magnetization direction. After ME cooling procedure P arises below 26 k i.e. in transverse conical spin state [4]. The direction of P was seen to reverse along with the cooling electric field therefore the observed P was confirmed to be spontaneous polarization. However the obtained P is about 2 $\mu c/cm^2$ which is much smaller than the conventional ferroelectrics like $BaTiO_3$. Nevertheless $CoCr_2O_4$ exhibit some interesting property .i.e. the direction of polarization was reversed with reversal of magnetic field. Furthermore they showed that both ferromagnetic and ferroelectric domain wall were clamped. Such a strong coupling between magnetization and polarization is indeed very interesting for practical application. Similar spinels with A site ion with Fe and Ni were shown to be magnetoelectric as well by Maignan et al [6].

So far, most of the spinels reported to show magnetoelectric (ME) coupling are attributed to the contributions from the magnetic B-site ion; therefore we made an attempt to study Co_3O_4 in which the magnetism has its origin in the A-site Co^{2+} ions since Co^{3+} in octahedral site is diamagnetic. Furthermore presence of ME and magneto dielectric coupling in Fe_3O_4 [22] [23] and Mn_3O_4 [69] respectively has prompted us to investigate Co_3O_4 in detail for ME coupling.

VI.2. Experimental Methods:

VI.2.1. Sample preparation and structural characterization:

Co_3O_4 powder was synthesized by heating Cobalt carbonate ($CoCO_3$) up to 600°c for 12 hrs. The powder was then pressed into pellets and then sintered for 15 hrs at 800°C. Two different pellets CO1 and CO2 were prepared. The sintering temperature is same for both pellets but the sample CO1 was furnace cooled and the sample CO2 was quenched. This is to study the effect of oxygen vacancies or conductivity on the sample dielectric behavior. Figure VI – 4 gives the profile matching of the regular X-ray pattern in space group $Fd\bar{3}m$ for sample CO1. All the peaks correspond to cubic phase of Co_3O_4 with space group $Fd\bar{3}m$. The lattice constant is given by a = 8.09 $\pm$ 0.02 Å. Sample CO2 is the same as sample CO1.

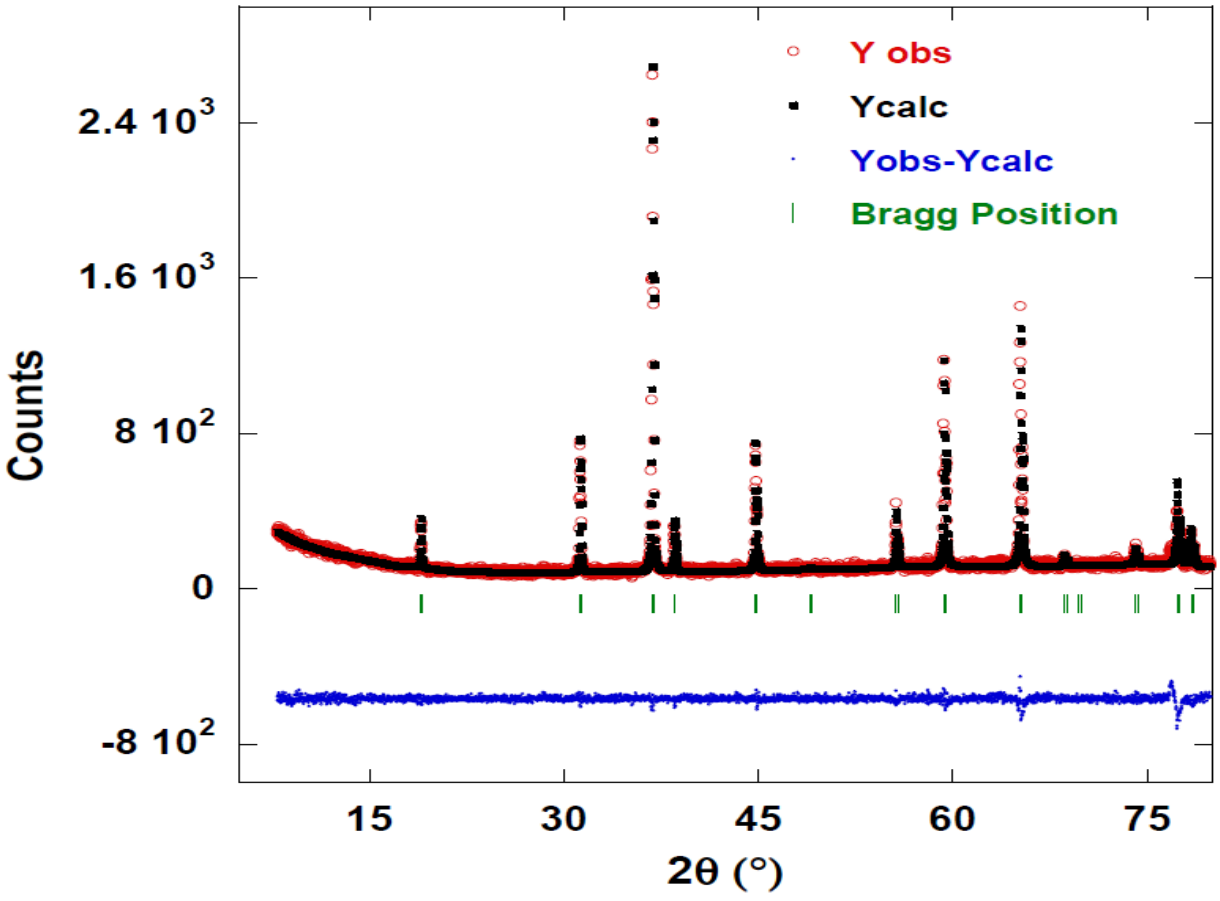

Figure VI-4: The observed and calculated pattern of the regular X – ray diffraction for sample CO1.

VI.2.2. Scanning electron microscopy (SEM):

SEM was done to study the microstructure and particle size of Co_3O_4. Fig VI – 5 gives some SEM images of Co_3O_4 sintered pellet. It can be seen that agglomerates have started to form. These agglomerates were typically in the spherical shape with an average diameter of 20 – 30 μm. However the individual particle size is much smaller with distribution in the range of 150 – 600 nm. The back scattered image did not reveal any impurity in the sample (not shown).

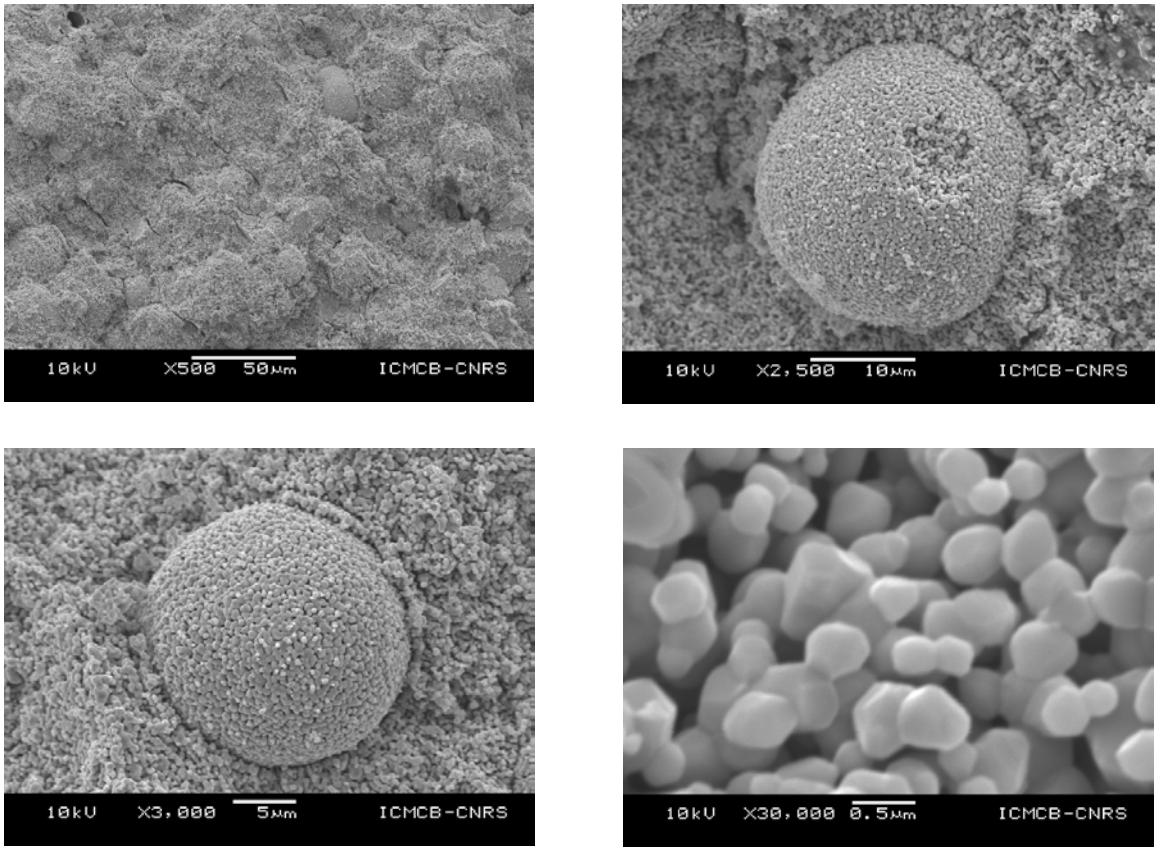

Figure VI-5: SEM images of Co_3O_4 ceramics. Some agglomerates are in the spherical shape with average diameter of 20-30 μm; particles size distribution within the sample is in the range of 150-600 nm.

VI.2.3. Bulk Characterization:

The sintered pellets were gold sputtered to make electrodes and thin silver wires were glued on each electrode with the help of silver paste to make electrical contacts. For dielectric measurements under cryogenic temperatures the sample was put in the sample holder of Physical Property Measurement System (PPMS) Quantum Design which was then connected to the Wayne Kerr 6500B impedance/gain phase analyzer which can scan frequency in the range of 100 Hz to 10 MHz. PPMS can regulate temperature from 2 K to 380 K and magnetic field up to 90 kOe or 9 Tesla. A Stanford Research Systems PS 350 high voltage DC power supply was used to pole the sample and a Keithley

6517B electrometer was used to measure the pyroelectric current. Magnetic measurements on the samples were done using Magnetic Property Measurement System (MPMS) Quantum Design. This instrument can reach upto 50 kOe (or 5 Tesla) in magnetic field and temperature in the range of 1.8 K to 400 K. The same set up can be used to perform hysteresis and ac magnetic measurements as well. Heat capacity measurements were performed by a relaxation method with the PPMS and using two tau model analysis. Data were taken in the temperature range 2 – 60 K. For these measurements samples were a plate obtained from compressing the powder samples. ESR measurements were performed using an X-band Bruker spectrometer operating at 9.4 GHz. An Oxford Instruments ESR 9 He cryostat operating in the temperature range 4 – 300 K was used for temperature dependence studies of ESR spectra intensities.

VI.3. Results and discussion:

VI.3.1. Magnetic susceptibility and magnetization:

The magnetic susceptibility of a polycrystalline Co_3O_4 sample was measured in zero field cooled (ZFC) and field cooled (FC) conditions with an applied field of H = 100 Oe between 300 to 5 K. Fig VI – 6 shows the temperature dependence of susceptibility and inverse susceptibility for Co_3O_4 in ZFC mode. With decrease in temperature susceptibility increases monotonically and at about 40 K shows a broad maximum after which it decreases. At the same temperature inverse susceptibility shows a broad minimum. Inset to the figure shows the slope of the susceptibility ($d\chi/dT$) as a function of temperature. A sharp maximum at about 30 K is apparent indicating the antiferromagnetic transition temperature T_N. Above 100 K the inverse susceptibility is linear and can be represented by the Curie – Weiss paramagnetic behavior which is given by

$$\chi(T) = \chi_0 + \frac{C}{T - \theta_W} \qquad \textbf{EqVI-2}$$

Where χ_0 is the temperature independent susceptibility, C is the Curie-Weiss constant and θ is the paramagnetic Curie temperature. The fit for χ(T) curve using Eq (VI – 2) over the temperature range 100 to 300 K yields θ_W = -121 K $\pm$ 2, χ_0 = 1.0 X 10^{-4} emu/(mol –Oe) and C = 2.79$\pm$0.5 K emu/(mol Co^{2+}). The effective magnetic moment per mol Co (μ_{eff}) is calculated by using the formula

$$C = N\mu_{eff}^2/3k_B \qquad \textbf{EqVI-3}$$

where N is the density of Co^{2+} ions per mole and k_B is the Boltzmann constant. We obtain μ_{eff}=4.72(2) μ_B where μ_B is the Bohr magneton, which is greater than the spin only value for free Co^{2+} ions (3.87 μ_B), indicating spin – orbit coupling of Co^{2+}ions contribution as described by Roth [25]. The obtained value of μ_{eff} and θ_W is consistent with the literature [26] [27]. The Co^{3+}ions in 16d position are in

octahedral crystal field which split up the 3d orbitals in to higher e_g and lower t_{2g} levels. Due to the large gap between these levels in octahedral symmetry, the six d electrons of Co^{3+} ($3d^6$) cation fill up the three lower energy t_{2g} levels and therefore Co^{3+} has zero magnetic moment in Co_3O_4. Only Co^{2+} ions in tetrahedral (8a) position is contributing to the magnetic behavior of Co_3O_4 [25]. Accordingly the estimated μ_{eff} is about 4.72 μ_B.

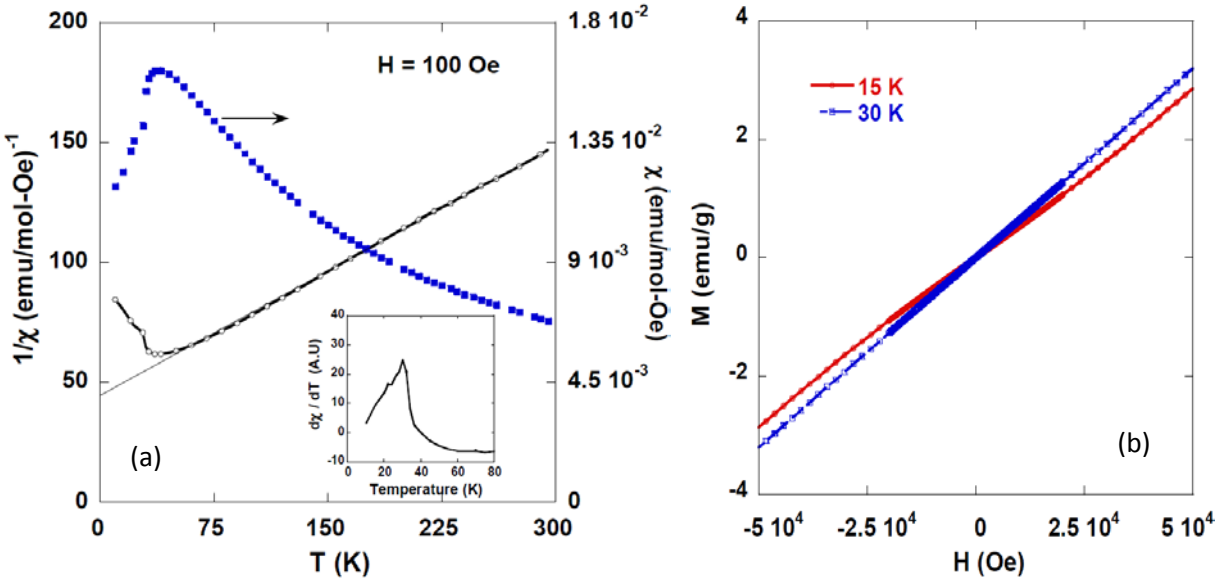

Figure VI-6: (a) Susceptibility and inverse susceptibility as a function of temperature for Co_3O_4 in ZFC mode. Inset shows the slope of susceptibility ($d\chi/dT$) as a function of T. (b) magnetization as a function of applied field for Co_3O_4 at 15 and 30 K.

Magnetization curve as a function of applied field is shown in figure VI – 6 (b). At 30 K magnetization displays a linear relationship with the applied field and at lower temperature magnetization slightly deviates from linearity as seen at 15 K.

VI.3.2. Conductivity Measurements:

The behavior of conductivity as a function of temperature was studied with the impedance/gain phase analyzer between 300 and 5 K in PPMS. Figure VI -7 (a – d) shows the reactance as a function of resistance over the frequency range 100 Hz to 1 MHz measured on slowly cooled CO1 sample. At 300 K (fig Vi – 7 (a)) traces of three semicircles is seen which could be attributed to bulk, grain boundary and electrode interface from high frequency(far left) to low frequency (far right) respectively [28]. A detailed analysis of these different contributions is not needed for the present thesis; we give only the qualitative picture. At room temperature the resistance is quite low in the range of few hundreds of ohms. As the temperature is decreased, resistance of the bulk increases dramatically at 100 K as shown in fig VI – 7 (b). With further decrease in temperature at about 30 K bulk resistance becomes very large that only portion of the semicircle can be seen in the available

frequency window as shown in fig VI – 7(c). Below 30 K resistance can no longer be measured and sample becomes very insulating fig VI – 7(d). It is important to notice here that the transition from semiconducting to insulating behavior happens after the long range antiferromagnetic order sets in at 30 K. Similarly dc resistivity could not be measured below 60 K due to very high resistance at low temperatures (not shown).

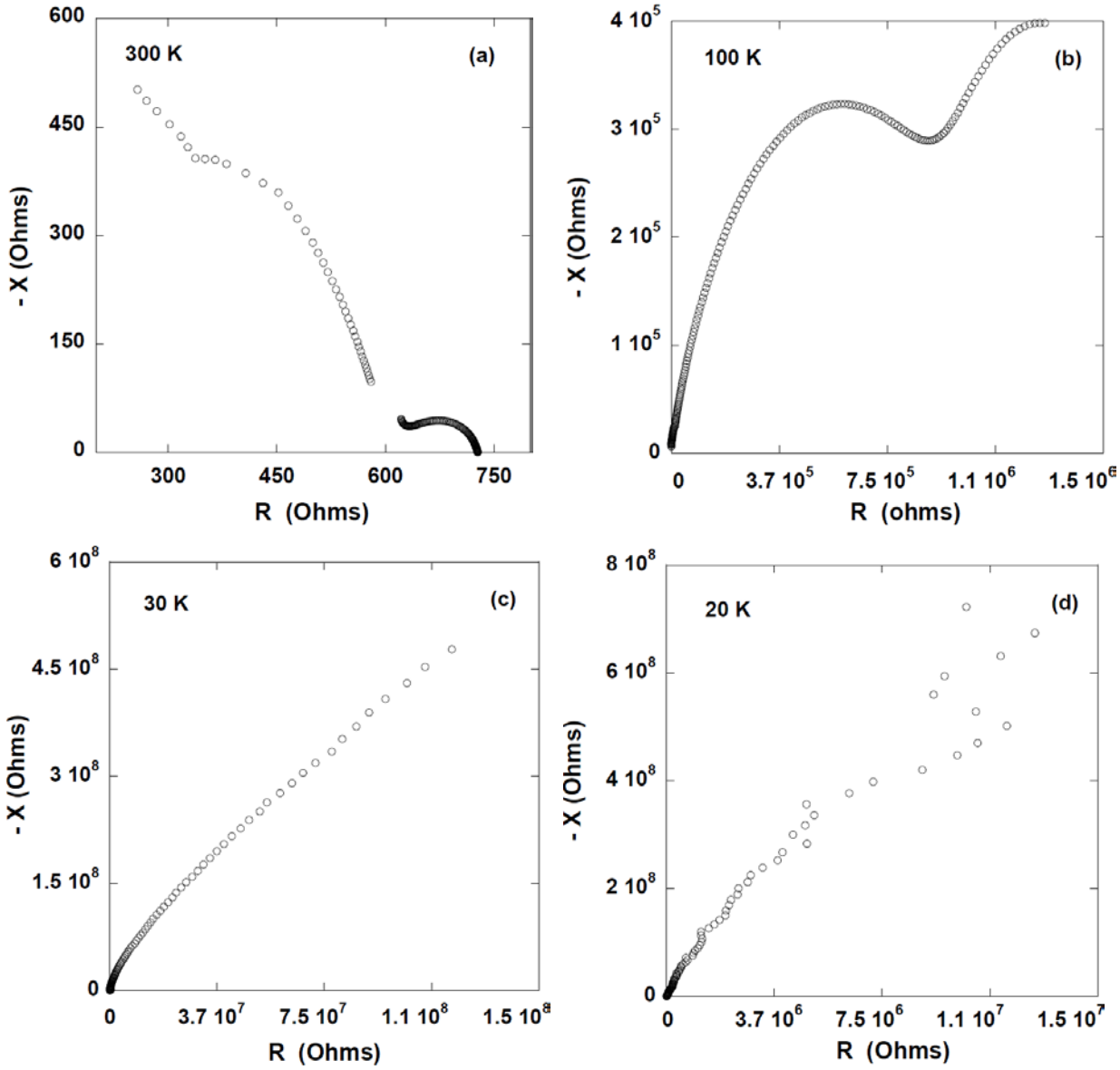

Figure VI-7: Reactance as a function of resistance at several temperatures for CO1 sample. (a) 300 K, (b) 100 K, (c) 30 k and (d) 20 K. Notice that below 30 K resistance cannot be measured.

VI.3.3. Dielectric behavior of Co_3O_4 under magnetic field:

The conductivity measurement described above indicated an insulting behavior at low temperature and therefore dielectric properties were studied at low temperatures under magnetic field. The high temperature dielectric properties of Co_3O_4 were dominated by its high conductivity and they will not be discussed here. Prior to dielectric measurements the PPMS was calibrated as

described in chapter 2 to ensure that no external factors like electrode, sample holders etc. contributes to the sample dielectric behavior under magnetic field.

Figure VI – 8 (a) gives the temperature dependence of dielectric constant for sample CO1 with (45 kOe and 90 kOe) and without magnetic field at 11 kHz. Dielectric constant increases slowly till T_N and above that there is a steep rise which relates to the conductivity in the high temperature range. Under zero magnetic field (red curve) no particular anomaly was found at T_N but when the magnetic field of 45 kOe was applied a small sharp peak was visible at the magnetic transition and at 90 kOe the sharp anomaly is more pronounced. Furthermore below T_N the magnitude of the dielectric constant is enhanced by magnetic field down to the lowest temperature measured and above T_N dielectric constant with and without magnetic field merge showing that the observed effect is due to the appearance of long range magnetic order in Co_3O_4. The corresponding imaginary part of permittivity (ε'') remains almost constant and very low till 22 K above which it shows dramatic increase due to increase in conductivity (See fig VI – 8 (b)).

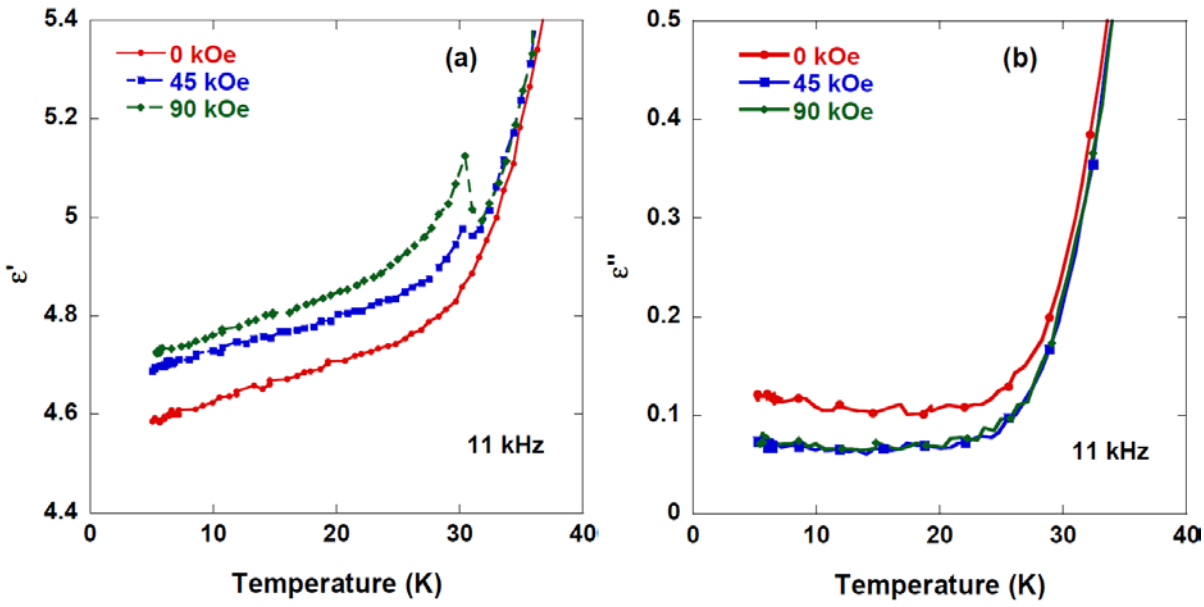

Figure VI-8: (a)Dielectric constant as a function of temperature for CO1 sample with (45 and 90 kOe) and without magnetic field at 11 kHz. (b) Corresponding imaginary part of permittivity as a function of temperature for the magnetic field and frequency given in figure (a). A sharp peak is induced in dielectric constant by the magnetic field at the magnetic transition temperature**.**

This increase in conductivity is associated with antiferromagnetic transition at 30 K as shown by conductivity measurements. Magnetic field did not give rise to any sharp anomalies in imaginary part of permittivity which is seen in the real part of permittivity. However magnetic field affect the magnitude of ε'' below T_N and it can be seen from fig VI – 8 (b) that magnetic field has slightly suppressed ε'' below 30 K compared to 0 kOe curve. The dielectric losses ($\tan\delta = \varepsilon''/\varepsilon'$) stay below 5 % at the magnetic transition (30 K) and below 2 % at 5 K. The observed peak in the real part

resembles that of ferroelectric peak in many ferroelectrics. One of the main features of the ferroelectric peak is that it is frequency independent. Such frequency independence of the observed peak in real part of permittivity is demonstrated in figure VI – 9 (a).

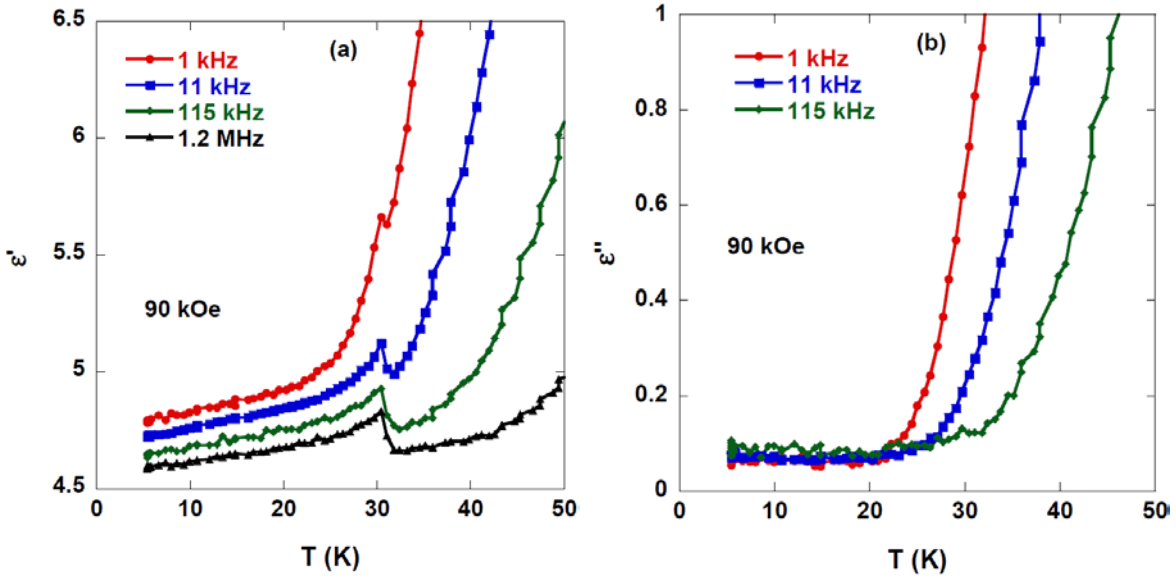

Figure VI-9: Temperature dependence of (a) real part and (b) imaginary part of permittivity for CO1 sample at several frequencies under magnetic field (90 kOe). Dielectric anomaly in real part shows frequency independence similar to ferroelectric type peaks. Below 22 K imaginary part remains constant for all frequencies.

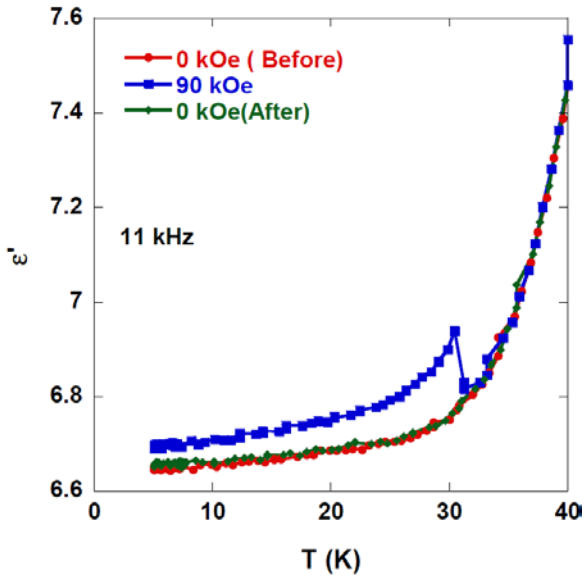

Figure VI-10: Dielectric constant as a function of temperature with and without magnetic field for CO2 sample at 11 kHz.

As the conductivity contribution to the dielectric constant decreases with increase in frequency the ferroelectric type peak is clearly seen. The drastic increase of dielectric constant above T_N is due to the conductivity. The temperature dependence of the imaginary part of permittivity at several

frequency shows that all the curve merge below 22 K and it stays constant till 5 K (figure VI – 9 (b)). To confirm the reproducibility of the results dielectric measurements were performed on CO2 sample. Figure VI – 10 gives the dielectric constant as a function of temperature with and without magnetic field for CO2 sample. A dielectric peak under magnetic field is observed at 30 K similar to CO1 sample. Furthermore the dielectric constant before and after the application of magnetic field did not show any peak and were the same corroborating that the results were reproducible. The dielectric peak also showed frequency independence (not shown). Furthermore isothermal dielectric measurements (not shown) reveal that neither the real part nor losses show a relaxation versus time with and without magnetic field unlike the previous report by Iliev et al. [29].

VI.3.3.1. Critical field for the induction of polar state in Co_3O_4:

The application of large magnetic field of 45 and 90 kOe induced a ferroelectric type anomaly in the dielectric constant of Co_3O_4. However low field measurement of dielectric properties should be performed to deduce the critical field at which the polar state in Co_3O_4 is induced. Figure VI – 11 gives the dielectric constant as a function of temperature at different magnetic fields for Co_3O_4.It can be seen that a magnetic field of 20 kOe has induced a sharp peak in the capacitance. However the magnitude of the peak is not strong and it is close to the low field dielectric constant at 10 kOe which does not display any peak in the capacitance. The dielectric peak due to 40 kOe magnetic field is larger in magnitude and above the background capacitance compared to peaks by lower magnetic fields. Therefore critical field can be taken as 40 kOe for the induction of polar state in Co_3O_4.

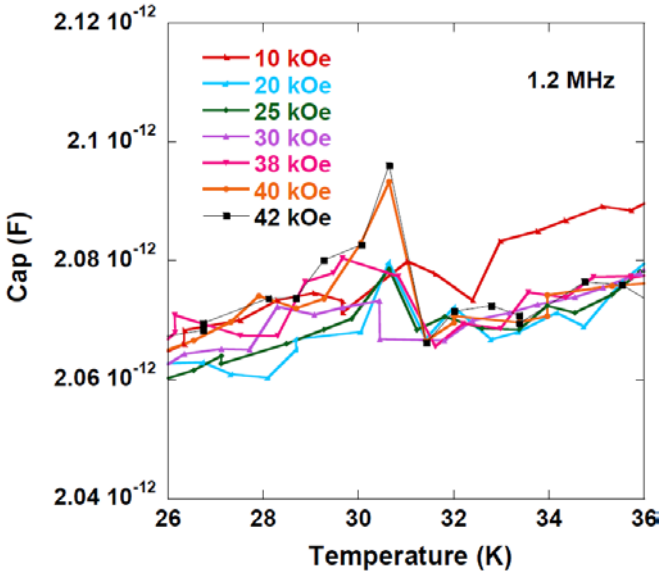

Figure VI-11: Capacitance as a function of temperature under different magnetic fields in Co_3O_4at 1.2 MHz.

VI.3.4. Pyroelectric Measurements:

For pyroelectric measurements a poling static field of ±641 kV/m was applied at 60 K during cooling which is the standard poling procedure for pyroelectric experiments in ferroelectric materials. At 5 K the poling electric field was removed and pyrocurrent as a function of temperature was measured during warming at 5 K/min. The effect of magnetic field on polarization was deduced by cooling the sample from 60 K under 90 kOe magnetic field as well as 641 kV/m electric field applied simultaneously. The polarization was measured during warming after removing electric field leaving the magnetic field intact. This procedure is called magnetoelectric (ME) cooling.

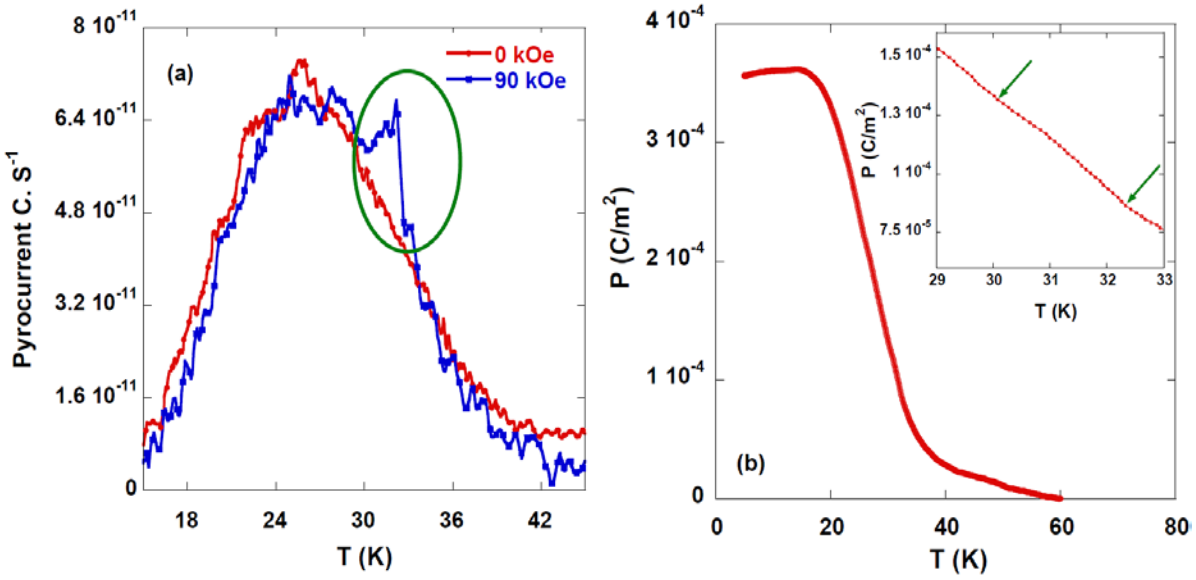

Figure VI-12: (a) Pyrocurrent as a function of temperature with 0 and 90 kOe magnetic field. A maximum is seen in both curves close to 26 K, in addition a sharp maximum is seen under 90 kOe magnetic field which is superimposed on the broad maximum. (b) Polarization versus temperature under 90 kOe magnetic field. Inset to (b) gives the zoom of polarization curve close to T_N and green arrows indicate contribution of magnetic field to the polarization seen as a small shoulder.

Figure VI – 12 (a) gives the pyrocurrent as a function of temperature for the sample CO1 with 0 and 90 kOe magnetic field. Maximum of the pyro current with and without magnetic field is around 26 K along with an additional sharp peak close to 32 K under 90 kOe magnetic field indicated by green circle. We ascribe the broad maximum to the change in conductivity happening in this temperature range and which is not altered by the magnetic field. On the other hand, we state that the sharp peak at 30K is associated with the polar or ferroelectric transition under magnetic field. Both the broad and sharp 30K anomalies can be reversed on reversing the sign of the poling electric field. The polarization under 90 kOe magnetic field computed from the pyro current is plotted as a function of temperature and shown in figure VI – 12 (b). A maximum polarization value of 350μC m^{-2} was obtained resulting from the integration of the broad pyroelectric anomaly, i.e. related to conductivity processes. On top of this contribution, the effect of magnetic field was superimposed which is clearly

demonstrated in the inset to the VI – 12 (b). A small shoulder marked by green arrows at T_N shows the contribution of 90 kOe magnetic field to the pyrocurrent. The polarization induced by magnetic field is about 40 μC m^{-2}which is comparable to the most of the known spinels which are found to show multiferroic effect (See table VI – 1). To better understand the microscopic origin of both the broad anomaly and the sharp magnetic field anomaly, we undertook ESR experiments.

Table VI-1: List of spinels with coupling between electrical and magnetic order.

Spinel Compound	Space Group	T_S (K)	T_N / T_C (K)	Magnetic order	T_F (K)	Polarization (μC/m^2)	Reference
$CoCr_2O_4$	Fd-3m	--	93 (ferri)	CL and transverse spiral at 26 K	26	2	[8]
$FeCr_2O_4$	Fd-3m	140 (C-T)	80 (ferri)	CL and conical at 35 K	--	35	[21] [30]
$NiCr_2O_4$	$I4_1/amd$		74 (ferri)	CL and CL AFM at 31 K	--	33	[21] [30]
$MnCr_2O_4$	Fd-3m	--	51 (ferri)	CL and conical at 16 K	--	MD	[30]
CdV_2O_4	Fd-3m	95 (C - T)	33 (AFM)	CL	same as T_N	5	[10]
$LiCuVO_4$	Imma	--	2.5 (AFM)	Helical	same as T_N	30	[31]
Mn_3O_4	$I4_1/amd$		42 (ferri)			MD	[24]
$ZnCr_2Se_4$	Fd3m	--	21.2 (AFM)	Proper Screw type	same as T_N	15 (underrotating H)	[32]
Co_3O_4	**Fd-3m**	**--**	**30 (AFM)**	**CL**	**same as T_N**	**40**	**Current thesis**

Definitions of symbols: T_S = structural transition, T_N = Neel temperature, T_C = ferro or ferrimagentic transition temperature, T_F = Ferroelectric transition temperature, AFM – antiferromagnetic, CL – collinear magnet, MD – Magnetodielectric.

VI.3.5. Electron Paramagnetic Resonance (EPR):

EPR spectra recorded at several temperatures in the zero field cooled (ZFC) regime are shown in fig VI - 13. Spectra of powder sample were similar to ceramics ones and are not shown. As expected in the case of anisotropic antiferromagnets, no EPR line was observed in the AFM phase of Co_3O_4 for both powder and ceramics samples.

Single line of Lorentzian shape at g=2.235 is observed for both samples at $T \geq 28$ K indicating phase transition from AFM to PM state. The observed difference in the T_N in comparison to reported in literature (40-30 K) is due to the particle size contribution: the size of grains in the ceramics sample is 100-600 nm (see SEM images in fig VI- 5). The resonance at g = 2.235 is originating from Co^{2+} ions

($3d^7$), in tetrahedral site of Co_3O_4. In such an environment Co^{2+} is in high spin state S=3/2 with fully filled low lying e_g orbitals and the 3 remaining electrons in t_{2g} orbitals. Magnetic moment of Co_3O_4 is arising mainly from Co^{2+} spins and spin-orbit coupling. The intensity of the resonance is high and very similar in ceramics and powder samples which suggest equivalent concentration of centers in both samples.

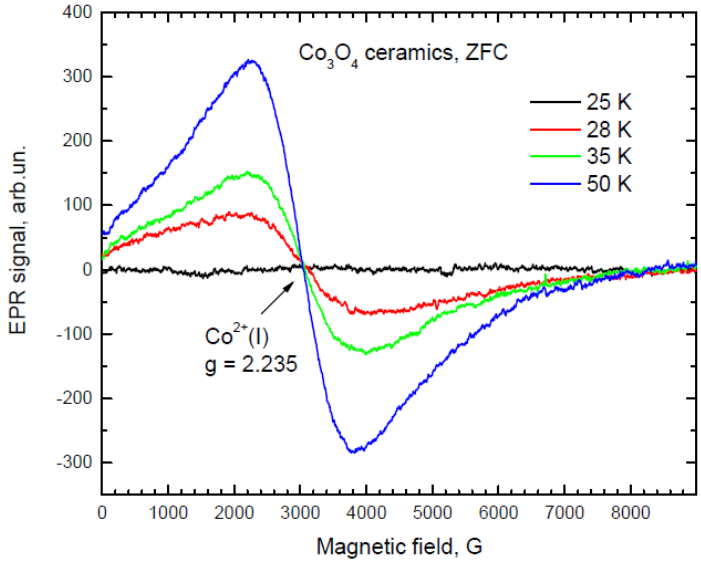

Figure VI-13: First derivative of standard (sample was cooled down to 4 K and after magnetic field was applied to record spectra) EPR spectra at several temperatures recorded for the ceramics sample.

As changes in dielectric and magnetic properties of Co_3O_4were observed in FC regime, we also performed EPR experiments in FC regime: at room temperature magnetic field of 6000 or 9000 G was applied and samples were cooled down to 4 K prior to each EPR measurements. Some spectra recorded below and above T_N in ZFC and FC regimes are presented in figure VI – 14 (a & b). Figure VI – 14 (c) shows the spectra in FC regime for a magnetic field strength of 6000 and 9000 G. Inset to fig VI – 14 (c) highlights a significant change in the intensity of the low magnetic field resonance (at g=5.072) marked as Co^{2+}(II); central resonance at g=2.235 is slightly decreased in peak-to-peak intensity.

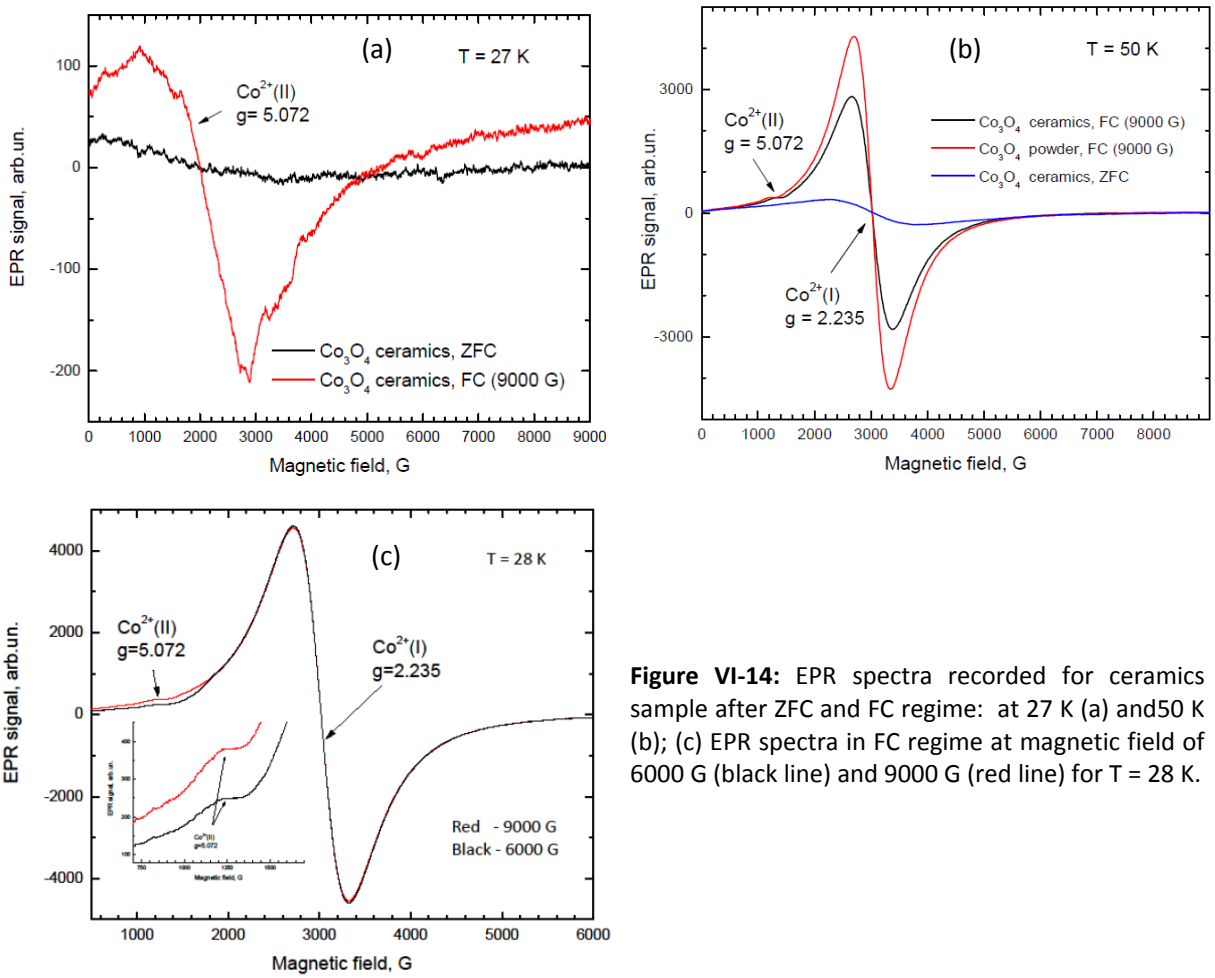

Figure VI-14: EPR spectra recorded for ceramics sample after ZFC and FC regime: at 27 K (a) and50 K (b); (c) EPR spectra in FC regime at magnetic field of 6000 G (black line) and 9000 G (red line) for T = 28 K.

This reflects redistribution of an amount of defects contributing to the EPR. The increase of the resonance intensity with the magnitude of the applied magnetic field is in agreement with an intermediate strength of the exchange interaction. Magnetic field induced similar effects on both powder and ceramics samples: (i) below T_N a new broad resonance is observed in low magnetic field region (0 - 3000 G); (ii) above T_N new resonance is detected on the left hand wing of the main resonance at g=5.072.

From EPR results we can conclude: (i) valence states of both Co^{2+} and Co^{3+} ions are not changing under externally applied magnetic field, e.g. no direct charge localization at cobalt ions around T_N; (ii) a broad resonance observed in the AFM phase and in FC regime is a signature of magnetic field influenced spin disordering in the material due to which total magnetic moments are not fully compensated and EPR is possible; (iii) new resonance appeared in FC regime and above T_N is most probable due to the p-d hybridization between cobalt and oxygen ion's orbitals leading to the d^8L state (where L denotes a hole at the oxygen 2p orbitals). In this case cobalt spins (or magnetic moment) are pointed toward oxygen ions and this orientation is kept in the AFM phase, so called canted spins which are generating electronic polarization via the spin-orbit interaction, and hence influences the materials dielectric and magnetic properties.

VI.3.6. The origin of dielectric anomaly under magnetic field in Co_3O_4:

The dielectric measurement shown in fig VI -8 indicates that a ferroelectric like anomaly in real part of permittivity is induced only under magnetic field. A critical field of 40 kOe is required to induce such an anomaly as seen from fig VI – 11. This anomaly becomes stronger with field up to the maximum of 90 kOe. Furthermore the anomaly is frequency independent and reproducible as shown in fig VI – (9 & 10). This calls for the anomaly to be identified as ferroelectric phase transition. However lack of evidence from piezoelectric and hysteresis measurements forbade us from assigning this anomaly to be ferroelectric, instead we will call this as polar anomaly. In addition the observed anomaly happens exactly at the temperature where Co_3O_4 undergoes magnetic transition from paramagnetic to antiferromagnetic state (~30 K). Hence there is a coupling between magnetic and electrical property in Co_3O_4 under field cooled condition. This coupling is further evidenced by polarization measurement which shows a broad peak due to the decrease in conductivity and a sharp peak at 32 K observed only under field cooling (see fig VI -12 (a)). The induced polarization under magnetic field is comparable to other spinel multiferroics as shown from table VI -1. Furthermore the critical field for the induction of polar state in Co_3O_4 is about 40 kOe reflecting the same phenomenon as $CuFeO_2$ where the threshold field is 65 kOe [5].

The coupling between electrical and magnetic property could be extrinsic or intrinsic. From the dielectric measurements it can be seen that the imaginary part of permittivity and dielectric losses (< 5%) are low in the temperature range where the polar anomaly appears (see fig VI -8 & 9). In the same temperature range polarization starts to appear which reaches a maximum at 26 K. This lead us to infer that the increase in polarization is mostly due to the charge localization with decrease in temperature and under the application of electric field a space charge is created shown as a black curve in fig VI -15. This space charge is disturbed when a magnetic field of high magnitude is applied which lead to the shift in the space charge layer shown as a red curve in fig VI -15. This in turn is transferred into an anomaly in the dielectric constant. Therefore the Catalan model based on the magenetoresistive artifact must be invoked similar to the tuning of polaron losses and artificial magnetocapacitance in Fe doped $BaTiO_3$ seen in Chapter 3 [1] [2].

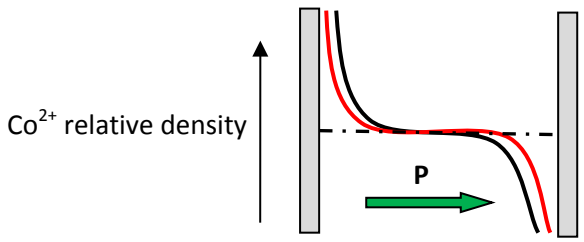

Figure VI-15: Space charge distribution in Co_3O_4 under electric field only (black curve) and shift of space charge seen as red curve due to simultaneously application of electric and magnetic field.

The above explanation based on charge localization is valid from the view point of dielectric and polarization measurement only which is more macroscopic. However this model is not entirely supported by our results from EPR. Let us consider that in case of electron localization of $Co^{3+} \rightarrow Co^{2+}$ significant increase in the EPR lines intensity has to be observed below 30 K which is not the case and also electron localization at Co^{2+} is not possible as it will give an unusual valence state of cobalt. Furthermore in Co_3O_4 electronic conductivity is dominant and therefore hole conductivity can be ignored. These results from EPR point towards a more intrinsic coupling between electrical and magnetic property in Co_3O_4. Then the obvious question is how does an intrinsic polar state is created under magnetic field, as the space group of Co_3O_4 is centrosymmetric.

From fig VI -14 (b) it can be seen that above Neel temperature a strong resonance at g = 2.235 attributed to paramagnetic Co^{2+} ions in tetrahedral environment is seen. A weak resonance is seen at g = 5.072 and it is superimposed on the strong resonance. This scenario is same as the pyro current where a sharp peak due to ME cooling is super imposed on broad maximum. This weak resonance is observed as a broad resonance at 27 K under FC regime (see fig VI – 14 (a)). Generally no EPR line should be observed at this temperature as the Co_3O_4 is in antiferromagnetic state. Then the presence of broad resonance suggests that there are uncompensated spins due to canting of antiferromagnetic moments under magnetic field cooling. The polarization can then appear based on the mechanism explained in spin current and inverse Dzyaloshinskii – Moriya (DM) model described by Katsura et al and Sergienko et al respectively [17] [18]. The fact that the weak resonance at g = 5.072 is seen above Neel temperature (where the spin orientation is expected to be random) is due to pinning of spins owing to the p-d hybridization between oxygen and cobalt ions.

VI.3.7. Conclusion:

Co_3O_4 ceramics were investigated for multiferroic property using dielectric and pyroelectric measurements. The dielectric constant displays a ferroelectric type anomaly under magnetic field at 30 K where the Co_3O_4 undergoes antiferromagnetic transition. It also shows that the observed effect is reproducible. In addition pyroelectric current shows a broad maximum at 26 K due to decrease in conductivity and an additional sharp maximum observed only under ME cooling is superimposed on the broad maximum. To our knowledge such a distinct peak in pyroelectric current due to ME cooling is observed for the first time in any multiferroic materials. This shows that there is a coupling between electrical and magnetic property in Co_3O_4 which could be extrinsic or intrinsic. However the evidence from the EPR results shows that canting of antiferromagentic moments under magnetic field cooling induces polarization based on spin current model. Therefore the observed effect is more

intrinsic to Co_3O_4. These results are very interesting as it is observed on simple oxides which have been investigated for several decades. This is a motivation for the scientific community to research for such exotic properties in already known simple oxides.

VI.4. References:

[1] J.E. Greedan. *J. Mat. Chem*, 11:37, 2001.

[2] C. Lacroix, P. Mendels and F. Mila, editors. *Introduction to Frustrated Magnetism*. Springer Series in Solid State Sciences, 2011.

[3] G. R. Blake, L. C. Chapon, P. G. Radaelli, S. Park, N. Hur, S-W. Cheong and J. Rodríguez-Carvajal. *Phys. Rev. B*, 71:214402, 2005.

[4] X. Fabrèges, S. Petit, I. Mirebeau, S. Pailhès, L. Pinsard, A. Forget, M. T. Fernandez-Diaz, and F. Porcher. *Phys. Rev. Lett*, 103:067204, 2009.

[5] T.Kimura, J.C. Lashley and A.P.Ramirez. *Phys. Rev. B*, 73:220401, 2006.

[6] S. Seki, Y. Yamasaki, Y. Shiomi, S. Iguchi, Y. Onose and Y. Tokura. *Phys. Rev. B*, 75:100403, 2007.

[7] S.Seki, Y.Onose and Y. Tokura. *Phys. Rev. Lett*, 101:067204, 2008.

[8] Y. Yamasaki, S. Miyasaka, Y. Kaneko, J.-P. He, T. Arima and Y. Tokura. *Phys. Rev. Lett*, 96:207204, 2006.

[9] J. Hemberger, P. Lunkenheimer, R. Fichtl, H.-A. Krug von Nidda, V. Tsurkan and A. Loidl. *Nature*, 434:364, 2005.

[10] G. Giovannetti, A. Stroppa, S. Picozzi, D. Baldomir, V. Pardo, S. Blanco-Canosa, F. Rivadulla, S. Jodlauk, D. Niermann, J. Rohrkamp, T. Lorenz, S. Streltsov, D. I. Khomskii and J. Hemberger. *Phys. Rev. B*, 83:060402, 2011.

[11] R. Seshadri. *Sol. Stat. Sci*, 8:259, 2006.

[12] G.Toulouse. *Commun. Phys*, 2:115, 1977.

[13] P.W. Anderson. *Phys. Rev*, 102:1008, 1956.

[14] A. Harrison. *J. Phys: Conden. Matt*, 16:S553, 2004.

[15] N. Tristan, J. Hemberger, A. Krimmel, H-A. Krug Von Nidda, V. Tsurkan and A. Loidl. *Phys. Rev. B*, 72:174404, 2005.

[16] Y. Tokura and S. Seki. *Adv. Mat*, 22:1554, 2010.

[17] H. Katsura, N. Nagosa and A.V. Balatsky. *Phys. Rev. Lett*, 95:057205, 2005.

[18] I. A. Sergienko and E. Dagotto. *Phys. Rev. B*, 73:094434, 2006.

[19] J.M.Hastings and L.M.Corliss. *Phys. Rev*, 126:556, 1962.

[20] K. Tomiyasu, J. Fukunaga and H. Suzuki. *Phys. Rev. B.*, 70:214434, 2004.

[21] A. Maignan, C. Martin, K. singh, Ch. Simon, O.I. Lebedev and S. Turner. *J. Sol. Stat. Chem*, doi: 10.1016/j.jssc.2012.01.063, 2012.

[22] G. T. Rado and J. M. Ferrari. *Phys. Rev. B*, 15:290, 1977.

[23] K. Yamauchi, T. Fukushima and S. Picozzi. *Phys. Rev. B*, 79:212404, 2009.

[24] R. Tackett, G. Lawes, B. C. Melot, M. Grossman, E. S. Toberer and R. Seshadri. *Phys. Rev. B*, 76:024409, 2007.

[25] W.L. Roth. *J. Phys. Chem. Solids*, 25:1, 1964.

[26] Y. Ikedo, J. Sugiyama, H. Nozaki, H. Itahara, J. H. Brewer, E. J. Ansaldo, G. D. Morris, D. Andreica and A. Amato. *Phys. Rev. B*, 75:054424, 2007.

[27] T. Fukai, Y. Furukawa, S. wada and K. Miyatani. *J. Phys. Soc. Jpn.*, 63:4067, 1996.

[28] D.C. Sinclair and A.R. West. *J. Appl. Phys*, 66:3850, 1989.

[29] M. Iliev, S. Anglev, I.Z. Kostadinov, V. Bojchev and V. Hadjiev. *Phys. Stat. Sol*, 71:627, 1982.

[30] N.Mufti, A.A.Nugroho, G.R. Blake and T.T.M. Palstra. *J. Phys: Condens. Matt*, 22:075902, 2010.

[31] F. Schrettle, S. Krohns, P. Lunkenheimer, J. Hemberger, N. Büttgen, H.-A. Krug von Nidda, A. V. Prokofiev, and A. Loidl. *Phys. Rev. B*, 77:144101, 2008.

[32] H. Murakawa, Y. Onose, K. Ohgushi, S. Ishiwata and Y. Tokura. *J. Phys. Soc. Jpn.*, 77:043709, 2008.

[33] G. Catalan. *Appl. Phys. Lett*, 88:102902, 2006.

[34] M. Maglione. *J. Phys: Conden. Matt*, 20:322202, 2008.

General Conclusion and Perspective:

Throughout this thesis we studied the mobility and localization of charges and their effect on dielectric and ferroelectric properties of material. In some cases magnetic properties are studied as well. Under the application of external stresses like electric and magnetic field either the mobility or localization of charges are disturbed leading to interesting property in the material. These charges could be electronic or ionic. As seen in chapter 1 this mobility can be long range motion of charges or local hopping of charges like polarons. Long range motion of charges occurs when the conductivity of the investigated sample is high. Generally this happens at high temperatures where the mobility of ions or electrons is thermally activated. On the other hand short range motion of charges occurs at quite low temperatures where the motion is in the range of unit cell.

Following this, three different Fe doped $BaTiO_3$ single crystals were studied with dielectric spectroscopy under external magnetic field. Out of these three crystals only 0.75 at% and 0.3 at% Fe doped crystals were considered as the crystal quality and doping percentage was not sure for crystal with 0.135 at% Fe. The dielectric spectroscopy on these crystals revealed two relaxations one at high temperature assigned as domain wall relaxation and other at low temperature (≈ 30 K) due to polaron relaxation. The application of external magnetic field on domain wall relaxation show considerable effect on both capacitance and losses. This is due to the fact that the magnetic field affects the localization of free charges (which are created during Fe doping) on domain walls. In particular the effect is more pronounced close to the relaxation maximum as previously shown by Maglione [2]. However we found that this tuning under magnetic field is not reproducible due to the kinetics of interface with temperature i.e. number domain walls varies with each thermal cycling of the sample. On the other hand application of external magnetic field on low temperature relaxation affects only the losses but not the capacitance since here there is no interface for the charge to localize. According to Catalan model we need both free charges and interfaces to affect the capacitance extrinsically [1]. Furthermore we found that losses are affected by magnetic field because the external field affects the way the charges are hopping between centers. This is supported by our results from ESR. It would be also interesting to investigate heterovalent doping in other ferroelectric single crystals for example La doped $BaTiO_3$, La doped $PbTiO_3$, Fe doped $SrTiO_3$ etc. This is planned as future work.

Next we investigated $KTiOPO_4$ (KTP) which has both ferroelectric and conductivity property. The conductivity in KTP is due to the mobility of K^+ ions through the channels which are predominantly along c – axis. The impedance measurement shows that KTP undergoes superionic transition at 200 K

below which it becomes insulator in accordance with previous reports. Also the pyroelectric current appears only below 200 K showing that polarization is screened by conductivity of KTP at high temperatures. Interestingly at the same temperature the piezoelectric resonance undergoes splitting. This shows that there is coupling between conductivity and polarization properties in KTP. This is not surprising since both the ferroelectric property and conductivity in KTP has common origin which is K^+ ions. We would like to point out that such a coupling is observed for the first time as far as we know. It was found that domains cannot cause such splitting as splitting of domains will only cause broadening. It was assumed that the splitting is the direct consequence of creation of space charge due to localization of K^+ ions at the electrode - sample interface which splits the elastic compliance. This in turn affects the resonance frequency to split. The bias electric field experiment points towards the presence of space charge in the sample. To confirm its presence μ-Second Harmonic Generation (SHG) mapping was done on both normal and periodically poled KTP (PPKTP) single crystals. A clear presence of space charge at the interface was seen. Furthermore it was found that a considerable amount of charges are also localized on domain walls in PPKTP. This result was compared to well-known ferroelectric like $BaTiO_3$ single crystals which did not show any such space charge layer. Though μ-SHG map reveals space charge currently it is not possible to understand some of the behavior of the sample for example we don't know why the SHG intensity is decreasing at high temperatures. Therefore more detailed experiments are warranted along with Raman spectroscopy which could shed light on the behavior of KTP with temperature.

As a next step in my thesis we synthesized and characterized new Nasicon type phosphates for potential mutliferroic behavior while they are most of the time investigated for their ionic conductivity. The Nasicon phosphates of formula $BaFeTi(PO_4)_3$ (BFTP) and $BiFe_2(PO_4)_3$ (BiFP) was successfully synthesized by solid state reactions. The compound BFTP crystallizes in centrosymmetric $R\bar{3}c$ space group which is the usual space group of Nasicon type phosphates. However an extra peak was not taken into account by this space group therefore actual space group might be different. This requires good quality single crystals to determine the space group and it is planned for later. On the other hand millimeter size single crystals of BiFP were grown successfully and space group determined by X – ray diffraction indicates $P6_3/m$ with hexagonal symmetry. Full refinement showed that Bi^{3+} cation are statistically displaced away from the symmetrical site along the c axis. This could give rise to polarization at least at the local level. Magnetic measurement of BFTP exhibits an antiferromagnetic type peak at 13 K in ZFC whereas FC curve shows strong irreversibility. Nature of magnetic transition is still ambiguous which calls for further detailed experiments whereas BiFP shows typical antiferromagentic type behavior below 22 K in both ZFC and FC which is taken as the transition temperature. Magnetization as a function of applied field for BiFP points towards a

possible spin flop transition. Dielectric measurement of BiFP on ceramics did not show any ferroelectric type anomaly but they undergo relaxation and the origin of which is still not clear. X – ray diffraction versus temperature in the range of occurrence of dielectric relaxation could be used to link this relaxation to the Bi dynamics. By making suitable substitution in BiFP it might be possible to induce long range order which may invoke ferroelectricity.

Finally we studied Co_3O_4 for potential intrinsic multiferroic behavior. We found that dielectric constant displays a ferroelectric type anomaly exactly at the temperature where Co_3O_4 undergoes magnetic transition. This anomaly was found only under magnetic cooling. Though the anomaly displays frequency independence, lack of evidence from piezoelectric and hysteresis measurements forbade us from assigning this anomaly as ferroelectric instead we call it as polar anomaly. The pyroelectric current shows a broad maximum at 26 K due to decrease in conductivity and a sharp maximum at ≈32 K which was observed only under magnetic field. This shows that there is a strong coupling between electrical and magnetic property in Co_3O_4. From the dielectric and pyroelectric measurements the effect of magnetic field on the space charge seemed to the origin of polar anomaly. However EPR results show a more intrinsic effect due to the canting of antiferromagnetic moments which creates polarization according to spin current model. Growing single crystals of Co_3O_4 is now necessary to thoroughly understand the process leading to induction of ferroelectricity under magnetic field. Single crystal would allow detailed experiments like Neutron, Synchrotron and Raman spectroscopy. Following this it will be worth to reinvestigate simple oxides for novel properties.

References:

[1] G. Catalan. *Appl. Phys. Lett*, 88:102902, 2006.

[2] M. Maglione. *J. Phys: Conden. Matt*, 20:322202, 2008.

List of Figures:

Acknowledgements

"Alone we can do so little; together we can do so much"

— Helen Keller

True to the above statement no great work is possible without the help of others. In that respect my PhD would not be possible if not for many people who have helped me throughout the last three years. This is a small attempt from my side to thank those who have helped me by devoting their time, sharing their knowledge and being patient with me.

First and foremost is my thesis supervisor Dr. Mario Maglione. He has shown great patience with me. Though it is a cliché statement it carries a lot of truth. As I was not from science background I had to learn everything from zero. He has been truly patient in teaching me all those basics which are essentially to lead this PhD. I also admire his diligence and sincerity that he has shown in his job. He has been an excellent mentor and very supportive throughout my PhD. I was also impressed by his interest in willingness to participate in experiments. It is suffice to say that without him my PhD wouldn't be successful. Thank you Mario for all the help you have extended to me.

Next I would like to thank Dr. Claude Delmas for providing me an opportunity to do my PhD at ICMCB. Thanks also for your valuable advice and discussions especially in the solid state chemistry part.

I am also greatly indebted to Dr. Jacques Darriet for his help in structure determination. His enthusiasm in research has motivated me to a great extent in my PhD. I regret to say that often I could not keep up with your speed. Thank you Jacques I learned a lot from you.

My sincere gratitude also goes to Dr. Alla Artemenko for helping me in ESR spectroscopy and for invaluable discussion I had with her. Thank you Alla for your help and interpretation of ESR results, I had great fun working with you.

I am also greatly indebted to Prof. Vincent Rodriguez (ISM) for providing his time and help with regard to Second Harmonic Generation experiment. I also appreciated his friendly demeanor towards me. He has have been very patient to answer some of the basic questions posed by me. Thanks a lot Vincent, I am fortunate to have worked with you.

My heartfelt thanks to all the members of group 4 for an enriching and a memorable experience. I always felt I was one of you irrespective of my origins. I really appreciate the effort you all made in integrating me. I will always remember the discussions we had over coffee and lunch time and of course the experience of doing research with you all. I would like to thank you all for trying to teach me French though at times I tested your patience.

I have had the privilege of working with other researchers in the lab who came out of their way to help me. I would like to thank them here. They are Rodolphe Decourt, Benoit Glorieux, Philippe Veber, Christine Labrugere, Cathy Denage, Alain Wattiaux , Olivier Nguyen, Eric Lebraud, Stéphane Toulin, Viraphong Oudomsack, Lionel Teule-Gay. However this list not exhaustive.

This section wouldn't be complete without acknowledging my girl friend Louise Savri. Her presence by my side through good and bad times has enabled me to face any situation. Without her I would have succumbed to stressful situation during the past three years. Equally her parents had been a great source of support and motivation. Thank you Louise for your unconditional love and support.

I would also like to thank all my friends who have supported and encouraged me throughout my thesis.

Finally I would like to thank my loving parents for their affection, care and sacrifice and also for believing in me irrespective of their ordeals. I have no hesitation in saying that my success is not possible without their encouragement and affection. I am fortunate to have you as my mom and dad. My gratitude also goes to my sister Vidhya and her husband Vijay for their support and coming all the way from Scotland.